CFD Modelling of Hydrogen Safety Aspects for a Residential Refuelling System

By

Thomas Beard

A Doctoral Thesis

Submitted in partial fulfilment of the requirements for the award of Doctor of Philosophy of Loughborough University

June 2017

Wolfson School of Mechanical, Electrical and Manufacturing Engineering

Loughborough University

Abstract

This work concerns the modelling of scenarios for a residential hydrogen refuelling system. Such a system is under construction within the Engineering Safe and Compact Hydrogen Energy Reserves (ESCHER) project. Non-reacting and reacting simulations are compared against experimental data before being applied to a residential garage scenario. The non-reacting simulations utilise natural ventilation, which utilises the natural buoyancy of hydrogen and vent locations to disperse flammable mixtures. This is favoured over mechanical ventilation, which could fail.

The non-reacting work focuses on investigating the most suitable venting configuration for a release of hydrogen from a refuelling system located within a residential garage. Different vent configurations are examined initially before proceeding to take into account atmospheric conditions, wind, and the presence of a vehicle for the two best venting configurations. This is to determine the venting configuration that would diminish the accumulation of a flammable mixture, as well as dissipating the mixture quickest after the release has stopped. The modelling strategy utilised for this work is validated against two different sets of experimental data, prior to the investigation into residential garages. The predicted and experimental results show good agreement for the modelling procedure suggested.

The reacting investigations are for both premixed and non-premixed combustion. The non-premixed combustion investigates the temperature distributions and as such the possible harm to people for such a scenario, compared against experimental data. The results show some over predictions of the temperatures. The premixed combustion investigates the potential overpressures that may occur if a homogeneous mixture was to form and ignite, within a residential garage. This work is preceded by a validation of the combustion model with the predicted results compared to data from The University of Sydney. The validation results show that the modelling strategy matches the peak overpressures accurately.

The non-reacting studies show that having a lower vent opposite the release and an higher vent near the release produces the smallest flammable mixture as well as dissipating the mixture to the external surroundings quickest. The non-premixed reacting work shows good agreement with experimental results. The premixed

reacting work shows that the garage would destruct with major consequences to people and surroundings. This work would be applicable to any potential usage of indoor refuelling for hydrogen vehicles, helping to determine a suitable configuration for mitigating hydrogen releases. It should be noted that all such work is geometrically dependent and as such the strategy proposed would be useful for investigating individual scenarios.

Acknowledgements

It is with gratitude, that I would like to acknowledge all of the people that have helped and supported me. This work would not have been possible without them.

Firstly, I am extremely obliged to my main supervisor Professor Weeratunge Malalasekera for his constant help, advice and support throughout the entirety of this work. I am also thankful to my second supervisor Dr Salah Ibrahim for the advice and support, especially on the combustion modelling performed for the premixed combustion validation. I would also like to thank all of the academics working on the Engineering Safe and Compact Hydrogen Energy Reserves (ESCHER) project.

Secondly, I would like to acknowledge the Wolfson School of Mechanical, Electrical and Manufacturing Engineering for providing the studentship for this work, without which this work would not have been possible.

I would like to express gratitude to my colleagues Dr Maxim Bragin, Dr Mohamed Abdel-Raheem, Asela Uyanwaththa and Ruipengyu Li (Brendan) for the conversations regarding hydrogen safety, modelling and combustion. I am thankful to my close friends Joe Paterson and Joe Wood for their support throughout the process as we embraced the rollercoaster together.

Finally I leave the biggest obligations to my family for their support and encouragement throughout the entire process, without which I doubt this work would have been finished.

Publications

1. **Beard, T.**, Bragin, M., Malalasekera, W. and Ibrahim, S.S. (2014). Numerical simulation of hydrogen discharge in a partially enclosed space. *12th International Conference on Combustion and Energy Utilisation (ICCEU)*. University of Lancaster, UK.

2. Bragin, M., **Beard, T.**, Malalasekera, W. and Ibrahim, S.S. (2015). Numerical simulation of hydrogen release and combustion into an enclosure. *8th International Conference on Sustainable Energy and Environmental Protection (SEEP)*. University of West of Scotland, UK.

3. **Beard, T.**, Bragin, M., Malalasekera, W. and Ibrahim, S.S. (2015). Numerical simulation of hydrogen combustion in an enclosure. *Institute of Physics, Combustion Physics Group Early Career Researchers Meeting*. Loughborough University, UK.

4. **Beard, T.**, Malalasekera, W. and Ibrahim, S.S. (2015). Numerical simulation of hydrogen release into a hypothetical residential garage. *Midlands Energy Consortium Postgraduate Student Conference*. Loughborough University, UK.

5. **Beard, T.**, Bragin, M., Malalasekera, W. and Ibrahim, S.S. (2015). Numerical simulation of hydrogen discharge in a partially enclosed space. *Energy Procedia*, 66, 153-156.

6. **Beard, T.**, Bragin, M., Malalasekera, W. and Ibrahim, S.S. (2017). Numerical simulation and validation of hydrogen dispersion in partially enclosed geometries. To be submitted to *International Journal of Hydrogen Energy*.

Contents

Nomenclature

Latin Letters

b	Progress Variable
C	Model Constant
C_{EBU}	EBU Model Constant
C_p	Heat Capacity (J/ kg-K)
$C_{\varepsilon 1}$	Model Constant
$C_{\varepsilon 2}$	Model Constant
C_μ	Model Constant
D	Diffusion Coefficient
D_ω	Cross Diffusion Term
F_i	Body Forces
h	Mixture Enthalpy (J)
h_k	Species Specific Enthalpy (J/kg)
k	Turbulent Kinetic Energy (m^2/s^2)
ℓ	Turbulent Length Scale (m)
Le_k	Lewis Number
m	Mass of Substance (kg)
n	Model Constant
P	Pressure (Pa)
$\tilde{P}$	Probability
P_k	Turbulence Source Term

R	Radial Position (m)
r	Radius (m)
s	Stoichiometric Ratio
Sc_k	Species Schmidt Number
S	Source Term
t	time (s)
T_i	Turbulence Intensity
u	Velocity (m/s)
W	Molecular Weight (kg/kmol)
x	Geometrical Spacing (m)
Y	Mass Fraction
Z	Mixture Fraction
Z''^2	Mixture Fraction Variance

Greek Symbols

δ_{ij}	Kronecker's Delta
ε	Turbulent Energy Dissipation Rate (m^2/s^3)
ϑ	Turbulent Velocity Scale (m/s)
μ	Dynamic Viscosity (kg/m-s)
μ_t	Turbulent Viscosity (kg/m-s)
ρ	Fluid Density (kg/m^3)
σ_h	Prandtl Number
τ_{ij}	Viscous Stress Tensor

τ_t	Turbulent Mixing Time (s)
ϕ	Scalar Quantity
ϕ	Equivalence Ratio
χ	Scalar Dissipation Rate (1/s)
ω	Turbulence Frequency (1/s)
$\dot{\omega}$	Reaction Rate (kg/s)

Subscripts and Superscripts

b	Burnt
f	Fuel
i, j, k	Vector Direction
k	Species
max	Maximum
mean	Average
o	Oxidiser
R	Radial Position
ref	Reference
rms	Root Mean Square
t	Turbulent
u	Unburnt

Operations

$\bar{}$	Mean
$\tilde{}$	Favre Average

′ Fluctuations

Abbreviations

ATEX Atmosphères Explosibles

CFD Computational Fluid Dynamics

CJ Chapman Jouget

DDT Deflagration-to-Detonation Transition

DNS Direct Numerical Simulation

DSEAR Dangerous Substances and Explosive Atmospheres Regulations

EBU Eddy Break-Up Model

EDC Eddy Dissipation Concept Model

ESCHER Engineering Safe and Compact Hydrogen Energy Reserves

FDS Fire Dynamic Simulator

FSI Fluid Structure Interactions

HSE Health and Safety Executive

HSL Health and Safety Laboratory

HS-LIF High Speed Laser Induced Fluorescence

ISAT In-Situ Adaptive Tabulation

LES Large Eddy Simulation

LFL Lower Flammability Limit

LIF Laser Induced Fluorescence

LPG Liquid Petroleum Gas

NIST The National Institute of Standards and Technology

PDF Probability Density Function

PPDF	Presumed Probability Density Function
PRD	Pressure Relief Device
RANS	Reynolds-Averaged Navier Stokes
RNG	Renormalisation Group
SCRS	Simple Chemical Reacting System
SGS	Sub Grid Scale
SIMPLE	Semi-Implicit Method for Pressure-Linked Equations
SST	Shear Stress Transport
SWACER	Shock Wave Amplification through Coherent Energy Release
SwRI	Southwest Research Institute
TFC	Turbulent Flame Speed Closure Model
TNF	Turbulent Non-Premixed Flames

List of Figures

List of Tables

Chapter 1 – Introduction

1.1 Introduction

The emissions from the procurement and use of fossil fuels for energy are becoming a major issue. The 2015 United Nations Climate Change Conference, in Paris, had a major focus on reducing the global temperature increase. There is a specific focus on reducing CO_2 emissions, which will reduce the global temperature rise and by extension damage to the environment (The Committee on Climate Change, 2015). The major sectors that produce CO_2 in the UK are Power, Transport and Industry. The majority of CO_2 in the sectors mentioned is commonly from the use of fossil fuels. There are various solutions for these sectors that can be implemented with the exception of transport. This is one of the more difficult areas to replace fossil fuels (The Committee on Climate Change, 2015). The use of carbon capture storage could aid in the reduction of CO_2 however we are also seeing a depletion of fossil fuels, so a green replacement would be superior.

The government needs to decide on the routes that it wishes to take to reach its commitments to the emissions reductions. This is especially prevalent in the transport sector (The Committee on Climate Change, 2015). There are two solutions for the transport sector, one is to use electric vehicles and the other is hydrogen fuelled vehicles. However hydrogen as a fuel has its benefits, due to the storage capacity compared to batteries used for electric vehicles. The downside to both technologies is the recharging stations/system. Electric recharging takes some time for a full charge, whilst hydrogen refuelling stations are sparse (Tobin, 2015). This is shown in Figure 1, a map of the UK that highlights all accessible hydrogen refuelling stations (Zap Map, 2016).

Another problem with electric cars is that most have an approximate range of 100 miles, with the exception of Tesla but that comes at a hefty price (Carbuyer, 2016; Schaal, 2015). The advantage for hydrogen cars is that the range is 300+ miles on a full tank (Carbuyer, 2015; Vaughan, 2015). However this is currently mitigated by the lack of infrastructure for refuelling and thus reduces the effective range to half the full range, 150+ miles.

Figure 1 A map of the hydrogen refuelling stations currently within the UK (Zap Map, 2016).

The potential use of hydrogen as an energy source for domestic transport was also increased greatly when Toyota released the patents on a lot of their hydrogen vehicles (Financial Post, 2015). Yet still the problem facing the UK is the lack of infrastructure, with ITM Power opening the first hydrogen refuelling station outside of the South of England, in Yorkshire in 2015 (BBC, 2015; Markillie, 2015). However there is still a major lack of refuelling stations, as shown in Figure 1, this is what the ESCHER project research aims to achieve.

The ESCHER project is aimed at producing a residential hydrogen refuelling system via a two stage metal hydride compression system to produce the required pressure for delivery to a hydrogen vehicle. The total amount of hydrogen to be supplied to the vehicle is 600 g which should be enough for daily commuting. This should also be enough to get someone to the nearest public hydrogen refuelling station, when they increase in number. This work is performed jointly with the Universities of Nottingham and Birmingham, who have worked on developing the materials and designing the

system. There is also a need to prove the safety of such systems and how to mitigate any dangers that may arise, this work aims to address such issues.

The safety is a big concern with any new equipment but compounded further when it involves hydrogen. This is not just because of the risks associated with hydrogen but more so the public opinion of it. Historical incidents such as the Hindenburg (airships.net, 2009) and Fukushima Daiichi disasters (World Nuclear Organisiation, 2015) to name a few, do not help with the perception. The aforementioned disasters consisted of hydrogen combustion, however this is possible for other fuels as well. This is similar to airplanes that combust due to faults (National Transportation Safety Board, 2000). Unfortunately it normally takes an accident before people take notice of errors and design flaws.

The safe usage of hydrogen as a fuel for transport is evident by an experiment performed in America by (Swain, 2001). A hydrogen car and a petrol car were both ignited, in different places on the vehicles because the leak sources were different. The conventional (petrol) vehicle had a leak source underneath the car, replicating a break in the fuel line. The hydrogen vehicle had a leak source at the top of the storage tank, replicating the pressure relief device (PRD) in operation. The hydrogen vehicle was also built to industrial standards, circa 2000. The two leak sources were chosen because they are the most severe single failure modes (Swain, 2001). Figure 2 – 4 show the outcomes from the experiment.

Figure 2 Shows a hydrogen car (left) and conventional car (right) at time 0 seconds.

Figure 3 Shows a hydrogen car (left) and conventional car (right) at time 3 seconds.

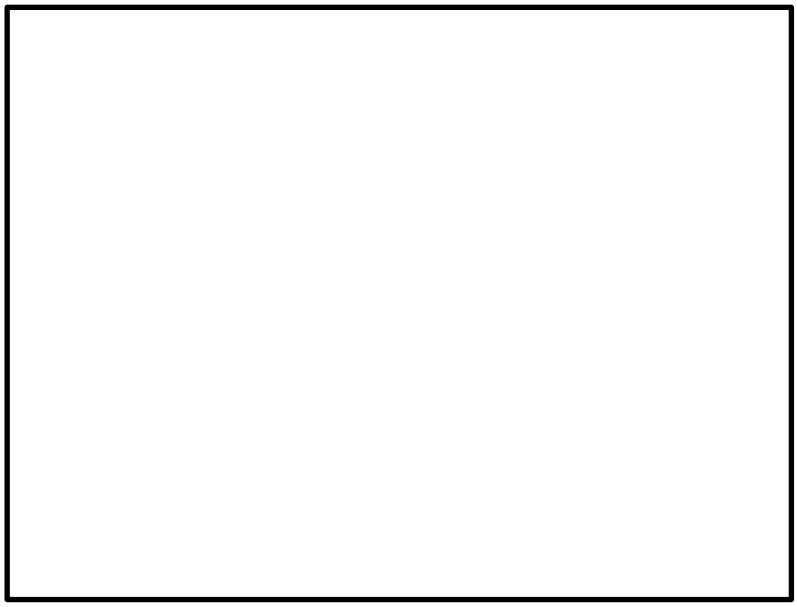

Figure 4 Shows a hydrogen car (left) and conventional car (right) at time 60 seconds.

Figure 2 shows the hydrogen car on the left and petrol car on the right. This is at time zero, and as such prior to ignition. Figure 3 is three seconds after ignition. It is clear that the hydrogen car has a jet flame from the boot of the vehicle whilst the petrol car has a flame underneath the centre of the car. This then proceeds to Figure 4 which is 60 seconds after ignition. Here the hydrogen flame is diminishing; this is due to the tank pressure and as such the amount of hydrogen left in the tank. It would seem that there is no damage to the vehicle, whilst the petrol car has been fully engulfed by the fire. This information could help to alleviate the public perception of the dangers of hydrogen as a fuel. However this is solely dependent on the failure mode and thus

the location of the leak and ignition. A different failure mode and by proxy different release location could significantly alter the results.

1.2 Motivation

The work contained within this thesis uses CFD modelling, with the commercial code STAR-CCM+, as a tool for investigating hydrogen safety for refuelling within a residential setting. The numerical modelling is designed to capture the varying physical processes as well as the complex chemical interactions that occur when hydrogen is released indoors from a refuelling system. Various parameters can be examined with much greater ease than experimental techniques, at less expense and with no potential for accidents.

The need for this is such that the modelling criteria would become publicly available and is easier to use than an in-house code. The possible repeatability of this work could aid others to utilise this work for other geometrical configurations. This would then help to pave the way for a hydrogen infrastructure and the use of hydrogen as a fuel for transport. The conclusions from this work would be useful, although this work is geometrically dependent, hence the results may alter for different geometries. This work also differs from current research by other institutions as this focuses on a different release location. The majority are investigating hydrogen released from a car in an enclosure, whilst this work treats the car as a solid obstacle, instead the release is from a refuelling system within this work.

The combustion of hydrogen, especially when confined, is also of importance. This is because the harm to humans as well as the damage to structures is also of interest. There is the possibility of an explosive mixture forming, this work utilises a homogeneous mixture to investigate such phenomenon. These scenarios are investigated to gain knowledge into the potential behaviour of the various phenomena within enclosures.

This work is useful for the progression of hydrogen infrastructure. This has the potential to revolutionise the transport sector and more whilst helping to reduce emissions. Coupling this with further research has the potential to make hydrogen the ‘new petrol’.

1.3 Objectives

The main objective of this research is to determine the most suitable ventilation configuration, to limit the associated risks attached to residential hydrogen refuelling. A secondary objective is to determine the potential harm if ignition was to occur. The following objectives will combine to answer the two above:

1. Determine a suitable modelling strategy, mesh and turbulence model, for non-reacting scenarios when hydrogen is released into an enclosure.
2. Investigate the venting strategies for non-reacting releases, within the setting of a residential garage and under various atmospheric conditions. This is aligned against proposed safety criteria.
3. Investigate the modelling strategies for reacting premixed hydrogen explosion scenarios.
4. Investigate the modelling strategies for reacting hydrogen diffusion flames arising from releases.
5. Investigate the potential harm and/or damage that may occur in the eventuality of a hydrogen release igniting after a homogeneous mixture has developed.

1.4 Thesis Outline

Chapter 1 gives a brief introduction to the reasoning behind this study and its importance. The current perception of hydrogen is explained and how this study can change the public opinion. Previous research is shown which would help to alter public opinions whilst the findings from this work would also add to this.

Chapter 2 is the literature review which outlines the current research and regulations within the field. There is particular focus on hydrogen dispersion, combustion and harm criteria.

Chapter 3 is the background theory of numerical modelling and combustion. This will show the governing equations solved and the numerical techniques employed within the software. Combustion theory for the various regimes and how they can be solved is also explained.

Chapter 4 is the dispersion validation, which was completed for two different experiments. The first validation; is for different turbulence models and a mesh sensitivity study. The second then employs the results from the first for further validation on a different geometry.

Chapter 5 is the dispersion studies which consist of simulations on a geometry that resembles a residential garage. The studies investigate various venting configurations, atmospheric conditions and vehicular presence against a proposed set of criteria. The aim of this is to determine the best ventilation configuration which would reduce the flammable volume present were a hydrogen release to occur.

Chapter 6 considers modelling of premixed hydrogen for reacting safety assessments. This chapter investigates a homogeneous mixture comparing results against experimental data using the University of Sydney combustion chamber. The aim is to determine the most suitable strategy for modelling this phenomenon.

Chapter 7 is the non-premixed models for reacting safety assessment. This is a validation for the non-premixed combustion regime. Established data, in the form of the Sandia flame, is used for the validation of non-premixed combustion modelling.

Chapter 8 considers the application of the reacting modelling strategies discussed in chapters 6 and 7. This chapter contains both of the combustion regimes discussed previously. The first section investigates a homogeneous mixture using the same geometry as chapter 5. This is then compared against the harm criteria outlined in chapter 2, to determine the potential harm and damage that is possible. The second section investigates diffusion flames using a geometry similar to a garage.

Chapter 9 is the conclusions which summarises the study and deduces the contributions that have been made throughout the work. There is also an outline for potential work in the future.

Chapter 2 – Literature Review

2.1 Introduction

This chapter is a review of the literature that is relevant to the work. Firstly, the chemistry of hydrogen is discussed, with a comparison against some common fuels. This is followed by the safety considerations, which reviews harm criteria and current regulations. Recent works for non-reacting releases of hydrogen are covered next. This consists of numerical and experimental work, and is used to deduce areas for further investigation. This is followed by recent numerical and experimental work on hydrogen combustion. The aim of this work is the same as the previous, in that it is used to shape the areas of investigation for this work. Finally a brief overview of metal hydrides is given. This is because metal hydrides are going to be used in the refuelling system.

2.2 Hydrogen Chemical Properties

Hydrogen is one of the most abundant elements by mass on Earth. In normal conditions it is seen as dihydrogen, H_2, which is nominally referred to as hydrogen. The hydrogen atoms are bonded together via a covalent bond; this is due to the atomic arrangement of a single electron. The hydrogen molecule has a bond enthalpy of +436 kJ mol^{-1} and a bond length of 74 pm (Atkins et al., 2010; Molkov, 2012). Hydrogen is colourless, odourless and lighter than air (Molkov, 2012; Pritchard et al., 2009). Hydrogen consists in two forms, either ortho- or para-, these depend on the nuclear spins of the atomic hydrogen in the diatomic. Ortho-hydrogen has parallel spin states while para-hydrogen has the opposite. The two different spin states have a minimal difference in chemical properties, especially on the combustion chemistry. The majority of data applies to normal hydrogen, which is 75% ortho- and 25% para-hydrogen, which are considered at room temperature (Molkov, 2012).

There is quite a difference between hydrogen and other widely used fuels. Table 1 shows a comparison of some key characteristics for hydrogen, natural gas and LPG. Data is taken from (H2tools.org, n.d.; Lewis and von Elbe, 1987; Molkov, 2012; Pritchard et al., 2009; U.S. DOE, 2015, 2009).

Hydrogen has a low viscosity in comparison with methane and propane which means that it has a higher propensity to leak. This raises issues when making sure a system will contain hydrogen. When combined with the vast flammability and detonability ranges this means the chance of an ignition and as such combustion occurring is increased. Although the lower flammability limits of all three chemicals are very similar, the lower ignition energy of hydrogen means there is a higher probability of ignition. The low ignition energy of 0.02 mJ is for a 2:1 H_2:Air mixture (Lewis and von Elbe, 1987; Pritchard et al., 2009). However the low density and high diffusivity of hydrogen means that hydrogen would want to rise and disperse. Incorporating this inbuilt safety mechanism with a vent would mean that the hydrogen can release to atmosphere over time, thus lowering a flammable volume. This is especially the case if the geometry containing a leak is well ventilated. However the high diffusivity of hydrogen could also cause it to diffuse into materials used for construction (Molkov, 2012). The low density of hydrogen means that it is extremely buoyant and will accumulate at the greatest possible height. This effect is seen as one of the greatest assets of hydrogen, due to its inherent safety contribution (Molkov, 2012).

When hydrogen combusts the flame is almost invisible, thus making it very difficult to detect. The maximum burning velocity of hydrogen, 6.4 times greater than the other common fuels, can be both dangerous and helpful. It is dangerous because it causes the flame to be very difficult to stop or confine, this is why the suggestion for a hydrogen flame is to leave it to burn whilst shutting off the gas supply. There is also the increase in rates of pressure rise and the chance for a greater explosion pressure. The quicker flame speed decreases the probability of secondary fires occurring. Although the hydrogen flame is almost invisible the heat and turbulent effects on the surrounding atmosphere combined with the combustion products yield a fire signature (Molkov, 2012). This is only helpful when you know what you are looking for/at.

Table 1 Characteristics of hydrogen, natural gas and LPG.

Property	Hydrogen	Natural gas	LPG
Density (kg/m^3) *	0.09	0.8	1.88
Viscosity (Pa-s x 10^{-6}) *	0.083	0.651	0.819
Diffusion coefficient in air (m^2/s x 10^{-4}) *	0.61	0.16	0.12
Specific heat, constant pressure (J/g-K)	14.89	2.22	1.56
Flammability limits in air (vol%)	4.0 – 75.0	5.3 – 15.0	2.1 – 9.5
Detonability limits in air (vol%)	13.0 – 65.0	6.3 – 13.5	3.1 – 7.0
Ignition energy in air (mJ)	0.02	0.29	0.26
Auto-ignition temperature (°C)	585	540	487
Flame temperature in air (°C)	2045	1875	1925
Maximum burning velocity (m/s)	2.6 – 3.06	0.39 – 0.45	0.45 – 0.47
Quenching gap (mm) *	0.6	2.0	2.0
Thermal energy radiated to surroundings from flame (%)	5.0 – 10.0	10.0 – 33.0	10.0 – 50.0

*at normal temperature and pressure – 1 atmosphere and 20°C

The vast detonability range of hydrogen does mean that there is a higher risk of detonation. This is mitigated by its increased diffusivity and buoyancy, which makes the detonability range to be reached when outside.

There are two different equations of state that can be used when modelling a release of hydrogen, the ideal gas equation or the real gas equation, although the pressures stored at mean the ideal gas equation is suitable. However it depends on the storage conditions as to which equation is used. For releases with a pressure below 10 MPa the ideal gas equation is suitable; however above 10 MPa the real gas equation should be used. This is because hydrogen will not behave ideally. The consequence of using the wrong equation is that the ideal gas equation would over-predict the mass flow rate and therefore the total mass released (Molkov, 2012) .

When reacted with oxygen a highly exothermic reaction occurs. Although at normal temperatures the reaction proceeds very slowly, unless the reaction is activated by either a catalyst or a spark. When this happens the reaction proceeds at a quicker rate such that an explosion can be seen. The stoichiometric mixture is a mixture where all the reactants, fuel and oxidiser, are consumed (Molkov, 2012). This is shown by the following:

$$2H_2 + O_2 \rightarrow 2H_2O \qquad \Delta_r H^\theta = -242\ kJ\ mol^{-1}$$

Therefore the stoichiometric concentration of hydrogen in oxygen is 66.6%. However the stoichiometric mixture in air is of much greater importance. Assuming air is just made up of 21% oxygen and 79% nitrogen, by volume. This is excluding the minority substances that actually make up about 1% of the ambient air. The chemical reaction within air is:

$$2H_2 + (O_2 + 3.76N_2) \rightarrow 2H_2O + 3.76N_2$$

This creates a stoichiometric concentration for hydrogen of 29.59% by volume, calculated via [2/(2+1+3.76)=0.2959].

The equivalence ratio is the ratio between the actual fuel-to-oxidiser ratio and the stoichiometric fuel-to-oxidiser ratio. There are two different ways of calculating this number, either using the mass or the number of moles. Using either method will yield the same result, as the equation is dimensionless. An equivalence ratio of one is a stoichiometric mixture, less than one is a lean fuel mixture and greater than one is a fuel rich mixture (Molkov, 2012; Poinsot and Veynante, 2005; Turns, 2000; Versteeg and Malalasekera, 2007).

Another method is to use the fuel-oxidiser ratio. However this yields different answers when using mass or number of moles. Therefore it seems advantageous to use the equivalence ratio (Molkov, 2012; Poinsot and Veynante, 2005; Turns, 2000; Versteeg and Malalasekera, 2007).

Due to the way hydrogen can dissociate from its diatomic form. There is a chance of free atoms at higher temperatures. Due to the nature of this splitting it can be a strong reducing agent. This is especially the case when diffusing from the high temperature flame to the pre-heating area in front of the flame. The heat released when the atoms recombine can increase temperatures (Molkov, 2012). Hydrogen can dissociate either homolytically or heterolytically. Homolytic dissociation is when the bond breaks symmetrically, giving one product. Heterolytic dissociation is when the bond breaks unsymmetrically, giving two products (Atkins et al., 2010).

Homolytic dissociation:

$$H_2(g) \rightarrow H(g) + H(g) \qquad \Delta_r H^\theta = +436\ kJ\ mol^{-1}$$

Heterolytic dissociation:

$$H_2(g) \rightarrow H^+(g) + H^-(g) \qquad \Delta_r H^\theta = +1675\ kJ\ mol^{-1}$$

The two different dissociation methods would yield different reaction mechanisms for combustion. Homolytic dissociation would be expected first due to the lower enthalpy. It is envisaged that during combustion, as the temperature rises, the reaction mechanism could follow the heterolytic route.

The Homolytic dissociation actually produces hydrogen radicals. The currently understood reaction between hydrogen and oxygen occurs via a radical chain mechanism (Atkins and de Paula, 2009). The forward mechanism has about 20 reactions, yielding a total of 40 reactions when the reverse reactions are taken into account. There are 8 main species involved which are: H_2, O_2, H_2O, H, O, OH, O_2H and H_2O_2. These are aided by another chemical that removes excess energy from the system (Atkins and de Paula, 2009; Mueller et al., 1999) are just some of the people that have expressed this.

There are many detailed reaction mechanisms produced for hydrogen combustion. The reaction mechanism used depends on many different parameters. The main parameters are the equivalence ratio, pressure, temperature and flame type (Konnov, 2008; Strohle and Myhrvold, 2007, 2006). When trying to create or use a reduced mechanism there are different issues that arise. The usefulness of a reduced mechanism depends on the area of interest; different parts of a reduced mechanism are more relevant for certain areas. For example, a mechanism that is needed for auto-ignition may not be as valid for flame speed (Strohle and Myhrvold, 2007, 2006). Mechanisms can perform very well under some conditions and then poorly under others. However some are seen to perform better in general than others and just need minor adjustments. Fundamental mechanisms such as (Mueller et al., 1999; Warnatz et al., 1999) are used as starting points. However some reactions are over looked in mechanisms, hence the varying number of reactions, although this can be due to the conditions that are being investigated (Hong et al., 2011; Lewis and von Elbe, 1987).

The reaction mechanisms all precede in stages; starting with initiation, ending with extinction and other reactions including chain-branching occurring as intermediaries. There are many different views on the reactions that can occur at these steps, some brief reactions are described as follows (Atkins and de Paula, 2009; Warnatz et al., 1999):

$$H_2 + O_2 \rightarrow 2OH$$

$$H_2 + OH \rightarrow H_2O + H$$

$$H + O_2 \rightarrow OH + O$$

$$H_2 + O \rightarrow OH + H$$

$$O_2 + H + M \rightarrow HO_2 + M$$

This brief mechanism (Atkins and de Paula, 2009; Warnatz et al., 1999) does not include all of the species that can contribute to the reaction mechanism, although it does show how complex the reaction can be. There are still many other ways for the reaction to start, precede and finish (Kuo, 1986; Lewis and von Elbe, 1987; Turns, 2000).

2.3 Safety Considerations

2.3.1 Safety Objectives

The safety assessment of any installation is of utmost importance. The provision of such an assessment needs a defined set of objectives aligned against relevant harm criteria. This section reviews the relevant criteria.

There are three standard safety requirements for any system, including the use of hydrogen systems indoors. These are the preservation of, and safety to, life as well as the protection of property and the environment.

The priority is obviously for safety of life, although protection of property could affect this. This is normally for residents and the general public. However site workers and first responders also need to be taken into account. The targets for life safety are as follows (Saffers and Molkov, 2014):

1. Residents can depart the building in a timely manner, or the consequences to residents are acceptably low.
2. First responders can operate in reasonable safety.
3. The collapse or debris from failure does not endanger first responders or people near the building.

Architects and building designers would need to take into consideration methods of reducing damage during design of new builds, specifically estates. This is such that the escalating effect of damages on surrounding property is limited or preferably prevented (Saffers and Molkov, 2014).

The environmental impact from any potential accident needs to be estimated and considered during the planning phase. This is mainly to diminish the probability of a domino effect occurring. The effects on fauna and flora, asphyxiation and cold burns, also need to be acknowledged. This is performed by the local authority and any potential regulatory bodies for residential buildings. When industrial bodies are involved the Health and Safety Executive (HSE) become involved.

2.3.2 Overview of Relevant Harm Criteria

There are numerous potential negative consequences, for humans and the environment, which need to be taken into account for indoor hydrogen installations. These criteria are discussed and surmised in the ensuing sections.

2.3.2.1 Asphyxiation

Evacuation for risk of asphyxiation would be needed when volumetric concentrations of hydrogen are greater than or equal to 9% by volume. This is when initial signs of asphyxiation are shown due to oxygen displacement, whilst there is a risk to life with concentrations greater than or equal to 42% (HySafe, 2007).

2.3.2.2 Temperature

The temperature effects on humans are dependent on the surrounding air temperatures. This is specifically the case within enclosures where the high air temperature can be more critical compared to the thermal radiation (Hundseid and Ingebrigtsen, 2001). Table 2 outlines the temperature effects on humans at varying levels with data taken from (Bryan, 1986; Hundseid and Ingebrigtsen, 2001).

Table 2 Effect of air temperature on humans.

Temperature (K)	Temperature (°C)	Physiological Response
400	127	Difficulty breathing.
413	140	5 minute tolerance limit.
422	149	Temperature limit for escape. Difficulty breathing by mouth.
433	160	Rapid, unbearable pain with dry skin.
455	182	Irreversible injury after 30 second exposure.
476	203	<4 minute tolerance for respiratory systems with wet skin
582	309	Third degree burns after 20 second exposure. No escape possible.

2.3.2.3 Thermal Radiation

The thermal radiation emitted by a flame may also have consequences on life, as well as on structures. The thermal radiation emitted is characterised by a radiant heat flux. It is recommended that people do not exceed a heat flux of 5 kW/m^2 when outside (Raj, 2008). However in certain circumstances this is unavoidable. Therefore the radiant heat fluxes that can cause harm to humans are characterised in Table 3. The data is taken from (Lees, 1996; Raj, 2008; Saffers, 2010).

Table 3 Effect of radiant heat fluxes on humans.

Radiant Heat Flux (kW/m^2)	Physiological Response
1.5	None – Safe level for public.
5	Tolerable for first responders with adequate protective clothing.
6	Maximum exposure for occupants. Painful in 12 seconds and lethal after 38 seconds.
9.5	2^{nd} degree burns after 20 seconds.
12.5 – 15	1^{st} degree burns within 10 seconds. 1% mortality rate within 1 minute.
25	100% mortality rate in 1 minute. Significant injury in 10 seconds.
35 – 37.5	1% mortality rate within 10 seconds.

The radiant heat fluxes that can cause damage to structures and the environment are shown in Table 4. The heat fluxes for structural damage are significantly higher than those for humans. The data is taken from (Lees, 1996; Saffers, 2010)

Table 4 Effect of radiant heat fluxes on structures and the environment.

Radiant Heat Flux (kW/m^2)	Environmental and Structural Response
5	Significant window damage.
8 – 12	High propensity for the domino effect.
10	Heating of structures. Increase of temperature and pressure in liquid and gas storage.
16	Structural failure for prolonged exposure, excludes concrete.
20	Concrete structures can withstand for prolonged period of time, several hours.
30	Non-pilot ignition of wood.
38	Damage to process equipment and storage tanks.
100	Weakening of steel.
200	Concrete structures fail in 30 – 60 minutes.

2.3.2.4 Over-pressure

The over-pressure is the pressure increase above the local atmospheric pressure. This is normally caused by combustion and/or explosions. Over-pressure can have catastrophic consequences for humans, both direct and indirect. The direct consequences of over-pressures are shown in Table 5, the data is from (Gallego and Valero, n.d.; Saffers, 2010; Stewart, 2010; Zipf and Cashdollar, n.d.).

Table 5 Effect of direct over-pressure contact on humans.

Over-pressure (kPa)	Physiological Response
6.9 – 8	Minor injuries to people in the open.
10 – 21	Serious injuries to people inside, with some fatalities.
30	Increased risk of fatality inside.
34 – 105	Ear drums rupture, potential limitation on evacuation.
54	Fatal head injuries occur.
560	Severe lung damage occurs.
910	50% mortality rate inside, 15% in the open.
1400	100% mortality rate inside.

The indirect consequences of over-pressure on humans are shown in Table 6, again taken from (Saffers, 2010; Zipf and Cashdollar, n.d.). The in-direct consequences yield from structures being impacted by a pressure wave.

The word missile corresponds to any object that is forced to move by the pressure wave. They are normally caused by fragmentation of structures.

Structural damage caused by over-pressure can also have consequences for people, even if they were lucky enough to not be effected initially. The structural response to over-pressure is given in Table 7, the information is taken from (Lees, 1996; Mercx et al., 1991; Saffers, 2010; Zipf and Cashdollar, n.d.).

The other major consequence that could happen is the domino effect to neighbouring structures. The threshold for this can be defined as 20 kPa (Saffers, 2010).

Table 6 Effect of indirect over-pressure contact on humans.

Over-pressure (kPa)	Physiological and Structural Responses
3 – 6.9	Glass fragments, producing missiles that cause damage.
6.9 – 13.8	Skin lacerations caused by missiles.
10.3 – 20	People knocked down by pressure wave.
13.8	Potential to be thrown against objects by pressure wave.
27.6 – 34.5	50% mortality rate caused by missile wounds.
48.3 – 68.9	100% mortality rate caused by missile wounds.

Table 7 Effect of over-pressure on structures.

Over-pressure (kPa)	Structural Response
0.7 – 1	5% of window panes break.
1.4 – 3	50% of window panes break. Habitable after repairs.
3 – 6	90% of window panes break. Minor structural damage.
6 – 14	Doors and window frames break.
9	Clad building steel frames distort slightly.
14 – 28	Unhabitable, partial collapse of roof and some external walls. Non-reinforced concrete/cinder block walls shatter. Residential structures collapse.
30	Buildings not specifically designed destroyed.
35 – 80	50 – 75% of external brickwork destroyed or unsafe. Most buildings collapse.
80 – 260	Near complete destruction of reinforced buildings.
50 – 100	Displacement of cylindrical storage and failure of pipework.

2.3.3 Current Regulations and Standards

It is worth noting that as it currently stands there are no regulations that are applicable for hydrogen storage and use within residential buildings. However it is envisaged that the current regulations will be altered from the regulations that stand for the work place. In the UK any standards that are related to residential buildings are not currently governed by the Health and Safety Executive (HSE). Residential standards are covered by a local authority, normally the council or fire brigade. This could raise issues as different governing bodies may take various viewpoints.

The need for the standards is to minimise the probability of any failure which could result in loss of life as well as damage to property and people. They would also help to neglect the common perceptions of hydrogen (Hawksworth, 2000). There are minimal hydrogen specific regulations although hydrogen is covered by broader regulations, related to various fuels. The majority of regulations that are hydrogen specific are related to fuel cells.

The main regulation in the UK is “The Dangerous Substances and Explosive Atmospheres Regulations” (DSEAR) 2002 (Health and Safety Executive, 2002). This directive is for employers but can be used for residential buildings also. This is based on the EU directives known as ATEX 137 (European Parliament, 2000) and ATEX 95 (European Parliament, 1994). ATEX is shorthand for the French title of ATEX 95, the first regulation, which is ATmosphères EXplosibles. These are discussed in depth later as they are EU wide. There is one exception that is in the DSEAR which is not in either of the ATEX directives. This is the need to have arrangements in place with the relevant emergency services and initial responders to deal with any incidents and emergencies.

ATEX 137 (European Parliament, 2000) is a directive, set by the EU, which deals with the protection of workers from the risk of explosive atmospheres. This directive states that it will not be applied to the manufacture, handling, use, transport or storage of explosive or chemically unstable substances. This means that the directive is applicable for hydrogen, as there is a possibility of an explosive atmosphere forming. The term explosive atmosphere means a mixture with air, in atmospheric

conditions, of flammable substances, which after ignition; combustion spreads throughout the entire unburnt area.

The basic principles for protecting against explosions are:

1. Preventing the formation of explosive atmospheres. Where the activity disallows this then following take precedent:
    a) Avoidance of ignition sources to the explosive regime.
    b) Mitigating the effects of an explosion, such that safety of people is sustained.
2. Measures may be combined or supplemented for protection against propagation of explosions.

The directive also states that a risk assessment must be carried out that takes account for:

1. The probability that an explosive atmosphere occurs and its duration.
2. The presence of any ignition sources, electrostatic discharges included, and if they could be active or effective.
3. The installation itself and any substances that could interact/react.
4. Gauging any possible effects.
5. Any connections from the potential area to others.

The risk assessment should then be used to aid the writing of a document, known as the explosion protection document. This document is designed to provide evidence that a risk assessment has been performed and that any necessary protection measures have been implemented. The location where an explosive atmosphere may occur can be classified into one of six zones. This classification is then used within the document; with the proviso that any area with a classification has appropriate warnings in place. This document must be in place before any work and must be revised if any changes are made to the area in question.

The classification into a zone is only needed if special precautions are used for protection, as it is then deemed to be potentially hazardous. The zones are then decided upon depending on the timespan and probability of an explosive atmosphere being formed. Although there are six zones, Table 8 shows how the zones are decided upon. It can be seen that hydrogen would fall into zone 2 whilst a metal

hydride would fall into zone 22, for the system that is being designed within the ESCHER project.

Table 8 Classification of the hazardous zones (European Parliament, 2000)

Zone	Substance	Probability	Timespan	Equipment Category
0	Gas, vapour or mist	Frequently	Continuous or long	1
1	Gas, vapour or mist	Likely		1 or 2
2	Gas, vapour or mist	Not likely	Short	1, 2 or 3
20	Dust	Frequently	Constant or long	1
21	Dust	Likely		1or 2
22	Dust	Not likely	Short	1, 2 or 3

The equipment category in Table 8 is used within ATEX 95 (European Parliament, 1994). This is covered later within this section.

There are many protective measures that need to be enforced. The major measure for the gaseous explosive atmosphere is to remove the mixture to a safe area. When using hydrogen this would be via venting to the atmosphere, whilst making the release externally safe. There is also a need to take into account any other substances that could be harmful and negating the effect they can induce. The prevention of ignition hazards is also needed, this includes electrostatic ignition. Whilst it can be relatively easy to prevent the majority of ignition sources, electrostatic ignition can be very difficult to overcome; as such suitable clothing should be worn. Any other equipment that will be used within the classified zone also needs to be suitable for use within the designated category. Whilst maintenance and use of the equipment should diminish the probability of an explosion, if an explosion does occur there should be systems in place to negate the consequences. Ideally there should be a warning system in situ, such that a warning is given before an

explosive atmosphere has been reached. The area that can contain an explosive atmosphere should be verified before any equipment is used. This verification must be carried out by suitable people.

There is the possibility of making technical adjustments to this directive, if suitable technical progress has been made. This directive has also made a guide of good practise for all EU member states that is non-binding in nature. However each member state should have regulations and laws in place that enforce this directive, the DSEAR in the UK.

ATEX 95 (European Parliament, 1994) is another directive set by the EU, which focuses on equipment and protective systems for use within explosive atmospheres, this relates to the final column in Table 8. It actually gives minimum conditions for all countries within the union. This is such that even if a member state has its own regulations; there will be no impingement on trade with other states. Although the directive is mainly focused on equipment within a potentially explosive atmosphere, there is also focus on the use outside of these areas. This is for the focus on minimising the explosive atmosphere. However if the equipment is designed for use within a residential setting, where explosive atmospheres are not intended to exist, then this directive does not apply.

Equipment is classed as machines, apparatus, control components and instrumentation. For which the intended use is within the generation, storage, measurement, control and conversion of energy. Protective systems are defined as units that are intended to stop the developing explosions at once and/or limit the range of the flames and pressures. The equipment can be split into either surface use or the mining industry, only the surface usage is covered here. The surface use category has three sub-categories, shown in Table 9, all of which can be applicable to hydrogen.

Table 9 The level of protection needed for the sub-categories. (European Parliament, 1994)

Category	Level of protection needed
1	Very high
2	High
3	Normal

The equipment and protective systems have to be designed such that they prevent explosive atmospheres forming, the ignition of such atmospheres and finally the mitigation of the affects if an explosion occurs. They should be designed such that all possible faults are considered, whilst the misuse of the equipment needs to be anticipated as well. The surrounding, atmospheric, conditions also need to be taken into account. Any materials need to be selected such that no reaction would occur and as such an explosion would not be initiated. Any other potential ignition source, including electrostatic, must not occur or have appropriate measures in place. The ignition sources must not be able to become active at all. The protective measures need to be independent such that if one fails another is not affected. The protective systems should be designed such that any explosion is mitigated, whilst preventing any spreading via chain reactions or flashover. They must also be able to work if a power failure was to occur or there is any other external interference. When planning the prevention and mitigation measures, the maximum pressure and temperature possible need to be used. This is for the scenario that an explosion does occur. Finally, the system should be able to sustain its integrity in the event of an explosion (European Parliament, 1994).

The dispensing of hydrogen from an installation to a vehicle is covered by the standard SAE J2601 (SAE, 2014a). The standard covers both 35 and 70 MPa vehicle tanks and has the protocol for communicating and non-communicating refuellers. The upper bound for temperature reached within the vehicle tank is 85°C whilst the maximum pressure is classed as 125% of the nominal working pressure of the tank. The vehicle tank has a pressure range that is greater than 0.5 MPa or lower than the nominal working pressure. Anything outside of this range then refuelling will not occur. The lower limit is because of the excessive heat that would be generated within the refuelling process. This is because the refuelling time is designed to be at

most three minutes. The upper limit is because above this the tank would already have the maximum amount of hydrogen. There is an ambient external temperature range of between -40°C and 50°C. The flow rate of hydrogen from the nozzle has to be less than or equal to 60 g/s. A pressure pulse is sent from the nozzle to the vehicle to determine the pressure in the tank to determine the initial pressure inside (SAE, 2014a) . The nozzle and receptacles are covered by the standard SAE J2600 (SAE, 2012). This is in place to test and make sure that nozzles and receptacles do not allow a different, mainly greater, pressure class to be used on a tank. They are not allowed to be made of materials that could generate a spark. They should be able to withstand the pressures set out in SAE J2601 (SAE, 2012). The standard, SAE J2799 (SAE, 2014b), covers refuellers that can communicate with the vehicle. The basic concept is shown in Figure 5. The rest of the standard covers the programming of the communication.

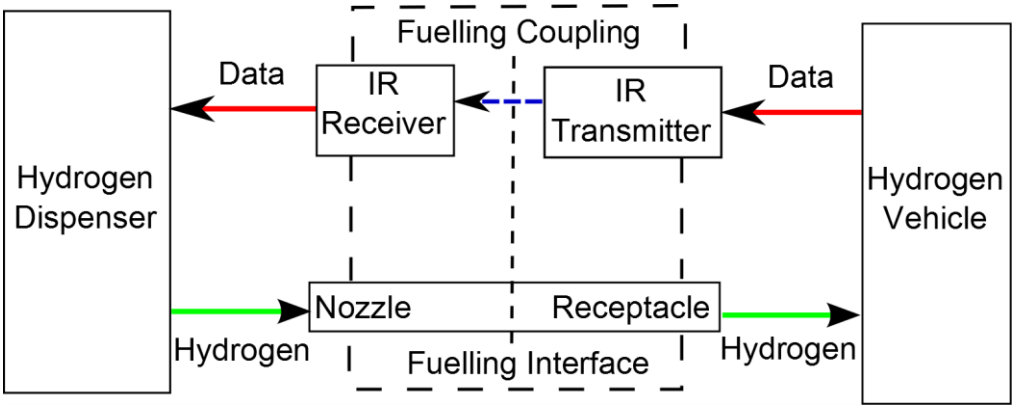

Figure 5 Basic hydrogen gas fuelling design (SAE, 2014b)

The Health and Safety Laboratory, HSL, have come up with some installation guidance on behalf of The Health and Safety Executive, HSE (Pritchard et al., 2009). These guidelines sum up the regulations and standards discussed above. A major point that is not really covered previously is the siting of any vents. The vents need to be sited such that they take into account any other buildings and/or openings (Pritchard et al., 2009).

2.4 Hydrogen Dispersion

2.4.1 Introduction

The modelling of hydrogen dispersion is extremely important; this is because hydrogen can ignite in the correct conditions. Therefore the possible effects of a hydrogen leak need to be established. This is due to the vast limits of flammability and detonability of hydrogen in air. Modelling the dispersion is necessary as hydrogen will mix with air on release and there is a high probability that a combustible and/or detonable mixture will be formed. The formation of these clouds varies considerably due to many factors, although they are mainly spatial and temporal. Although the combustion modelling after a leak is very important, the dispersion of hydrogen is seen as a prerequisite. This is to determine the stratification and mixing of the hydrogen. The results of a dispersion model can then be implemented into a combustion model.

When using computer modelling there is a need to validate against experimental data, this is normally done on a smaller scale. As previously discussed hydrogen-air mixtures can ignite, which can make experiments very dangerous. This has meant that helium has been used as a surrogate. It also has buoyant characteristics like hydrogen; therefore it is very useful for dispersion simulations. However helium will act differently, for example: hydrogen is 8% more buoyant then helium. It has been seen that the maximum deviation between hydrogen and helium concentrations can be 15% (Swain, 1998). However it is envisaged that the experimental conditions would play a part in the deviation between the two chemicals.

The following factors, proposed by (Swain, 1998), are seen as having the major influences on hydrogen distribution; the geometry the leak flows in to, the flow rate of the leak, the total volume of the gas leaked and any gas motion that is already in existence. Due to these factors there are three main classifications to determine a leak, with two subdivisions. These are:

1) Leak flows into an enclosed geometry.
2) Leak flows into a partially enclosed geometry (vents in place).
3) Leak flows into an unenclosed geometry (outdoors).

The subdivisions are the same for all three classifications and are:

a) Total volume of leaked gas.
b) Flow rate of leaking gas.

These classifications can be used to generalise the type of risks that can be incurred. For an enclosed geometry the major risk is from the total volume of leaked gas. This is because an ignition could occur at any time. A delayed ignition would cause greater overpressures that could be dangerous where as an early or almost instantaneous ignition would result in a flame direct from the leak source. In an enclosed geometry the hydrogen would rise to the highest point available and over time it would then diffuse to the lower levels of the room. Therefore if the total volume released is lower than the lower flammability limit then eventually all risk would subside.

The risk for an unenclosed geometry is mainly from the flow rate of the leak. This is because hydrogen can rise unimpeded, therefore not accumulating. There is a very minimal chance of any overpressures during release as there are no geometric constraints, the main constraint being a cover above the release.

The risk for a partially enclosed geometry, with vents, is a combination of both the total volume leaked and the leak flow rate. Which of these factors are more important is determined by the geometry and the location of the leak. The positioning of the vent/s is of utmost importance. Vents near the top of the enclosure would allow the hydrogen to exit, although how much depends on whether a vent is placed near the bottom as well. This is because the lower vent would allow fresh air to enter and replace the mixture that is leaving. However if there is only one vent placed near the top then this would have to allow air flow in and mixture flow out, hence reducing the amount of removal (Swain, 1998).

The above criteria can be used to determine the areas that more interest is needed in, although this is also problem dependent. The main areas of concern for the development of a hydrogen energy economy are leaks into unenclosed and partially enclosed geometries. Due to the nature of the current project more emphasis has been put on leaks within a partially enclosed geometry, with a little interest in unenclosed geometries and none on enclosed geometries.

2.4.2 Unenclosed Geometries

The study of hydrogen dispersion for unenclosed geometries is very useful, if hydrogen is stored externally. This is because it is important to determine how a release of hydrogen would act when not bounded and the possible consequences that could occur. Studies that are performed for this type of geometrical scenario are usually pertained to releases near buildings. This is needed as the effects have the possibility to be disastrous see Figure 6, as could have been the case in Stockholm on 3rd March 1983 (GEXCON, 2012). This depicts the results of a hydrogen release and ignition. A vehicle was delivering chemicals when the driver heard a noise. This was hydrogen gas releasing from gas bottles. The hydrogen leak then ignited causing the damage seen within Figure 6.

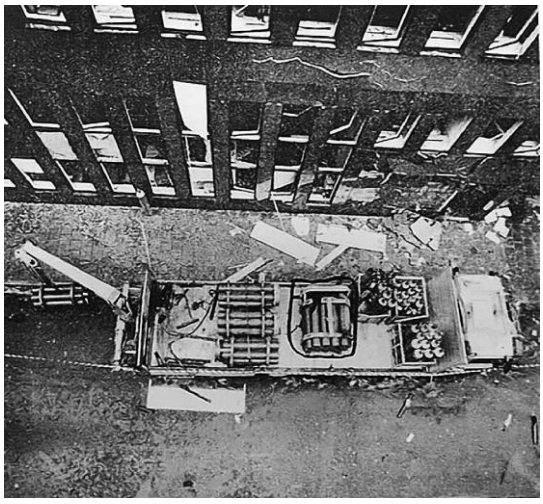

Figure 6 The delivery vehicle after the blast in Stockholm (Venetsanos et al. 2003).

Simulations have been performed using various codes; they all solve the conservation of mass, continuity and momentum equations. Turbulence is also modelled in the simulations although different models can be employed, such as k-ε theory or eddy viscosity formulation. The main issues when simulating leaks in unenclosed geometries is the atmospheric conditions and the position of the release. This causes major problems for validation of such work. This is due to the inherent problems of using the correct atmospheric conditions. The portrayal of results can also have issues. This is because using volume, mass or mole fractions can be difficult. Therefore using the volume or mass of the flammable mixture seems to be a more appropriate approach.

The simulations are normally performed such that the release is positioned between two obstacles, normally buildings. This is because a channel for the flow of the hydrogen is created; it is also more realistic for residential releases. However the height of the buildings can influence the dispersion of the flammable cloud. This is due to the atmospheric currents being impinged more below the height of the building and as such having a differing effect on the mixture. The direction of the release also has a significant part in this as well, as it could actually be impeded.

Two scenarios that have been modelled are a leak based between two buildings (Schmidt, 1999) and the incident that occurred in Stockholm (Venetsanos et al., 2003). Both scenarios have releases positioned closer to one of the buildings. The modelling of the Stockholm incident means that they have data to validate their model. The former uses information based on a liquid hydrogen spillage. This has meant that some parameters have been used that would normally be expected with high pressure releases, because of the vaporisation of the liquid hydrogen to gaseous hydrogen (Schmidt, 1999).

The scenario (Venetsanos et al., 2003) replicates the accident that occurred in Sweden in 1983, the results of which are depicted in Figure 6. A fixed total volume of hydrogen is considered to be released. This would mean that the hydrogen would dissipate into the atmosphere if it was unimpeded and ignition did not occur. This is shown in the results as the flammable volume is at its greatest at 10 seconds. The decrease in volume, of hydrogen, after this point cannot be attributed to diffusion into the atmosphere as ignition occurs. However it would be expected that the total volume would decrease although at a much slower rate. The height of the buildings, the roof starts at 18 m, causes the hydrogen to be impinged and therefore the lower flammability cloud reaches 15 m. The atmospheric currents that have been applied also mean there is more lateral movement as well.

The scenario in Schmidt (1999) has two buildings with a release situated slightly closer to one building with different release and atmospheric velocities. The simulation is a steady simulation rather than transient. The effects of different release velocities and atmospheric currents are studied. The release velocities used vary from 100 m/s – 1294 m/s. These are quite realistic velocities for a high pressure release. The atmospheric velocities vary from 1 m/s – 20 m/s, the flow direction is

always in the same plane as the channel between the buildings. The results show that high velocity releases are more hazardous, this is due to more hydrogen closer to the floor and a bigger volume of flammable and detonable mixtures being formed. The buildings also influence the concentration profiles as well as variation in atmospheric currents. This can be seen when using an iso-surface of 4%.

For two different release velocities, 400 m/s and 1294 m/s, and an atmospheric current of 10 m/s there is a vast difference between the sizes of the flammable mixtures. The releases are in the direction of the channel and the same direction as the atmospheric current imposed. The slower release has a conical shaped volume, compared to the faster release where the mixture has expanded between the buildings much more. The slower release does not make contact with either building where as the faster release is almost at the roof of the near building and very close to the far building.

When the release is vertical then the formation of the flammable mixture can change. It is less likely to form at a lower height. However the release velocity and atmospheric current can play a significant role in the dispersion of the flammable mixture. For a high release velocity, 1294 m/s, and a very small atmospheric current, 1 m/s, then the flammable cloud diffuses vertically and horizontally. Such that it would seem like a bubble of flammable and detonable mixtures is formed. If the release velocity is smaller, 100 m/s, and the atmospheric current is greater, 20 m/s, then the region of flammability formed is much smaller and the distance that hydrogen is at a low height is very small. This is due to the drift of the flammable region and the decay of the concentrations, due to convection dependency on the spatial distance from release.

When hydrogen is released externally the vertical dispersion can be dependent on the temperature and the concentration of the mixture. The weaker the concentration of the mixture the less likely it is to disperse as the density is more similar to air. However this is mainly dependent on the release temperature, a lower temperature has an increased volume of flammable mixture (Ramamurthi et al., 2009).

The major problem with trying to validate models for external releases is that it is very difficult to get accurate data. This is mainly due to not being able to predict atmospheric conditions. Iso-surfaces that show the flammable region are very useful

for visualisation over the domain. When it comes to plotting any data using the volume and mass of hydrogen seem to be much better, compared to using volume percentage.

It would also be more useful if when comparing different conditions, such as release velocity or atmospheric conditions, that only one is changed at a time. For example keeping the same release velocity and direction and only changing the atmospheric current velocity. This would make an analysis much easier as changing multiple conditions does not help to show the effects of the changes. The use of steady simulations can be helpful for the final composition however when dealing with hydrogen it is envisaged that transient solutions are much more helpful.

2.4.3 Partially Enclosed Geometries

A partially enclosed geometry is an enclosure with some openings, there is no maximum or minimum size or number for the openings. The dispersion is mainly effected by the direction of the leak and the positioning of the openings, normally vents in a building. For example a leak from the underside of a vehicle would flow along the bottom of the vehicle filling any cavities. Once the hydrogen reaches the edges of the base the buoyance will drive the flow upwards. This is assuming no atmospheric currents.

A useful experiment for validation of dispersion is when hydrogen leaks, with a volume flow rate of 9.44×10^{-4} m^3/s, into an enclosure of 2.9 m by 0.74 m by 1.22 m with two vents, see Figure 7. The steady state is reached at approximately 400 seconds. The leak is at one end of the enclosure with the two vents placed such that one was in the roof and the other is just above the ground at the far side of the leak. The experiment performed had four sensors placed. The concentration at quasi-steady state, in the simulations, for the roof sensors is approximately 4.75%. The lower level sensors reach quasi-steady state just before 400 seconds and at concentrations of around 1.5%. When the leak was placed in the centre of the enclosure there were some changes to the concentrations. The roof sensors recorded the same concentrations however the lower sensors increased to approximately 2.5% (Matsuura et al., 2008; Swain, 1998).

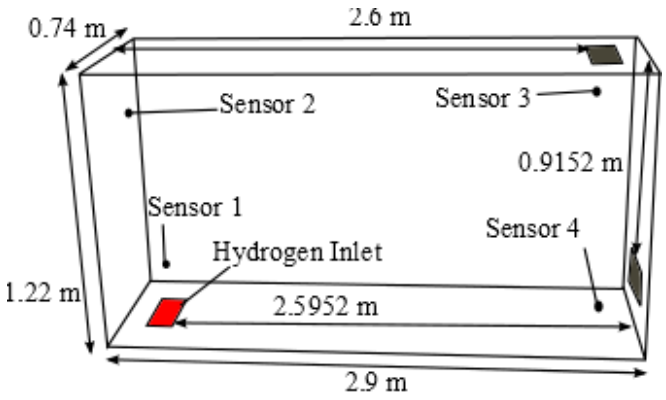

Figure 7 Schematic of experiment

The use of different sensors in experimental work can yield varying results. Thermal conductivity sensors used in the above problem recorded a concentration of approximately 5.25% at the roof sensors in quasi-steady state; however the sensors near the ground seem to be more similar (Matsuura et al., 2008).

The vent positions can have a vast difference on the concentrations and stratification. When a higher vent is placed above the release then the concentrations are lowered. This is if the lower vent is kept in place, although the position of the lower vent is dependent on the position of the leak. When the roof vent is at its furthest point and the lower vent is then raised the concentrations can increase quite significantly. This is because air is then flowing in closer to the ceiling, causing hydrogen to remain at lower heights whilst reducing the mixing. It also causes less extraction to take place as the air flow is extremely close to the roof vent (Matsuura et al., 2008). The effect of the vents is dependent on the position of the release within the geometry. If the leak is in the centre then vents on opposite walls can work quite well, so long as they are still one higher and the other lower (Papanikolaou et al., 2011).

Changing the pressure at the vents also affects the concentration of hydrogen. When the pressure at the roof vent is decreased then concentration also lowers. The greater the decrease in pressure, at the roof vent, the more the concentration decreases. When the pressure at the lower vent decreases there is an increase in concentration. This is because the two vents then change the way they work, the roof vent flows in and lower vent flows out. A smaller reduction in pressure, 0.5 Pa, causes a greater increase in concentration compared to a pressure decrease of 3.0 Pa. This is deemed to be due to the smaller amount of hydrogen being exhausted, because of the small dynamic pressure of hydrogen (Matsuura et al., 2008).

The effects of atmospheric currents on the concentration of hydrogen have differing views. However the geometry plays a part as to the affect that the atmospheric current plays. For a leak from a vehicle the atmospheric currents will have a negligible effect (Swain, 1998). This is because there is an opening almost completely around the vehicle. Therefore any atmospheric current would just drive more of the hydrogen out the other side. However for a building this is not an option. It has been seen that the direction and velocity of the atmospheric current can alter the concentration. This depends on the location of the leak and the vents that are affected by the atmospheric current. If the wind is towards the lower vent then this generally decreases the concentrations. Whilst when this is opposite the lower vent, towards an upper vent, then the concentrations are normally increased (Matsuura et al., 2008). The effect of atmospheric currents is dependent on whether the flow is towards the lower vent or upper vent. If towards the lower vent then the outflow is aided, the opposite occurs if flow is in the direction of the upper vent (Matsuura et al., 2008; Prasad et al., 2010).

The number of vents can also alter the concentration of hydrogen. If only one vent is used then the concentration will be higher. Whether the vent is placed in the roof or near ground level there is a negligible effect. This is because a single vent does not really allow the buoyancy of hydrogen to take effect as the flow rate at the vent must match the flow rate of the leak whilst also allowing air to flow into the geometry. When this occurs the flow is seen to be oscillating. When a second vent is added then the buoyancy affects the flow out of the vent. The buoyancy drives the hydrogen out of the roof vent which allows a lower vent to have air flow into the geometry. This flow then aids the mixing of the hydrogen and results in an increase of the flow at the roof vent, whilst also affecting the concentration stratification. The position of the lower vent has a negligible effect on the accumulation of hydrogen. The size of the lower vent can alter the concentration of hydrogen however this effect is almost negligible unless the vent size is drastically reduced. The roof vent size has a big effect on the concentration of the hydrogen, however as the size increases this effect reduces. The strongest factor to reduce the concentration is the position of the roof vent, ideally it would be placed above the leak source (Prasad et al., 2011; Swain, 1996). A study of different release rates with different vent sizes showed that doubling the vent size resulted in at least halving the hydrogen concentration in the

domain. The larger size reduced the time taken to reach quasi-steady state. The vents were placed in the same wall of the geometry and were both changed. However it was noted that the higher the leak flow rate the more hydrogen that remained in the system. A similar study showed that placing vents diagonally opposite actually increases the hydrogen concentration by approximately one tenth (Brady et al., 2012). This phenomenon was seen to work well with varying flow rates as well. When an intermediate vent is added between the upper and lower vents, there is a further reduction of the mixture concentration. So long as the intermediary vent is placed above the neutral plane (Prasad et al., 2010).

For realistic cases, sloped roofs need to be modelled or at least investigated. It has been seen that releases into geometries with sloped roofs has a negligible effect on the concentration of the hydrogen mixture formed (Swain, 1996). A study comparing roof inclination, the inclination is measured from the horizontal, was performed with a a hydrogen flow rate of 10 l/min. A flat roof was found to have a standard mixture concentration of 13.1% after five hours. This is compared to a roof with a 63.4^0 which had a standard mixture concentration of 12.9% after the same time. It was stated that the roof angles 26.6^0 and 45^0 produced concentrations in-between the values for a flat roof and 63.4^0 sloped roof. These values are with no forced air for ventilation and a roof vent placed in the centre of the ceiling. These simulations had not reached quasi-steady state after five hours. Therefore a forced air flow was used on a lower vent. This caused the quasi-steady state to be reached after twenty minutes. The concentrations at this point were 0.32% and 0.24%, for the flat and 63.4^0 sloped roofs respectively. When increasing the leak flow rate there is an increase in the concentration of the hydrogen mixture formed. However the roof angle still has a negligible effect. There is a difference of 0.2% for a 100 l/min flow and 0.7% for a flow of 1000 l/min compared to the 10 l/min flow rate. The maximum concentrations reached were 2.5% and 19.7% respectively, both of these concentrations are for a flat roof (Swain, 1996). This shows that leak flow rate and forced air flow, rather than roof angle, have a greater effect on the hydrogen concentrations.

A different study (Hajji et al., 2014) looked at the effect of roof inclination on hydrogen mixture concentration. Angles were measured from the roof apex from 180^0 - 90^0 in increments of 30^0. The leak flow rate was 994 l/min which can be comparable to data

from the study discussed above. However there was no forced air flow in this simulation which results in quasi-steady state not being reached. The results for the simulations show that an apex angle of 120^0 yields the lowest hydrogen concentration (Hajji et al., 2014). There was one vent placed in the simulation however this has already been proven to be extremely pitiable. This can explain the main deviation between these results and the results discussed above.

One analytical method is to split the domain into two layers (Zhang et al., 2010), the upper layer consisting of hydrogen and the lower air. The buoyancy of hydrogen is replicated by a hot stream release. Whilst the hydrogen concentration was calculated by the temperature rise generated (Zhang et al., 2010). Hydrogen dispersion can also be calculated analytically by determining where the neutral buoyancy plane lies, this is where the pressures internally and externally are equal (Prasad, 2014; Prasad et al., 2010). The problem with these analytical methods is that it assumes a uniform concentration above the separation between air and hydrogen. This is because diffusion cannot be incorporated into these methods. CFD techniques utilise diffusion which results in non-uniformity within the mixtures.

For a periodic release of hydrogen, the concentration of the flammable mixture is more time dependent. The concentration will increase as the release occurs, reaching the highest point once the release has ceased. After the release has stopped the concentration, of the upper layer, decreases (Zhang et al., 2010). This would be expected as the hydrogen would diffuse and mix into the lower volume. This would obviously cause the lower layer to have an increase in hydrogen, until eventually a homogeneous mixture is formed.

The analytical method underestimates the total flammable volume of hydrogen until the mole fraction of hydrogen reaches the lower flammability limit, LFL. As such it overestimates once the LFL has been reached. CFD models have issues as well, mainly that model parameters need to be adjusted to match experimental data, especially when using LES (Zhang et al., 2010).

The Fire Dynamic Simulator (FDS) (NIST, 2013), which incorporates LES has been used to simulate hydrogen releases into enclosures. It is deemed a suitable package for the modelling of hydrogen dispersion (Prasad et al., 2011; Zhang et al., 2010). However it is necessary to make sure that constants are at an appropriate value. For

example a Smagorinsky coefficient of 0.2 can significantly over-predict the volume of hydrogen. The Smagorinsky coefficient is utilised in LES modelling to determine the filter cut off for eddies. However this is deemed to be problem dependent as different values have been used (Prasad et al., 2011; Zhang et al., 2010).

A numerical study has also shown that the size of the orifice for a hydrogen leak can have a small effect on the concentration. It has been found that the turbulent diffusion coefficient is greater than the normal diffusion coefficient, at the leak orifice vicinity (Prasad et al., 2011). This would lead to more diffusion via turbulence, which shows the need for modelling turbulence when modelling buoyant gases. The flow eventually becomes almost laminar when only one vent, placed in a wall, is used. This would mean the normal diffusion coefficient would be larger (Choi et al., 2013; Prasad et al., 2011). However closer to the release point it is deemed that turbulent diffusion could still play a part. The size of the leak orifice is also closely linked with the pressure of the release in determining the dispersion of the hydrogen. This is due to an under-expanding jet being formed and results in convection over-powering diffusion. The geometry of the orifice can also affect the development of the hydrogen jet, an elliptical orifice disperses greater than a circular orifice (Shishehgaran and Paraschivoiu, 2014).

In a cylindrical container with only an opening at the roof, it has been viewed that a release of a buoyant gas would have mixing driven by natural convection with diffusion having a small part. A buoyant gas, such as hydrogen, released initially rises in bulk, like a bubble. The flammable zone of hydrogen would fill the entire domain after 2.3 seconds from release (Cisse and Karim, 2007). This is due to hydrogen having such a vast flammable range.

There is also the chance for sonic releases to occur when hydrogen leaks from a high pressure container. This causes an increase in momentum which yields greater mixing, although this can have both positive and negative influences. However simulations can make over-predictions when working with sonic jets. It is thought that this deviation could be caused by the internal set up of the nozzles used. The small jets have more fluctuations in the resulting plumes, this implies lower averaged measurements. There can also be differences in measuring methods for varying nozzle sizes (Middha et al., 2009). Impinged releases, for example a release with a

plate above it (Middha et al., 2009), show that hydrogen behaves similar to when released in a building. However an impingement causes more rapid mixing with the surrounding air (Prasad et al., 2010). Where the building roof acts like the plate and the hydrogen then spreads from the impingement. The hydrogen flows across the impinging surface before rising again, if it is possible. Although for sonic releases there is not as much diffusion from the jet.

Hydrogen vehicles that store the hydrogen in tanks are required to have pressure relief devices (PRD's). These work by releasing the hydrogen in the tank quickly, this normally occurs under the presence of abnormally high temperatures, such as fires. This is designed to decrease the probability of catastrophic failure, such as explosions. A high mass flow rate released causes an over-pressure development; which could cause damage to a structure (Brennan and Molkov, 2013; Prasad, 2014). The size of the PRD needed depends on the pressure and amount of hydrogen stored; a smaller PRD will decrease the overpressures from the release but will take much longer. The articles mentioned above used different geometries and numbers of vents. A single vent was used in the earlier study (Brennan and Molkov, 2013), whilst multiple vents were used in the latter (Prasad, 2014). They both agree that the over-pressure caused from such a release can damage buildings. This shows that high pressure releases whether sonic or not can be very dangerous.

2.5 Hydrogen Combustion

2.5.1 Introduction

The combustion of hydrogen needs to be reviewed due to the potential consequences that can arise from the ignition of a leak, as seen in Figure 6. Safety analysis of a system needs to account for the potential outcomes were a leak to ignite.

The combustion can take many forms depending on whether it is premixed or non-premixed before ignition. Non-premixed combustion generally takes the form of a fire. Premixed combustion has the propensity to propagate (deflagrate) and detonate. The change from deflagration to detonation is known as deflagration-to-detonation

transition (DDT) (Sathiah et al., 2012). All of these phenomena are looked at in the following sections.

2.5.2 Fires

Recently experiments have been performed to replicate hydrogen releases and fires within enclosures. This is due to envisaged allowance of hydrogen vehicles being stored inside garages. The Health and Safety Laboratory, UK, (HSL) have performed some experiments for the HyIndoor project (Hyindoor, 2012). The National Institute of Standards and Technology, USA, (NIST) have also had experiments performed under contract by Southwest Research Institute (SwRI) (Blais and Joyce, 2010). The NIST experiments were summarised in the paper by (Pitts et al., 2012). Both sets of experiments involve releasing hydrogen into an enclosure, of similar size to residential garages, followed by ignition.

The experiments performed on behalf of NIST were such that hydrogen was released into a vented enclosure. The enclosure was normally empty but some experiments were in the presence of vehicles. The vehicles used were old vehicles that are not comparable with the current hydrogen vehicle technology. The ignition occurred at different concentration levels, thus to determine the overpressures that could be achieved. There were multiple pressure transducers and thermocouples placed within the enclosure, as well as hydrogen sensors to record the concentration. A constant release rate, of 83.3 g/min for 60 minutes thus releasing a total of 5 kg of hydrogen, was used at atmospheric conditions. This is to simulate a failure in the pipework between the car tank and the fuel cell for the midline of hydrogen tanks that will be available (Blais and Joyce, 2010).

The enclosure used had interior dimensions of 6.1 m by 6.1 m by 3.5 m and was built to withstand some overpressures, whilst observing many characteristics representative of residential garages. The foundations laid were steel I-beams while the three walls were constructed of hollow concrete blocks that were stacked without the use of mortar. The concrete blocks were reinforced by steel bars welded to the foundations and then filled with concrete. The walls were then further supported by external heavy steel I-beam buttresses. The roof was flat and made of wood with no weather proofing used. The roof was not attached to the walls, but was secured

allowing for some lift. This is so that the roof could move if overpressures were great enough, whilst not producing large missiles/debris. The front of the enclosure was made of wood and secured such that it could move under moderate overpressures. Openings were located both in the roof and a wall for visualisation and lighting, all were covered with poly-methyl methacrylate sheets. Any potential leaks were then sealed with duct tape and filling.

The hydrogen concentrations were measured using thermal conductivity sensors, which were located vertically. The sensors were vertical from (3.05, 5.49) m, with (0, 0, 0) located at the left-front corner using standard notation. That position corresponds to the centreline whilst being 0.61 m away from the rear wall. 8 sensors were located at z = 0.38, 0.76, 1.14, 1.52, 1.90, 2.29, 2.59 and 3.05 m. When a vehicle was present within the enclosure the highest placed sensor was then moved to the interior of the vehicle and another sensor was placed within the engine block of the vehicle.

Different systems were employed to measure the combustion of the hydrogen-air mixtures formed. Thermocouples were used, located at the H_2 sensor positions as well as a horizontal array of 7 thermocouples along the centreline at a height of 2.59 m. There were 6 ionisation pins used located along the same line as the horizontal array of thermocouples. Two pressure sensors were used with locations at (3.04, 5.94, 2.59) m and (6.10, 3.04, 2.59) m. External atmospheric conditions were measured locally, within 50 m of the enclosure. Numerous camera types were used to record videos as well. The pressure and ionisation sensors started recording when triggered, the trigger was the first time the ionisation sensors picked up a recording.

Ignition initially used electric sparks, 1 J and 10 J; however this was unreliable for lower hydrogen concentrations. Therefore 80 J squib charges triggered by voltage pulses were used (Blais and Joyce, 2010).

Tests with and without conventional vehicles were performed, the problem with using conventional vehicles is that they are not designed the same way as hydrogen vehicles. As such the results need to be looked at more carefully as they can be misleading. There was also a problem with the trigger system which meant that there were no ionisation or pressure recordings. For example, within the published analysis

performed by staff at NIST there are 13 experiments and yet only pressure data for three is shown (Pitts et al., 2012).

To use this data set for numerical validation would pose many problems. However if it was to be assumed that the initial concentrations could be matched, the problem of the deformation of the structure poses a problem. This could be accounted for if the numerical model accounted for Fluid Structure Interactions (FSI). This is because numeric readings would be different to the experiments. The lower concentration, 8.7%, causes the front to move and the door to be bowed. Therefore even this lower concentration could pose problems.

The full report (Blais and Joyce, 2010) states that of the 22 experiments performed there is pressure data for just 10. This is attributed to a lack of energy produced for tests involving ≤12% to trigger the system. There were also problems with wiring which caused some failure.

The HSL performed 12 experiments within the framework of the Hyindoor project (Hooker et al., 2015). The aim was to investigate the effect of passive ventilation on hydrogen jet fires. This work would be useful as very little is known about the behaviour of hydrogen jet fires inside enclosures. The test geometry was the 31 m^3 testing enclosure at HSL's Harpur Hill site in Buxton, UK. Different release rates and regimes were investigated alongside various venting configurations. The experimental enclosure is located externally, for obvious reasons, and as such was susceptible to various atmospheric conditions.

The majority of cases developed into well-ventilated fires, high oxygen content and low hydrogen content. This comes about because of the relatively low release rates applied. Under-ventilated fires were also investigated by decreasing the vent area. The behaviour of indoor jet fires depends on the release rate, venting area and the thermal properties of the enclosure. The release was located at the centre of the enclosure, which contained 24 thermocouples to measure temperature. The flame was ignited via a propane pilot light.

Whilst there have been 12 experiments performed, some of the results are presented in (Hooker et al., 2015). However there is also a summary of the results within the final report from the Hyindoor project (Jallais et al., 2014).

The experiments performed within the Hyindoor project were supported by blind simulations performed at the University of Ulster (Molkov et al., 2014) prior to the experimental results being available.

This was performed to study the effects of release rate as well as vent size and orientation on an indoor hydrogen fire. They looked at whether the flame would be sustained inside an enclosure, whether it would become an external flame or self-extinction would occur. They also looked at the vent orientation and its effect on alleviating overpressures.

The model that is used incorporates the renormalisation group (RNG) k-ε turbulence model, the eddy dissipation concept (EDC) model for combustion and a reduced mechanism, of 8 species and 18 reactions, for chemistry. This is peculiar as a full mechanism, excluding NO_X production, consists of 10 species and 20 reversible reactions. The in-situ adaptive tabulation (ISAT) algorithm is used to accelerate the chemical calculations by a few orders of magnitude, thus reducing computational time. The geometry used was a cube, with a volume of 1 m^3, a single vent is located centrally at the top of a wall. The release was located centrally and modelled as a pipe with internal diameter of 5.08 mm. Different release rates, vent sizes and orientations were used to examine the effects on fires. The release velocities that were studied are 60, 150, 300 and 600 m/s. The reaction zones were viewed using the presence of the hydroxyl species. The ambient temperature was set to 293 K.

A release velocity of 60 m/s gives a well-ventilated fire which would sustain as a jet flame. This is due to air flowing in through the vent and thus sustaining oxygen for the flame. A release velocity of 600 m/s gives an external flame. The transition from internal to external flame starts to occur after approximately 20 seconds. The reaction rate decreases within the enclosure as the transition occurs. The phenomenon occurs because the release rate is so great, such that air cannot enter the enclosure via a single vent. This is evident as the oxygen content is almost zero a 35 seconds. Both of the simulations were performed for the same vent size and orientation, vertical.

When the vertical vent size is decreased the flame then self-extinguishes for the higher release velocity. This occurs when the external reaction zone separates from the internal reaction zone. This is caused by air flowing into the enclosure through

the entire vent. The use of a horizontal vent showed that as release velocity increased, the combustion regime changed from external flame to self-extinguishing.

It is shown that the release velocity determines whether the fire will be sustained indoors, exhibit an external flame or will self-extinguish. The overpressures produced, even for the highest release velocity, still do not exceed the low limit for damage to civil structures, 14 kPa. The vertical vent is not as effective at overpressure reduction compared to the horizontal vent (Molkov et al., 2014). It is planned for this work to get developed more when experimental data is finalised within (Hyindoor, 2012).

2.5.3 Deflagration

Deflagration is the propagation of combustion at subsonic speeds; it occurs rapidly with a high energy release and is driven by heat transfer. There can be multiple pressure peaks depending on the configuration, for example vent area and ignition position. Normally three peaks are profound, which account for the vent cover, external explosion and the flame. The initial peak is the vent cover failing, followed by a peak for the external explosion of unburnt mixture and lastly a peak that is due to the flame. The internal overpressure increases when the vent size decreases, this is due to less unburnt gas mixture being expelled (Rocourt et al., 2014).

Hydrogen deflagration can be modelled by both LES and RANS and a study was performed investigating both (Tolias et al., 2014). The numerical results are compared against experimental data. The RANS turbulence model was the k-ε model, both turbulence models used RNG. Combustion was modelled by a turbulent flame speed concept. A variable sized mesh, finer in areas of interest, was performed for deflagrations in a tunnel using both methods. A near stoichiometric mixture was used, 30% by volume of hydrogen, and was placed within a 10 m long stretch of the centre of the tunnel. The effect of vehicles within the area of interest was also examined. When the tunnel was empty it was noted that there was negligible difference between the models, however there is a delay in the peak pressure for the RANS model. This delay is believed to be due to the fluctuating part of the velocity (Tolias et al., 2014). Both models over-predict after peak pressure has been reached. This is thought to be due to heat transfer, as this was ignored from the model.

When the tunnel has vehicles placed inside the flammable region, there seems to be good agreement with the experimental results for both types of modelling. However yet again there is a delay for the RANS model for the same reasons as before. The LES model for the empty tunnel took approximately 47 hours of running time on a quad core modern CPU, whereas the RANS model took longer by about 1.29 times. This is because the mesh was kept the same for both models.

Simulations were performed to investigate mesh adaptation (Sathiah et al., 2012). This is because the main area of interest surrounds the flame front. These simulations were compared against experimental data on a small scale and large scale. The experiments utilised methane-air and hydrogen-air propagating flames respectively. The combustion model used was the turbulent flame speed closure (TFC) model coupled with the k-ε turbulence model. The trends of the numerical results match the experimental, although the incident times are quicker for the numerical results. This is believed to be due to simulation assumptions on ignition source size and quasi turbulent flame speed.

Adaptive meshing is especially suited for vast and/or complex geometries. The method can be set such that the adaptation takes place depending on a model variable (Sathiah et al., 2012). The method employed can also accommodate more than one variable for the adaptation. A comparison between adaptive meshing and static meshing showed that there was negligible or no difference between the two types on a range of parameters. The computational time for both was also shown and unsurprisingly the adaptive mesh performs much more effectively.

The large scale simulation above was performed again using diluents during the deflagration. Carbon dioxide and helium are used as opposed to water, for the diluting species. Comparison of physical properties showed that as the dilution increased as did molecular diffusivity for both options, but the CO_2-He mixture performed slightly better. Thermal diffusivity was investigated with increases of the diluents. When water is increased the thermal diffusivity decreases, the opposite is found for the CO_2-He mixtures. The adiabatic flame temperature decreases when the dilution is increases, water performs better at reducing the adiabatic flame temperature (Sathiah et al., 2014).

2.5.4 Detonation

Detonation is the propagation of combustion at supersonic speeds; it has a highly exothermic front which then propagates a shock wave. The shock wave normally proceeds as a vast overpressure followed by a decrease in pressure. Depending on the geometry, rarefaction waves could occur which under suitable conditions exceed the initial shockwave. The initial combustible mixture would be incompressible, after detonation the mixture then becomes compressible. The propagation of the shockwave is followed by a combustion wave, where both regions are coupled together (Bédard-Tremblay et al., 2008; Heidari et al., 2011).

There is a need to have an extremely fine mesh when modelling a detonation. This is due to the thin shockwave front. The need for such fine meshes means that 2D modelling can be preferred. It is suggested that initial motion, prior to detonation, and further dispersion should be neglected. Whilst due to the speeds, that occur, a single step Arrhenius rate is needed. This is because of the Chapman-Jouguet (CJ) wave speed, which depends on the released heat. Walls can be modelled as completely solid; as such they would reflect the shock wave. However in reality that is highly unlikely. When modelling geometries with obstacles, these would increase the propensity for a DDT to occur. The work that has suggested this (Bédard-Tremblay et al., 2008) simulated the transition artificially by increasing the energy so that a shock would occur greater than the CJ value. This is set in a small region to act as the detonation ignition. As expected the results show the shock wave propagating, more horizontally at first, but then reaching a solid wall and then reflecting from the wall. It was found that the size of the combustible mixture, geometry, mass of hydrogen and time of ignition can have an effect on the maximum overpressure reached. There is also a point where the shock wave and the combustion reaction become separated (Bédard-Tremblay et al., 2008).

Calculating large scale detonations requires some simplification such that the computational power can be utilised more efficiently (Heidari et al., 2011). To capture the shockwave an extremely fine mesh is needed, in the order of microns. This is currently not possible due to the lack of computational power, especially for large scale detonations, such as that used by (Heidari et al., 2011). Therefore an alternative is to tune a model to achieve the correct combustion energy release and

detonation states, pre and post, whilst calculating the wave speed. Although a coarse grid would not capture the internal intricacies of the shock wave and the wave could be smeared over multiple cells. There is also the possibility of numerical diffusion accelerating the wave. Therefore a single step global mechanism can be used to diminish stiffness. This would allow a coarse simulation, using mm, to then capture overpressures and confinement pressures, which would depend on the energy and not the kinetics. The Arrhenius equation can still be used although there is a need for the correct pre-exponential factor and activation energy. The rate of energy release needs to be correct otherwise all data will be wrong. The explicit Euler scheme was used for time, whilst a total variation diminishing scheme was used to capture the shock (Heidari et al., 2011).

The above simulation was performed for a tunnel, where the tunnel was filled with a hydrogen-air mixture and ignition occurred at one end of the tunnel. Ignition was simulated by an area of increased temperature and pressure that was approximately equal to the CJ detonation values. The use of lower values would not initiate or cause oscillations prior to detonation whilst higher values can cause instabilities in the wave. The energy required for the detonation to occur was equivalent to 200 g of TNT. Reflection of the shock waves caused an increase in the pressure, greater than the leading pressure, in some areas. The simulation followed the same trend as experimental data, although in general the peak pressure was lower than the experiments. This is expected due to the coarseness of the mesh. Due to the inherent nature of the mesh and its incapability to measure the von-Neumann peak, this method is not ideal for safety engineering (Heidari et al., 2011).

Setting the ignition values seems to be an issue. Two different options for the start have been used, higher CJ values and equal CJ values. Clearly setting the ignition values to those similar to the CJ values is more beneficial as has been shown by the results (Heidari et al., 2011).

2.5.5 Deflagration-to-Detonation Transition

This phenomenon is of great importance when dealing with hydrogen, as it is viewed as the more likely way for a detonation to occur. There is a higher chance for this to occur when obstacles are involved. This is due to the flame changing from laminar to

turbulent, although that is not always the case. This depends on whether the flame and shock waves are coupled or not. The exact mechanism depends on the conditions (Ivanov et al., 2013).

A model has been developed (Gamezo et al., 2007) that uses the Navier-Stokes equations with the ideal gas equation and a one-step Arrhenius equation. An adaptive mesh was incorporated, to save computational costs. The problem with using a one-step Arrhenius equation has been discussed previously. The combustible mixture used was stoichiometric at normal temperature and pressure. Ignition was simulated by a region of hot burnt material. Hot reaction products expand and force the unburnt reactants to move towards the opening, as the flame propagates it gets complicated due to interactions with the obstacles. This increases the flame surface area which then causes a quicker release of energy and as such an acceleration of the flame. The obstacles cause the flame to become wrinkled due to instability. The unreacted flow then becomes sonic and shocks begin to form in front of the flame. There is a slight distance between the leading shock and flame front. The leading shock diffracts at obstacles and also reflects from walls and the ground. This causes the Mach stem to increase after diffracting at every obstacle. Where the Mach stem collides with an obstacle a hot region is formed. The hot spots that are generated are seen to make small flame kernels where a detonation then occurs. It is deemed that the detonation appears when the temperature gradient allows the chemical energy source to move with the shock speed, this amplifies the shock strength. If this does not occur then more hot spots are created which can start a detonation. It is viewed that the Mach stem and obstacle collisions are one cause for re-ignition (Gamezo et al., 2007).

There is a view that using a one-step reaction for the chemistry is not representative at all and the temperature gradient method does not satisfy the actual physics, regarding a hot spot ignition, appropriately (Ivanov et al., 2013). Therefore more complex chemistry is ideally suited; as such has been incorporated. It was seen that the flame acceleration was due to either the temperature or density increasing. It was proposed that the increase of flame speed up to the local speed of sound generates a pressure pulse. This pulse is within the reaction zone and increases until a shock is developed that is strong enough to cause detonation (Ivanov et al., 2013). All eight chemical species are used in the reaction mechanisms whilst the numerical model

employed was the coarse particle method. This method splits a time-step into three separate calculations. A stoichiometric mixture was again used, with normal temperature and pressure as initial conditions. It was also shown that flame speeds and pressures are achieved much quicker when using 3D simulations compared to 2D simulations, this is because of the increased freedom. It was also shown that initial perturbations in the flame front can be accredited as the cause for detonation. This is because they increase the flame surface and as such increase the amount of fuel consumed. This in turn yields a greater rate of heat released which arises to an increased flame velocity. This increase causes compression of the unreacted gas and as such shocks are induced further in front of the flame. Originally flame acceleration is related to the flame stretching whilst once a shock has been caused it is due to the coupling between shock and flame. There is also a shorter distance for this phenomenon when modelled in 3D as opposed to 2D (Ivanov et al., 2013).

There is a theory that has been suggested known as Shock Wave Amplification through Coherent Energy Release (SWACER) (Lee et al., 1978; Lee and Moen, 1980). This theory has a higher level of physical insight. This theory suggests that detonation needs amplification of shock waves from numerous localised explosion points (Heidari and Wen, 2014). This agrees with the above work. The adaptive mesh technique is also viewed as the best way to perform these simulations. This is due to the computational cost savings whilst keeping a high level of accuracy. In a 2D simulation using detailed chemistry a delay in ignition of detonation is seen compared to single step chemistry. It was noted that detailed chemistry may not be very accurate due to the mechanism being validated for specific conditions (Heidari and Wen, 2014).

2.6 Metal Hydride Storage

The use of metal hydrides as hydrogen storage and compressors is increasingly growing (Gkanas et al., 2015; Züttel, 2003). Numerous studies, both experimental and numerical, have been performed to study the adsorption and desorption of metal hydrides. One major problem is that a slight change of the chemical composition of the metal hydride can significantly alter its behaviour.

The most likely configuration for usage of metal hydrides, as compressors for refuelling, is shown in Figure 8. This is the method that is being used for the ESCHER project. The required pressure for delivery depends upon the pressure of the tank, as described in section 2.3.3. The shown pressure here, 350 bar, is due to that being used for the ESCHER project.

The electrolyser can be replaced with any form of hydrogen production. There will also be a refuelling interface between the second stage metal hydride and the vehicle.

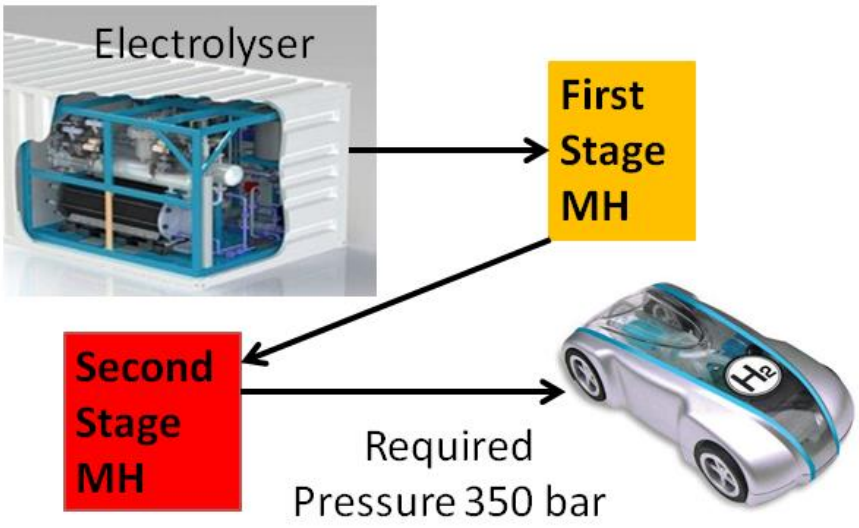

Figure 8 Configuration for metal hydride refuelling system.

2.6.1 Metal Hydride Chemistry

Metal Hydrides are formed with the majority of the elements in the f- and d-block of the periodic table. The majority of these are actually alloys with varying composition. Most metal hydrides work via a reversible process, where they adsorb and desorb, depending on the temperature. Adsorption occurs at lower temperatures with desorption the opposite. This is because adsorption is exothermic whilst desorption is endothermic. It is also deemed a safer method of storing hydrogen because it minimises the chance of an uncontrolled release. There are three main types of metal hydride; magnesium-based, complex and intermetallic (Atkins et al., 2010; Züttel, 2003).

Intermetallic compounds seem to be the better option, due to the excellent reversible hydrogen uptake at low pressures and just above room temperature. The only

downfall to these compounds is the low mass percentage of hydrogen that can be adsorbed. This is because of the high molar masses of the metals. These compounds can have varying stoichiometry, which yield different types. These normally fall in to the following categories: AB_2, AB_5, AB, A_2B and BCC. The main focus is on AB_2 and AB_5 compounds. AB_5 types are typified by $LaNi_5$, when hydrogen is adsorbed it becomes $LaNi_5H_6$. Although using a mass comparison it yields 1.5 percent of hydrogen by mass. The stoichiometry AB_2 is also referred to as Laves phases. The element represented by A is normally Ti, Zr or any Lanthanide, whilst B is usually a 3d metal. These normally have good kinetics and better capacities for hydrogen adsorption. The problem with these compounds is that they are thermodynamically stable at room temperature which restricts desorption of hydrogen. A_2B and BCC compounds are good for the percentage mass of hydrogen they can contain, however they both need high temperatures and pressures to operate (Atkins et al., 2010).

There have been numerous studies on metal hydrides and there use as compressors (Lototskyy et al., 2014) review this area. Some studies have even gone as far as connecting vessels together much like a multi-component metal hydride compressor (Bhuiya et al., 2014; Li et al., 2010; Muthukumar et al., 2012) to name a few. However there can be a problem when attempting to duplicate studies. This is because of the aforementioned issues regarding the chemical properties. For instance one of the most commonly used and readily available metal hydrides is LaNi5, however there are even differences for the chemical properties for this substance (Sandrock and Thomas, 2010). There are numerous models available to determine the adsorption and desorption of hydrogen (Gambini et al., 2008; Gkanas et al., 2015; Jemni and Ben Nasrallah, 1995; Kyoung et al., 2015; Laurencelle and Goyette, 2007). However they always rely on the heat transfer through the porous media. This is due to the inherent nature of the chemical reactions that occur; exothermic for adsorption and endothermic for desorption.

2.7 Conclusion

This chapter has discussed relevant information that pertains to the work in the following chapters. The harm criteria, section 2.3.2, are especially useful for determining the necessary information for aligning safety criteria. This is especially

the case for, Chapter 8. The criteria that is useful for the non-reacting work that follows, Chapter 5, is not the harm criteria but actually a chemical property. The LFL, taken from Table 1, which overrules the asphyxiation criteria as it is the lower concentration by volume.

The current regulations are also reviewed within the chapter. This is to show the current regulations that need to be adhered to when using hydrogen. Review of current works within the field of hydrogen safety is also included. This is to determine areas that can be investigated further, release locations and venting configurations for non-reacting releases. All the way to reacting work and the pit falls and positives that has occurred within this area. Finally an overview of metal hydrides is included to explain how they work.

Chapter 3 – CFD Theory

This chapter reviews the numerical formulation that has been used to investigate the objectives of this work. First is an introduction to CFD theory, after which are the governing equations for compressible flow. This is then followed by turbulence modelling, which includes the turbulence models that have been applied within the work. Following which there is a section describing combustion, entailed is the different combustion regimes after which are the combustion models employed to solve for the different regimes. Finally the computational framework within STAR-CCM+® is discussed.

3.1 Introduction

There are various modelling techniques that can be employed for modelling fluid flows, from analytical to varying levels of computational complexity. Analytically solving problems can be useful, however they are normally rough predictions and cannot encompass the full nature of a scenario (El-Amin et al., 2008; El-Amin and Kanayama, 2009, 2008; Prasad, 2014; Prasad et al., 2010; Versteeg and Malalasekera, 2007; Zhang et al., 2010). This is why computational models are used. They can reveal more of a problem and can recreate the nature of a system. However there is a trade to be made when using a computational model, between accuracy and time. The more accurate the solution the better, however the main reason for using a computational model is to save time. A simulation is deemed to be accurate depending on the convergence of the iterative process and grid independence. However a validation is also needed to prove that the physics and/or chemistry have been calculated correctly. The convergence is deemed appropriate when the residuals of the flow parameters have reached an acceptable level. The residuals are a representation of how well the discretised equations are solved. This is problem and software dependent, however a rough guide is 0.001 – 0.0001 (CD-adapco, 2015).

There are two main ways to utilise the iterative process depending on the problem at hand. These are termed either steady or unsteady and are descriptors for the flow behaviour. Steady flows are useful when the results do not need to be time

dependent. Unsteady flows are time dependent and commonly referred to as transient. However unsteady flows can become quasi-steady, this happens when there is no visible change of parameters with respect to time. Although a macroscopic view may look steady, it is not always the case when looked at in more detail (Versteeg and Malalasekera, 2007).

3.2 Governing equations

The governing equations are to ensure that laws of conservation in physics are represented correctly mathematically. This is done via the conservation of mass, momentum and energy. There is also the general transport equation, which calculates various other scalars (Poinsot and Veynante, 2005; Versteeg and Malalasekera, 2007).

The governing equations of fluid flows that will be shown are in differential form. These are derived using macroscopic properties, such as pressure, velocity and density, alongside their spatial and temporal derivatives.

The conservation of mass, as it suggests, means that mass is not created or destroyed. The conservation of mass is also known as the continuity equation, which, in differential form, is:

$$\frac{\partial \rho}{\partial \mathrm{t}} + \frac{\partial \rho \mathrm{u_i}}{\partial x_i} = 0 \tag{3.1}$$

Where ρ is the density and u_i is the velocity in direction x_i. The subscript i denotes the direction, x, y or z and the corresponding velocity u, v or w.

The conservation of momentum follows Newton's second law. The change in momentum is equal to the sum of the forces acting upon a particle. There are two types of forces that may act upon a fluid particle, surface and body forces. Body forces act upon the mass of the particle and tend to be included in source terms, gravity is included in this. Whilst the surface forces are normally due to the pressure or viscous forces (Versteeg and Malalasekera, 2007). The momentum is for all three spatial components, yielding three equations. This can be written as:

$$\frac{\partial \rho u_j}{\partial t} + \frac{\partial \rho u_i u_j}{\partial x_i} = -\frac{\partial P}{\partial x_i} + \frac{\partial \tau_{ij}}{\partial x_i} + F_i \tag{3.2}$$

where F_i is the body forces, including gravity. The pressure is denoted by P, the subscript j denotes a velocity component, u, v or w. The other new term introduced is τ_{ij} this is the viscous stress tensor, and is:

$$\tau_{ij} = \mu\left(\frac{\partial u_i}{\partial x_j} + \frac{\partial u_j}{\partial x_i} - \frac{2}{3}\delta_{ij}\frac{\partial u_k}{\partial x_k}\right) \tag{3.3}$$

Where μ is the dynamic viscosity and δ_{ij} is Kronecker's delta. Again the subscripts correspond to the spatial vectors and their corresponding velocity components.

The general transport equation is described next, whilst this isn't a governing equation in the sense of the laws of physics. This is an important equation for transporting scalars, but especially species which are important for reacting flows. The general transport equation is:

$$\frac{\partial \rho \phi}{\partial t} + \frac{\partial \rho u_i \phi}{\partial x_i} = \frac{\partial}{\partial x_i}\left(\rho D \frac{\partial \phi}{\partial x_i}\right) + S_\phi \tag{3.4}$$

Where D is the diffusion coefficient, ϕ is a scalar quantity and S_ϕ is the source term for scalar ϕ.

The final governing equation is for energy. This can vary between reacting and non-reacting flows. The reacting variation is:

$$\frac{\partial \rho h}{\partial t} + \frac{\partial \rho u_i h}{\partial x_i} = \frac{\partial}{\partial x_i}\left[\frac{\mu}{h}\frac{\partial h}{\partial x_j} + \mu\left(\frac{1}{Sc_k} - \frac{1}{\sigma_h}\right)\sum_{k=1}^{N} h_k \frac{\partial Y_k}{\partial x_i}\right] + \frac{\partial P}{\partial t} + S_h \tag{3.5}$$

This variation of the energy equation is for the enthalpy. Where: h is the mixture enthalpy, h_k is the specific enthalpy of species k, Y_k is the mass fraction of species k. σ_h is the mixture Prandtl number and Sc_k is the species Schmidt number.

The Prandtl number is defined as:

$$\sigma_h = \frac{c_p \mu}{k} = \frac{\text{Rate of momentum transport}}{\text{Rate of energy transport}} \tag{3.6}$$

The Lewis number is defined as:

$$Le_k = \frac{k}{\rho c_p D_k} = \frac{\text{Rate of energy transport}}{\text{Rate of mass transport}} \tag{3.7}$$

The Schmidt number is defined as:

$$Sc_k = \frac{\mu}{\rho D_k} = Le_k \sigma_h \tag{3.8}$$

If a single diffusion coefficient is used rather than individual species coefficients, coupled with the assumption of unity Lewis number. Then the enthalpy equation (3.5) becomes:

$$\frac{\partial \rho h}{\partial t} + \frac{\partial \rho u_i h}{\partial x_i} = \frac{\partial}{\partial x_i}\left[\frac{\mu}{\sigma_h}\frac{\partial h}{\partial x_j}\right] + \frac{\partial P}{\partial t} + S_h \tag{3.9}$$

If the flow has a low velocity then the term $\partial P/\partial t$ is neglected. As such this reduces the enthalpy equation to the same form as the general transport equation (3.4).

Previously mentioned was the mass fraction for individual species. The equation for this takes the form of the general transport equation (3.4). This is achieved by substituting Y_k for ϕ. This takes the form:

$$\frac{\partial \rho Y_k}{\partial t} + \frac{\partial \rho u_i Y_k}{\partial x_i} = \frac{\partial}{\partial x_i}\left[\rho D_k \frac{\partial Y_k}{\partial x_i}\right] + S_{Y_k} \tag{3.10}$$

Where Y_k and D_k are the mass fraction and molecular diffusion coefficient for species k, respectively. There are N-1 transport equations for species. The Nth species is computed from the continuity equation (3.1). The molecular diffusion coefficient can be associated with the Schmidt number (3.8). It can also be calculated by using kinetic theory, where the binary diffusion is based on Chapman-Enskog theory (Poling et al., 2001).

The governing equations, (3.1), (3.2) and (3.5) would be applicable for modelling directly if the spatial and temporal resolutions are extremely fine, i.e. DNS. However as mentioned previously this is difficult to use, due to computational power. This is why various modelling techniques have been formulated. The RANS technique is the method used within this work and as such the next section focuses on this.

3.3 Turbulence Modelling

3.3.1 Turbulence Modelling Overview

Turbulence modelling is used to capture fluctuations of the fluid flow, which occur when the Reynolds number is high. The majority of flows are turbulent which necessitates a need to model this phenomenon. Turbulence in its nature is random and chaotic, which transfers to flow properties such as velocity and pressure. The randomness of the process does not lend itself to a simplified description of the fluid motion. The fluctuations on the fluid produce additional stresses, known as Reynolds stresses. This section will look at the various modelling capabilities available for solving the Reynolds stresses.

There are three main computational techniques for modelling which are; Reynolds-Averaged Navier Stokes (RANS), Large Eddy Simulation (LES) and Direct Numerical Simulation (DNS). These are numerical methods used to capture the turbulence of a problem, when coupled with a turbulence model, and increase in accuracy from RANS to DNS. However all of these models still solve the conservation of mass, momentum (in all three dimensions) and energy (Versteeg and Malalasekera, 2007).

There are many RANS models however they all focus on the mean flow and its properties. These models can use coarser grids as they use the average properties. The most common models are given in Table 10 along with the amount of extra equations needed to be solved.

The mixing length and k – ε models are the most commonly used and as such the most validated models. They use the presumption that there is an analogy between the way the viscous and Reynolds stresses act upon the mean flow. The mixing length model describes the stresses in a simple algebraic form of the dynamic

turbulent viscosity. The main disadvantage of the mixing length model is that it struggles to describe flows that recirculate (Versteeg and Malalasekera, 2007).

Table 10 The different RANS models and the extra equations they need.

Model Name	Number of extra equations
Mixing length	0
Spalart – Allmaras	1
k – ε	2
k – ω	2
Algebraic stress	2
Reynolds stress	7

The Spalart – Allmaras model (Spalart and Allmaras, 1992) solves an extra equation for a kinematic eddy viscosity parameter, with a length scale specified, and is mainly used in external aerodynamics. A wall damping function is used which causes the kinematic eddy viscosity parameter to be equal to the kinematic eddy viscosity (Versteeg and Malalasekera, 2007).

The k – ε model focuses on mechanisms that affect the turbulent kinetic energy. It calculates the instantaneous kinetic energy as the sum of the mean kinetic energy and the turbulent kinetic energy, which is given by k. The ε term is the dissipation of the turbulent energy. This variable contains terms that are not known and cannot be measured. These can be defined by velocity and length scales. The turbulent kinetic energy defines the velocity scale whilst the length scale uses the computed k value to determine ε. The velocity and length scales are used to define the eddy viscosity. The transport equations for k and ε contain five constants that can be changed. Although these constants can be adjusted, they have been arrived at from comprehensive data fitting for a vast array of turbulent flows. The two terms are closely linked such that when one increases so does the other. When the turbulent kinetic energy decreases, ε decreases more rapidly so that no negative values accrue (Ferziger and Perić, 2002; Versteeg and Malalasekera, 2007).

The implementation of this model needs the means of calculating k and ε for inlet and initial conditions. This can occur by either direct entry or by using turbulence intensity and a characteristic length scale. The characteristic length scale is used to define the length scale used in the calculations, which is related to the size of the eddies within the problem. This model is the most widely used and validated whilst also not needing adjustment of constants for different cases. Different versions of the model have been made to take account of varying effects, such as buoyancy (Rodi, 1980). The disadvantage for this model is that it performs poorly for some scenarios, such as; unconfined flows, rotating flows, large extra strain flows (swirling) and anisotropically driven flows of Reynolds stresses (Rodi, 1980; Versteeg and Malalasekera, 2007).

The k – ω model has different variations just like the k – ε model. One such variation is the Wilcox model (Wilcox, 1993, 1988). This model uses the same turbulent kinetic energy as the k – ε model but uses a turbulence frequency, ω, which is defined as ε/k. However this model has issues with boundary conditions in a free stream. Therefore a variation was proposed to deal with this, known as the Menter Shear Stress Transport (SST) model (Menter, 1994, 1992a, 1992b). This is a hybrid model, using both the k – ε and Wilcox k – ω model. The Wilcox model is used at the near wall region with the k – ε model used in the fully turbulent region far from the wall. The equation for ε is changed to be $\varepsilon = k\omega$. The main use for these models is external aerodynamics although they can be suitable for more general use, with similar positives and negatives to the k – ε model (Versteeg and Malalasekera, 2007).

The algebraic stress model is a way of accounting for the anisotropy of the Reynolds stresses while not solving the transport equations for such parameters (Demuren and Rodi, 1984). The easiest way of doing this is by ignoring the convective and diffusive terms of these. A better way is to make the assumption that the sum of these terms is equal to the sum of the convective and diffusive terms of kinetic turbulent energy. This is possible because they are closely linked due to being turbulence properties. This model is advantageous as it models the anisotropy of the Reynolds stresses compared to other models. However it is not widely validated and is highly restricted for flows when assumptions of the transport for convection and diffusion are not applicable (Versteeg and Malalasekera, 2007).

The Reynolds stress model is similar to the transport equation for turbulent kinetic energy but also has a rotation term and a pressure-strain interaction or correlation (Launder et al., 1975; Rodi, 1980). The rotational term uses a standard equation which uses a rotation vector and alternating symbol, positive to negative depending upon the rotation. However the pressure-strain term is more difficult and requires corrections to some terms. This type of model has the potential to describe the mean flow properties and Reynolds stresses without the need of adjustment for different cases. It also has the benefit of only needing initial and/or boundary conditions. However it is extremely computationally costly due to the extra equations that it solves and is not very well validated (Versteeg and Malalasekera, 2007).

LES is an intermediary that focuses on larger eddies. It involves spatial filtering that rejects smaller eddies, via a sub-grid scale model. The grid size needs to be finer than that needed for RANS. The sub-grid scale is used such that it ignores eddies below a certain cut-off limit. The connection between the larger and smaller eddies is resolved using a sub-grid-scale (SGS) model, this solves the SGS stresses that arise. This then means the time averaged, spatial filtered flow equations can be solved along with the SGS model. The cut off for the filter should not be smaller than the grid size used, as the value of the grid size would be kept, this means that for small filter sizes a fine grid is needed. In three dimensional grids with non-uniform spacing, the filter size is taken to be the cube root of the cell volume (Versteeg and Malalasekera, 2007). Further details are available in (Ferziger, 1977; Smagorinsky, 1963).

DNS models calculate all the turbulent fluctuations and the mean flow. The grid size needed for these calculations is extremely small. A small time step is also needed due to the speeds of some of the fluctuations. Due to the inherent complex nature, it is difficult to use DNS on complicated geometries. The grid discretisation needs to take account geometrical features and the turbulence scale. Although a small time step is needed, specific methods need to be used so accuracy and stability are ensured. This is so that a fluid particle only moves one grid space (Versteeg and Malalasekera, 2007). Further details are available in (Moin and Mahesh, 1998).

3.3.2 Underlying Turbulence Modelling Theory

The two main types of fluid flow are laminar and turbulent. A laminar flow is smooth with neighbouring layers that slide alongside each other. A turbulent flow has continual mixing of the neighbouring layers. This occurs when the Reynolds number is above the critical Reynolds number. The motion within a turbulent flow is chaotic and unpredictable. This is also known as unsteady, although can balance to what is known as a quasi-steady state. This should not be confused with the time dependency, sometimes referred to as unsteady.

The unpredictability of turbulent flows can be decomposed to the following:

$$\phi(t) = \overline{\Phi} + \phi'(t) \tag{3.11}$$

Equation (3.11) is known as the Reynolds decomposition. There is a steady mean value $\overline{\Phi}$ and a fluctuating part $\phi'(t)$. ϕ can be replaced by any flow property, e.g. velocity components or pressure. Whilst the flow properties may be 1D or 2D, the turbulent fluctuations are always in 3D. This is normally in rotating flows which are known as turbulent eddies.

The mean flow property $\overline{\Phi}$ is defined as:

$$\overline{\Phi} = \frac{1}{\Delta t}\int_0^{\Delta t} \phi(t)dt \tag{3.12}$$

The fluctuating property is by definition zero and is defined as:

$$\overline{\phi'} = \frac{1}{\Delta t}\int_0^{\Delta t} \phi'(t)dt \equiv 0 \tag{3.13}$$

The statistics of the fluctuating component are the most descriptive. The main descriptions are the variance and root mean square (r.m.s.). The variance is given by:

$$\overline{(\phi')^2} = \frac{1}{\Delta t}\int_0^{\Delta t} (\phi')^2\, dt \tag{3.14}$$

Whilst the r.m.s. is given by:

$$\phi_{rms} = \sqrt{\overline{(\phi')^2}} = \left[\frac{1}{\Delta t} \int_0^{\Delta t} (\phi')^2 \, dt \right]^{\frac{1}{2}} \tag{3.15}$$

The r.m.s. of the velocity components are the easiest to measure and as such of importance. These become, $\overline{u'^2}$, $\overline{v'^2}$ and $\overline{w'^2}$, and are used to express the mean kinetic energy per unit mass in the fluctuations. The total kinetic energy per unit mass, k, of the turbulence at a location is:

$$k = \frac{1}{2}\left(\overline{u'^2} + \overline{v'^2} + \overline{w'^2}\right) \tag{3.16}$$

Equation (3.16) can be used to express the turbulence intensity, T_i. This is the average r.m.s. divided by a reference velocity and is linked to the turbulence kinetic energy, k.

$$T_i = \frac{\left(\frac{2}{3}k\right)^{\frac{1}{2}}}{U_{ref}} \tag{3.17}$$

The next step is to transform the governing equations, (3.1), (3.2) and (3.5), and the general transport equation, (3.4), into the turbulent flow equations. These are density-weighted averaged, also known as Favre averaged (Favre, 1969). This is in addition to the Reynolds averaging, which utilises the Reynolds decomposition, (3.11). Therefore the instantaneous velocity can be written as:

$$u = \tilde{u} + u'' = \frac{\overline{\rho u}}{\overline{\rho}} + u'' \tag{3.18}$$

Where the Reynolds decomposition has u', here the turbulent fluctuating part is denoted by u''. The variable $\tilde{u}$ is the Favre-averaged velocity. Using the Reynolds decomposition of density and pressure, coupled with the Favre decomposition for scalars, e.g. velocity, energy and species, for the governing and species transport equations yields the following (Poinsot and Veynante, 2005):

$$\frac{\partial \bar{\rho}}{\partial t} + \frac{\partial \bar{\rho}\tilde{u}_i}{\partial x_i} = 0 \tag{3.19}$$

$$\frac{\partial \bar{\rho}\tilde{u}_j}{\partial t} + \frac{\partial \bar{\rho}\tilde{u}_i\tilde{u}_j}{\partial x_i} = -\frac{\partial \bar{P}}{\partial x_i} + \frac{\partial\left(\overline{\tau_{ij}} - \overline{\rho u_i'' u_j''}\right)}{\partial x_i} + S_i \tag{3.20}$$

$$\frac{\partial \bar{\rho}\tilde{h}}{\partial t} + \frac{\partial \bar{\rho}\tilde{u}_i\tilde{h}}{\partial x_i} = \frac{\partial}{\partial x_i}\left[\Gamma_h \frac{\partial \tilde{h}}{\partial x_j}\right] + \frac{\partial \bar{P}}{\partial t} + S_h \tag{3.21}$$

Where $\Gamma_h = (\mu/\sigma + \mu_t/\sigma_h)$ with σ_h being the turbulent Prandtl number.

$$\frac{\partial \bar{\rho}\tilde{Y}_k}{\partial t} + \frac{\partial \bar{\rho}\tilde{u}_i\tilde{Y}_k}{\partial x_i} = \frac{\partial}{\partial x_i}\left(\bar{\rho}D_k \frac{\partial \tilde{Y}_k}{\partial x_i}\right) + S_{Y_k} \tag{3.22}$$

The term $-\overline{\rho u_i'' u_j''}$ in (3.20) is known as the Reynolds stress tensor. It is not an actual stress but a representation of instantaneous fluctuations of the flow. The calculation of the turbulent flows within the RANS equations needs turbulence models to predict the Reynolds stresses and as such close the system of equations. The models available have been discussed briefly in section 3.3.. The Boussinesq approximation is used to correlate the Reynolds stresses with the mean rates of deformation. It is similar to the viscous stress tensor (3.3), and is:

$$\tau_{ij} = -\overline{\rho u_i'' u_j''} = \mu_t\left[\left(\frac{\partial \tilde{u}_i}{\partial x_j} + \frac{\partial \tilde{u}_j}{\partial x_i}\right) - \frac{2}{3}\delta_{ij}\frac{\partial \tilde{u}_k}{\partial x_k}\right] - \frac{2}{3}\bar{\rho}k\delta_{ij} \tag{3.23}$$

Where δ_{ij} is Kronecker's delta, k is the turbulent kinetic energy per unit of mass, (3.16), and μ_t is the turbulent viscosity. The expression for the turbulent viscosity depends upon the model that is used. This is covered in the next section, which describes the three turbulence models that have been used in the work.

3.3.3 Turbulence Models Used

This study utilises three turbulence models, this section describes those models. The three models all consist of two equations. All three models consist of an equation for the turbulent kinetic energy, k, and a term for the dissipation. The first is the standard

k-epsilon model, followed by the realisable variant of this model. The last is the k-omega SST model. These models assume isotropic turbulence, fluctuations are equal in all directions, which is not realistic (Poinsot and Veynante, 2005; Versteeg and Malalasekera, 2007).

3.3.3.1 Standard k-epsilon

This is the most common and well known RANS turbulence model. The model has been around for over 40 years, first formulated by Launder and Spalding (Launder and Spalding, 1974). This model solves the dissipation in the form of the turbulent/viscous dissipation rate, ε. Initial and boundary conditions also need to be prescribed. Both k and ε can be defined in different ways, either by intensity and length scale or via viscosity and length scale (CD-adapco, 2015; Versteeg and Malalasekera, 2007).

$$k \approx \frac{3}{2}\left(T_i \vartheta\right)^2 \tag{3.24}$$

$$\varepsilon \approx \frac{C_\mu^{\frac{3}{4}} k^{\frac{3}{2}}}{\ell} \tag{3.25}$$

$$\varepsilon \approx \frac{\rho C_\mu k^2}{\left(\frac{\mu_t}{\mu}\right)\mu} \tag{3.26}$$

$$\mu_t = C\rho\vartheta\ell = \rho C_\mu \frac{k^2}{\varepsilon} \tag{3.27}$$

Where T_i is the turbulence intensity, ϑ is the velocity scale, ℓ is the length scale and C and C_μ are constants.

Equations (3.24) – (3.27) are for the initial and boundary conditions. The parameters k and ε also use transport equations within the model. These are:

$$\frac{\partial \bar{\rho} k}{\partial t} + \frac{\partial \bar{\rho} \tilde{u}_i k}{\partial x_i} = \frac{\partial}{\partial x_i}\left[\frac{\partial k}{\partial x_i}\left(\mu + \frac{\mu_t}{\sigma_k}\right)\right] + P_k - \bar{\rho}\varepsilon + S_k \tag{3.28}$$

Where S_k is a user source term and P_k is a source term, given by:

$$P_k = -\overline{\rho u_i'' u_j''} \frac{\partial \tilde{u}_i}{\partial x_j} \tag{3.29}$$

The Reynolds stresses in (3.29) are solved via the Boussinesq approximation (3.23).

And the epsilon transport equation is:

$$\frac{\partial \bar{\rho}\varepsilon}{\partial t} + \frac{\partial \bar{\rho}\tilde{u}_i \varepsilon}{\partial x_i} = \frac{\partial}{\partial x_i}\left[\frac{\partial \varepsilon}{\partial x_i}\left(\mu + \frac{\mu_t}{\sigma_\varepsilon}\right)\right] + C_{\varepsilon 1}\frac{\varepsilon}{k}P_k - C_{\varepsilon 2}\bar{\rho}\frac{\varepsilon^2}{k} + S_\varepsilon \tag{3.30}$$

Where S_ε is a user source term.

Equations (3.28) and (3.30) contain model coefficients. These coefficients are devised from data fitting to vast amounts of experimental data (Versteeg and Malalasekera, 2007). Hence the earlier claim that the model is relatively accurate.

Table 11 contains the coefficients used and the corresponding values.

Table 11 Coefficients used in the standard k-epsilon turbulence model and the corresponding values.

Coefficient	Value
C_μ	0.09
σ_k	1.0
σ_ε	1.3
$C_{\varepsilon 1}$	1.44
$C_{\varepsilon 2}$	1.92

3.3.3.2 Realisable k-epsilon

This model is a development on the existing standard k-ε model (Shih et al., 1994). Transport equations for k and ε are solved yet again. However the difference

between this model and the standard variant are that there are differences to the ε equation. Therefore for ease the k equation is not given as it is the same as equation (3.28). There is also an alteration to the C_μ coefficient. It is no longer constant but an expression of the mean flow properties (CD-adapco, 2015). The new epsilon equation is:

$$\frac{\partial \bar{\rho}\varepsilon}{\partial t} + \frac{\partial \bar{\rho}\tilde{u}_i \varepsilon}{\partial x_i} = \frac{\partial}{\partial x_i}\left[\frac{\partial \varepsilon}{\partial x_i}\left(\mu + \frac{\mu_t}{\sigma_\varepsilon}\right)\right] + C_{\varepsilon 1} S_\varepsilon + C_{\varepsilon 1}\frac{\varepsilon}{k} P_k - C_{\varepsilon 2}\bar{\rho}\frac{\varepsilon}{k + \sqrt{\nu\varepsilon}} + S_\varepsilon \quad (3.31)$$

It can be seen that there is an additional term, $C_{\varepsilon 1} S_\varepsilon$ and the penultimate term is also different to (3.30). The coefficient C_μ now becomes a variable which is based upon the strain and rotation rates. The coefficient $C_{\varepsilon 1}$ is also a variable which is a function of the time scale ratio of the turbulence to the mean strain. These are not given here but can be found in (CD-adapco, 2015; Shih et al., 1994).

Therefore Table 11 is now redundant for this model. The new coefficients are given in Table 12.

Table 12 Coefficients used in the realisable k-epsilon turbulence model and the corresponding values.

Coefficient	Value
C_μ	Variable
σ_k	1.0
σ_ε	1.2
$C_{\varepsilon 1}$	Variable
$C_{\varepsilon 2}$	1.9

3.3.3.3 k-omega SST

This model is a development of the k-ω model, developed by Wilcox (Wilcox, 1988), and is different to the k-ε model by the method of which the dissipation is resolved.

The SST variation, developed by Menter (Menter, 1994, 1992a, 1992b), combines the best of both the k-ε and k-ω models. This model satisfies the near wall problems that the k-ε model contains whilst utilising that model in far field regions. This is performed via a transformation from one region to the other. The aforementioned transformation is performed on the ω equation such that an extra source term appears. This extra term is because of cross-diffusion invoked by the relationship between ε and ω. This can be performed because of the relationship $\omega = \varepsilon/k$.

The parameters k and ω also use transport equations. The k equation is slightly different to (3.28) whilst obviously the ω equation is going to be different.

$$\frac{\partial \bar{\rho} k}{\partial t} + \frac{\partial \bar{\rho} \tilde{u}_i k}{\partial x_i} = \frac{\partial}{\partial x_i}\left[\frac{\partial k}{\partial x_i}\left(\mu + \mu_t \sigma_k\right)\right] + P_k - \beta^* \bar{\rho} \omega + S_k \qquad (3.32)$$

Where P_k is the same as equation (3.29) and S_k is a user source term.

$$\frac{\partial \bar{\rho} \omega}{\partial t} + \frac{\partial \bar{\rho} \tilde{u}_i \omega}{\partial x_i} = \frac{\partial}{\partial x_i}\left[\frac{\partial \omega}{\partial x_i}\left(\mu + \mu_t \sigma_{\omega,1}\right)\right] + \gamma_2 P_\omega - \beta_2 \bar{\rho} \omega^2 + D_\omega + S_\omega \qquad (3.33)$$

Where S_ω is a user defined source term and D_ω is the cross diffusion term and is:

$$D_\omega = 2\bar{\rho}\sigma_{\omega,2}\frac{1}{\omega}\frac{\partial k}{\partial x_i}\frac{\partial \omega}{\partial x_i} \qquad (3.34)$$

Equation (3.34) may also contain a blending function, which is not shown here.

The term P_ω is similar to that of P_k with a few alterations to the Boussinesq approximation, as shown below:

$$P_\omega = -\overline{\rho u_i'' u_j''}\frac{\partial \tilde{u}_i}{\partial x_j} = \bar{\rho}\left[\left(\frac{\partial \tilde{u}_i}{\partial x_j} + \frac{\partial \tilde{u}_j}{\partial x_i}\right) - \frac{2}{3}\delta_{ij}\frac{\partial \tilde{u}_k}{\partial x_k}\right] - \frac{2}{3}\bar{\rho}\omega\delta_{ij} \qquad (3.35)$$

Equations (3.32) – (3.34) contain model coefficients. These model coefficients have been optimised (Menter et al., 2003) based upon experiences with the model in a range of computational problems. The coefficients are given in Table 13.

Table 13 Coefficients used in the k-omega SST turbulence model and the corresponding values.

Coefficient	Value
β^*	0.09
β_2	0.0828
σ_k	1
$\sigma_{\omega,1}$	0.5
$\sigma_{\omega,2}$	0.856
γ_2	0.44

The definition for k is the same as equation (3.24). However ω needs to be defined, although the definitions are similar to equations (3.25) – (3.27), which are;

$$\omega \approx \frac{\sqrt{k}}{\ell \beta^{*\frac{1}{4}}} \tag{3.37}$$

$$\omega \approx \frac{\rho k}{\mu\left(\frac{\mu_t}{\mu}\right)} \tag{3.38}$$

$$\mu_t = \rho \frac{k}{\omega} \tag{3.39}$$

Equations (3.36) – (3.39) are for the initial and boundary conditions. However the conditions can still be prescribed the same way as previously, using intensity with length and velocity scales or via direct input of the model variables.

3.4 Combustion Modelling

The modelling of combustion is necessary to aid the prediction of the temperature, species and various flow parameters that will change during the phenomenon. This lends itself to many applications, including safety analysis. The combustion models tend to deal with the chemical reactions that occur and the resultant effect on the flow. The species and energies related to the reactions are then utilised in the governing equations of the fluid flow.

Combustion modelling is an important process, with many applications, and involves turbulent flow, heat transfer and chemical reactions amongst other processes both physical and chemical. It is important to predict the flow, species concentrations, possible emissions, pressures and other parameters. This is normally for the design and improvement of equipment. Another application is to predict dangerous areas and as such aid in the mitigation of any damage.

Combustion modelling is important for any safety study, hence the inclusion in this work. This section gives an overview of various combustion models before continuing on to the different combustion regimes, which are likely to be encountered. This is followed by the combustion models that have been utilised within this work.

3.4.1 Combustion Modelling Overview

The basic equations of CFD are already well suited for the transport and heat transfer, whilst chemical reactions need to be implemented along with radiative heat transfer with extra models. Gaseous combustion can be split into two categories; premixed and non-premixed. Premixed combustion is when the fuel and oxidant are combined prior to combustion and then ignition occurs. Non-premixed combustion is the opposite and is when the fuel and oxidant are mixed, from different streams, and combustion occurs where the conditions are correct. These flames are also known as diffusion flames, because the fuel and air mix together via diffusion prior to combustion (Versteeg and Malalasekera, 2007).

The energy of combustion reactions is defined using thermodynamics. The internal energy and enthalpy are normally used. The enthalpy of combustion can be defined using the enthalpies of formation of the chemical species involved (Atkins and de

Paula, 2009). The stoichiometry and equivalence ratios, see section 2., are very important to combustion as they define the mixture of the chemicals involved.

The maximum possible flame temperature, also known as the adiabatic flame temperature, is achieved when the mixture is completely burnt. This is under either a constant pressure or volume and when no work is performed or energy is transferred to the surroundings. Complete combustion does not always happen though and reactions can be reversible, this is known as dissociation. Some species may be created and used in different reactions, even though a reaction could be reversible. The resulting mixture after combustion and dissociation would need to be known, this resultant mixture would be in equilibrium. This is found through the second law of thermodynamics. The time taken to reach equilibrium is determined by the chemical kinetics of the reactions. The rates of reactions are used in the transport equations for all species as source terms. Due to species possibly getting used in further reactions, other than a reversible reaction, just the forward reactions can be used. Reaction rates are normally expressed via the Arrhenius equation. The problem with this is that some of the parameters, such as activation energy and pre-exponential constant, are reaction dependent. Detailed reaction mechanisms can be very big, hydrogen has at least 20 reversible reactions. Solving for all of these can be computationally expensive, due to the evaluations of kinetics and transport of species. Therefore it is normal to use a reduced mechanism, although there is a trade between accuracy and computational cost. Therefore it is normal to compare a reduced mechanism to the detailed version and if possible against experimental data.

The continuity and momentum equations can be used without change for combustible flows. The transport equation is then utilised for individual species, using the mass fraction of the species, as well as any other important parameters like turbulence. The energy equation is normally an adapted transport equation for enthalpy. This is because the temperature of a flow depends on the thermodynamic state and mixture composition. However some models do not require an enthalpy transport equation, such as the laminar flamelet model. Most parameters of the energy equation are calculated using computer packages, such as CHEMKIN (Reaction Design, 2014) or DARS (CD-adapco, 2016), when using detailed chemistry models.

There is a simple chemical reacting system (SCRS) model that is more concerned with the over-arching combustion process. This uses a simple chemical reaction and is not interested with detailed kinetics but assumes that reactants are equal to products, in stoichiometric proportions. It also assumes an infinitely fast reaction and therefore ignores any intermediary reactions. The SCRS model can be applied for laminar diffusion flames by calculating species and temperatures. Due to the assumptions this model can have inaccuracies, mainly because of the minor species being ignored (Versteeg and Malalasekera, 2007).

Turbulent non-premixed combustion is more complex than laminar simulations, even if simple chemistry is assumed. A major problem to be focused on is the heat generation in specific areas, which causes density to vary depending on the position. The turbulent flow would also have density fluctuations. Variables in a reacting flow are averaged in the same manner as general variable decomposition in Reynolds averaging. This yields an extra term in the Reynolds averaged equation, when compared to the instantaneous version. However to negate this extra calculation an averaging method is used, known as Favre averaging (Favre, 1969). However most experimental results are time averaged and as such a conversion is needed for Favre averaged simulation results to match experimental results (Versteeg and Malalasekera, 2007).

A statistical approach to calculate the average quantities would negate the need for a conversion between Favre averaged and time averaged results. A popular method is using a probability density function (PDF) approach (Bilger and Kent, 1974; Lockwood and Naguib, 1975; Pope, 1976). This is extremely useful for the density weighted mixture fraction. There are many different PDF methods and can be found in most mathematics textbooks (Versteeg and Malalasekera, 2007).

A chemical equilibrium model (Kent and Bilger, 1973) can be used for turbulent combusting flows when intermediary reactions are taken into account. As discussed above there are packages that can be used for the concentrations of species at equilibrium, including any minor species. This can be used in place of fast reacting chemistry. This method can be adjusted to partial equilibrium, so that some species are at partial equilibrium and others are not. This would be advantageous as minor species may not be in equilibrium (Versteeg and Malalasekera, 2007).

The eddy break-up model (EBU) (Spalding, 1971) is a simple yet efficient model. The rate at which fuel is consumed is as a function of the local flow properties. A mixing controlled reaction rate is used and is a function of the turbulence time scale. However kinetically controlled reactions can be used, expressed by an Arrhenius kinetic rate. This model has high dependency on the performance of the turbulence model.

The EBU model has been modified to an eddy dissipation concept (EDC) model (Ertesvåg and Magnussen, 2000). This model incorporates the significance of finer structures of the flow on the chemistry. It utilises the kinematic viscosity as well as turbulent kinetic energy and dissipation to define a mass fraction (Versteeg and Malalasekera, 2007).

The laminar flamelet model is a compromise between the need for detailed chemistry and simplicity (Peters, 1986, 1984). It views the turbulent flame as a mixture of stretched laminar flamelets. This is because turbulent flames can be described as wrinkled laminar sheets of reaction that are moving. It also considers major heat releases to occur in narrow regions. These are the flamelets which are at least considered to be in the turbulent flame. This is based on the assumption that the chemical reactions will occur quicker than the turbulent time scales. This would mean that reactions occur within a local vicinity. The properties of the flamelets are calculated once outside the flow field so that a laminar flamelet library can be constructed. This library consists of relationships between scalar properties and the mixture fraction. Due to the turbulent flow and the flame stretching a parameter, such as strain rate or scalar dissipation rate, is included in the flamelet library. The advantage of this method is that it can include detailed chemistry much easier. This is because the majority of the parameters are contained within the flamelet library.

3.4.2 Combustion Regimes

Combustion can occur in two modes, flame and non-flame (Turns, 2000). The difference between these two modes is the presence of a flame front. This work focuses on flames, as this is the more likely scenario. Flames can be defined as premixed or non-premixed (diffusion) (Turns, 2000). There are also partially premixed flames which as the name describes are a combination of both flame types. The

differences between premixed and diffusion flames is to do with the state of the mixture before ignition occurs. Both premixed and non-premixed flames are investigated within this work.

Premixed flames have both the fuel and oxidiser (air) mixed before ignition. This can be before entering a fluid domain with ignition at the inlet, like a Bunsen burner or an engine (Turns, 2000; Versteeg and Malalasekera, 2007). It can also be within the entirety of an enclosure, giving a homogeneous mixture.

Non-premixed flames have the fuel and oxidiser mixed separately, such that reaction occurs at the interface between the two (Turns, 2000). They can be mixed prior to ignition via diffusion (Versteeg and Malalasekera, 2007).

Both flame types can be influenced by turbulence, such that they can be either laminar or turbulent (Poinsot and Veynante, 2005). This work only pertains to turbulent flames. Turbulent combustion is the interaction between the chemistry and turbulence, which can increase the turbulence. This is caused by flow accelerations through the flame front by the heat released and the changes in viscosity and density by temperature. The turbulence can also alter the flame structure which could increase or decrease the flame (Poinsot and Veynante, 2005).

This work utilises the RANS equations, for combustion the drawback is that averaged flow fields are used. This means that variables, such as temperature, are instantaneously viewed as a constant which corresponds to the mean value at a given location (Poinsot and Veynante, 2005).

The description of the combustion models used to solve both types of flame is given in the following section.

3.4.3 Combustion Models

Two combustion models have been used within this work, one for each type of combustion. Firstly the premixed model is described, followed by the non-premixed model.

3.4.3.1 Premixed Combustion Model – Eddy Break-Up Model

The model used for premixed combustion is the Eddy Break-Up (EBU) model, first formulated by Spalding (Spalding, 1971). This uses the local flow properties to determine the rate of fuel consumption, such that turbulence controls this rate (Poinsot and Veynante, 2005; Versteeg and Malalasekera, 2007). This is expressed in the form of a turbulent mixing parameter (turbulent time scale). However before this is explained the equations for the model need to be addressed. This utilises the Favre-averaged equation for species transport (3.22), which is given below (CD-adapco, 2015; Poinsot and Veynante, 2005; Versteeg and Malalasekera, 2007):

$$\frac{\partial \bar{\rho}\tilde{Y}_f}{\partial t} + \frac{\partial \bar{\rho}\tilde{u}_i\tilde{Y}_f}{\partial x_i} = \frac{\partial}{\partial x_i}\left(\bar{\rho}D\frac{\partial \tilde{Y}_f}{\partial x_i}\right) + \tilde{\dot{\omega}}_f \tag{3.40}$$

However now the source term, $\widetilde{S_{Y_k}}$, from (3.22) becomes $\widetilde{\dot{\omega}_f}$ in (3.40). This is the mean reaction rate for a species and should not be confused with the turbulence frequency in section 3.3.3.3. The mass fraction subscript is now replaced by f, which denotes fuel. The equation for the mean reaction rate is (CD-adapco, 2015):

$$\tilde{\dot{\omega}}_f = -\bar{\rho}C_{EBU}\frac{1}{\tau_t}b(1-b)\left(Y_f^u - Y_f^b\right) \tag{3.41}$$

where C_{EBU} is a model coefficient, τ_t is the turbulent mixing time (to be defined later), Y_f^u is the unburnt fuel mass fraction, Y_f^b is the burnt fuel mass fraction and b is defined as:

$$b = \frac{\tilde{Y}_f - Y_f^b}{Y_f^u - Y_f^b} \tag{3.42}$$

However when the equivalence ratio is ≤ 1 then $Y_f^b = 0$. Then using this relationship and substituting (3.42) into (3.41) gives:

$$\tilde{\dot{\omega}}_f = -\bar{\rho}C_{EBU}\frac{1}{\tau_t}\frac{\tilde{Y}_f}{Y_f^u}\left(1-\frac{\tilde{Y}_f}{Y_f^u}\right)Y_f^u \tag{3.43}$$

Equation (3.43) is similar to those in (Poinsot and Veynante, 2005; Versteeg and Malalasekera, 2007; Veynante and Vervisch, 2002). However there is the additional Y_f^u placed at the end (CD-adapco, 2015).

The last term to define is the turbulent mixing time, τ_t. This is defined as (CD-adapco, 2015; Ferziger and Perić, 2002; Poinsot and Veynante, 2005; Veynante and Vervisch, 2002):

$$\tau_t = \frac{k}{\varepsilon} \approx \frac{1}{\omega} \tag{3.44}$$

This is because of the relationship $\omega = \varepsilon/k$. Equation (3.44) shows two possible definitions for the turbulent mixing scale. (Ferziger and Perić, 2002) state that the method employed should be dependent on the turbulence model utilised. However that is not the case with the software used for this work.

Equation (3.43) shows that the progress of the combustion is controlled by τ_t. This can be deduced because only the turbulence and fuel mass fraction can change. The fuel mass fraction gives information on the state of the combustion which means that the turbulent mixing time influences the rate of combustion.

3.4.3.2 Non-Premixed Combustion Model – PPDF

The non-premixed model that is used within this work is the Presumed Probability Density Function (PPDF) (Jones, 1980; Peters, 1986; Veynante and Vervisch, 2002). The fundamentals are that some parametric variables are tracked within the domain, such as mean mixture fraction. Then other variables, such as species, temperature and density, are obtained as functions of the parametric variables. These variables are stored in a look-up (PPDF) table. This is after an averaging process using a presumed probability distribution, which represents the turbulent fluctuations (CD-adapco, 2015; Poinsot and Veynante, 2005; Versteeg and Malalasekera, 2007).

STAR-CCM+ has different variations of this model. Firstly, there is an option for the equation of state, known as adiabatic and non-adiabatic. The adiabatic variations use a PPDF specific ideal gas model, which interpolates species, density and temperature from a PPDF table. The non-adiabatic variations use the ideal gas law, which only interpolates species from the PPDF table. Density is from the ideal gas

law and temperature is calculated from the enthalpy and species (CD-adapco, 2015). The non-adiabatic variation is used within this work.

There are two other model types that can be used. These are known as the equilibrium or flamelet models. These are alongside the two other variations for the equation of state. The equilibrium PPDF model assumes local instantaneous equilibrium conditions. The flamelet PPDF model accounts for non-equilibrium and finite-rate chemistry effects (CD-adapco, 2015). Both of these variations are investigated during the work.

The PPDF model utilises equations for mixture fraction, $\tilde{Z}$, and mixture fraction variance. The mixture fraction is defined as (CD-adapco, 2015):

$$\widetilde{Z} = \frac{m_f}{m_f + m_o} \tag{3.45}$$

Where m_f is the mass of atoms from the fuel and m_o is the mass of atoms from the oxidiser. A transport equation is solved for the mixture fraction, which follows a similar form to (3.22). The mixture fraction variance, $\widetilde{Z''^2}$, is defined as (CD-adapco, 2015):

$$\widetilde{Z}''^2 = \left(\widetilde{Z} - \overline{Z}\right)^2 \tag{3.46}$$

There is also a transport equation for the mixture fraction variance, which follows a similar form to (3.22). The shape of the PDF depends solely on these two variables. The PPDF of the mixture fraction utilises a beta function which is (CD-adapco, 2015):

$$\widetilde{P}(Z) = \frac{Z^{a-1}(1-Z)^{b-1}}{\int_0^1 Z^{a-1}(1-Z)^{b-1}\,dZ} \tag{3.47}$$

Where $\tilde{P}$ is the probability and should not be confused with pressure. a and b are related to mean and variance by:

$$a = \frac{\overline{Z}}{\widetilde{Z}''^2}\left[\overline{Z}\left(1-\overline{Z}\right) - \widetilde{Z}''^2\right] \tag{3.48}$$

$$b = a\frac{\left(1-\overline{Z}\right)}{\overline{Z}} \tag{3.49}$$

Equations (3.48) and (3.49) are slightly different to those in other sources (Poinsot and Veynante, 2005; Versteeg and Malalasekera, 2007; Veynante and Vervisch, 2002).

The equilibrium PPDF model connects the mixture fraction to the conserved scalars via:

$$\phi = \widetilde{Z}\phi_f + \left(1-\widetilde{Z}\right)\phi_o \tag{3.50}$$

Where ϕ is a conserved scalar and the subscripts f and o represent fuel and oxidiser respectively. The averaged value of a scalar is dependent on the mixture fraction and enthalpy for the non-adiabatic equilibrium PPDF model. The averaged scalar can be obtained by:

$$\phi(Z,h) = \int_0^1 \phi(Z,h)\widetilde{P}(Z,h)dZdh \tag{3.51}$$

The mapping for the mean of any scalar to the mean mixture fraction and variance is computed through a PPDF table, compiled at the start. This is performed via a look-up of the table and then interpolation.

The flamelet PPDF model uses a different definition for ϕ, compared to (3.50). The equation for this model is (CD-adapco, 2015):

$$\phi = \phi(Z,\chi) \tag{3.52}$$

Where χ is the scalar dissipation rate, which is:

$$\chi = \left|\Delta Z\right|^2 = \left(\frac{\partial Z \partial Z}{\partial \chi_K \partial \chi_K}\right) \tag{3.53}$$

The flamelet library used is generated for different values of χ, whilst tabulating results as functions of Z and χ, this gives equation (3.52). Finally the averaged scalar is obtained by:

$$\phi(Z,\chi) = \int_0^1 \phi(Z,\chi)\widetilde{P}(Z,\chi)dZd\chi \tag{3.54}$$

The mapping for the scalar in (3.54) is obtained in the same way as that for (3.51).

3.5 Solution Algorithm

The solution algorithm is the method used to solve the equations that model the physics. The equations become discretised before use within the model. There are many variations of discretisation, thus further information is available in (CD-adapco, 2015). There are many different solution algorithms, however the method used in the work is the SIMPLE algorithm. SIMPLE stands for Semi-Implicit Method for Pressure-Linked Equations. The method was devised by (Patankar and Spalding, 1972) and is a predictor-corrector method.

A flowchart of the algorithm is given in Figure 9 (CD-adapco, 2015; Versteeg and Malalasekera, 2007).

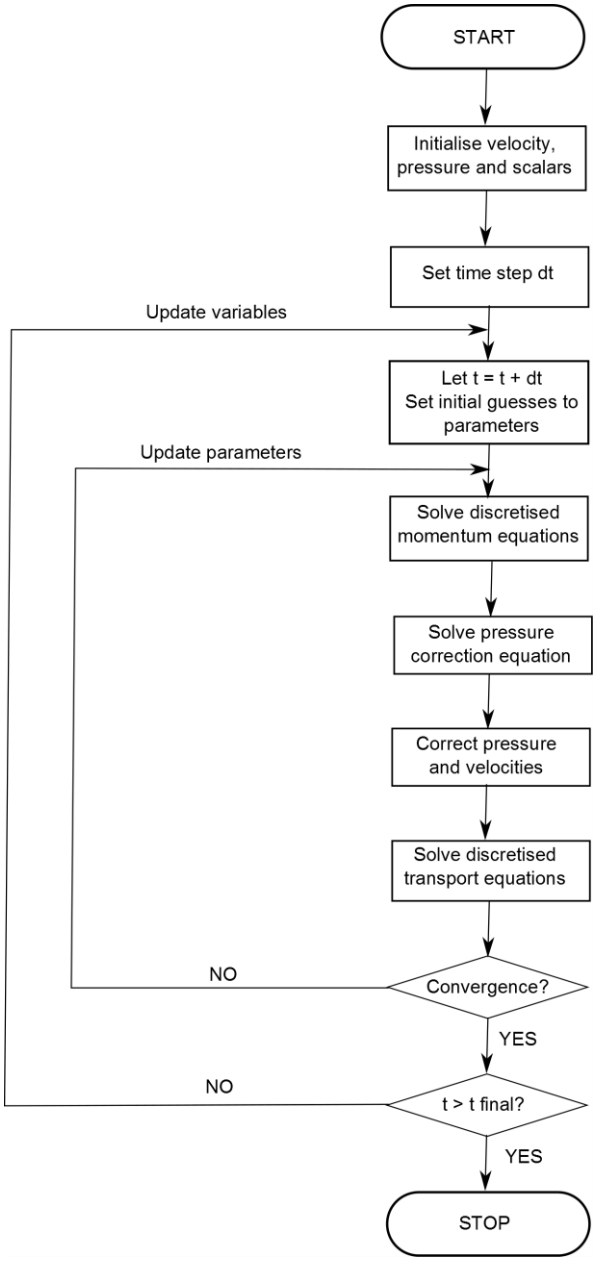

Figure 9 Flowchart of the SIMPLE algorithm.

3.6 Conclusion

This chapter has explained the governing equations for compressible flows and the transformation into the Favre-averaged equations. The concept of turbulence has been approached and the various models used have been explained. The theory of combustion and the models that are utilised have been discussed. Finally, the solution algorithm that is used is given.

Chapter 4 – Models for Non-Reacting Safety Assessment

4.1 Introduction

Investigating the initial phases of a release before an ignition is important. This is because it is preferable to limit the amount of flammable volume that accumulates, as such decreasing the possibility of ignition. By extension this could limit the potential damage and harm after ignition. There can be numerous possibilities that need to be examined, this is why modelling such problems becomes favourable. However all models need to be compared against experimental results to prove the validity and accuracy of them.

The validation of models has the potential to be endless, with continual improvement of model coefficients to fit experimental data. This is why the majority of model coefficients are fitted against numerous experimental data sets of varying problems. Whilst this would make a model increasingly accurate for a specific problem, it may not be completely transferable for another problem. It also hinders advancement into investigating other problems.

The work within this chapter relies on two different experiments, consisting of different geometrical configurations for assessment of the non-reacting modelling. Firstly, a smaller configuration is used to examine meshing strategies and sensitivity. This is followed by a turbulence model comparison utilising the results of the mesh sensitivity study. Secondly, the recommendations from the first configuration are applied to a larger geometry. This is more replicable with a residential garage and is why this was chosen. Two different release rates are used with one taking into account atmospheric conditions.

The chapter continues with the first study, on the smaller geometry. There is an initial mesh sensitivity study which is followed by an investigation into three turbulence models. The results of these studies are then applied to the second, larger, geometry. Here two different experiments are investigated, looking at different vent configurations and atmospheric conditions. This is performed to give increased

confidence in the proposed methodology on a similar geometry for the studies in Chapter 5. All of the experimental data was extracted using the software, WebPlotDigitizer.

4.2 Case Study 1 – Matsuura & Swain Data

This experiment was a release of hydrogen into a partially enclosed geometry, which resembles a hallway. The release was located at one end of the enclosure with vents located at the other end. The experiment was chosen because of its repeatability, namely that the experiment was conducted by two different research groups a decade apart and in different continents, (Swain, 1998) in the USA and (Matsuura et al., 2008) in Japan. Multiple data sets give more confidence in the modelling and show the potential for deviation between experiments.

This case study is split into two sections; the first is a mesh sensitivity study whilst the latter is a turbulence model comparison. However before the results, the experimental configuration and then numerical modelling will be explained.

4.2.1 Experimental Configuration

The experimental configuration employed is representative of a hallway, with the release source located at one end and 2 vents located opposite. Figure 10 is a photograph, taken from the publication of (Matsuura et al., 2008), of the experimental set up that was used. The inlet is visible by a dark rectangle at the base of the Perspex.

Figure 10 Photograph of the experimental rig used by (Matsuura et al., 2008).

Figure 11 shows the geometries that are used in the modelling and is comparable to Figure 10. The exterior surrounding the Perspex hallway is also used during the modelling. This is used so boundary conditions are not needed on the vents. This creates a realistic representation of the physics at the vents. Alongside this the walls of the enclosure were modelled as 5 mm thick, similar to the Perspex walls visible in Figure 10. The larger outer domain is used because it is then similar to that in (Matsuura et al., 2008).

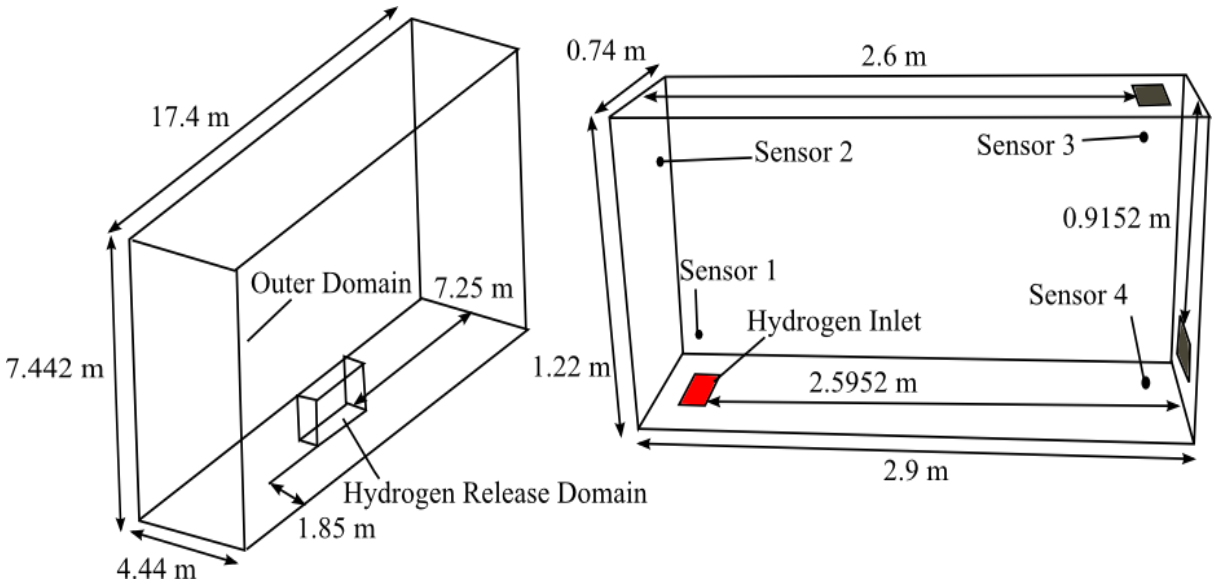

Figure 11 Geometries used for simulation (left – full numerical domain, right – hallway).

Figure 11 right is the geometry of the hallway, used in both the numerical domain and experiments. The inlet and vents all have the same dimension, 0.3048 m by 0.1524 m, whilst the enclosure had a volume of 2.35 m^3, dimensions for which are depicted in Figure 11. Pure hydrogen was released into the enclosure with a volume flow rate of 9.44 x 10^{-4} m^3/s, which corresponds to a mass flow rate of 7.7408 x 10^{-5} kg/s. The hydrogen concentration was measured at four locations, two upper sensors and two lower sensors, with one of each at separate ends of the enclosure. The sensor locations in Figure 11 right are given in Table 14.

Table 14 Sensor locations for case study 1.

Sensor	x coordinate (m)	y coordinate (m)	z coordinate (m)
1	0.152	0.152	0.596
2	0.152	1.009	0.219
3	2.676	1.009	0.596
4	2.676	0.152	0.219

4.2.2 Numerical Setup

The numerical model consisted of transient equations for continuity, momentum, energy and species, equations (3.1), (3.2), (3.5) and (3.22), for H_2 and O_2. Oxygen is modelled because air is treated as 79% nitrogen and 21% oxygen. Turbulence was also modelled; the information for the turbulence models employed has been given in section 3.. The diffusion of the species is accounted for by molecular diffusivity. The diffusion coefficients are calculated according to kinetic theory (CD-adapco, 2015). The extension to binary coefficients is accounted for by Chapman-Enskog theory (Poling et al., 2001). This is instead of the standard Schmidt number concept, which is not used due to the inherent physical discrepancies that arise when hydrogen is present in vast quantities. These discrepancies are due to the vast differences in diffusivity for hydrogen compared to oxygen and nitrogen.

The equations are solved using the SIMPLE algorithm, as explained in section 3.5 Solution Algorithm. Under relaxation is applied to stabilise initial iterations. The initial conditions for the turbulence modelling were calculated via the turbulence intensity and length scale which were assumed to be 1% and 0.3048 m respectively. These values are the same as those from (Matsuura et al., 2008) who performed the experiments.

The boundary conditions applied were a mass flow inlet and a pressure outlet. The pressure outlet is located at the top of the outer domain. The mass flow inlet had a constant temperature, pressure and mass flowrate. The pressure was set to atmospheric whilst the temperature was 300 K. The species at the inlet was pure

hydrogen with the mass flow rate of 7.7408 x 10^{-5} kg/s. Turbulence was again calculated via the turbulence intensity, which was 1%, and the turbulence length scale, which was 8.89 x 10^{-4} m. The pressure outlet was located at the top of the external geometry. This is deemed to be far enough away as to not interfere with the flow at the vents. The pressure prescribed here was atmospheric whilst the turbulence intensity was 1% and the length scale was 0.3048 m. The walls were modelled as smooth with a no-slip condition for the shear stresses. The vents were built in such a way that there were no constraints placed upon them and the flow was not constricted. The time step for the calculations varied depending on the mesh imposed; the coarse mesh used 0.08, medium mesh 0.05 and fine mesh 0.03 seconds. These values are chosen such that the Courant number remains the same.

4.2.3 Mesh Sensitivity Study

The mesh sensitivity study was performed using the same turbulence model, namely the k-ω SST model. The meshes that are compared have non-uniform cell sizing throughout the numerical domains. This is to save on computational expenditure, whilst ensuring accuracy in areas of interest. The meshes examined are given in Table 15.

The meshing strategy was such that the smallest cell size is used around the inlet and vents, with a slightly larger cell size used in-between these regions. The larger cell size is used for the majority of the external domain. All of the control volumes are hexahedral. The results for the mesh sensitivity study will now be given.

Table 15 Mesh comparison characteristics.

Mesh Name	Smallest Cell Size (m)	Largest Cell Size (m)	Total Number of Cells
Coarse	0.035	0.35	569781
Medium	0.025	0.25	1033850
Fine	0.015	0.15	3264235

4.2.3.1 Mesh Sensitivity Results

Transient data was extracted for the experiments from (Matsuura et al., 2008; Swain, 1998) for comparison against the numerical outputs from the simulations. The mesh sensitivity results are given per sensor, such that there are individual graphs for every sensor. This is given in order and provided as such to avoid confusion.

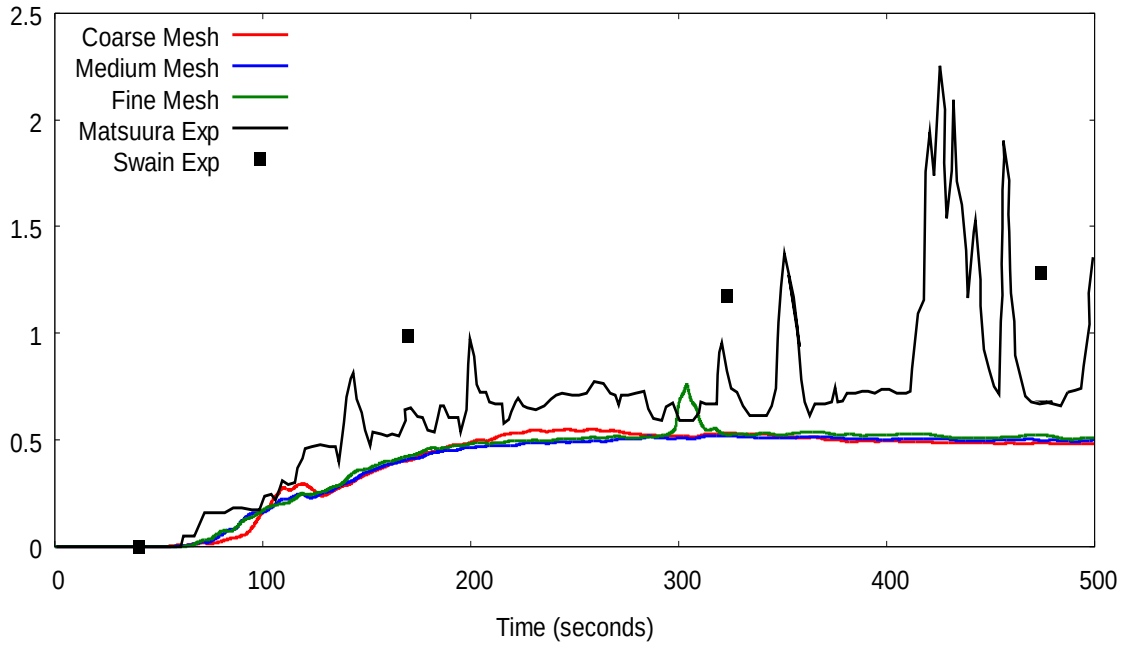

Figure 12 Sensor 1 mesh comparison.

Figure 12 shows that the difference between all three of the meshes, at sensor 1, is negligible, whilst there is a slight under-prediction against the Matsuura data (Matsuura et al., 2008). The difference between the coarse mesh and the fine mesh at 500 seconds is 0.03 volume % hydrogen concentration. There is a vast difference with the Swain data (Swain, 1998), as this reaches 1.28 volume % at the last reading. However the difference with the Matsuura data (Matsuura et al., 2008) is approximately 0.25 volume %, this is taken from the time region of 475 seconds. The differences between the numerical and experimental data could be explained by the incumbent error that may occur in the positioning of the sensor. This is possible because the numerical 'sensor' yields data for a specific point, taking the maximum value of the cell at that location. The experimental sensor would be bigger and as such could induce a positional error.

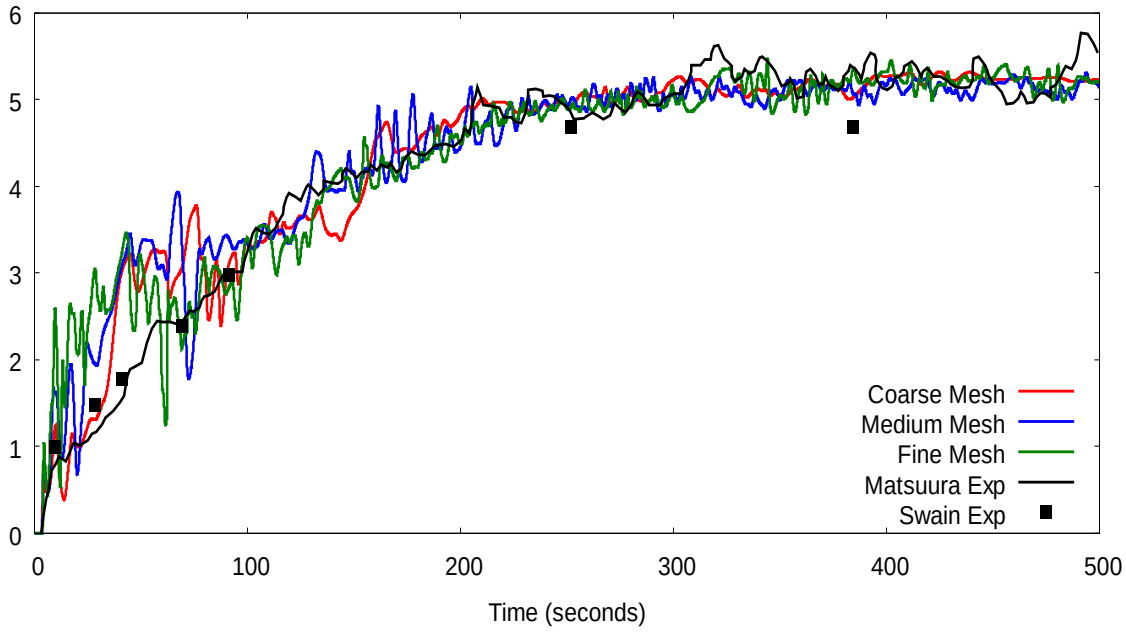

Figure 13 Sensor 2 mesh comparison.

Figure 13 shows that the differences between the meshes, at sensor 2, are small. This is shown by a hydrogen concentration variation of 0.02 volume % between the coarse mesh and the fine mesh, with the medium mesh situated in between. There is an over-prediction of hydrogen when compared to the data from Swain, whilst an under-prediction when comparing against the Matsuura data. However this does not explain the almost perfect matches between the Swain and Matsuura data up to 100 seconds. There is also an over-prediction initially for the numerical work during the accumulation phase of the release. However the numerical results tend to the experimental results after 100 seconds.

The fluctuations that are evident within the quasi-steady state, post 250 seconds are attributed to impingement on the roof. The impingement on the roof then causes circulation in the domain and around the area which encompasses the sensor.

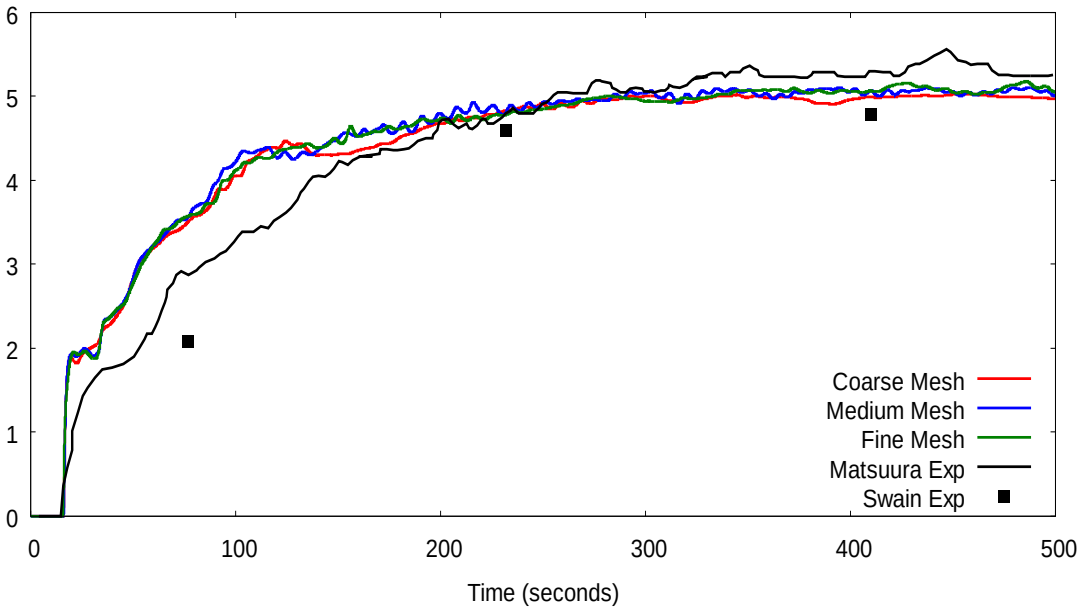

Figure 14 Sensor 3 mesh comparison.

Figure 14 shows that at sensor 3 there are again minor differences between the three meshes studied. The difference, during the quasi-steady state circa 400 seconds, between the coarse mesh and the fine mesh is 0.08 volume % of hydrogen. The medium mesh results are between the coarse and fine results. Similarly to the results for sensor 2, there is an under-prediction of the Matsuura data and an over-prediction of the Swain data. The difference between the two experimental sets of data is 0.47 volume % with the numerical results sitting in the middle of these two.

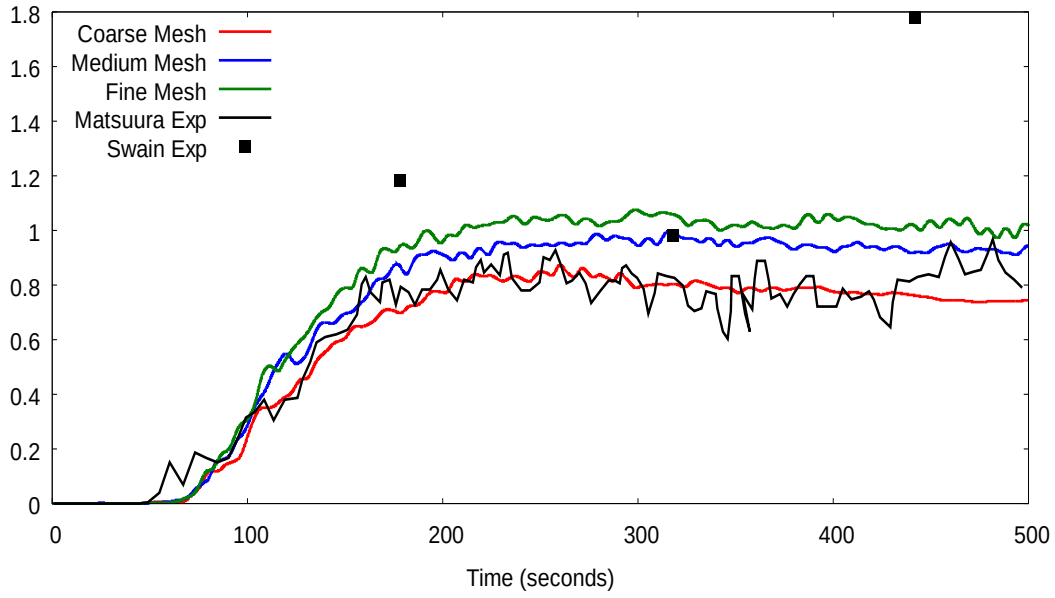

Figure 15 Sensor 4 mesh comparison.

Figure 15 shows a comparison of the numerical results against the experimental results for sensor 4, located near the lower vent. There are bigger differences between the meshes; the coarse mesh reads 0.74 volume %, medium 0.94 volume % and the fine 1.01 volume %. Although in the grand scheme of things the difference between the medium and fine mesh is still small, 0.07 volume %. The medium and fine mesh both show concentrations in between the two experimental data sets, slightly over-predicting the Matsuura data. The Swain data reaches 1.78 volume % whilst the Matsuura data reaches approximately 0.85 volume %, which is quite a significant difference.

There are many possible reasons for the discrepancies between the two sets of experimental results. Although it is my view that the differences between the experimental data sets is due to an improvement in sensors over the 10 years between the experiments. There is also the possibility of the atmospheric conditions being different at the two locations of the experiments. However from Figures 12 – 15 it can be construed that the differences between the medium and fine mesh are negligible and as such the medium mesh is suitable to be used for further investigation.

4.2.4 Turbulence Model Comparison

The turbulence model comparison utilises the medium mesh that has been explained previously and deduced to be independent. The different turbulence models used are the standard and realisable k-epsilon models as well as the k-omega SST model, which have been explained in section 3.3.. The results of the turbulence model comparison will now be shown and explained.

4.2.4.1 Turbulence Model Comparison Results

The results are portrayed similar to that of section 4.2.3.1.

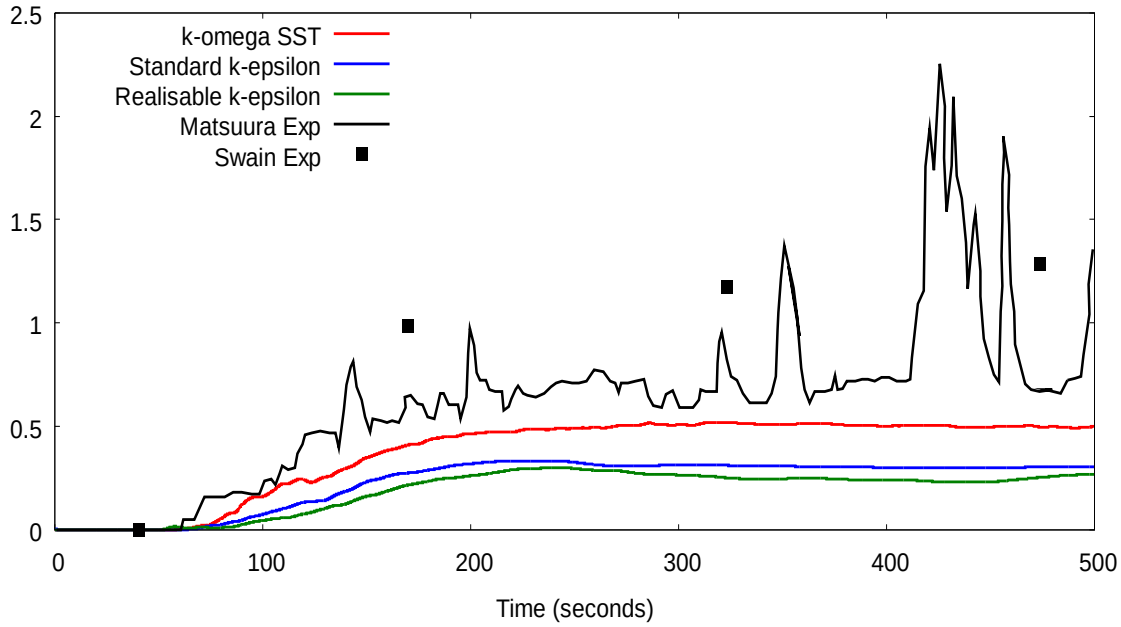

Figure 16 Sensor 1 turbulence model comparison.

Figure 16 contains graphical representation of the numerical and experimental results at sensor 1, for the turbulence model comparison. It can be seen that there are significant deviations between the turbulence models at sensor 1. This is evident by the difference between the standard k-epsilon model, recording 0.3 volume % hydrogen concentration, compared to the k-omega SST model which recorded a hydrogen concentration of 0.499 volume %. The realisable k-epsilon model performs even worse than the standard version of the k-ε model.

Table 16 shows the error comparison for the different turbulence models at sensor 1 for the time range 100 – 500 seconds, every 50 seconds. The error is calculated using the following equation:

$$Error\% = 100 * \left| \frac{Simulation - Experiment}{Experiment} \right|$$

The experimental data used for the error calculation is the Matsuura experimental data. The final row of the table is the average error for each turbulence model. It is clear that the k-omega SST model performs better than the others, with an average error of 40.3%. The standard k-epsilon model has an average error of 63.6% whilst the realisable k-epsilon model has an average error of 71.1%. The errors seem large but this is due to the small concentrations that are recorded for the simulations and experiment. This causes smaller deviations to be exacerbated.

Table 16 Error comparison for the turbulence models at Sensor 1.

Time (second)	Standard k-epsilon model % error	Realisable k-epsilon model % error	k-omega SST model % error
100.75	67.3	80.5	30.5
149.1	57.9	70.7	36.5
199.35	67.3	73.2	52.5
252.1	54.3	58.6	30.4
300.4	47.1	55.2	13.9
350.7	77.6	82.0	62.9
401.2	59.1	67.2	31.9
449.15	63.9	72.2	40.4
499.4	77.6	80.1	63.2
AVERAGE	63.6	71.1	40.3

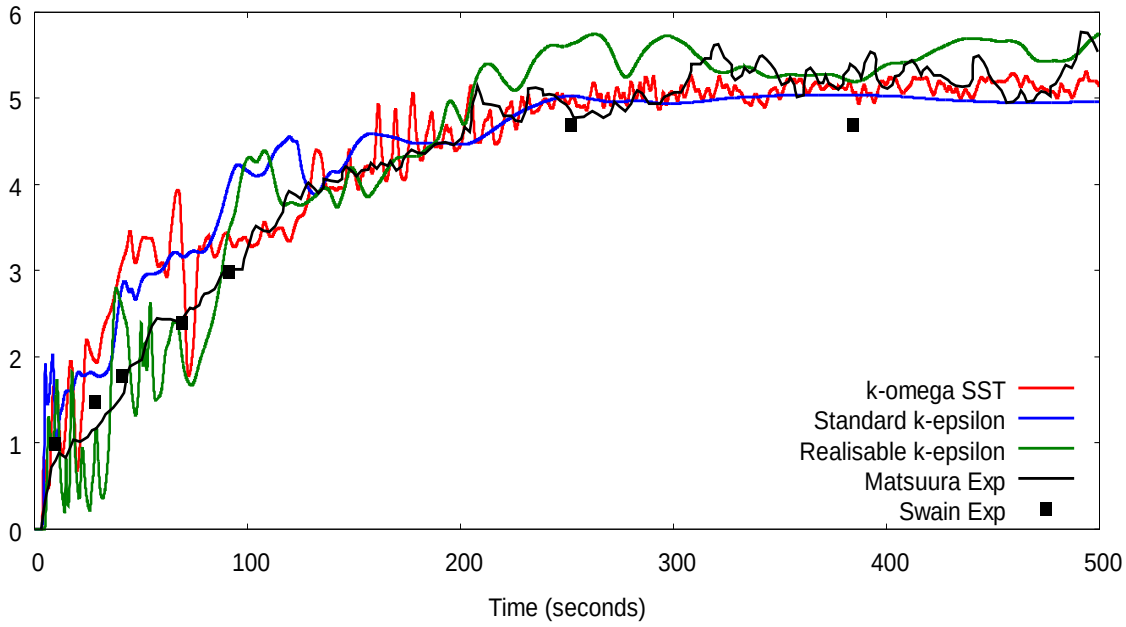

Figure 17 Sensor 2 turbulence model comparison.

Figure 17 shows the comparison of the predicted concentrations for the turbulence models against recorded experimental data at sensor 2. It can be seen that at sensor 2 the k-ω SST model performs better than either of the k-ε models. The k-ω SST model reaches a hydrogen concentration of 5.14 volume %, compared with the 4.97 volume % hydrogen concentration recorded for the standard k-ε model. The realisable k-ε model over-predicts the hydrogen concentration, recording 5.65 volume %.

Table 17 Error comparison for the turbulence models at Sensor 2.

Time (second)	Standard k-epsilon model % error	Realisable k-epsilon model % error	k-omega SST model % error
99.95	27.8	32.4	2.7
150.95	8.9	0.5	1.3
200.45	1.7	4.3	1.3
249.55	1.9	13.7	0.4
300.45	2.4	12.5	0.2
349.55	3.7	0.6	4.2
400.45	1.6	5.6	1.4
449.55	4.9	8.8	0.6
499.4	10.4	3.6	6.8
AVERAGE	7.0	9.1	2.1

Table 17 contains the error comparison at sensor 2 for the time range 100 – 500 seconds, in intervals of 50 seconds. The simulated data is compared against the Matsuura data. The final row of the table is the average error for the models. This shows that the k-omega SST model performs better than the others with an average error of 2.1%. The standard and realisable k-epsilon models have average errors of 7.0 % and 9.1% respectively. The errors are significantly lower than sensor 1 which is due to the higher concentrations seen at this location.

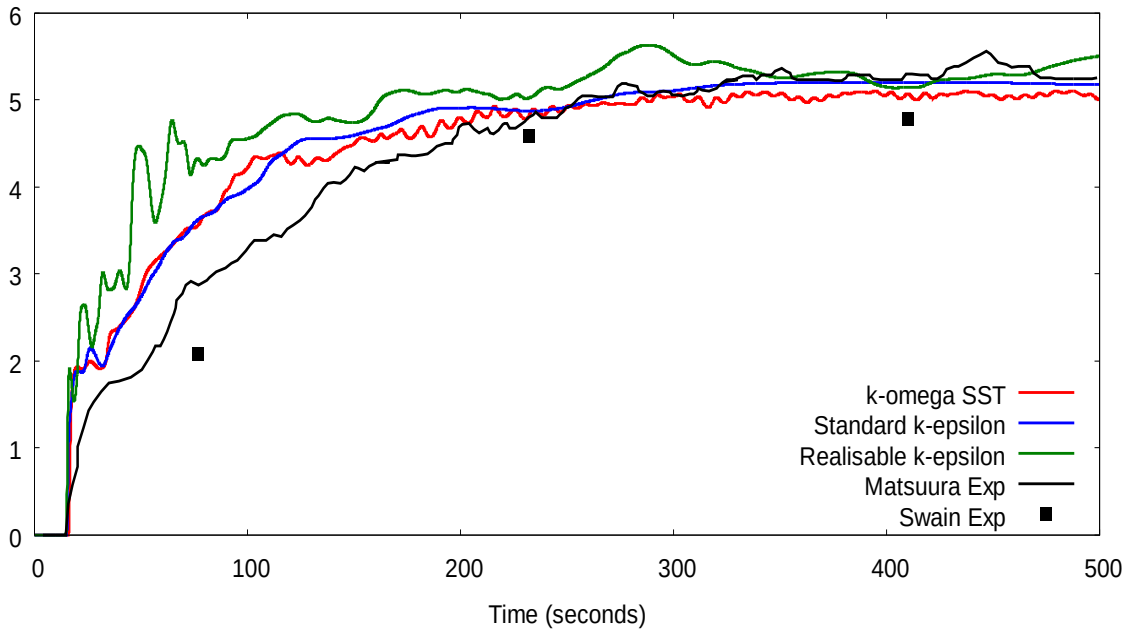

Figure 18 Sensor 3 turbulence model comparison.

Figure 18 shows the predicted and recorded data for the turbulence model comparison at sensor 3. Once again the realisable k-ε model over-predicts again, with a recorded concentration of 5.45 volume %. The standard k-ε model is a better match for the Matsuura data, as the recorded concentration is 5.18 volume % compared to the 5.24 volume % for the experimental data. The k-ω SST model under-predicts compared to the Matsuura data, as it records a concentration of 5.08 volume %. However the k-ω SST model is still between the two different experimental results.

Table 18 shows the errors between the turbulence models and the experimental data for the range 100 – 500 seconds, in intervals of 50 seconds. The final row of the table is the average error for each turbulence model. The turbulence model with the lowest average error is the standard k-epsilon model with a percentage of 5.1%. The realisable k-epsilon and k-omega SST models recorded average errors of 9.6% and 6.5% respectively.

Table 18 Error comparison for the turbulence models at Sensor 3.

Time (second)	Standard k-epsilon model % error	Realisable k-epsilon model % error	k-omega SST model % error
99.2	21.3	39.2	28.5
150.2	8.7	12.0	6.5
199.35	4.8	8.7	2.4
249.15	0.2	4.9	0.01
299.0	1.0	9.4	0.4
350.7	3.2	2.1	5.3
401.2	0.7	1.8	3.0
450.3	5.1	3.4	7.8
499.0	1.4	4.7	4.6
AVERAGE	5.1	9.6	6.5

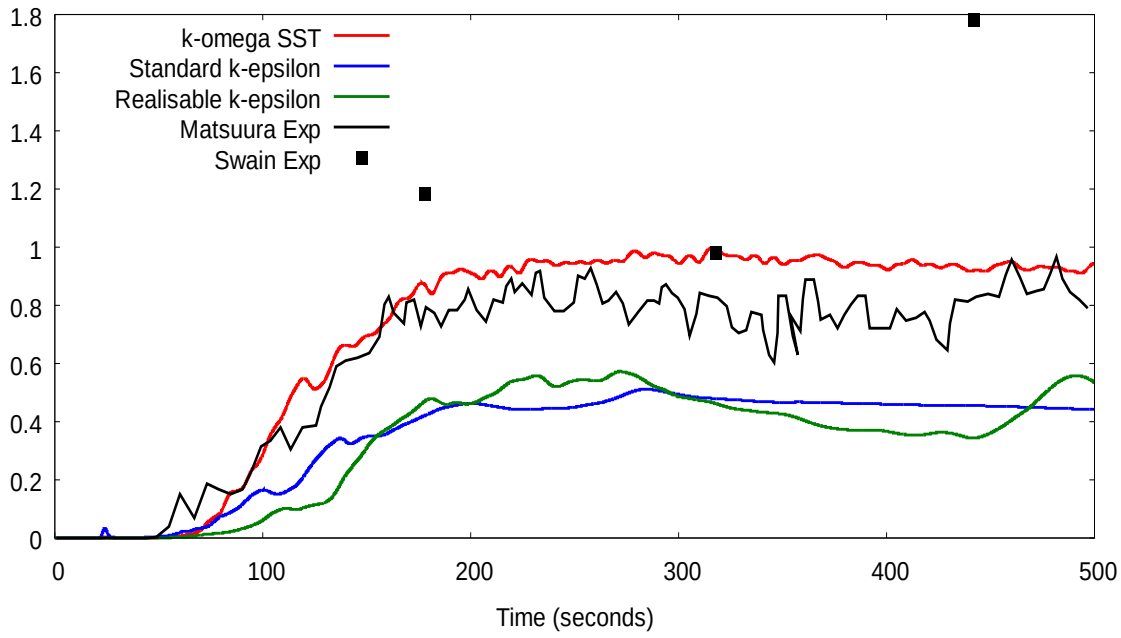

Figure 19 Sensor 4 turbulence model comparison.

Figure 19 is a graphical representation of the predicted and recorded concentrations at sensor 4. It can be seen that at sensor 4 the k-ω SST model over-predicts the Matsuura data whilst under-predicting the Swain data. This model records a hydrogen concentration of 0.94 volume %. Both the standard and realisable k-ε models under-predict the Matsuura data, with recordings of 0.44 and 0.52 volume % respectively.

Table 19 Error comparison for the turbulence models at Sensor 4.

Time (second)	Standard k-epsilon model % error	Realisable k-epsilon model % error	k-omega SST model % error
98.9	48.1	82.2	13.9
151.0	45.1	49.5	9.6
198.65	46.0	46.3	6.9
249.65	44.4	33.1	16.7
299.5	40.2	41.0	14.5
351.6	44.0	49.1	13.2
401.5	36.2	49.4	28.2
448.75	45.9	57.5	9.6
496.8	44.1	30.7	17.2
AVERAGE	43.8	48.8	14.4

Table 19 shows an error comparison of the turbulence models at sensor 4 for the range 100 – 500 seconds, in intervals of 50 seconds. The final row of the table shows the average error for each turbulence model. The lowest average error is for the k-omega SST model with an error of 14.4%. The standard and realisable k-epsilon models have average errors of 43.8% and 48.8% respectively.

Table 20 Combines the average errors for all sensors and turbulence models.

Sensor	Standard k-epsilon model % error	Realisable k-epsilon model % error	k-omega SST model % error
1	63.6	71.1	40.3
2	7.0	9.1	2.1
3	5.1	9.6	6.5
4	43.8	48.8	14.4
AVERAGE	29.9	34.7	15.8

Table 20 combines the average errors at all locations for each turbulence model. The final row contains the average error for each model investigated. The k-omega SST model has a final error for the problem of 15.8%. This is followed in accuracy by the standard and then realisable k-epsilon models, with average errors of 29.9% and 34.7%.

The results from Table 20 prove that the most accurate model to use is the k-ω SST model; it records hydrogen concentrations at three of the sensors better than either of the k-ε models. It is far more accurate at the lower levels, although the accuracy is worse than the upper levels. The decrease in accuracy at the lower levels is due to the lower concentrations, which exacerbate the discrepancies more. The upper sensors, 2 and 3, show greater accuracy across all of the models used.

4.3 Case Study 2 – HSL Data

The second case study consists of two simulations which are compared against experimental data from HSL. This was performed as part of the Hyindoor project (Hyindoor, 2012). The experiments chosen consist of single and double vents, whilst the latter also accounts for atmospheric conditions. The geometry is comparable to that of a residential garage, which is why these experiments are used for comparison. The experimental information and data is taken from (Hooker et al., 2013).

4.3.1 Experimental Configuration

The experimental configuration is an ISO container, which is similar to a residential garage. The volume of the container is 31 m^3 and contains multiple vents, as shown in Figure 20, reproduced from (Hooker et al., 2013). Figure 20 shows the dimensions of the geometry alongside the location of the vents.

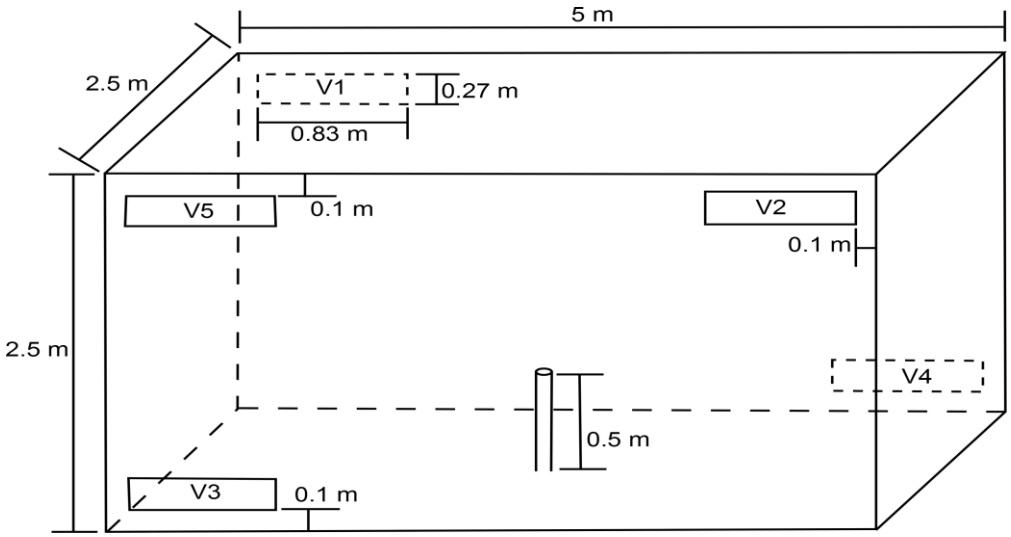

Figure 20 HSL experimental configuration.

The vents shown in Figure 20 can be open or shut depending on the venting configuration under investigation. The pipe shown is the inlet into the domain and is located centrally within the enclosure. The internal diameter of the pipe is 10 mm although the release pressure is relatively low, as a system of mass flow controllers are utilised.

The enclosure is located externally and as such atmospheric conditions need to be taken into account. Atmospheric conditions were measured near the enclosure. The most important information for simulating non-reacting experiments is the wind speed and direction. This was measured 3.4 m above the enclosure, 4.2 m above the ground.

The hydrogen concentration is measured using 27 oxygen sensors mounted in ‘layers’ at heights of 1 m, 1.75 m and 2.25 m. The locations are shown in Figure 21. The concentrations for each layer were then calculated by averaging the readings at each height.

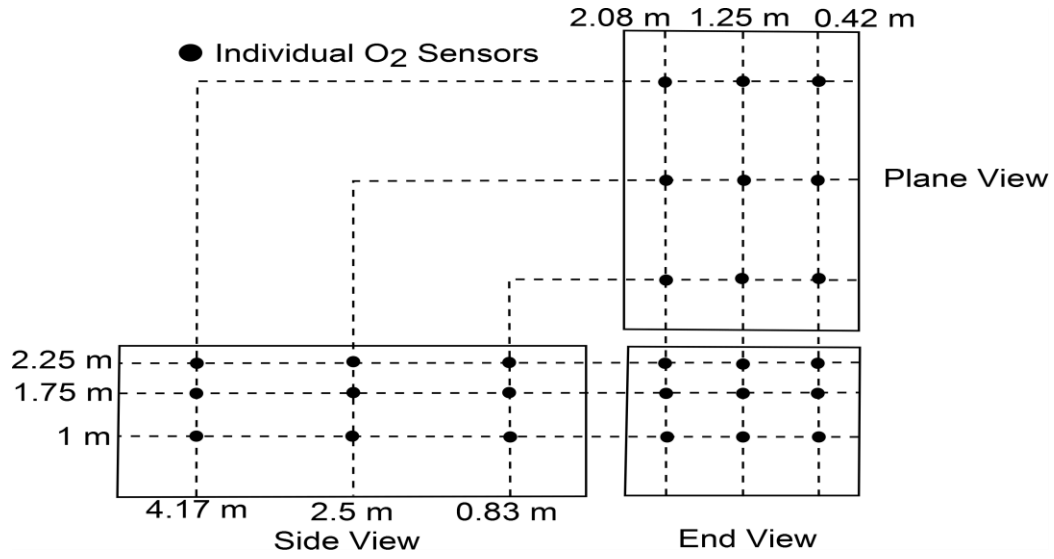

Figure 21 Sensor locations for the HSL experiments.

The two experiments used different release rates and venting configurations. The first experiment had a mass flow rate of 2 x 10^{-4} kg/s, which corresponds to a volume flow rate of 150 NL/min, for 50 minutes. This experiment only had a single vent, vent 1 in Figure 20, open. The wind direction was at the opposite wall to the open vent. The second experiment used a mass flow rate of 1.6 x 10^{-3} kg/s, corresponding to a volume flow rate of 1200 NL/min. This experiment had two vents open, one upper and one lower, which were vents 4 and 5 in Figure 20. This experiment only has transient data for the 1 m height however there are average data for all heights available. However the method used for averaging is not given and can therefore not be reproduced, this means that these readings are futile. The wind in this experiment was directed at the upper vent with an average wind speed of 3.1 m/s. However graphical data was given for the range 400 – 800 seconds, which shows some major oscillations (Hooker et al., 2013), which has been reproduced in Figure 22. It is evident that the average speed, of 3.1 m/s, stated in (Hooker et al., 2013) is clearly not viable as it does not represent the actual profile which is given in Figure 22 for the time range 400 – 800 seconds. Modelling this presents a problem as the preceding information is unknown.

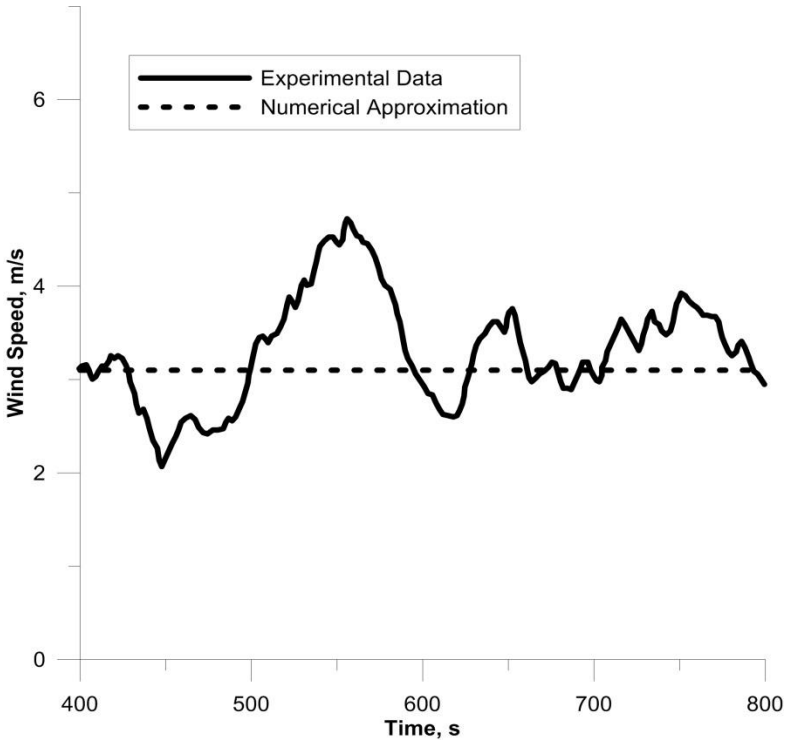

Figure 22 Wind profile for HSL experiment 2 (Hooker et al., 2013).

4.3.2 Numerical Setup

The numerical setup is similar to that utilised previously in section 4.2.2. This validation also used the outcomes from section 4.2.4.1, namely the medium mesh cell characteristics and the k-ω SST turbulence model.

The geometry was encased by an external domain with dimension 8 m by 8 m by 8 m; this was using the same logic as section 4.2.1. This was especially needed for the simulation with atmospheric conditions. There were a total of 674102 cells used for both the internal and external domains.

The simulation for comparison with experiment 2, with wind, was performed slightly differently. The first 100 seconds of the simulation had no hydrogen release, such that a wind profile was visible. After the 100 seconds the hydrogen release started, with the time reset to zero.

4.3.3 Results

The results for the first experiment are given, followed by the second experiment.

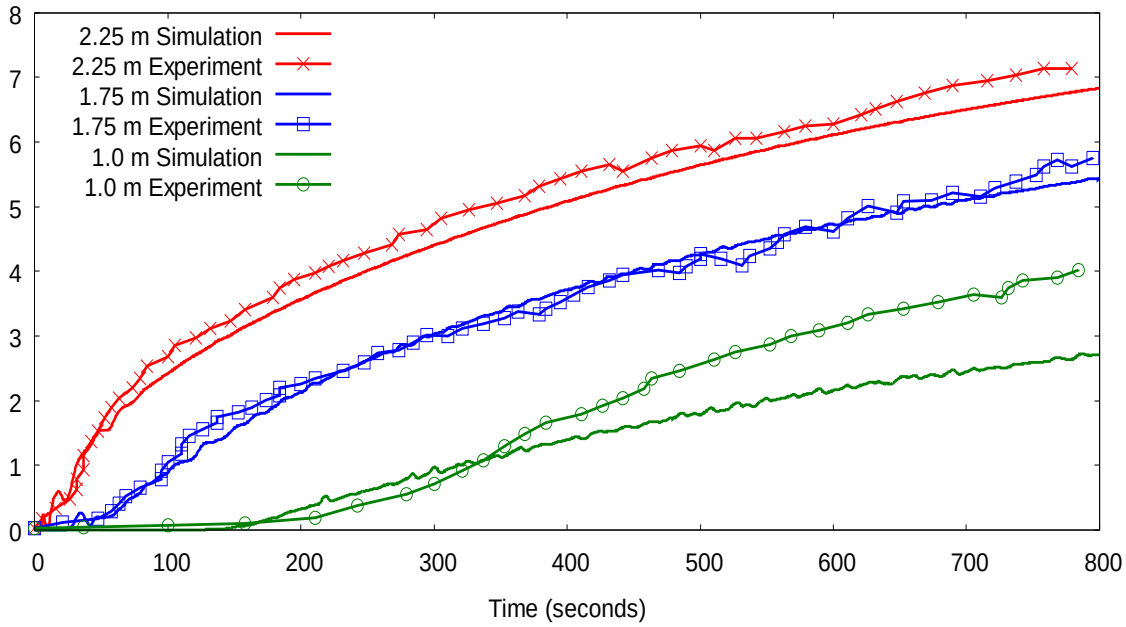

Figure 23 Results for HSL experiment 1.

Figure 23 shows the predicted and recorded hydrogen concentrations for the first HSL experiment. The predicted results show good agreement with the experimental data, especially for the upper levels of 2.25 m, red line, and 1.75 m, blue line. There is a very small under-prediction for the highest level, whilst the middle level is almost identical to experiments. The lower level of 1 m, green line, shows good agreement initially but there is an under-prediction after 350 seconds.

Figure 24 shows the hydrogen mole fraction, for the central plane parallel to the vents, at 800 seconds. This shows the behaviour of the hydrogen at the end of the simulation. The upper bound has been cut off at 0.08 hydrogen mole fraction such that the lower concentrations are visible. Unsurprisingly, the highest concentrations are within the jet directly above the release, which does not impinge upon the roof. It can also be seen that the flow of hydrogen is symmetric.

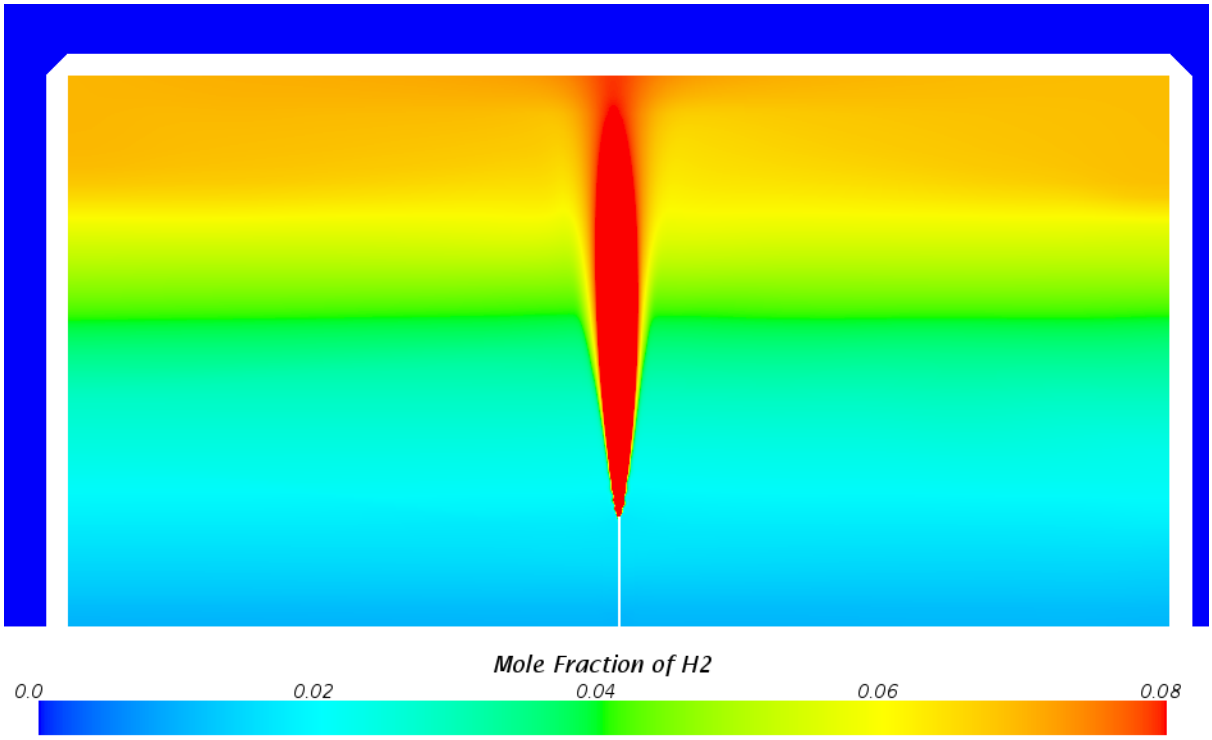

Figure 24 Planar image of hydrogen mole fraction for HSL 1, at 800 seconds.

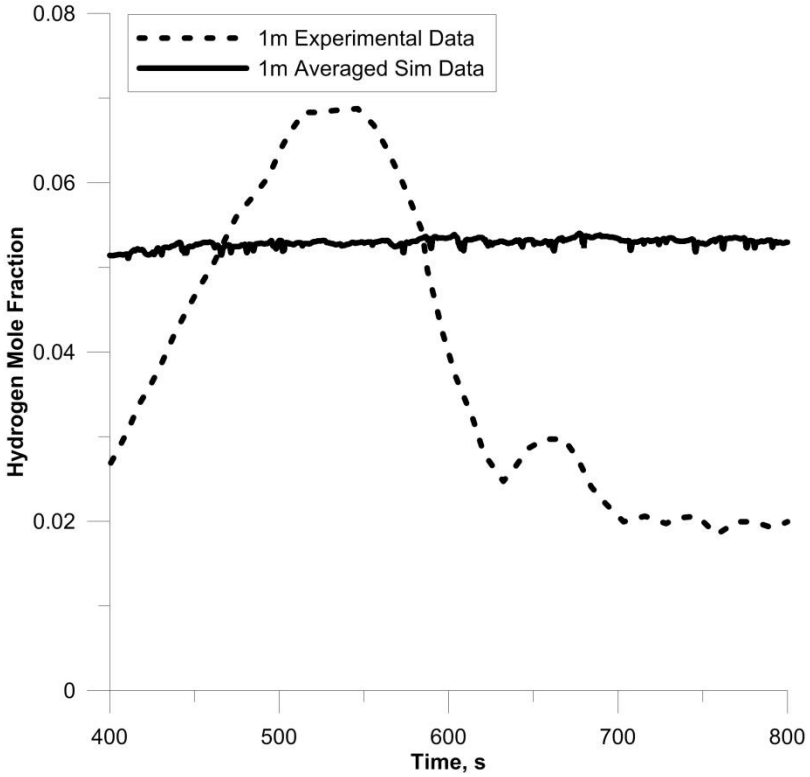

Figure 25 Results for HSL experiment 2.

Figure 25 shows the recorded and predicted hydrogen concentrations at a height of 1 m for the second HSL experiment used. This scenario had a wind profile present

which is given in Figure 22. The graph shows that the experimental measurements fluctuate due to the varying wind, whilst the simulation results show the concentration is almost constant. This happens because using an average wind profile is not an accurate prediction of the atmospheric behaviour. It is also not possible to predict either the wind or hydrogen behaviour prior to 400 seconds, which is why the average wind profile is used.

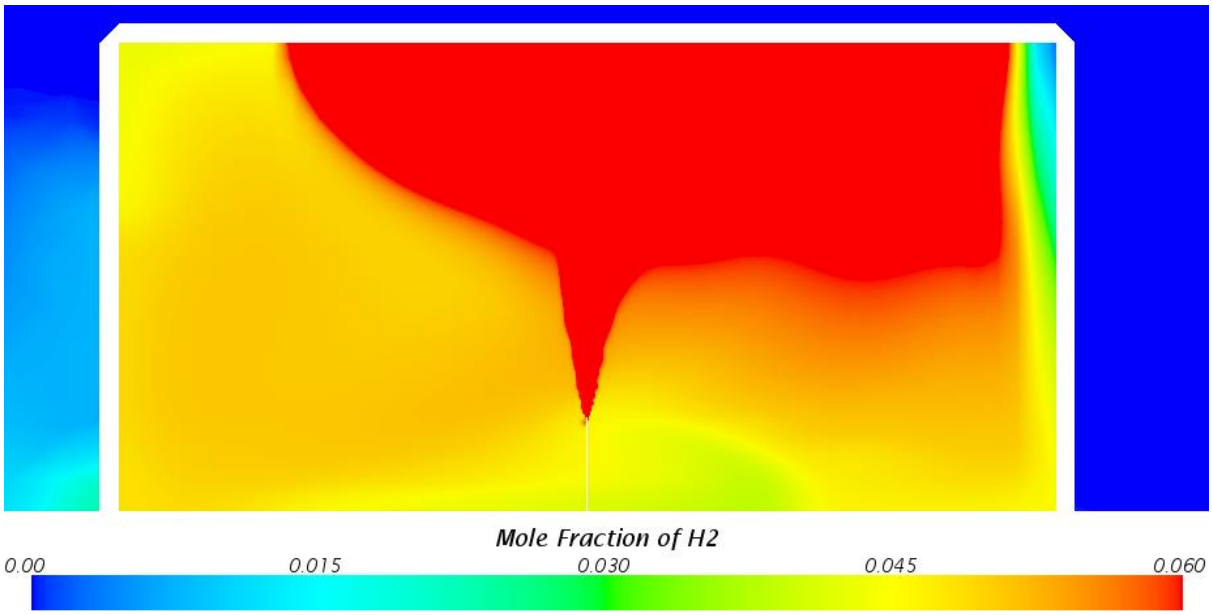

Figure 26 Planar image of hydrogen mole fraction for HSL 2, at 800 seconds.

Figure 26 shows the hydrogen mole fraction, representative of volume percentage, for the central plane, parallel to the vents. The upper bound is set to 0.06 hydrogen mole fraction such that the lower mole fractions have greater visibility. It is evident that the atmospheric conditions, combined with the multiple vents influence the flow of hydrogen, hence the lack of symmetry compared to Figure 24. The right hand side shows evidence of the flow coming into the enclosure, visualised by the low mole fraction near the wall. This also shows that the higher concentrations are too the right of the release.

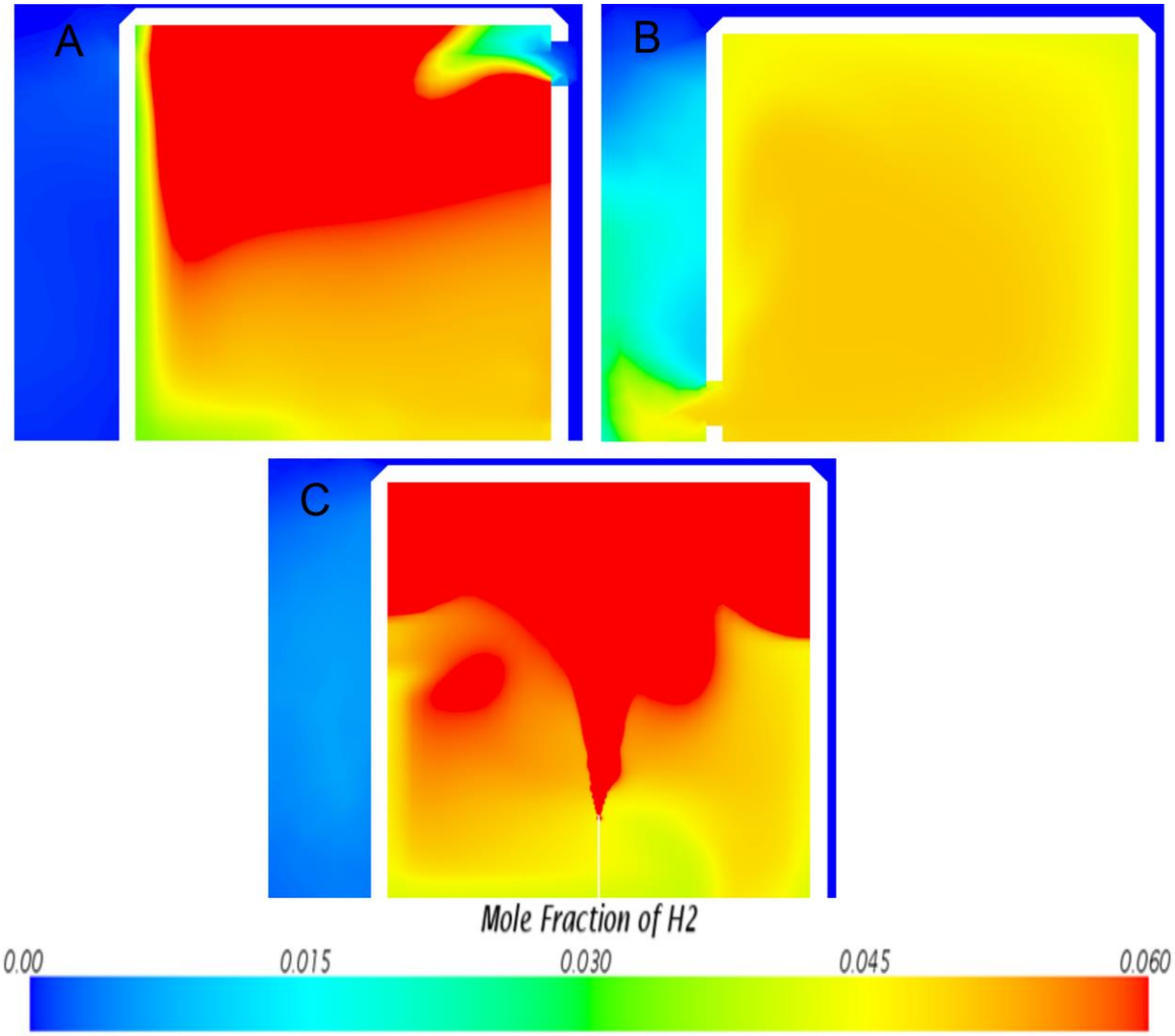

Figure 27 Planar images of hydrogen mole fraction, at 800 seconds. A is perpendicular to vent 5. B is perpendicular to vent 4. C is central and parallel to the other to planes.

Figure 27 depicts planar images of hydrogen mole fraction at three locations, and is perpendicular to the view in Figure 26. Figure 27 A is across vent 5, B is across vent 4 and C the centre of the enclosure. It is worth noting that the wind is coming towards vent 5. This shows that the atmospheric conditions aid mixing, evident by the almost uniform mixture depicted in Figure 27 B.

Figure 27 A shows the air flow enters the enclosure which meant the buoyancy of hydrogen is negated. This causes the higher concentrations to reach lower on the left hand side. This phenomena is the cause of the higher average concentration recorded, shown in Figure 25. Figure 27 C shows that the air flow across the enclosure causes asymmetry around the release point. This is again caused by the flow of air entering the enclosure at the upper vent, thus forcing the hydrogen out of the lower vent.

The results for the second HSL experiment, Figure 25, show that without accurate information it is impossible to model atmospheric conditions. However the results for the first HSL experiment, Figure 23, show an accurate prediction for the simulation against the experimental data, especially at higher levels. Therefore it can be concluded that the modelling techniques that were applied to that problem are suitable and can be trusted in moving forwards to modelling hypothetical scenarios.

4.4 Conclusion

This chapter has shown a mesh sensitivity analysis and turbulence model comparison to determine suitability for further work. This was then followed by further validation on a different geometry, to increase confidence in the modelling techniques.

The mesh sensitivity study shows that the medium mesh, which utilises cell sizes ranging from 0.025 m – 0.25 m, is suitable for further work. The more suitable turbulence model is the k-omega SST model, which has a total average error of 15.8%. This error is almost half as much as the next best, the standard k-epsilon model.

The second set of experiments utilised a bigger geometry than the first and two different experiments. The first experiment had a slower inlet velocity and only one vent open. The results between the recorded and predicted concentrations showed good agreement at three different heights. The second experiment had a quicker release rate, two vents open and was also influenced by atmospheric conditions, namely wind. The information available was for the time range 400 – 800 seconds, although an average wind speed was given. The average wind speed was used for the entire simulation, as no information was given prior to 400 seconds. The predicted results show an almost constant concentration whilst the recorded results show strong deviations. This is due to the wind that was acting upon the enclosure during the experiment.

The results give confidence in the meshing strategy and models to be used for further investigations.

Chapter 5 – Modelling of Non-Reacting Scenarios

5.1 Introduction

Natural ventilation is favourable for non-reacting safety studies because there are no dependencies. This is compared to mechanical (powered) ventilation, such as fans, which requires electricity and as such is subject to failure. Natural ventilation is boosted when hydrogen is used because of its density, 0.09 kg/m^3, compared with air, 1.23 kg/m^3, which induces buoyancy. The ideal scenario is that any leak can be dispersed externally before ignition occurs. The following work uses this scenario.

This chapter investigates venting strategies for a geometry that resembles a residential garage. The work applies the recommendations from Chapter 4. The aim of this work is to find the most realistic and suitable ventilation strategy to mitigate accidental releases of hydrogen. A single failure mode is assumed and as such a single release source is used. The failure mode is the connector between the refuelling tank and the vehicle. Another option could be the pressure relief device (PRD) however operational pressures are unknown at the moment.

5.2 Geometrical Configurations

The geometrical configuration considered is a volume which resembles a residential garage, which is naturally ventilated. The ventilation consists of vents located opposite and near the release source, a low vent opposite the release is always used. The number and position of the vents changes depending upon the investigation, whilst the total venting area remains 0.05 m^3. The addition of a vehicle is also considered for some of the investigations. There is an external domain encasing the garage geometry, following the same logic as Chapter 4. The main geometries in question are given in Figure 28.

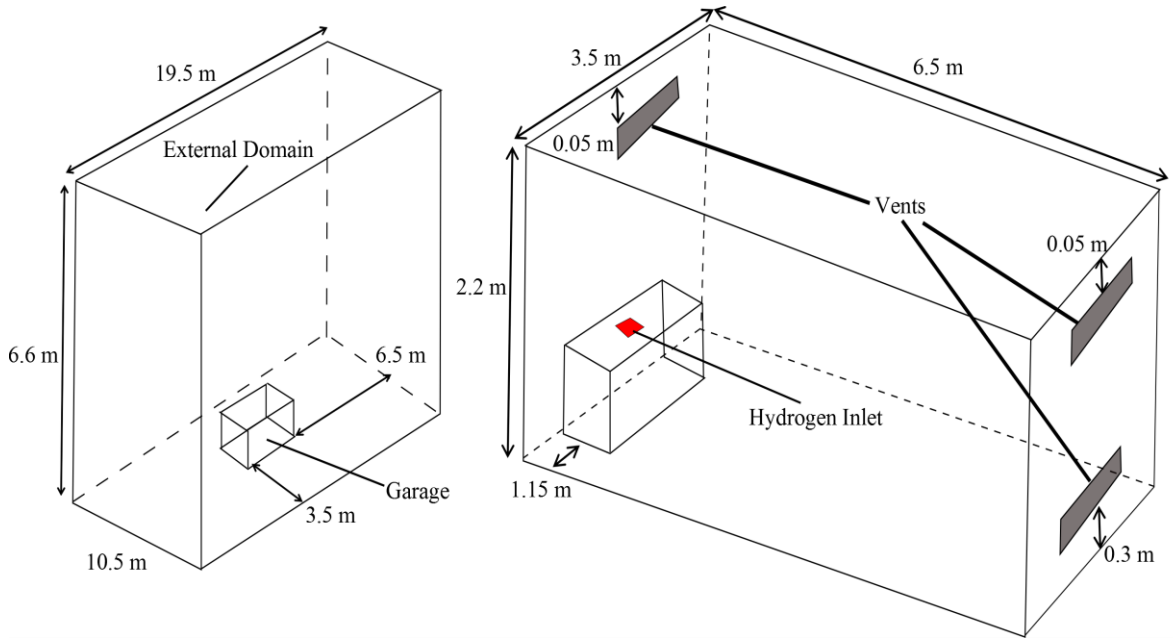

Figure 28 Initial geometry for studies (left - external domain, right – enclosure).

Figure 28 left is the external domain that is kept constant. Figure 28 right is the garage geometry that is used. The garage geometry does vary; the variations are the position of the vents, the number and size of the vents and the presence of a vehicle. The vents highlighted in Figure 28 right are the location of all of the vents used. The two vent configuration utilises vent sizes of 0.25 m by 0.1 m. The three vent configuration reduces the size of the vents opposite the release, also referred to as the door. The door vents reduce by half, such that the venting area in the door is the same however the vents themselves are smaller, 0.125 m by 0.1 m. The door vent reduction is used instead of reducing the upper vents so that the total venting area on each face is not reduced. This is to maintain ventilation regardless of atmospheric conditions. The hydrogen inlet has dimensions of 0.05 m by 0.05 m, and is located centrally in the top of the hydrogen equipment box. The hydrogen equipment box has dimensions of 1.2 m by 1.0 m by 0.6 m. The total volume of the garage is 49.33 m^3.

The other geometry that is used is similar to Figure 28 except with the addition of a car. The layout of which is shown in Figure 29. The volume of the car used is 5.79 m^3, thus yielding a total volume for the garage of 43.54 m^3. This is important for comparison of the flammable volume depicted later.

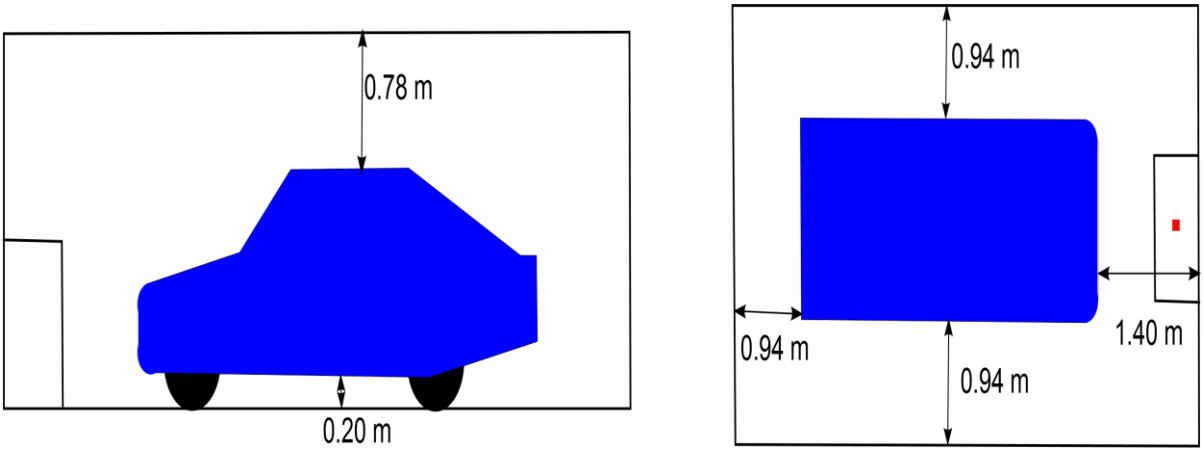

Figure 29 Vehicle location within enclosure.

The venting configurations used with the presence of the vehicle are three vents and two vents, upper vent near release. There is always a lower vent present in every scenario, the reasoning for this was explained in section 2..

Table 21 – Table 23 show the cases that are investigated. Multiple tables are used for ease of viewing. The case numbers are used to distinguish between the different scenarios for the results. Table 21 gives the first three cases, wind is not used and there is no vehicle present.

Table 21 Summary of the cases investigated with no vehicle or wind.

Case	Vent Positions	Vent Area (m^3)	Vehicular Presence	Atmospheric Conditions
1	Lower Upper Opposite	0.025 0.025	N/A	N/A
2	Lower Upper Near	0.025 0.025	N/A	N/A
3	Lower Upper Opposite Upper Near	0.0125 0.0125 0.025	N/A	N/A

Table 22 Summary of the cases investigated with wind but no vehicle.

Case	Vent Positions	Vent Area (m^3)	Vehicular Presence	Atmospheric Conditions
4	Lower Upper Near	0.025 0.025	N/A	1 m/s Towards Lower
5	Lower Upper Near	0.025 0.025	N/A	1 m/s Towards Upper
6	Lower Upper Near	0.025 0.025	N/A	5 m/s Towards Upper
7	Lower Upper Opposite Upper Near	0.0125 0.0125 0.025	N/A	1 m/s Towards Lower
8	Lower Upper Opposite Upper Near	0.0125 0.0125 0.025	N/A	1 m/s Towards Upper Near

Table 22 gives the cases that were used where wind was present. There was no vehicle used for these scenarios. The corresponding scenario with no wind was also used.

Table 23 Summary of the cases investigated with a vehicle but no wind.

Case	Vent Positions	Vent Area (m^3)	Vehicular Presence	Atmospheric Conditions
9	Lower Upper Near	0.025 0.025	✓	N/A
10	Lower Upper Opposite Upper Near	0.0125 0.0125 0.025	✓	N/A

Table 23 gives the cases that were used when the vehicle was present. Wind was not used for these scenarios. The corresponding scenario with no vehicle was also used.

5.3 Numerical Implementation

The numerical setup of the model is based upon the previous validation studies presented in Chapter 4. The turbulence model used is the k-omega SST model. The mesh utilises the same cell sizes as recommended from Chapter 4, namely the smallest cell size is 0.025 m with the largest being 0.25 m externally. The mesh uses hexahedral shaped cells. The numerical model solves transient equations for continuity, momentum, turbulence and transport of the species H_2 and O_2.

The boundary conditions when there were no atmospheric conditions were a pressure outlet in the top of the outer domain. When atmospheric conditions are modelled the other 3 boundaries are treated as pressure outlets along with the top. Whilst the other boundary is a velocity inlet with speed as required for that investigation.

The initial conditions imposed are zero velocity everywhere except when wind is investigated. Then there is an initial velocity present at the time of release that corresponds to the speed and direction under investigation. Air is treated as oxygen and nitrogen, which is throughout the domain prior to release. The initial turbulence

level is treated as small and as such the initial parameters are 1 % intensity, 0.01 m length scale and 0.01 m/s velocity scale. Atmospheric pressure is used whilst the temperature is 300 K.

The time step utilised for the release and dissipation phases is kept constant at 0.04 seconds. When wind is simulated there is no hydrogen release within the first 100 seconds. The time step in this initial phase is greater than that used for the rest of the study.

The release occurs for 500 seconds, after which the hydrogen inlet is closed. The timescale is chosen as it is the realistic length of time for metal hydride store desorption. The mass flow rate used for the inlet is a constant rate of 7.2 g/min. The total mass desorbed is 60 g over 500 seconds. The total mass desorbed and the timespan of the release are used due to the chemical processes of the metal hydrides chosen for the refuelling system (Nayebossadri et al., 2015). The constant release rate is used because the profile of the release rate is unknown.

The mesh strategy that is utilised is similar to that used previously in Chapter 4. The main area of interest is directly above the release, followed by the areas surrounding the vents and the upper portion of the enclosure. The area with least interest is the majority of the external domain, even when a wind profile is in use. This meshing strategy produces a total of 1.6 million cells without a vehicle and 1.5 million cells with a vehicle.

5.4 Analysis Criteria

The criteria for determining the suitability of the venting configurations has been devised taking into account the information in sections 2.3.2 and 2.. The criteria are defined as follows:

1. Flammable volume – the volume containing hydrogen-air mixtures above the Lower Flammability Limit (LFL).
2. Depth of flammable cloud – the depth the flammable cloud reaches within the enclosure. This is taken at the centre of the enclosure, chosen such that vents and the inlet will not influence the measurements.

3. Maximum concentration – this is taken at the centre of the roof of the enclosure. This is one of the more likely places for an ignition source to be present, e.g. a light source. The maximum cannot be taken across the entire garage because above the release location it would always be 100% until after the release has ceased.
4. Time for the flammable mixture to dissipate – This only starts once the release has stopped. This is so that the time when the concentration returns to a safe level is known, this is determined as below 4% the LFL. The quicker the better as the chance of ignition is reduced.

The flammable volume is coupled with the LFL, taken from Table 1. The depth of the flammable cloud is used instead of linking with asphyxiation because the concentrations for ignition to occur as drastically lower see section 2.3.2.1 and Table 1. The depth also gives a level at which ignition sources definitely need to be avoided. The maximum concentration is used to determine the severity that could happen were an ignition to occur. The closer to the stoichiometric value of 29% the stronger the reaction. This is compared against Table 1 which explains the limits for combustion and detonation alongside the minimum energy needed. The chemical properties are more heavily relied on here because the only relevant harm criterion is asphyxiation. However this criterion is overwritten by the chemical criteria due to the high levels of hydrogen needed to induce asphyxiation, section 2.3.2.1.

5.5 Results

The results are portrayed within the criteria defined in the previous section, 5.4, in order. Criteria 4, the time for dissipation, can be seen on all of the results given. Then within each section, graphical representations are shown in four different areas, coinciding with the cases under investigation. The case numbers are given in Table 21 – Table 23.The first being cases 1 – 3. This is followed by the atmospheric condition scenarios, cases 2, 4 and 6 and cases 3, 7 and 8. The final representation is for the scenarios with a vehicle inside the garage, cases 2, 3, 9 and 10.

5.5.1 Flammable Volume

The first set of scenarios under investigation is the empty configuration with no wind simulations, cases 1 – 3, depicted in Figure 30. These consist of three simulations varying the location and number of vents.

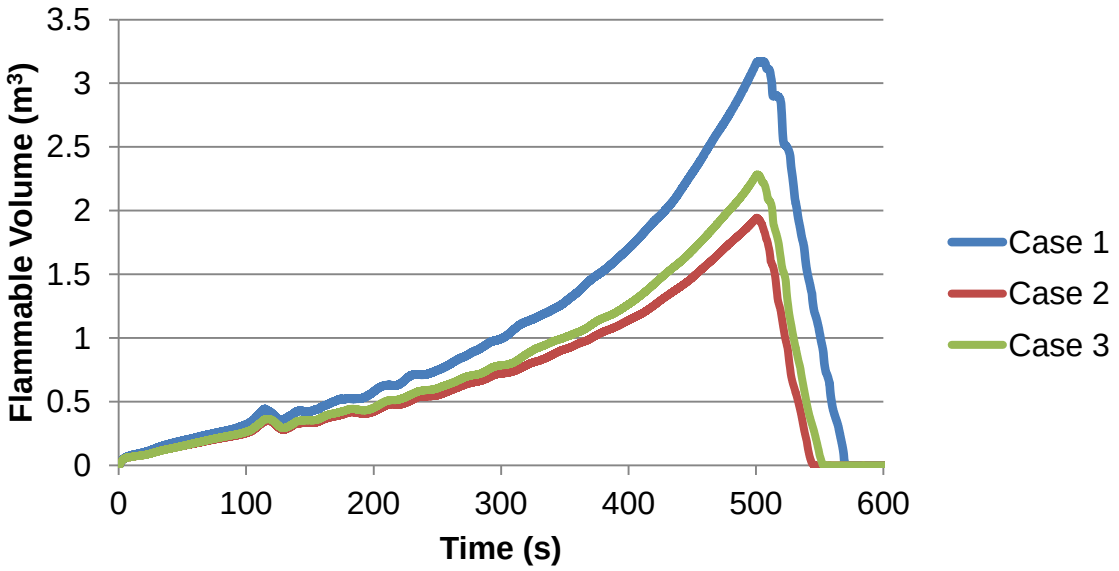

Figure 30 Flammable volume graph comparing cases 1 – 3.

Table 24 contains the information for the cases used within Figure 30.

Table 24 Case details for Figure 30.

Case	1	2	3
Vent Details	1 Lower 1 Upper Opposite	1 Lower 1 Upper Near	1 Lower 1 Upper Opposite 1 Opposite Near

Figure 30 shows the transient behaviour of the flammable volume for cases 1 – 3. The flammable volume evolution with time suggests that case 2 is the better configuration because of the lower peak flammable volume. The configuration used in case 3 performs marginally worse than case 2, whilst case 1 has a peak flammable volume over 1 m^3 greater. Case 3 performs worse than case 2 even

though it has an extra vent, this is due to the reduction in size of the lower vent used when moving from two vents to three.

The peak volume occupied for case 1 is 3.17 m^3, corresponding to 6.4 %. The peak for case 3 is 1.94 m^3, which is 3.94%, and case 2 is 2.28 m^3, or 4.63%. The times to vent the flammable volume are 71.4, 46.5 and 53.8 seconds, respectively.

There is a slight fluctuation for all three configurations circa 125 seconds. This is caused by the return of hydrogen after it has reached the opposite wall. This behaviour is similar to an undercurrent/rip tide on a shore.

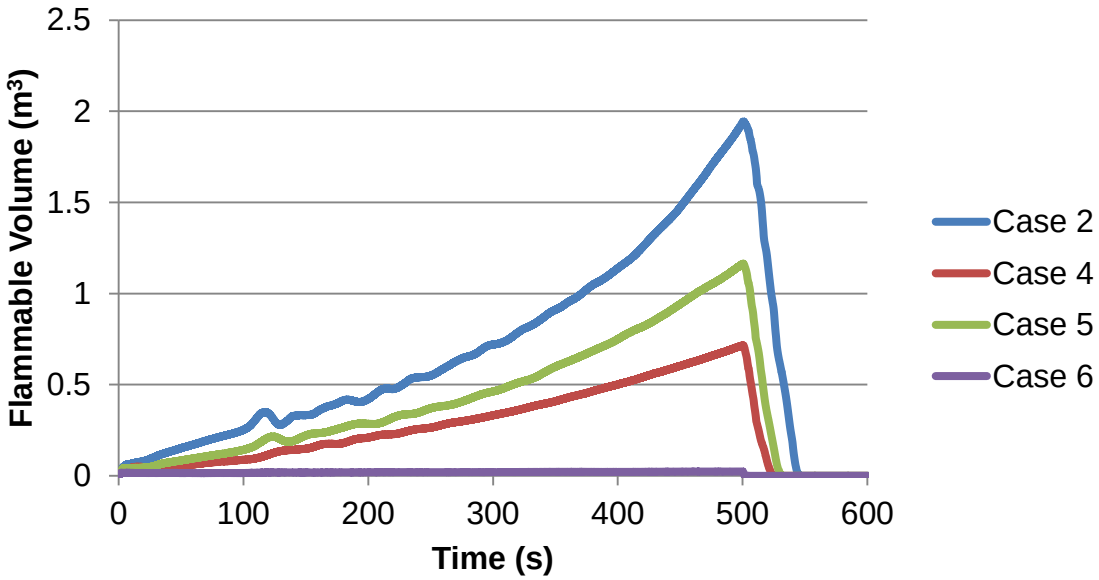

Figure 31 Flammable volume graph comparing cases 2, 4, 5 and 6.

Table 25 contains information on the cases depicted in Figure 31. All of the cases utilise the same venting configuration, 1 lower vent opposite the release and 1 upper vent near the release.

Table 25 Case details for Figure 31.

Case	2	4	5	6
Atmospheric Conditions	0 m/s	1 m/s towards Lower	1 m/s towards Upper	5 m/s towards Upper

Figure 31 shows the transient behaviour for cases 2, 4, 5 and 6. Case 2 is the same as that depicted in Figure 30. The flammable evolution with time shows that case 6 has a negligible flammable volume present, this is caused by the strong wind which causes mixing between the hydrogen and the air. Cases 4 and 5 show that even a moderate strength wind reduces the flammable volume compared to no wind present, case 2. Case 4 reduces the flammable volume as expected, because the air flows towards the lower vent.

The peak flammable volume for case 2 is 1.94 m^3, or 3.94%, whilst for case 6 it is 0.02 m^3 or 0.05%. Case 5 has a peak flammable volume of 1.16 m^3, or 2.36%, whilst for case 4 it is 0.72 m^3 or 1.45%. The negligible flammable volume for case 6 and to a lesser extent case 5 is attributed to an increase in the mixing of the hydrogen. This could be because the wind profiles are already prominent before the release occurs.

It is also evident that there are still fluctuations for cases 2 and 5 circa 125 seconds. This is again due to the hydrogen reaching the far wall and then flowing back. Case 5 is less prominent because of the inflow of air that is coming in through the upper vent, this decreases the flow back. Case 4 does not show this phenomenon, because the flow in at the lower vent slows the flow of hydrogen across the ceiling of the garage.

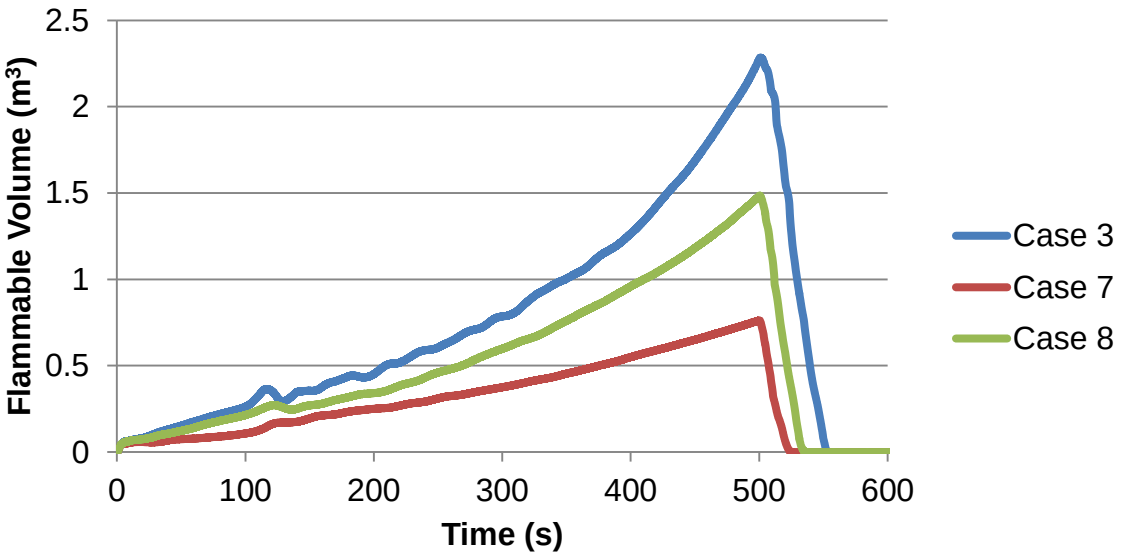

Figure 32 Flammable volume graph comparing cases 3, 7 and 8.

Table 26 contains the information on the cases depicted in Figure 32. All of the cases utilise a three vent configuration whilst investigating the effect of atmospheric conditions on this configuration.

Table 26 Case details for Figure 32.

Case	3	7	8
Atmospheric Conditions	0 m/s	1 m/s towards Lower	1 m/s towards Upper

Figure 32 shows the transient behaviour of the flammable volume for cases 3, 7 and 8. The flammable volume evolution with time is very similar to those observed previously, especially those in Figure 31. When the wind blows towards the lower vent, case 7, there is a drastic decrease in the flammable volume compared to when wind is not present, case 3. Case 7, wind blowing towards the vent near the release, also decreases the flammable volume compared to case 3.

This is evident by the peak flammable volumes of 2.28 m^3, or 4.63%, for case 3. Case 8 produced a peak of 1.48 m^3, or 3%, whilst case 7 was 0.76 m^3 or 1.54%. Case 8 seems to increase the mixing within the enclosure similar to that seen previously. Once again the reverse flow, after the hydrogen has reached the opposite wall, can be seen. The effect also decreases with the wind speed and direction similar to the two vent scenarios.

Table 27 contains the case details for Figure 33. None of the cases investigate atmospheric conditions. The cases investigate the influence of a vehicle on the two best performing venting configurations. The three vent configuration and the two vent, upper vent near release, configuration.

Table 27 Case details for Figure 33.

Case	2	3	9	10
Vent Details	2	3	2	3
Vehicle Presence	×	×	✓	✓

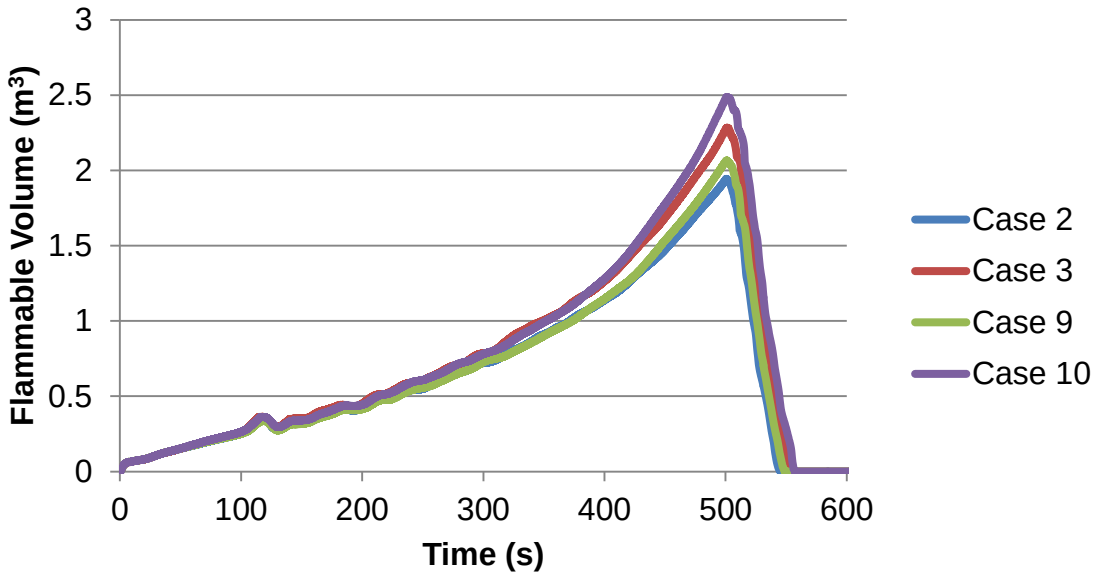

Figure 33 Flammable volume graph comparing cases 2, 3, 9 and 10.

Figure 33 shows the comparison between cases 2, 3, 9 and 10. The flammable volume evolution follows a similar trend for all four cases. Cases 2 and 9 are comparable against each other as they have the same venting configuration, without and with a vehicle present respectively. The same is for cases 3 and 10. It is evident that the presence of a vehicle increases the peak flammable volume, regardless of the vent configuration.

The peak flammable volume reached for case 2 is 1.94 m^3, or 3.94%, whilst for case 9 this rises to 2.07 m^3 or 4.74%. The observed effect is more profound when three vents are used, cases 3 and 10. Case 3 has a peak volume of 2.28 m^3, or 4.63%, compared to case 10 which is 2.49 m^3 or 5.71%. This phenomenon is caused because the mixing is being disturbed by the presence of the vehicle. Once again the phenomenon with the 'rebounding' hydrogen is present at 125 seconds.

Figure 34 – Figure 37 show central plane images of the hydrogen mole fraction at 500 seconds for all of the cases investigated. The central plane is parallel to the length of the garage.

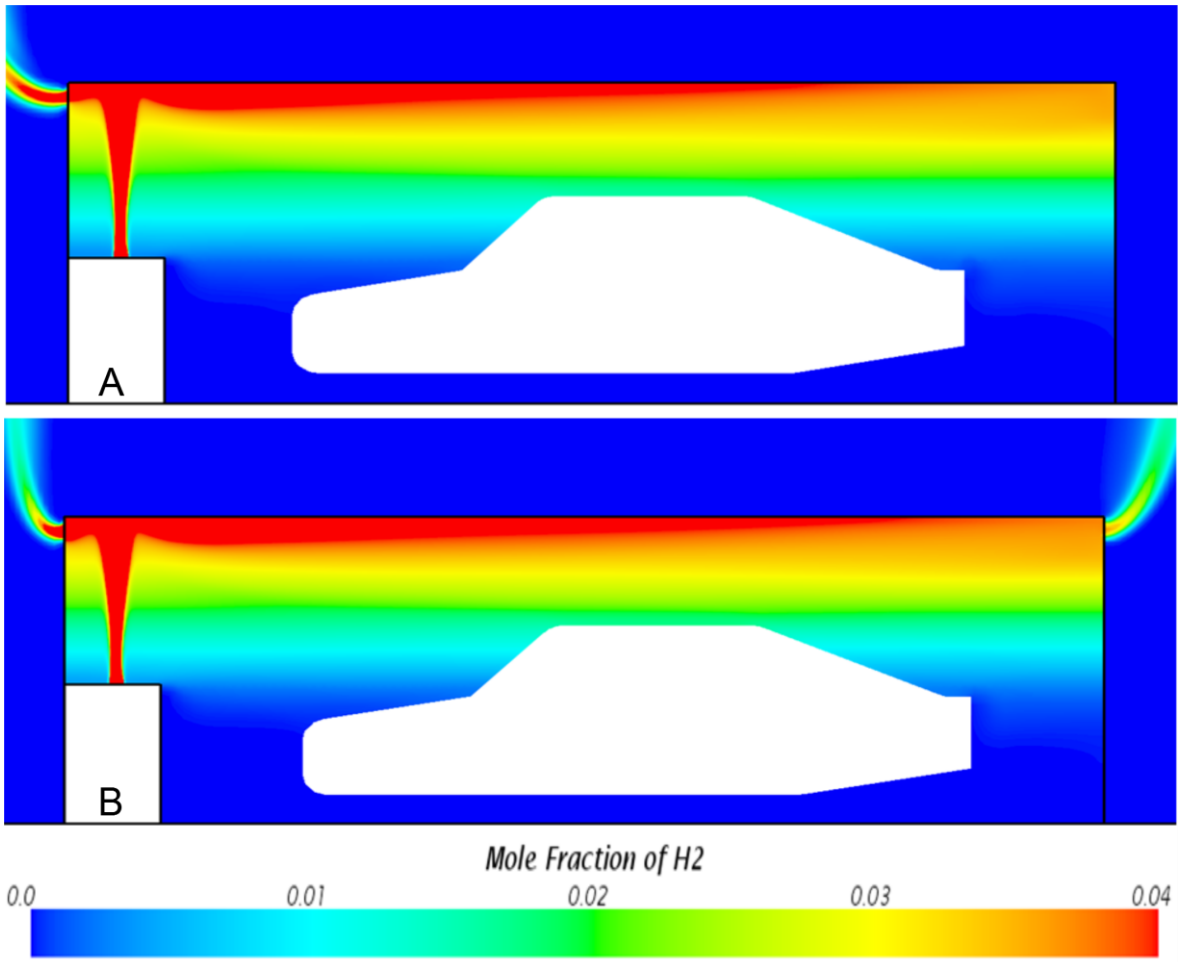

Figure 34 Planar hydrogen mole fraction images for; (A) case 9 and (B) case 10.

Figure 34 depicts the hydrogen mole fraction up to 0.04, the LFL, in the central plane for both case 9 (A) and case 10 (B). The images are taken at time 500 seconds, just before the release ceases. The images show minimal differences between the hydrogen enclosed within the garage. The major difference between the two is the hydrogen leaving the garage. The two vent scenario (A) has a stronger presence of flammable hydrogen leaving the garage. This is shown by the length of the flammable volume leaving the upper vent on the left. Whilst the three vent configuration (B) has a smaller presence of flammable mixture leaving the left upper vent, whilst no flammable hydrogen leaves via the right upper vent.

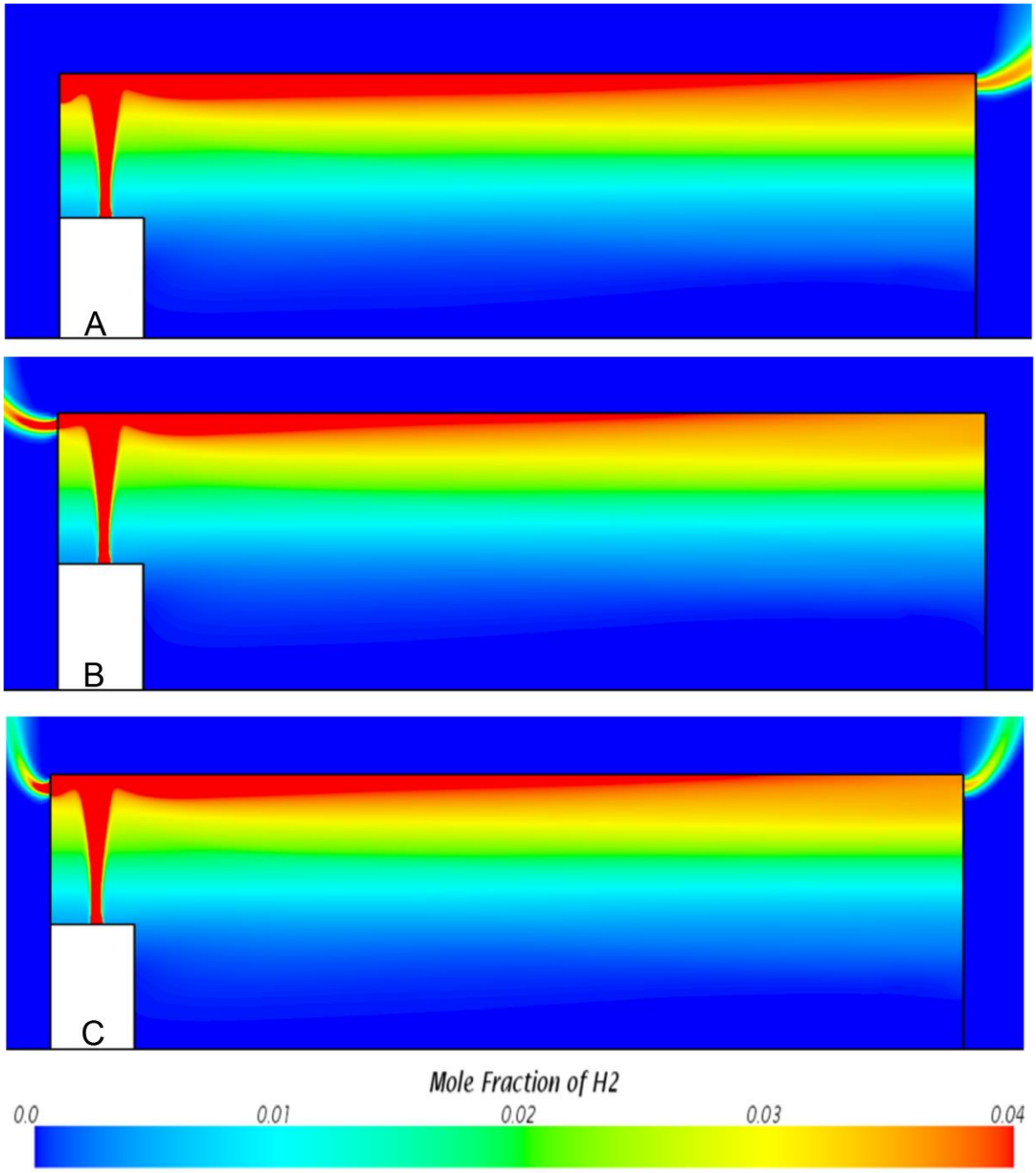

Figure 35 Planar hydrogen mole fraction images for; (A) case 1, (B) case 2 and (C) case 3.

Figure 35 shows the mole fraction of hydrogen for (A) case 1, (B) case 2 and (C) case 3. These are taken for the central plane at 500 seconds, with no atmospheric conditions present. It is clear that having both vents opposite the release (A) has the largest flammable volume, although no flammable volume exits at the upper vent. Placing the upper vent near the release (B) and (C) reduces the flammable volume, but also causes a flammable mixture to be present externally. Using three vents (C) has a slight increase of the flammable volume compared to (B) the upper vent solely

being located near the release. Interestingly, the flammable volume that exits the garage in (C) is reduced at the vent near the release whilst no flammable volume exits the garage via the upper vent opposite the release.

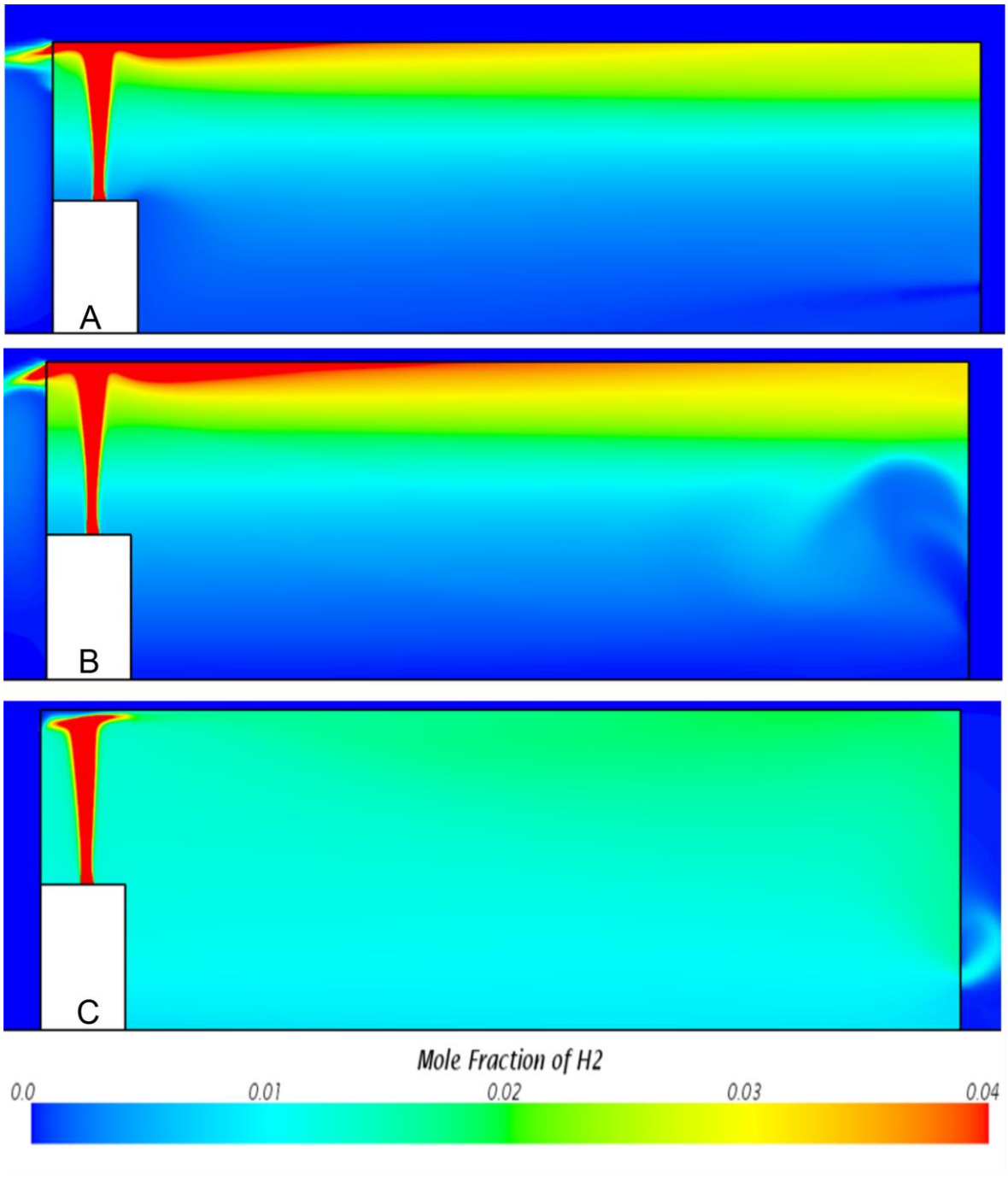

Figure 36 Planar hydrogen mole fraction images for; (A) case 4, (B) case 5 and (C) case 6.

Figure 36 shows images of the hydrogen mole fraction for the two vent with wind scenarios. (A) is for case 4, (B) is for case 5 and (C) is for case 6. The images shown are for the central plane at 500 seconds, just before the release ceases. When the wind is blowing towards the lower vent (A), the flammable volume decreases

compared to when there is no wind present, case 2. It is also evident that greater mixing has occurred, depicted by the blue ‘stream’ entering the garage on the lower left.

When the wind is towards the upper vent, cases 5 and 6, the wind speed alters the flow of hydrogen. A lower wind speed, case 5, depicted by (B) causes the flammable volume to increase internally and externally. This is because the wind speed does not prevent the natural buoyancy of the hydrogen from occurring but does hinder the flow. It also causes the lower vent to operate differently, there is no clear jet on the left now, compared to (A). However the mixing is still far greater than when there is no wind present case 2, hence the reduction compared to no wind.

The higher wind speed of case 6, 5 m/s, (C) behaves completely differently and counter intuitively. The higher wind speed prevents any hydrogen from leaving via the upper vent, because the wind is greater than the buoyancy of the hydrogen. This is shown by the presence of air inside the garage above the release. The instinctive opinion would be that the flammable volume must increase, however the greater wind speed significantly increases the mixing that occurs inside. This is shown by the almost uniform mixture present within the garage and the fact that the hydrogen leaves the garage via the lower vent, on the left. This shows that the release location also has a significant part to play in determining the physics of the flow.

Figure 37 shows the hydrogen mole fraction for cases 7 and 8, the three vent configuration with the presence of wind. Again the images are for the central plane at 500 seconds, just before the release ceases. (A) is for case 7, when the wind is 1 m/s towards the lower vent and (B) is for case 8, when the wind is 1 m/s towards the upper vent near the release. Once again the presence of atmospheric conditions has increased the mixing within the garage.

When the wind is towards the lower vent, case 7, (A) the flammable volume greatly decreases. The air flow prevents hydrogen from leaving the upper vent opposite the release, upper right, evident by the change in colour of the internal hydrogen mixture. The behaviour of the hydrogen flow outside the vent near the release is very similar to that of case 4.

When the wind is towards the upper vent near the release, case 8, (B) the flammable volume is greater than the opposite direction but still less than when wind is not present, case 3. The flow behaviour at the lower vent is again similar to the corresponding 2 vent simulation, case 5. However the upper vent near release behaviour is different, it would seem that the flammable hydrogen flows out but recirculates back inside. This is evident because there is no presence of a ‘jet’ of hydrogen leaving this vent. However the upper vent opposite the release has a significant mixture leaving via this vent.

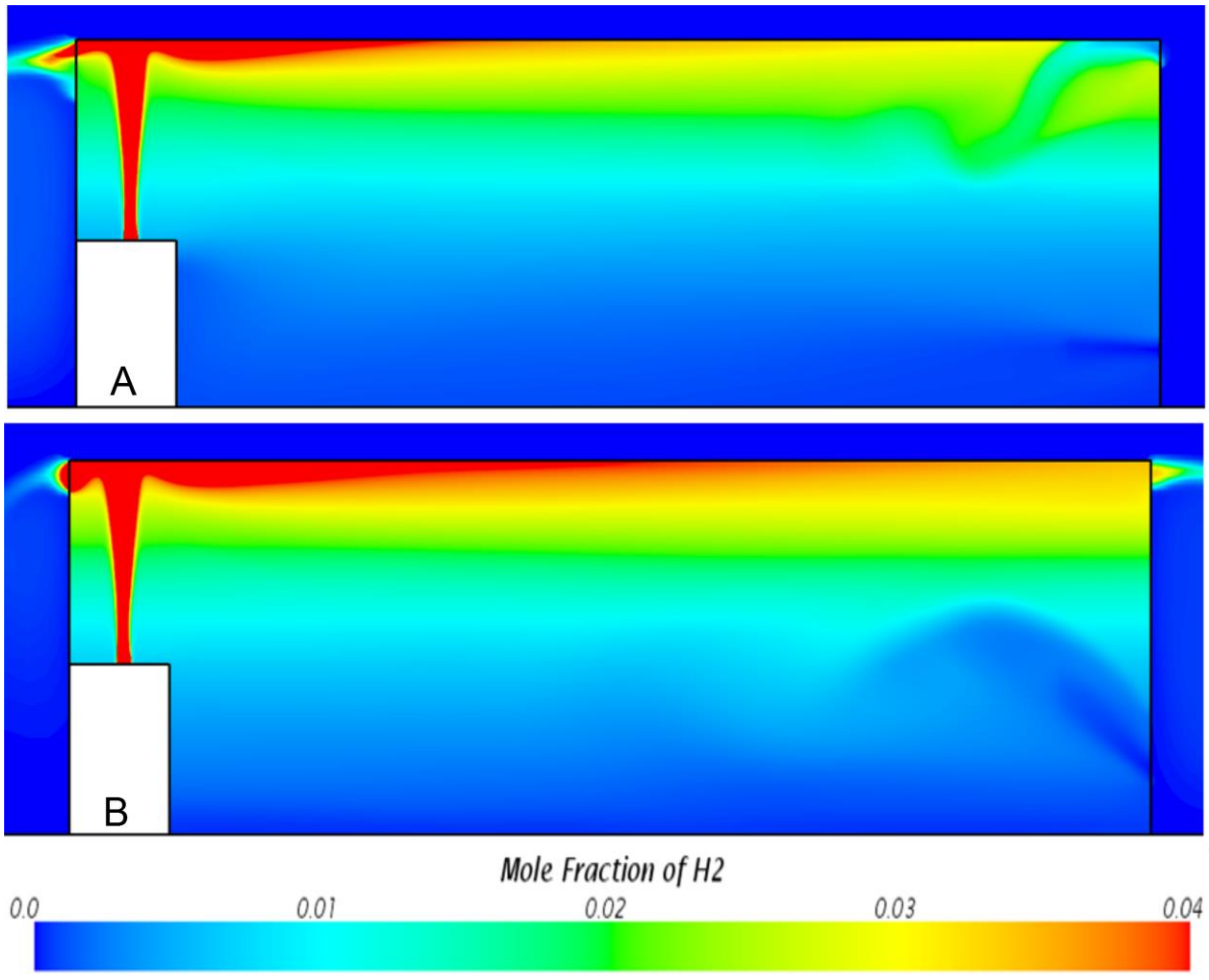

Figure 37 Planar hydrogen mole fraction images for; (A) case 7 and (B) case 8.

Table 28 Summary of the flammable volume criterion for all test cases.

Case	Peak flam vol (m^3)	Peak % occupied	Time to vent (s)
1	3.17	6.42	71.36
2	1.94	3.94	46.52
3	2.28	4.63	53.8
4	0.72	1.45	26.44
5	1.16	2.36	33.64
6	0.02	0.05	1.8
7	0.76	1.54	26.24
8	1.48	3.01	37.4
9	2.07	4.74	49.84
10	2.49	5.71	58

Table 28 contains the peak flammable volume, with percentage representation, and the time taken to remove the flammable volume from the garage. It can be seen that with the exception of case 1 all configurations vent under a minute.

It is also clear that the method for modelling wind alongside the leak position means that mixing dominates and as such the flammable volume decreases, and with this the time to vent decreases.

The configuration in case 2 also performs better than the configuration in case 3, by circa 7 seconds for venting. This increases to 9 seconds with vehicular presence, cases 9 and 10. This is due to the decrease in the lower vent area when using three vents as opposed to two.

5.5.2 Depth of Flammable Cloud

The results for the depth that the flammable cloud reaches at the centre of the enclosure are shown in the ensuing figures. The scenarios are grouped together in the same sets as the flammable volume results.

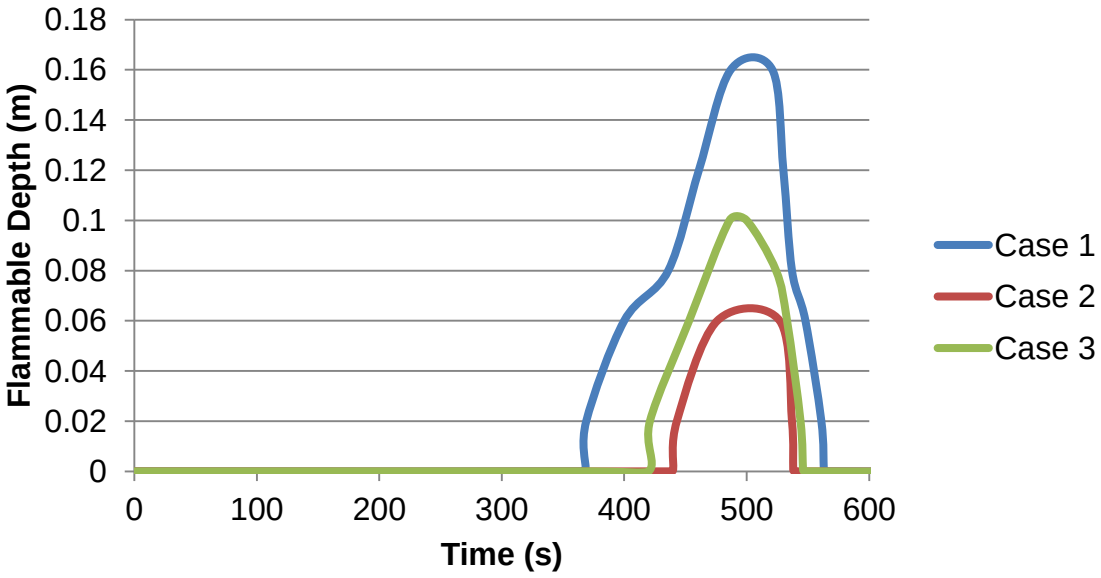

Figure 38 Flammable depth graph comparing cases 1 – 3.

Table 29 contains the information on the cases for Figure 38.

Table 29 Case information for Figure 38.

Case	1	2	3
Vent Details	1 Lower 1 Upper Opposite	1 Lower 1 Upper Near	1 Lower 1 Upper Opposite 1 Opposite Near

Figure 38 depicts the transient depths that the flammable cloud reaches at the centre of the garage. It is clear that the worst configuration for the flammable depth is case 1, which reaches a depth of 0.16 m from the roof. Case 2 reaches a depth of 0.06 m, whilst case 3 is almost in the middle of these at a depth of 0.1 m. Unsurprisingly, the peak is reached at 500 seconds. The time for the flammable cloud to dissipate follows the same trends as the flammable volume.

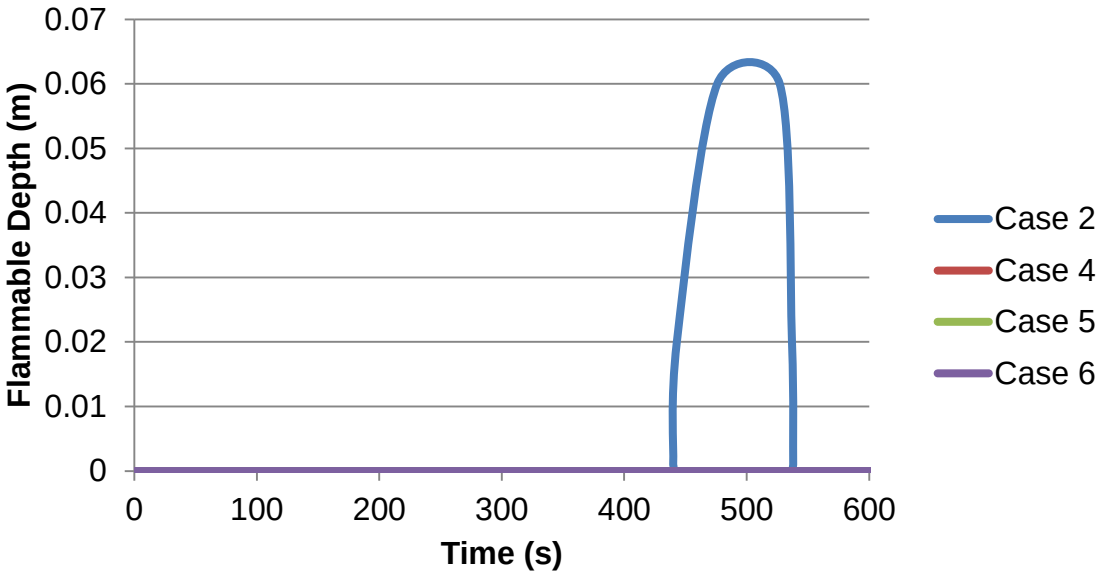

Figure 39 Flammable depth graph comparing cases 2, 4, 5 and 6.

Table 30 contains the case details for Figure 39. The vent configuration used within all of the cases is the two vent configuration, with the upper vent near the release.

Table 30 Case information for Figure 39.

Case	2	4	5	6
Atmospheric Conditions	0 m/s	1 m/s towards Lower	1 m/s towards Upper	5 m/s towards Upper

Figure 39 shows the flammable depth reached for cases 2, 4, 5 and 6. These cases are all 2 vents, with the upper vent near the release, and for cases 4 – 6 have wind blowing as well. It is seen that the presence of wind does not create a recordable flammable depth at the centre of the garage. This can be compared against Figure 36, which shows that the flammable volume does not reach the centre of the garage.

Table 31 details the case information for Figure 40. The vent configuration used is the three vent configuration.

Table 31 Case information for Figure 40.

Case	3	7	8
Atmospheric Conditions	0 m/s	1 m/s towards Lower	1 m/s towards Upper

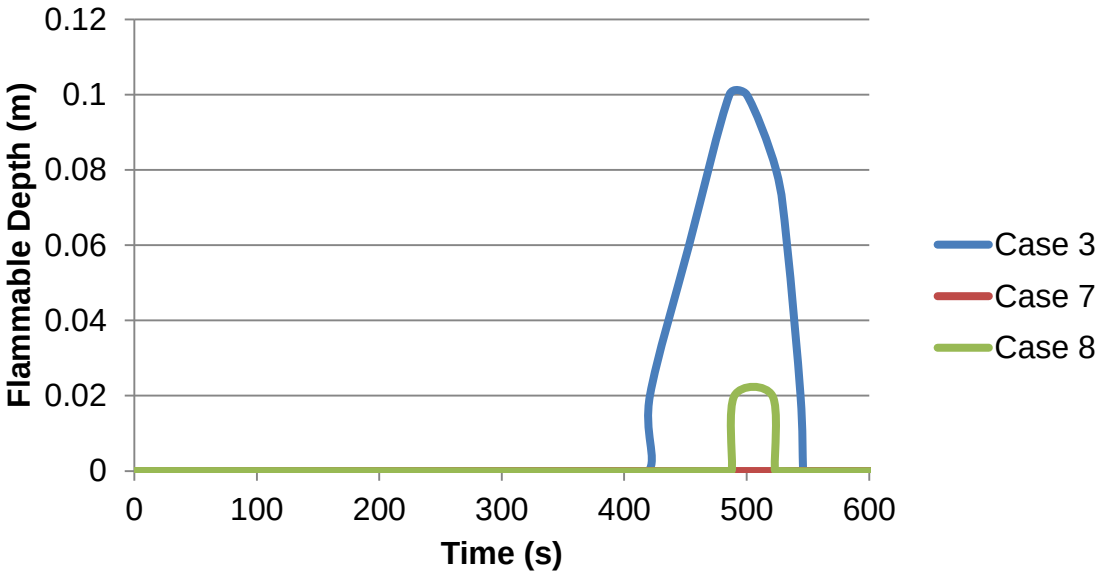

Figure 40 Flammable depth graph comparing cases 3, 7 and 8.

Figure 40 shows the depth reached by the flammable cloud for cases 3, 7 and 8. These are the three vent scenario investigating the influence of wind. Case 3 has the greatest depth, which is similar to case 2 in Figure 39. When wind blows towards the lower vent, case 7, there is no flammable depth at the centre, similar to case 4. However case 8 records a depth of 0.02 m, which is different to that seen for case 5.

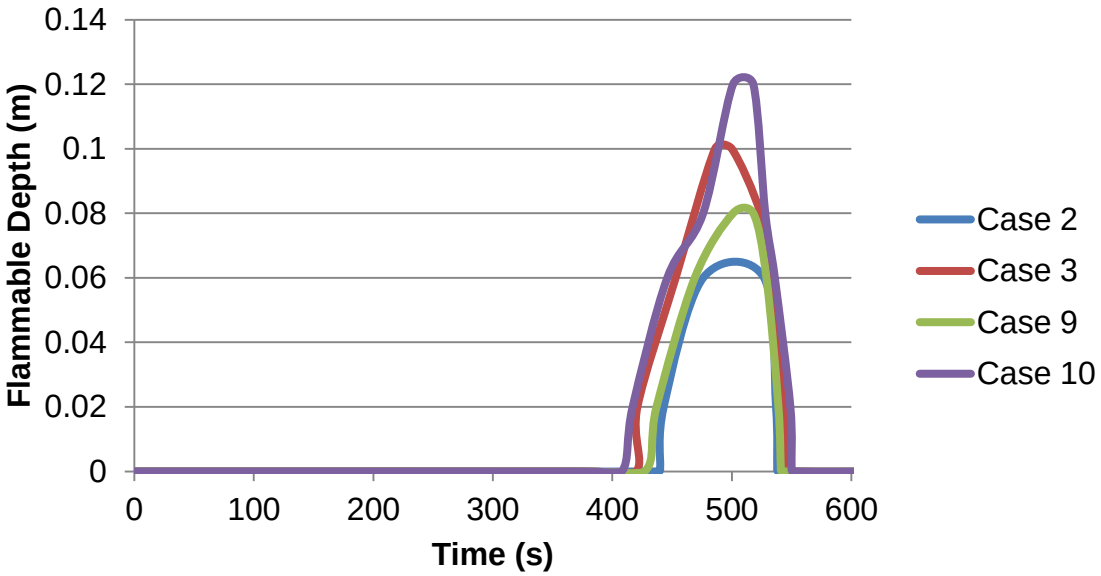

Figure 41 Flammable depth graph comparing cases 2, 3, 9 and 10.

Table 32 details the case information for Figure 41. The two vent configuration used is the upper vent near release configuration. There is no presence of atmospheric conditions.

Table 32 Case information for Figure 41.

Case	2	3	9	10
Vent Details	2	3	2	3
Vehicle Presence	×	×	✓	✓

Figure 41 shows the flammable depth for cases 2, 3, 9 and 10. The presence of a vehicle, cases 9 and 10, increases the flammable depth compared against cases 2 and 3 respectively. Case 9 reaches a depth of 0.08 m which is 0.02 m deeper than case 2, which does not have a vehicle present in the garage. The same increase can be seen between cases 3 and 10, with depths of 0.1 m and 0.12 m respectively.

Table 33 contains the maximum flammable depth and the time for the flammable volume to no longer be present at the centre of the garage. Unsurprisingly, the greatest depth reached is for case 1. This is 25% greater than the next nearest, which is case 10. The presence of a vehicle, cases 9 and 10, increases the depth by 0.02 m, regardless of the configuration. Case 8 shows a flammable depth compared to case 5, where the difference is a reduction in the lower vent area. Once again all scenarios dissipate in less than 1 minute, with the exception of case 1.

Table 33 Summary of the flammable depth criterion for all test cases.

Case	Peak Internal Depth (m)	Time to vent (s)
1	0.16	64
2	0.06	39
3	0.1	45
4	0	0
5	0	0
6	0	0
7	0	0
8	0.02	22
9	0.08	42
10	0.12	50

5.5.3 Maximum Concentration

The final criterion is the maximum concentration, which is measured at the centre of the roof of the garage. To keep with the trend, the results are grouped in the same sets as the previous two criteria.

Table 34 contains the case information for Figure 42. No atmospheric conditions or vehicular presence is investigated.

Table 34 Case information for Figure 42.

Case	1	2	3
Vent Details	1 Lower 1 Upper Opposite	1 Lower 1 Upper Near	1 Lower 1 Upper Opposite 1 Opposite Near

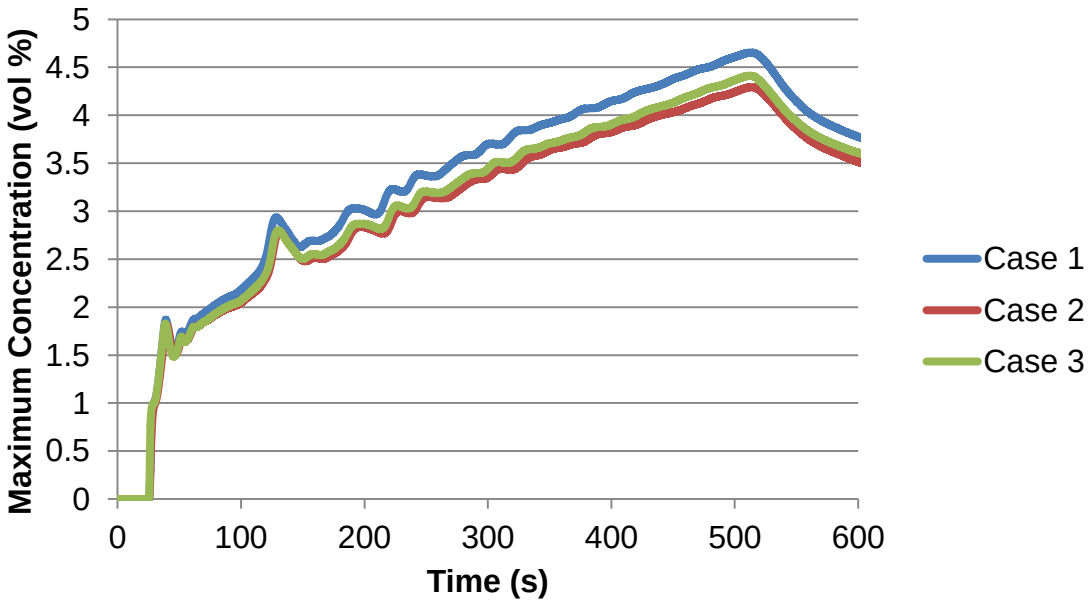

Figure 42 Maximum concentration graph comparing cases 1 – 3.

Figure 42 shows the maximum concentration for cases 1 – 3. These cases have no atmospheric conditions or vehicle present. Expectedly, case 1 again produces the highest concentration observed, peaking at 4.65 vol%. The other two configurations are both over the LFL, at 4.41 vol% and 4.29 vol%, for cases 3 and 2 respectively. The time of the peak concentration coincides with the time at which release ceases, circa 500 seconds. It is also evident that the now familiar trends are being observed yet again.

The oscillations are caused by the same phenomenon that induced them in the flammable volume graphs. Namely, flow rebounding off the far wall and travelling back again. This is proven by the same time, circa 125 seconds, having similar peaks. The first peak, circa 35 seconds, is caused by the initial flow of hydrogen across the roof. This initial flow has a slight decrease after the hydrogen front. This is best described with the analogy of water waves, with a lull after the arrival.

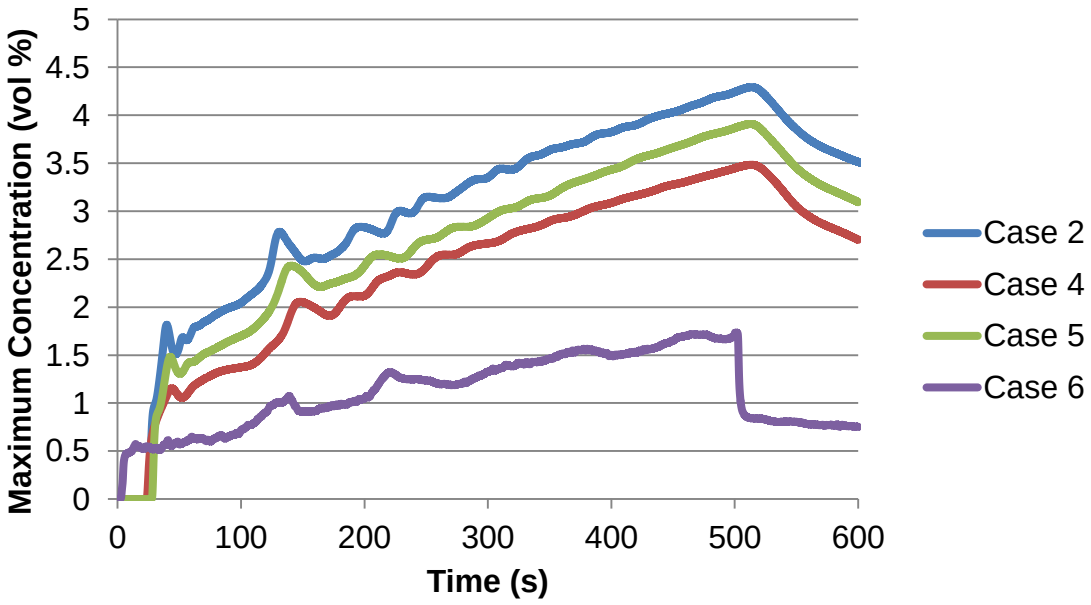

Figure 43 Maximum concentration graph comparing cases 2, 4, 5 and 6.

Table 35 details the case information for Figure 43. All of the cases involve the two vent configuration, with the upper vent near the release location. There is no presence of a vehicle in these cases.

Table 35 Case information for Figure 43.

Case	2	4	5	6
Atmospheric Conditions	0 m/s	1 m/s towards Lower	1 m/s towards Upper	5 m/s towards Upper

Figure 43 depicts the maximum concentration for cases 2, 4, 5 and 6. These cases consist of two vents in the presence of wind blowing. Interestingly, the only configuration that induces a maximum concentration above the LFL is the case with no wind, case 2. This is expected as there was no flammable depth present for cases 4 – 6. Case 5, with a wind of 1 m/s that flows towards the upper vent records the second highest concentration, with 3.91 vol%. If the release was to continue then this would certainly become greater than the LFL. Case 4, which has wind blowing at 1 m/s towards the lower vent, reaches a peak concentration of 3.48 vol%. Case 6, which has a wind of 5 m /s towards the upper vent, does not even reach half of the

LFL. The case 6 results are observed because of the significant increase in the mixing of the hydrogen with the air.

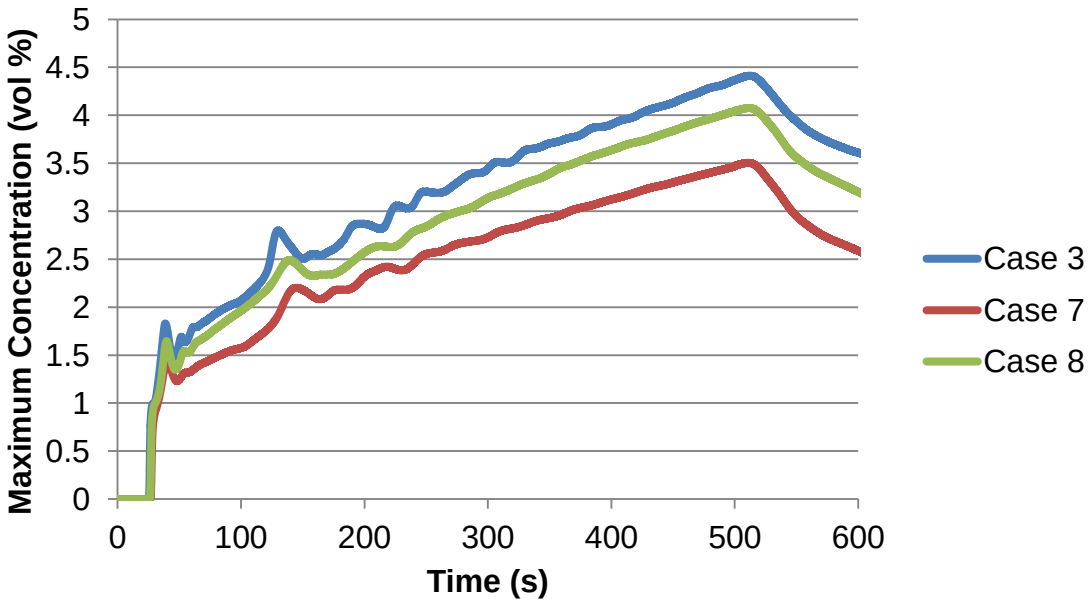

Figure 44 Maximum concentration graph comparing cases 3, 7 and 8.

Table 36 details the case information for Figure 44. The venting configuration used is the three vent configuration, without the presence of a vehicle.

Table 36 Case information for Figure 44.

Case	3	7	8
Atmospheric Conditions	0 m/s	1 m/s towards Lower	1 m/s towards Upper

Figure 44 shows the transient nature of the maximum concentration for cases 3, 7 and 8. These cases consist of three vents with atmospheric conditions. The largest recorded peak concentration is once again for the scenario with no wind blowing, case 3. Case 7, which is similar to case 4, reaches a peak of 3.5 vol%. However, case 8 reaches a peak concentration of 4.08 vol%. This is different to that seen for case 5, which recorded a concentration below the LFL.

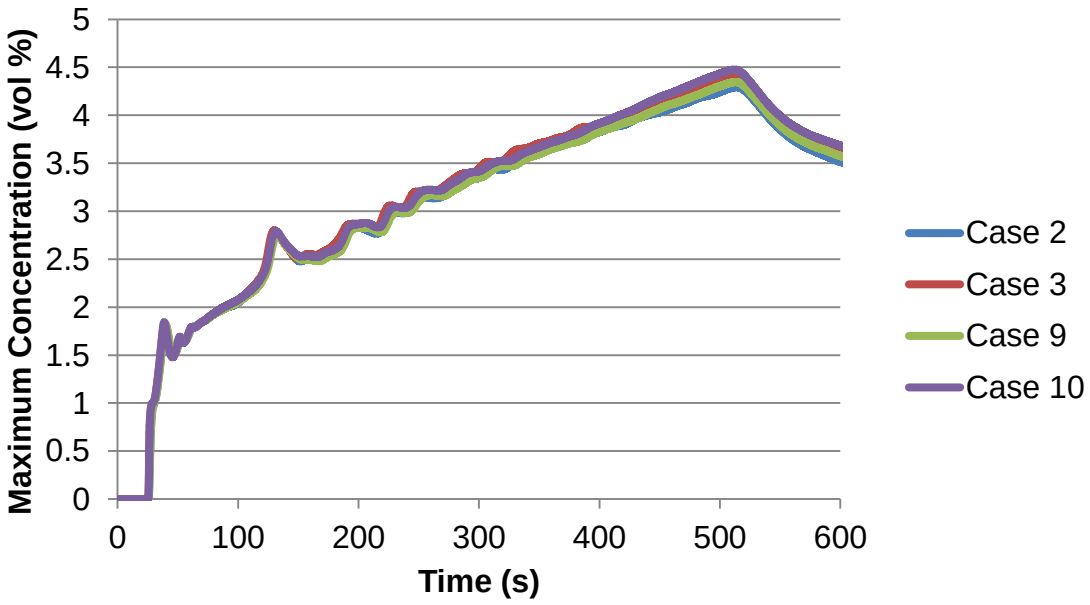

Figure 45 Maximum concentration graph comparing cases 2, 3, 9 and 10.

Table 37 details the case information for Figure 45. The two vent configuration investigated, utilises the upper vent near the release. There are no atmospheric conditions examined within these cases.

Table 37 Case information for Figure 45.

Case	2	3	9	10
Vent Details	2	3	2	3
Vehicle Presence	×	×	✓	✓

Figure 45 shows the comparison of the transient maximum concentration for cases 2, 3, 9 and 10. These cases compare the presence of vehicles for different venting strategies. The graph shows that there is negligible difference on the maximum concentration whether in the presence of a vehicle or not. The main difference between them is the number of vents, and by extension the reduction in the lower vent size. The difference between cases 2 and 9 is 0.046 vol% in favour of case 9, with a vehicle present. The difference between cases 3 and 10 is 0.064 vol% again in favour of the vehicle present, case 10.

Table 38 Summary of the maximum concentration criterion for all test cases.

Case	Max Conc. (vol %)	Time to vent (s)
1	4.65	63.12
2	4.29	38.84
3	4.41	44.72
4	3.48	0
5	3.91	0
6	1.73	0
7	3.50	0
8	4.08	21.88
9	4.34	41.44
10	4.48	49.36

Table 38 gives a summary of the peak concentration at the centre of the roof and the dissipation time for the concentration to become less than the LFL. Once again, case 1 incurs the highest peak, and similarly to the previous analysis also takes over a minute to dissipate. Case 6 has a concentration lower than half the LFL, which coincides with data for the other criteria. Case 8 is the only scenario that involves wind which reaches a concentration greater than the LFL. The presence of a vehicle increases the maximum concentration, although this effect is less profound than the number of vents.

5.6 Conclusion

This chapter started with an introduction into the geometry that is being investigated, which resembles a residential garage. This is followed by the numerical setup, based upon the work in Chapter 4. Then the analysis criteria, which is developed utilising information from sections 2.3.2 and 2.2 is explained. Lastly, all of the results are

shown and analysed. The only geometrical constant was a lower vent opposite the release, although the size did change.

The venting strategy that performs the worst is case 1, which has both of the vents located opposite the release, and occurs for all of the criteria used. Whilst case 2 has the best strategy, when compared against all of the scenarios that did not include wind blowing. This case had a lower vent opposite the release and a single upper vent near the release.

The presence of wind blowing produced some unexpected results, as the flammable volume and concentrations decreased compared to the corresponding cases with no wind. The location of the release source could be a reason for this, normally the release is in the centre of the enclosure. The method for initiating the wind profiles may also be the reason, the wind profiles are in place before the release occurs. This results in greater mixing especially for case 6, which had a wind speed of 5 m/s. This case had a negligible flammable volume and recorded a maximum concentration less than half of the LFL.

The presence of a vehicle, cases 9 and 10, also increases the flammable volume and concentrations compared to the corresponding scenarios without a vehicle, cases 2 and 3. This is caused by the vehicle acting as a blockage and as such hindering the recirculating flow.

This work suggests that case 2, two vents opposite each other with the lower vent opposite the release, is the most suitable. However the three vent configuration may be more suitable, but requires further investigation.

Chapter 6 – Models for Reacting Safety Assessment – Premixed

6.1 Introduction

Premixed combustion is prevalent in daily life via the internal combustion engine, which shows a positive use. However premixed combustion can also occur accidentally, such as at Fukushima (World Nuclear Organisiation, 2015). The problem here was a release of hydrogen which became homogeneous and then ignited, thus an unintended environment. The example given is one reason as to why premixed combustion needs to be integrated into safety analysis for a system. Whilst this would consider a worst case scenario, never the less it needs to be accounted for. This is to ascertain the potential overpressures that may be encountered, which could be lethal, for the given scenario.

This chapter utilises data from the University of Sydney Combustion Chamber, with data taken from Al-Harbi (2013). This chapter starts with an overview of the experimental details, followed by the numerical setup used for modelling the experiments. The fuel used is hydrogen and the equivalence ratio is 0.8, this is the highest equivalence ratio used at the University of Sydney for hydrogen. Finally, the predicted results are compared against the recorded results for three configurations.

6.2 Case Study – Sydney Combustion Chamber

The Sydney combustion chamber has been in development since 1999 and is in its third incarnation. It started off being used for conventional hydrocarbon fuels, in the first version. However it then had to be scaled down for use with hydrogen, which helped to ease the computational requirements for LES modelling, in later editions. Similar work to this chapter has been performed before using LES (Abdel-Raheem, 2015).The difference between the second and third versions is the viewing ports. The third version has a larger, rectangular viewing port compared to a small circular port in the second edition (Al-Harbi, 2013). This work aims to replicate a real explosion situation, with multiple obstacles located in front of the propagating flame.

The current chamber is designed such that it represents realistic situations of confined propagating premixed flames. The important factor in the design of the experimental chamber was the use of data in numerical validations. As such good optical access is essential, so that lasers may be used to record flow measurements. Taking this into consideration the experimental chamber is a simple rectangular enclosure. The chamber can have up to three baffle plates and an obstacle in the path of the flame.

6.2.1 Experimental Configurations/Details

The experimental chamber is built from Perspex, with a wall thickness of 20 mm. This was used such that minimal deformation is observed. The chamber is square in the cross section and has internal dimensions of 50 mm in width and 250 mm in height (Al-Harbi, 2013). This is shown in Figure 46, as well as all of the dimensions for the full comprehensive configuration.

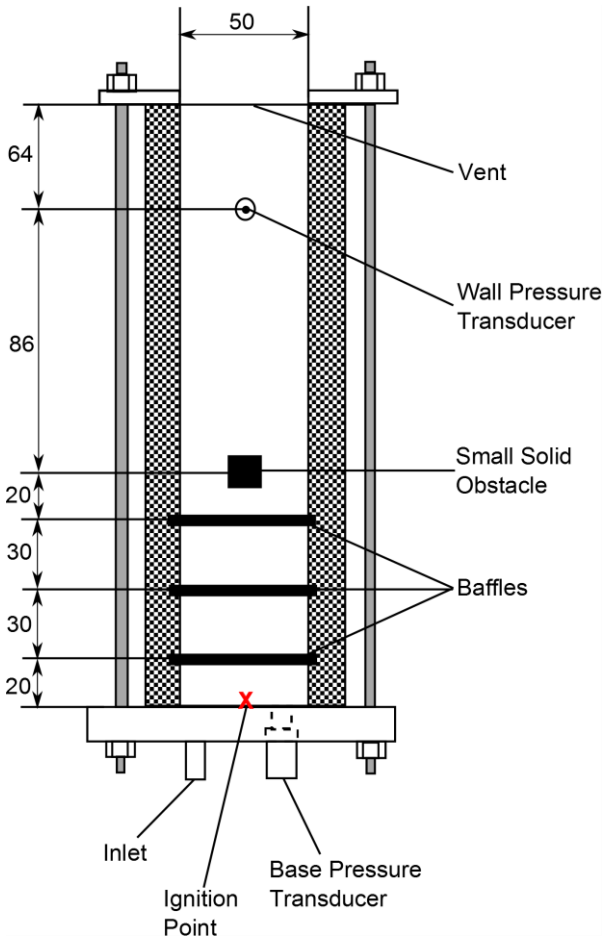

Figure 46 Planar view of the combustion chamber at University of Sydney (Al-Harbi, 2013).

Figure 46 shows the location of two pressure transducers, which were suitable up to pressures of 1 bar. The experimental data used later only uses the base pressure transducer. There are minimal differences between the incident times of the peak overpressures for the two transducers. The strength of the overpressures was different between the two transducers, the base transducer recording higher overpressures than the wall transducer. The base pressure transducer is located 10 mm away from the two walls. The ignition point is marked with a red cross, and is located centrally at the base of the chamber. Baffles and the obstacle are also shown and will be discussed in more detail.

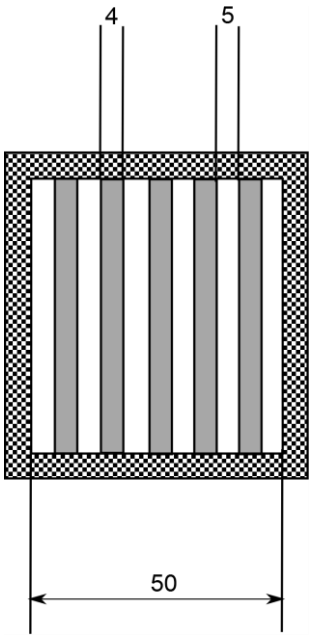

Figure 47 Dimensions and configuration of baffle plates applied.

Figure 47 shows the dimensions of the baffle plates that are used. The gaps between the baffles are 5 mm whilst the baffles are 4 mm wide. The baffle plates are 3 mm in depth. There can be up to three baffle plates inserted at once, however these are interchangeable. The small solid obstacle, that is located after the baffle plates, has a cross section of 12 x 12 mm. There is the option of using a larger obstacle, which has a cross section of 25 x 25 mm, however that is not used in these studies.

The system works by closing the vent during the filling stage, which is then opened to coincide with ignition. The inlet supplies a fuel/air blend of the required composition, into the chamber which is at atmospheric pressure. Before each experiment the fuel is injected into the chamber for 10 seconds. This was designed such that the mixture supplied is several times the volume of the chamber. This is done as a precaution to

purge any gaseous remnants from previous experiments. The flow then ceases and the gases inside the chamber are allowed to settle, hydrogen is left for 5 seconds. Then the stagnant mixture is ignited (Al-Harbi, 2013).

The combustible mixture within the chamber was ignited using laser ignition, instead of the conventional sparkplug ignition. The laser was chosen because it is non-intrusive and the timings are more accurate (Al-Harbi, 2013).

There are many different available configurations, 18 to be precise. These take into account the interchangeable baffles as well as the two different obstacle sizes. The experiments are grouped together depending on the size of the final obstacle. There are two experiments that would fall outside this setting, namely no obstacles at all and only all the baffles. This could be extended to investigate baffle configurations without the final obstacle, but this was not performed for any fuel with equivalence ratio of 0.8 (Al-Harbi, 2013).

Three different configurations are considered for this work, all of which have baffles and the smaller obstacle present. These are shown in Figure 48.

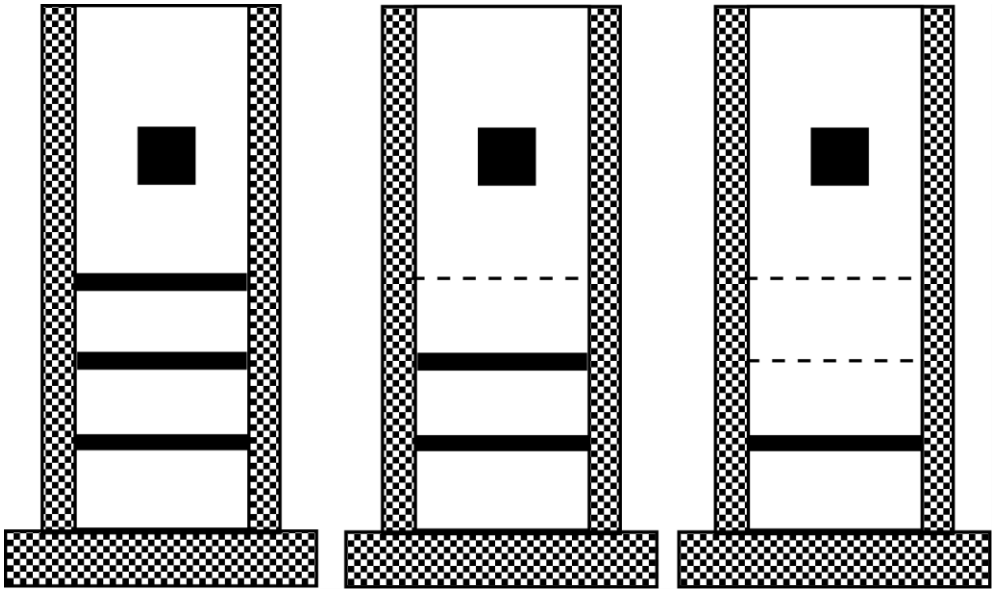

Figure 48 Configurations used showing obstacle arrangement.

Figure 48 shows simplified representations of the configurations that are under investigation within this study. The configurations are known as BBBS, BBOS and BOOS, from left to right respectively. The more obstacles that are located the more turbulence is generated.

The data generated from the experiments, consists of pressure recordings and flame position and speed. The pressure recordings used are from the base pressure transducer. Currently the method of utilising these is to digitally extract the information from (Al-Harbi, 2013). This method is not accurate but is deemed suitable considering there were 50 experiments for each configuration. The results have been averaged previously by (Abdel-Raheem, 2015). However there are time discrepancies between the experimental and averaged results, namely the time of the peak overpressure seems to be different between the raw and averaged results.

The other data sets are the flame position and speed. The flame speed is calculated from the flame position, based on the consumption flame speed (Poinsot and Veynante, 2005). The consumption flame speed, as the name suggests, is a measure of the speed at which the mixture is burnt. This is determined because the flame speed is calculated from u = dx/dt. Such that dt is fixed at the image sampling rate, of 5 kHz (Al-Harbi, 2013), and dx is the difference in height of the flame front, in successive images.

The flame position is determined using laser diagnostics which employed High Speed Laser-Induced Fluorescence of hydroxyl, OH, (HS-LIF-OH). The laser output was at 5 kHz, or 0.0002 seconds = 0.2 milliseconds. The same sampling rate was set for the high speed camera (Al-Harbi, 2013).

6.2.2 Numerical Model

The numerical modelling used the k-omega SST turbulence model alongside the premixed EBU model. These were discussed previously in Chapter 3. The turbulence model is chosen because of its robustness when dealing with near wall flows. All modelling is performed transiently with the implicit option, as expected due to the time dependency of the results. The time step used for the simulations is 0.01 milliseconds. The segregated approach is used, such that velocity and pressure are not solved simultaneously. The ideal gas law is also used, with a thermodynamic polynomial used to calculate the specific heats of species. The mesh consisted of hexahedral cells with a size of 0.9 mm. The size was chosen such that there were multiple cells around the baffles. The baffle height is 3 mm and the gap between baffles is 5 mm, as shown in Figure 47.

The initial conditions are atmospheric pressure and 300 K. This temperature is chosen because the experimental temperature ranged from 27 – 34 °C, with no information other than this available, the lower bound is used. The initial turbulence quantities are; intensity of 1%, length scale of 5 mm and velocity scale of 2 m/s. These are not truly representative of the experiments however the combustion model employed requires some initial turbulence for the combustion to start. These values are chosen such that they are deemed to be just enough for the combustion process to initiate.

The composition of the mixture is calculated by (6.1), taken from (Poinsot and Veynante, 2005).

$$Y_{H_2} = \frac{1}{1+\frac{s}{\phi}\left(1+3.76\frac{W_{N_2}}{W_{O_2}}\right)} \tag{6.1}$$

Hydrogen has a stoichiometric ratio (s) value of 8 (Poinsot and Veynante, 2005), whilst the equivalence ratio, ϕ, in the experiments was 0.8.

Using the knowledge that;

$$\sum_{\alpha=1}^{N} Y_\alpha = 1 \tag{6.2}$$

The mass fractions for oxygen and nitrogen can be calculated, using equations (6.1) and (6.2) alongside the percentage of oxygen in air. The mixture composition for the simulations is; Y_{H_2} of 0.002277, Y_{O_2} of 0.2277 and Y_{N_2} of 0.74953.

The boundary conditions for these scenarios are such that the top of the chamber is treated as a pressure outlet, whilst the rest of the chamber is treated as walls. The thermal treatment of the ‘walls’ is adiabatic. The no-slip condition is imposed for the shear stresses as well. The top of the chamber, outlet, has the same turbulence conditions as the initial conditions. The mass fractions here also correspond to the initial conditions. The pressure is treated as atmospheric, identical to the initial conditions.

6.2.3 Results

The results for the EBU model are dependent on the model coefficient, C_{EBU}, alongside the turbulence mixing scale, τ as discussed in section 3.4.3.1. The turbulence mixing scale is self-determining once the simulations start, however needs to be specified for the initial conditions. This is a problem as the default model coefficient, which is 1, is not suitable due to the low levels of initial turbulence. Therefore an investigation in to the value of the model coefficient is performed.

Figure 49 shows the overpressure comparison for differing values of the model coefficient against the experimental data for the BBBS configuration. This configuration is chosen because it induces the most turbulence for the flame.

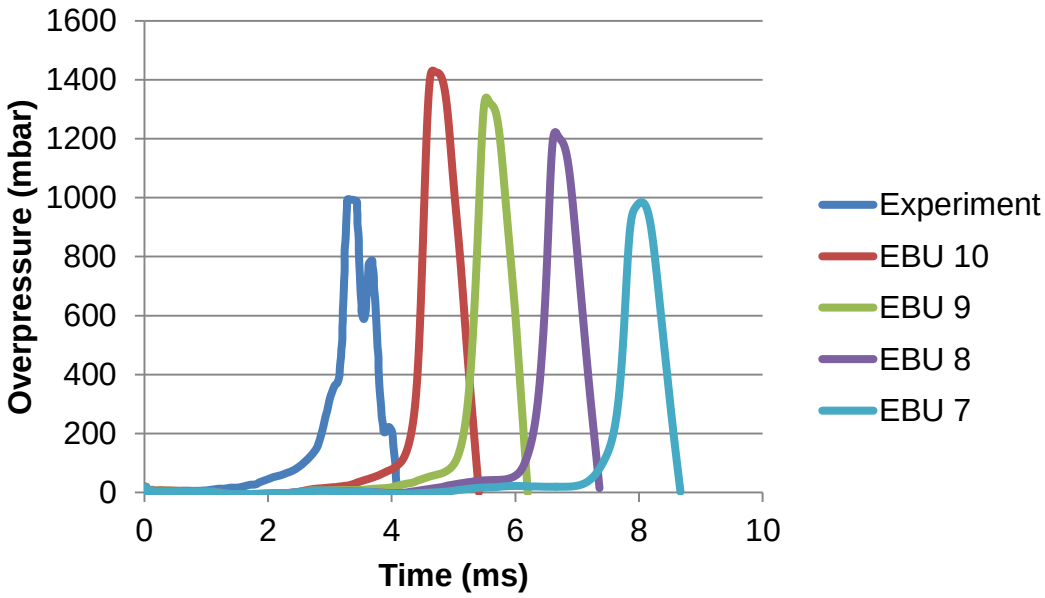

Figure 49 Graph showing the overpressure comparison for differing values of C_{EBU}.

Figure 49 shows the overpressures for EBU coefficients of 7, 8, 9 and 10 against experimental data (blue line on the left). It is clear the only EBU coefficient to match the experimental peak is $C_{EBU} = 7$. However, this is not the value recommended. This is because the experimental curve plateaus at 1000 mbar. This is definitely non-physical and is explained by the pressure transducer used in the experiments. The transducer had a maximum pressure of 1 bar and as such has missed the peak overpressure for the experiment. This can be extrapolated, such that the experimental peak pressure would be approximately 1200 mbar. This peak overpressure would match that of $C_{EBU} = 8$, as such this is the recommended value

for progression. This is applied to two other configurations, BBOS and BOOS. Although first a more detailed analysis is needed of the BBBS configuration.

6.3.3.1 BBBS

Firstly, the overpressures are compared in more detail, followed by the flame position and then the flame speed.

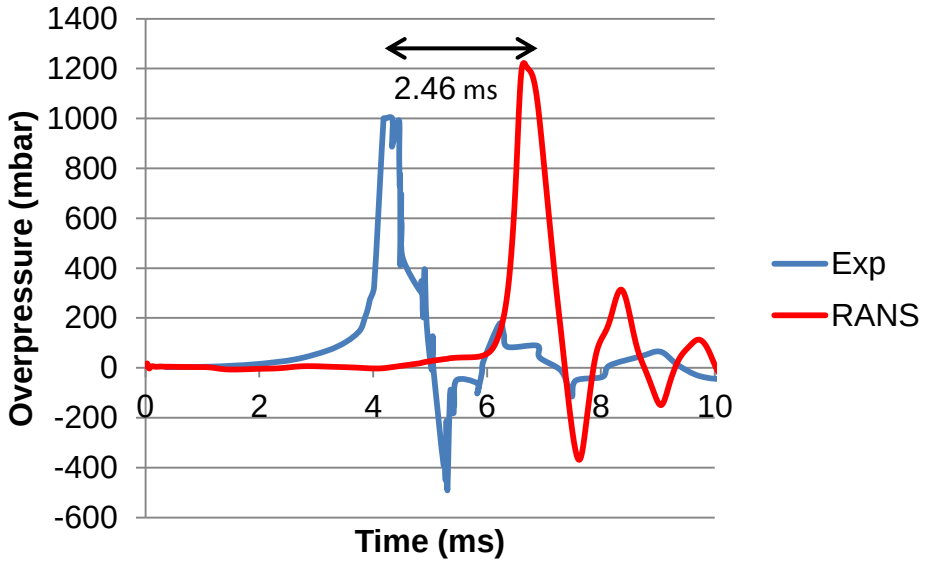

Figure 50 Overpressure comparison for BBBS configuration.

Figure 50 compares the recorded and predicted overpressures for the BBBS configuration. The predicted results show a time delay of 2.46 ms for the peak overpressure. The delay is due to the early phases of combustion, which are not captured accurately. This is caused because of the low turbulence levels at the start of the simulation, which the combustion model uses to progress the flame. There may also be an issue with the ignition, which takes significant time to develop with the software used. Due to the inability of the model to predict the early phase of combustion, a time shift is required. The time shift is -2.4 ms, which is applied to the predicted results, such that the peak overpressures are now aligned against each other.

Figure 51 shows the recorded and predicted peak overpressures for comparison when the predicted results are time shifted, -2.4 ms, for the BBBS configuration. The time shift creates similar arrival times of the peak overpressures. The choice of EBU coefficient seems to be correct, when comparing the slopes of arrival and decay

surrounding the peak pressures. Further investigation on the other configurations will conclude whether the value for the EBU coefficient, $C_{EBU} = 8$, chosen is correct.

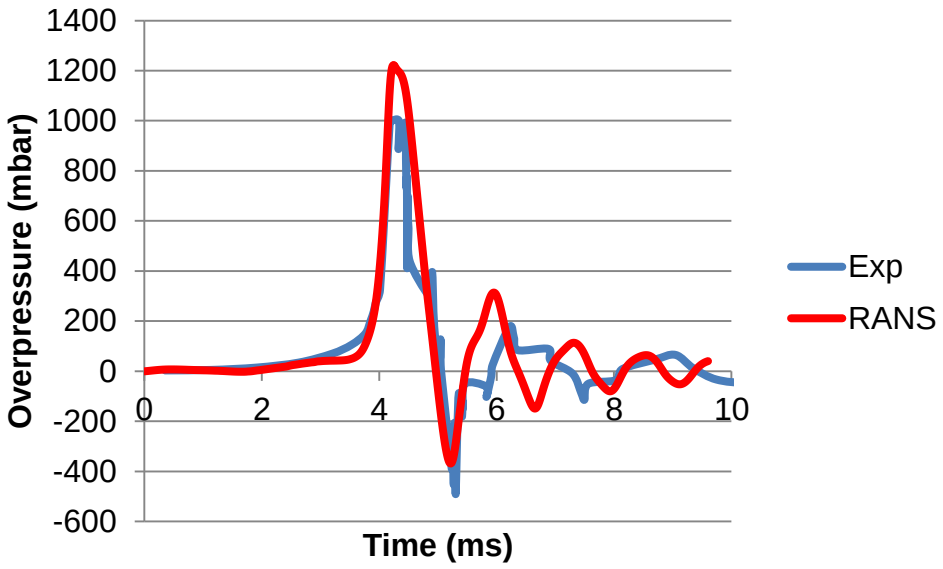

Figure 51 Time shifted overpressure comparison for BBBS configuration.

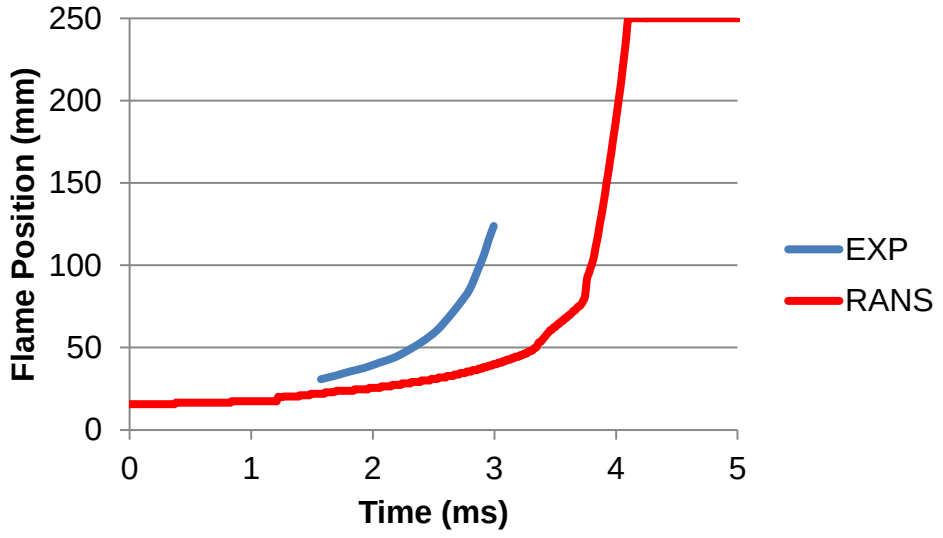

Figure 52 Flame position comparison for BBBS configuration.

Figure 52 shows the comparison of the recorded and predicted flame positions, after the simulation results have been time shifted. The time shift explains the reason that the simulation results already have a significant flame position at the start. It is clear that the simulation results are slower than the experimental results, evident by the slower time of arrival at all heights. This could be due to the combustion model, relying on the turbulence mixing time. Although another possible reason is that the

flame front definitions may not be comparable to the actual situation. The flame front in the simulations is defined as when the progress variable is equal to 0.5 (Abdel-Raheem, 2015; Gubba, 2009).

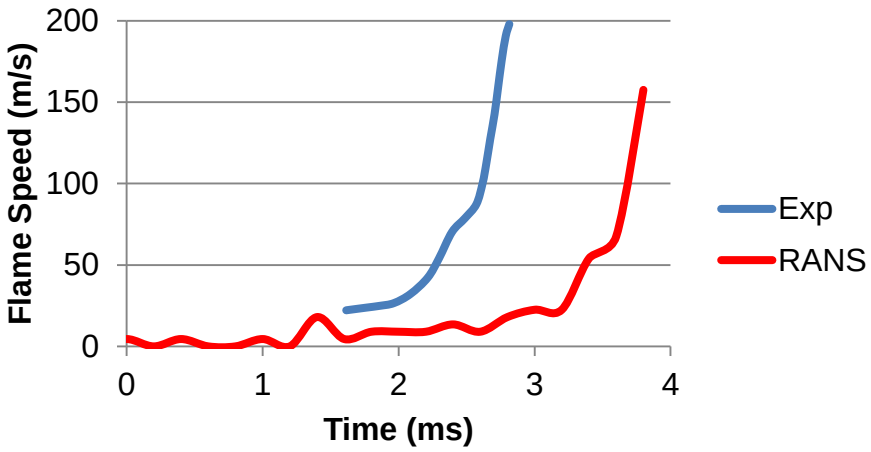

Figure 53 Flame speed comparison for the BBBS configuration.

Figure 53 shows the comparison between the recorded and predicted flame speeds for the BBBS configuration, with time shifted simulation results. The numerical results are time shifted by making the time 2.4 ms set to 0 ms and then proceeding from there. The simulations peak flame speed is almost 50 m/s slower than the experimental flame speed, however the trends of the speeds are similar. The major problem with the flame speed is that it is dependent on the flame position, any errors in the flame position are compounded when calculating the flame speed. This is the case for both the experimental and simulated results. However, both the flame position and speed trends are well reproduced by the simulations.

Figure 54 shows the numerically calculated flame structures at various times for the BBBS configuration. The time designations are given in Table 39. The timings given are raw and have not been time shifted.

Table 39 Time designations for Figure 54.

Designation	Time (ms)
A	0.5
B	1.0
C	2.0
D	5.0
E	6.0
F	6.4
G	6.5
H	6.6

Figure 54 shows the flame structures at various times for the BBBS configuration. The time designations are given in Table 39. It can be seen from images A – C that the initial flame structure is deformed, it should be hemispherical. This is caused by the combustion model and the initial turbulence levels. The time to reach the first baffle, image D, is at 5.0 ms. When compared to Figure 52, this is far slower than expected. This again suggests a problem with the initial phases of combustion. Images E and F, times 6.0 and 6.4 ms, show the flame propagating through the baffle plates, which is as expected. The speed also increases which is due to the increase of the turbulence levels. Images G and H, times 6.5 and 6.6 ms, show the flame propagating past the obstacle. Also evident in images G and H are some burning on the walls ahead of the flame front. This phenomenon is also shown by what looks like flame separation between baffles 2 and 3 for the same images. This is because the EBU model can overestimate the reaction rate in strained regions, where $1/\tau$ is large. These can be in flame holder wakes and walls (Poinsot and Veynante, 2005). This would seem to be evident here.

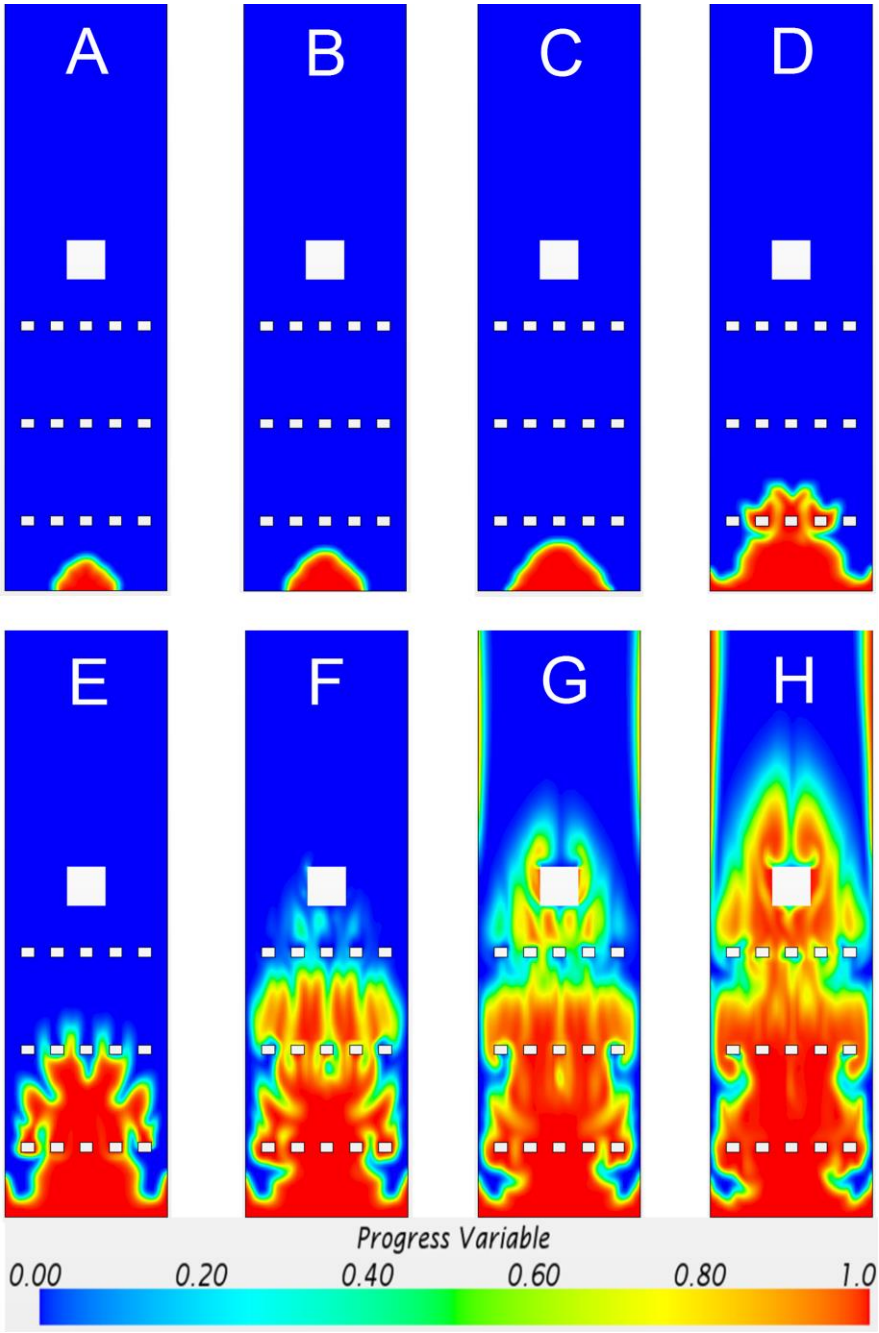

Figure 54 Flame structures, using the progress variable, for the BBBS configuration.

The flame position, and as such the flame speed, show deviations from the experimental results. The overpressures are modelled accurately, once a time shift has been considered. The peak overpressures do not match, due to the limit on the pressure transducers used in the experiments. Although the arrival and decay of the peak overpressures are consistent with each other, thus suggesting that the modelling assumptions are correct. However, this needs to be tested against other configurations to confirm the assumptions.

6.3.3.2 BBOS

The next configuration to be tested is the BBOS configuration, similar to the previous, however the last baffle is removed. This should decrease the turbulence levels that the flame encounters, thus giving a reduction in the peak overpressure.

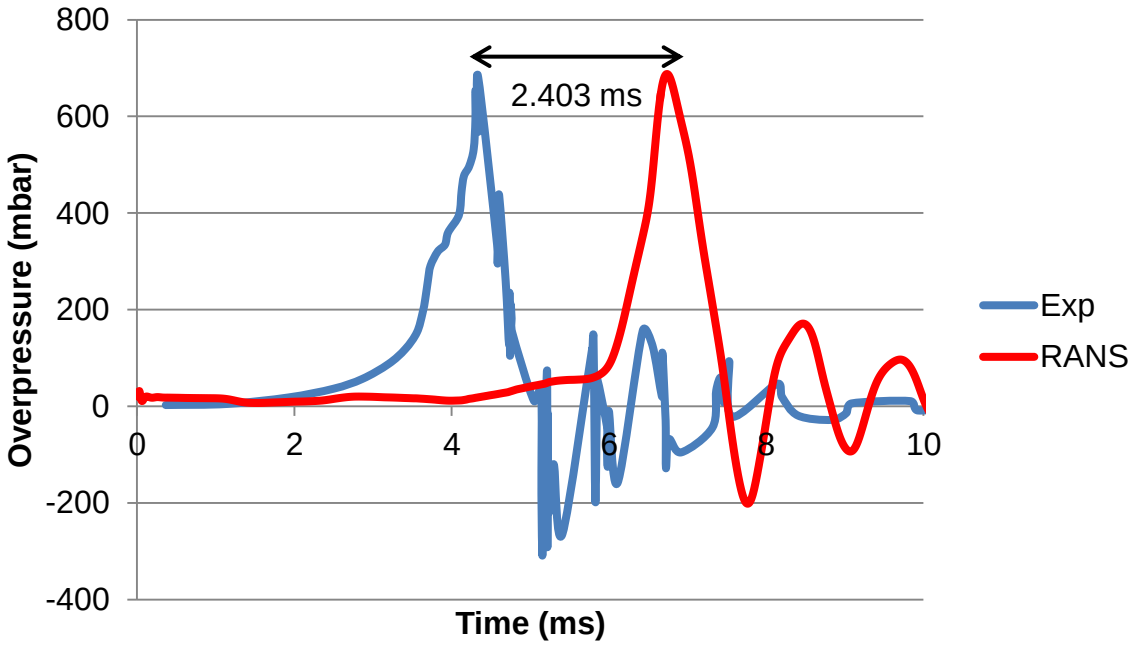

Figure 55 Overpressure comparison for BBOS configuration.

Figure 55 compares the recorded and predicted overpressures for the BBOS configuration. The predicted results show a time delay of 2.403 ms for the peak overpressure. The reasoning for the time delay is the same as the previous configuration. Therefore a time shift is again needed, the time shift is kept at -2.4 ms which is applied to the predicted results. This is because the only difference between the configurations is the removal of the last baffle, which would not alter the initial behaviour.

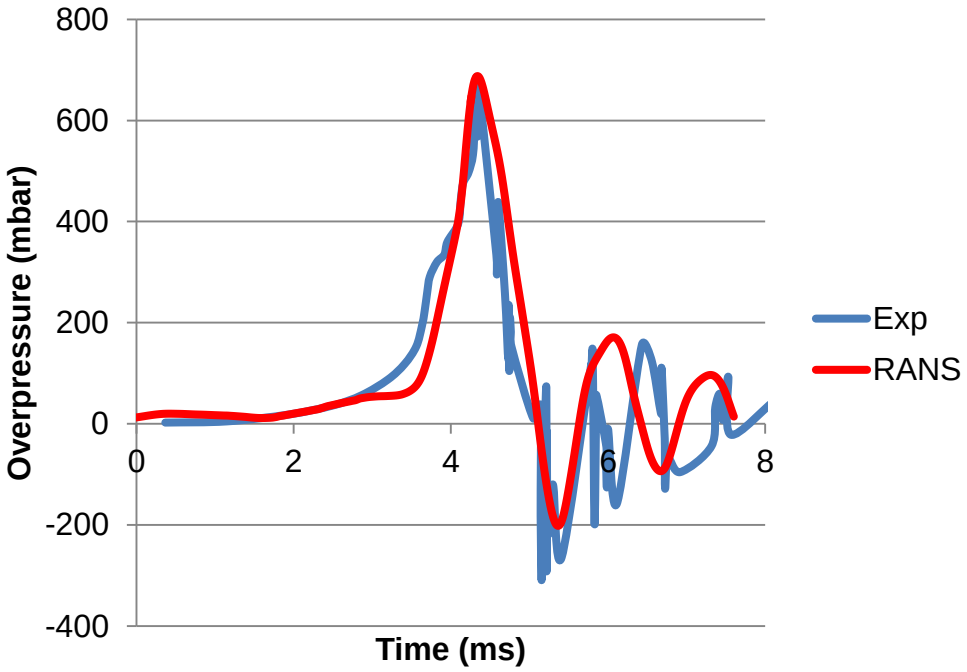

Figure 56 Time shifted overpressure comparison for BBOS configuration.

Figure 56 shows the recorded and predicted peak overpressures for comparison when the predicted results are time shifted, - 2.4 ms, for the BBOS configuration. The time shift again creates similar arrival times of the peak overpressures. The peak overpressures are comparable in magnitude, as well as the arrival and decay slopes. This is a clear indication that the model coefficient chosen is correct.

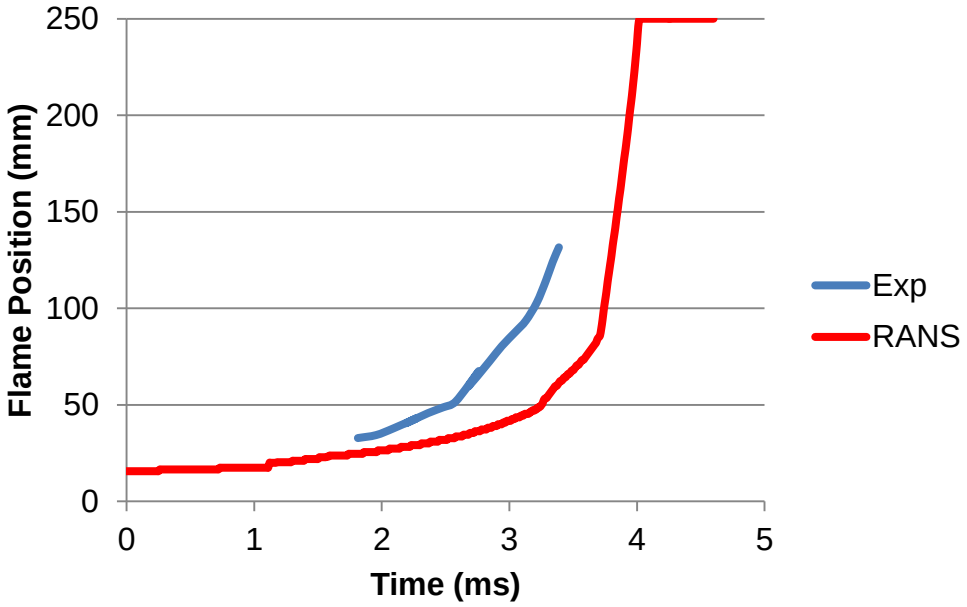

Figure 57 Flame position comparison for the BBOS configuration.

Figure 57 shows the comparison of the recorded and predicted flame positions, after the simulation results have been time shifted. Similar to Figure 52, the flame position is significant at the start. The simulated results are again slower than the experimental, although the trends match.

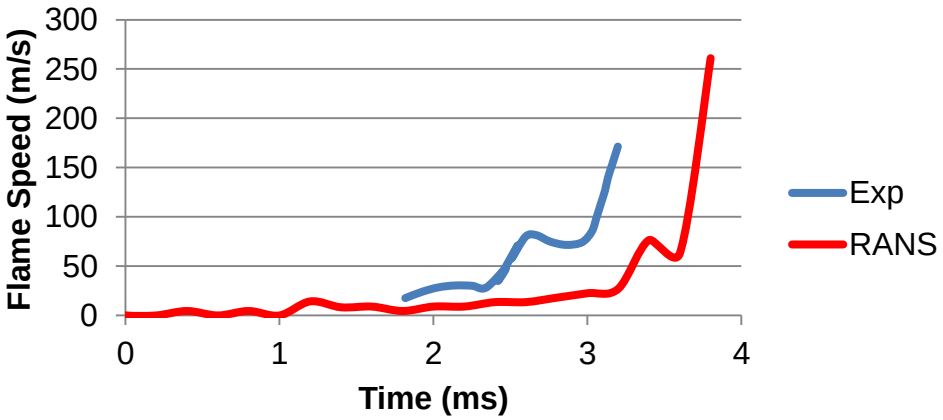

Figure 58 Flame speed comparison for the BBOS configuration.

Figure 58 shows the comparison between the recorded and predicted flame speeds for the BBOS configuration, after the simulation results are time shifted. The simulation peak flame speed is almost 100 m/s quicker than the experimental speed, however the trends are again matched. Similar to Figure 53, the major problem is that the flame speed is dependent on the flame position.

Figure 59 shows the numerically calculated flame structures at various times for the BBOS configuration. The time designations are given in Table 40. The timings given are raw and have not been shifted.

Table 40 Time designations for Figure 59

Designation	Time (ms)
A	0.5
B	1.0
C	2.0
D	5.0
E	6.0
F	6.4
G	6.5
H	6.6

The images in Figure 59 are for the same times and are similar to those in Figure 54, especially images A – E. Therefore these will not be explained here. Image F is different to the previous, because the last baffle is now removed, it shows the flame is higher due to the lack of obstruction. Image G shows some flame separation around the obstacle, with some slight burning at the walls. The flame here is lower in height than the corresponding image in Figure 54. This is due to the decrease in turbulence compared to the BBBS configuration. Image H shows the flames starting to recombine around the obstacle, with an unburnt pocket on the underside of the obstacle. There is also more burning at the wall compared to image G.

The overpressures are modelled accurately and the EBU coefficient used for the BBBS configuration is shown to be accurate. There are still deviations for the flame position and by extension the flame speed. Once again this is believed to be due to the definition of the flame front. The flame position induces errors when computing the flame speed. To further conclude the modelling is accurate a final configuration with a further reduction in turbulence is used for validation. This is the BOOS configuration, only the first baffle and the obstacle are present.

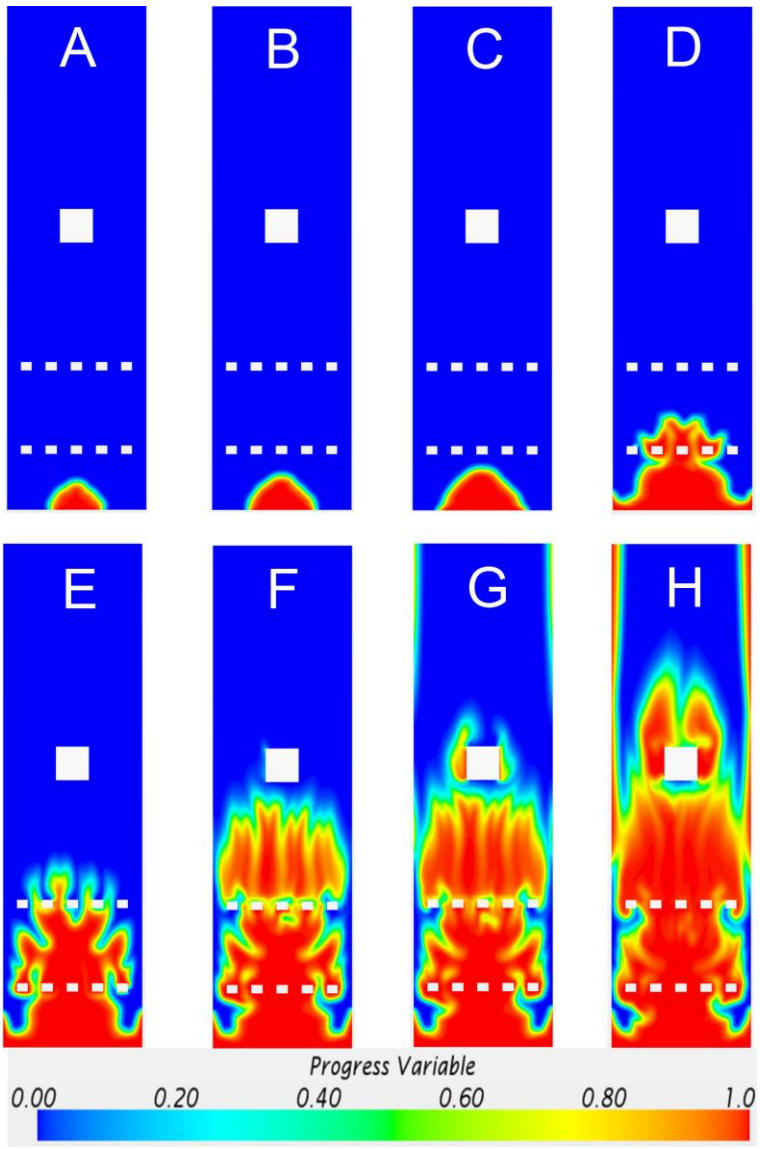

Figure 59 Flame structures, using the progress variable, for the BBOS configuration.

6.3.3.3 BOOS

The final configuration used for comparison is the BOOS, namely only the first baffle and obstacle are used. This would further reduce the turbulence that the flame front encounters as it propagates up the chamber. The further reduction in turbulence is expected to again reduce the peak overpressure.

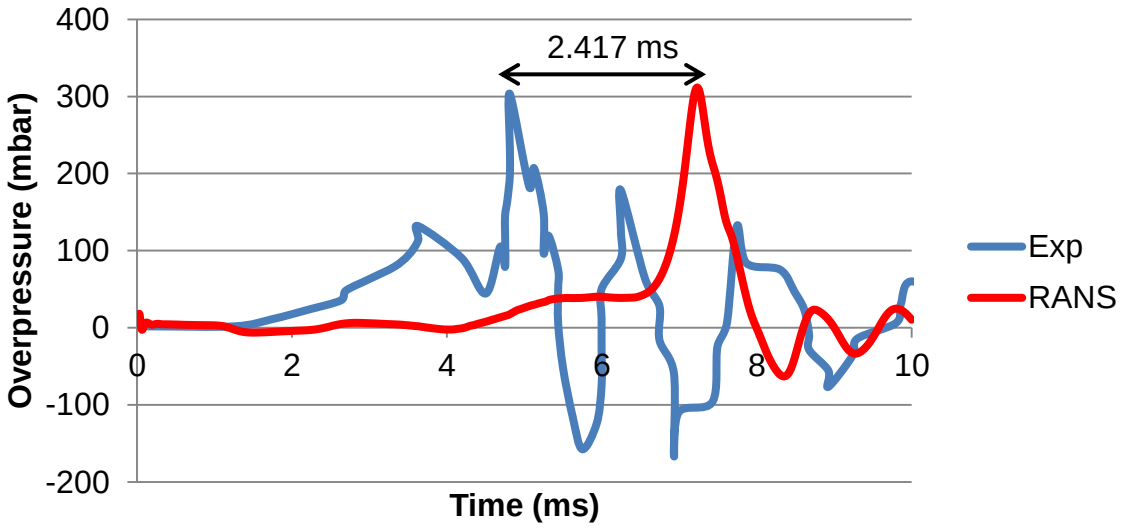

Figure 60 Overpressure comparison for the BOOS configuration.

Figure 60 shows the recorded and predicted overpressure for comparison from the BOOS configuration. The predicted results show a time delay of 2.417 ms for the peak overpressure. The reasoning for this delay has been explained previously. A time shift is again needed, and is kept at -2.4 ms, applied to the predicted results. This is such that it is kept constant between the configurations, as the reasoning for the delay is the same.

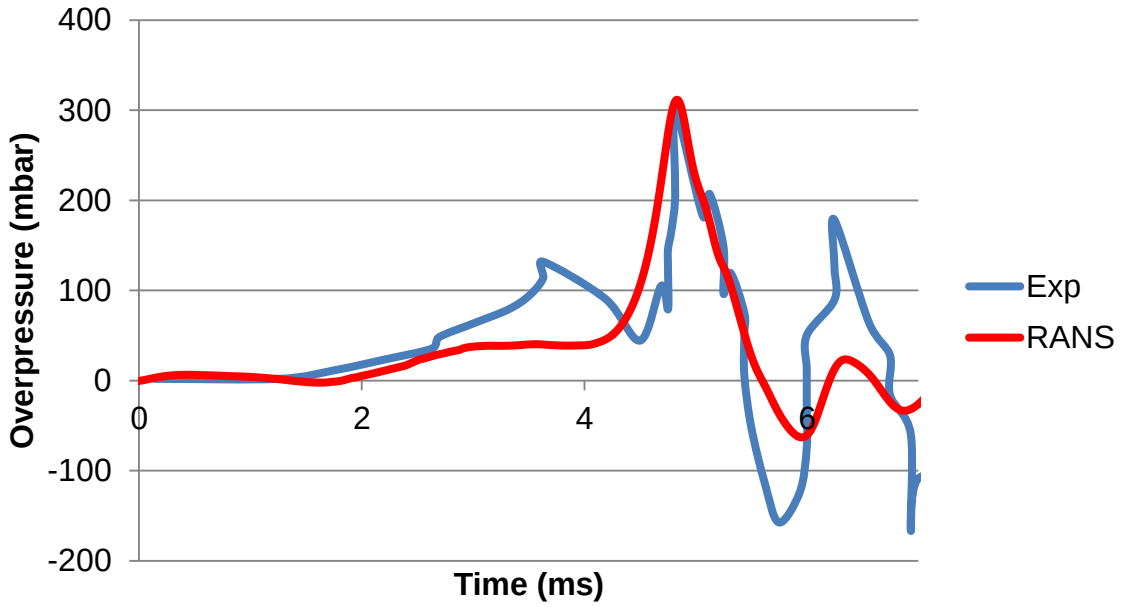

Figure 61 Time shifted overpressure comparison for the BOOS configuration.

Figure 61 shows the recorded and predicted overpressures for comparison when the predicted results are time shifted, -2.4 ms, for the BOOS configuration. The time shift

again aligns the peak overpressures, and the magnitudes of the maximum overpressures are comparable. There is a discrepancy between the predicted and recorded results circa 3 – 4 ms, where the experimental overpressure rises and is not replicated by the model. The overpressure decay after the peak is also not matched as well as previous configurations. However because the peak overpressures again match, it provides conclusive evidence that the EBU coefficient selected is correct. The time delays being comparable, all circa 2.4 ms, suggests that the delay is due to the early phases of the combustion process. This is when the turbulence levels are extremely low.

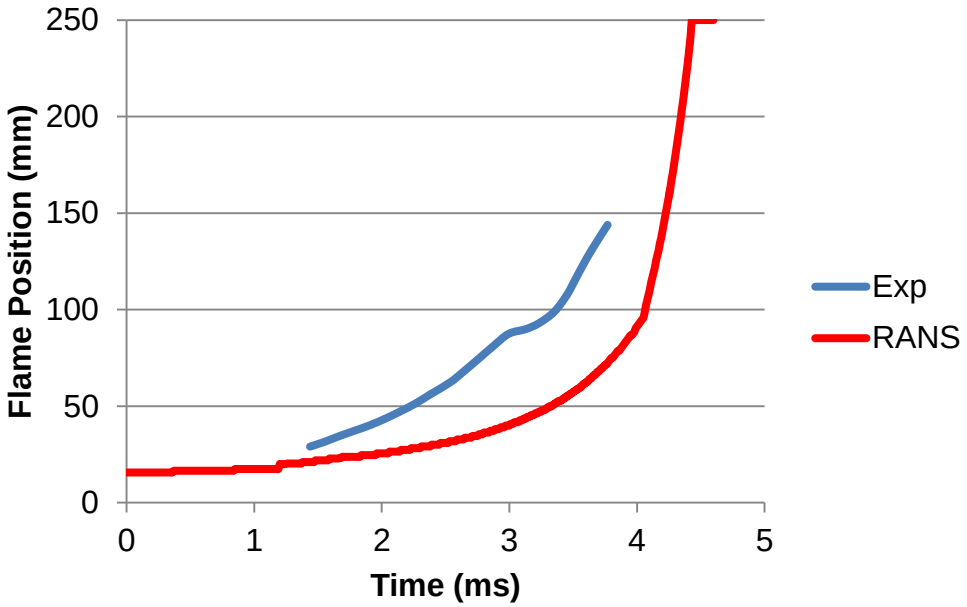

Figure 62 Flame position comparison for the BOOS configuration.

Figure 62 shows the time shifted recorded and predicted flame positions for comparison of the BOOS configuration. Similar to before, the predicted flame is significant at the start due to the time shift. The simulated results are also slower than the experimental again, whilst the trends are different for the configuration. However the cause for the difference is again believed to be because of the flame front definition.

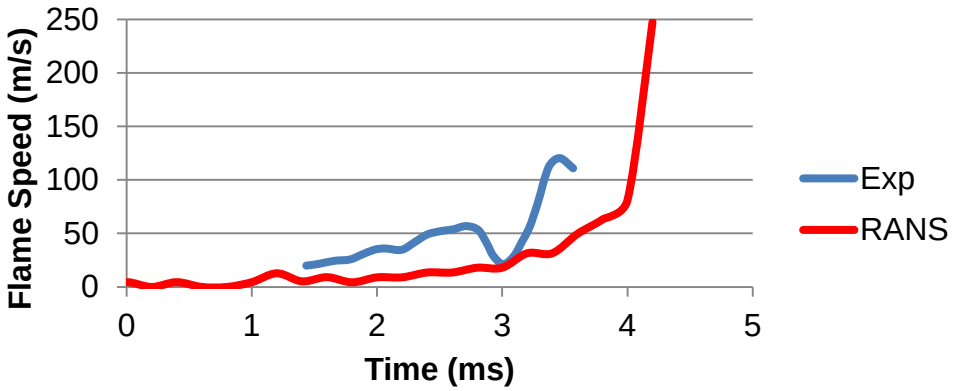

Figure 63 Flame speed comparison for the BOOS configuration.

Figure 63 shows the comparison between the recorded and predicted flame speeds for the BOOS configuration, after the simulation results have been time shifted. The predicted peak flame speed is approximately 125 m/s more than the recorded flame speed. This configuration shows no trend comparison between the recorded and predicted results, which is to be expected as the same occurs for the flame position. This is because the flame speed is reliant upon the flame position.

Figure 64 shows the numerically calculated flame structures at various times for the BOOS configuration. The time designations are given in Table 41. The timings given are raw and have not been shifted.

Table 41 Time designations for Figure 64

Designation	Time (ms)
A	0.5
B	1.0
C	2.0
D	5.0
E	6.0
F	6.5
G	7.0
H	7.7

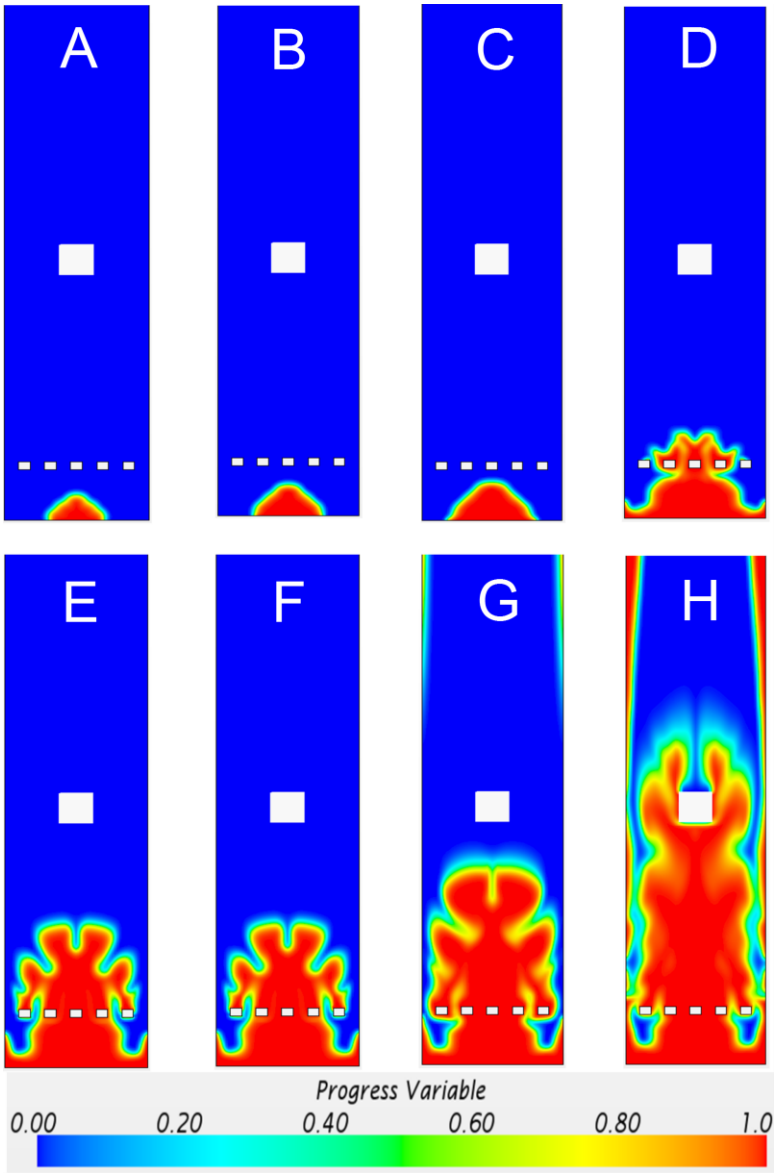

Figure 64 Flame structures, using the progress variable, for the BOOS configuration.

Figure 64 shows the flame structures for the BOOS configuration, images A – D are for the same times as Figure 54 and Figure 59. Therefore they will not be explained again here. Image E is taken at 6.0 ms, the same as the other configurations, and shows a similar flame shape. Image F, taken at 6.5 ms, is for the same as Image G on both other configurations. It shows that the flame does not propagate as quickly as the other configurations. Image G, taken at 7.0 ms, shows the flame is propagating towards the obstacle and the flame front is recombining, after passing the central baffle. There is also evidence of some burning on the wall. Image H, taken at 7.7 ms, shows the flame propagating past the obstacle. There are still pockets of unburnt gas lower down the chamber, however not at the underside of the obstacle. There is also more profound burning at the walls, this was explained earlier.

6.3 Conclusion

This chapter started with a brief background of the University of Sydney Combustion Chamber, followed by a description of the experiments performed. This is followed by the numerical setup used. The numerical setup utilises the k-omega SST turbulence model and the premixed EBU combustion model. The EBU model coefficient was investigated against the BBBS configuration, to determine the most suitable for progression. This was then extended to two other configurations for further investigation.

The initial study of the EBU coefficient found that using a value of 7 matches the peak overpressure for the BBBS configuration. However this is not the suggestion moving forwards, instead a value of 8 is suggested. This is because the experimental peak overpressure plateaus at 1000 mbar, which is not realistic. However an approximate extrapolation gives a peak overpressure circa 1200 mbar. This value corresponds to the peak overpressure when using an EBU coefficient of 8, which is used for further investigation.

The calculated peak overpressures for the other two configurations, BBOS and BOOS, matches the experimental peak overpressures accurately. A time shift, of 2.4 ms, was needed to align the incident times of the calculated peak overpressures for all of the configurations examined. This is due to early phases of combustion which are not captured accurately. This is because the EBU combustion model is reliant on turbulence to progress the flame. The turbulence levels at the start of the process are negligible.

The predicted flame positions and speeds do not match the experimental results. However the trends are very similar. This may be due to discrepancies in determining the flame front. The simulated flame position is when the progress variable is equal to 0.5. This may not be the case in the experiments.

The flame structures seem accurate, although there are some discrepancies, at the start and end of the simulations. Namely, the initial phases do not propagate as would be expected, hemi-spherically. The flame is also evident at the walls further up the chamber and some flame separation occurs. These are due to the combustion model used, which is heavily reliant on the turbulence to propagate the flame.

Chapter 7 – Models for Reacting Safety Assessment – Non-Premixed

7.1 Introduction

Non-premixed combustion is the probable scenario to occur from a system, such as that being investigated. This is because the most common single failure mode is that the pressure relief device will release the hydrogen contained into a partially enclosed or unenclosed geometry. This is because the hydrogen will mix with the air and were it to be ignited then create a diffusion flame. The main safety issue that arises from jet flames is the temperature reached and the heating of the surrounding areas. The pressure may however rise when the flame is within a confined enclosure.

This chapter investigates the non-premixed combustion, validating against simple jet flame data. Two different flames have been chosen for validation, a pure hydrogen flame (Barlow and Carter, 1996, 1994) and a hydrogen/nitrogen mixture (Meier et al., 1996). This data is heavily used for validation as it is taken from the Turbulent Non-premixed Flames (TNF) workshop website. Firstly there is a description of the experiments. This is followed by the numerical setup used and lastly the results for the flames investigated.

7.2 Case Study – Sandia Flame

The experimental data used for the validation of the combustion models is the Sandia Flame data for pure hydrogen (Barlow and Carter, 1996, 1994) and a hydrogen/nitrogen mixture (Meier et al., 1996). This data has been widely used for validation of jet flames (Ranga Dinesh et al., 2013, 2012) to name a few. The information that is of importance is the mixture fraction, temperature and water mass fraction. These are recorded at various heights up the chamber, which are all problem dependent. Whilst there are many heights that could be used, only three are chosen for the validation.

7.2.1 Experimental Configurations/Details

The experimental configuration is depicted in Figure 65. The burner for the pure hydrogen experiments is located within a vertical wind tunnel (Barlow and Carter, 1994). Lasers were used to measure concentrations of hydroxyl. This was combined with Raman and Rayleigh scattering to produce the measurements given. The spontaneous Raman scattering is used for the major species, whilst the Rayleigh scattering is yields temperature data (Barlow and Carter, 1996, 1994). The hydrogen-nitrogen mixtures only used Raman scattering to predict the major species and temperature. The burner used was surrounded by another nozzle which supplied the air (Meier et al., 1996). All of the experiments utilised Laser Induced Fluorescence (LIF).

The details of the experiments chosen are given in Table 42. The table consists of the jet (release) diameter, the mean velocity of the release and the chemical composition of the releases. It is quite clear that the pure hydrogen flame, flame H2, is significantly quicker than the hydrogen/nitrogen mixture, flame H2N2. This is due to the smaller inlet diameter.

Table 42 Sandia Flame experimental details.

Case	Flame H2	Flame H2N2
Inlet Diameter (mm)	3.75	8
Mean Jet Velocity (m/s)	296	42.3
H_2 %	100	75
N_2 %	0	25

The heights that are used for comparison are 84, 253 and 338 mm for flame H2. Flame H2N2 uses measurements at heights of 80, 160 and 320 mm.

Figure 65 shows the geometrical configuration that is used for the numerical studies, which is replicable of the experimental configuration. The fuel inlet, red circle, varies in diameter depending on the fuel composition, as shown in Table 42. The blue area

surrounding the fuel inlet is the air inlet, which has a flow speed of 1 m/s (Ranga Dinesh et al., 2013).

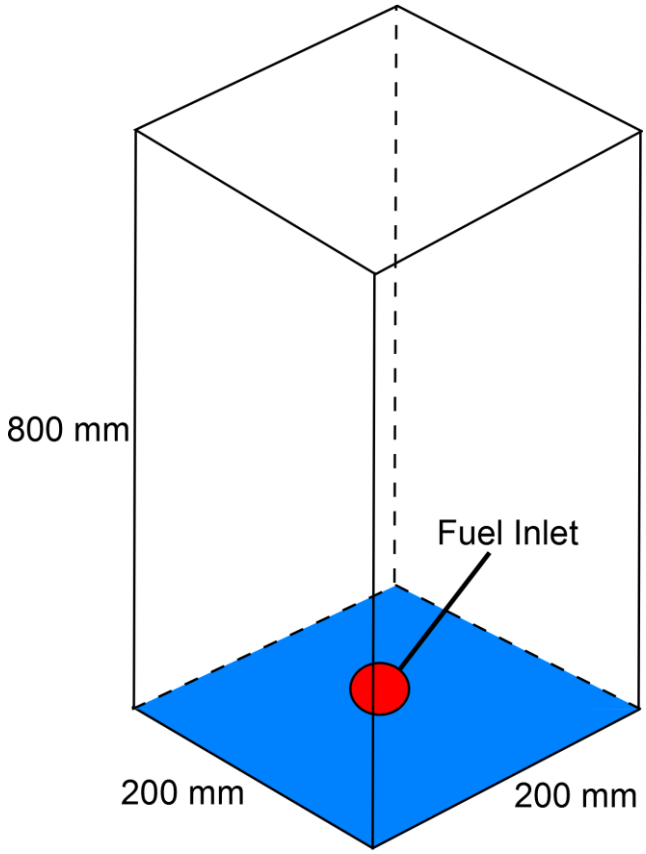

Figure 65 Diagram of the experimental configuration for non-premixed combustion.

The fuel inlet has been given as a mean velocity. The radial velocity is calculated based upon a turbulent pipe flow, using the following (Young et al., 2012);

$$u_{\max} = \frac{u_{mean}(n+1)(2n+1)}{2n^2} \tag{7.1}$$

$$u_R = u_{\max}\left(1-\frac{r}{R}\right)^{\frac{1}{n}} \tag{7.2}$$

Where n is equal to 7 for a turbulent pipe flow.

This gives the radial velocity profiles shown in Figure 66 and 67.

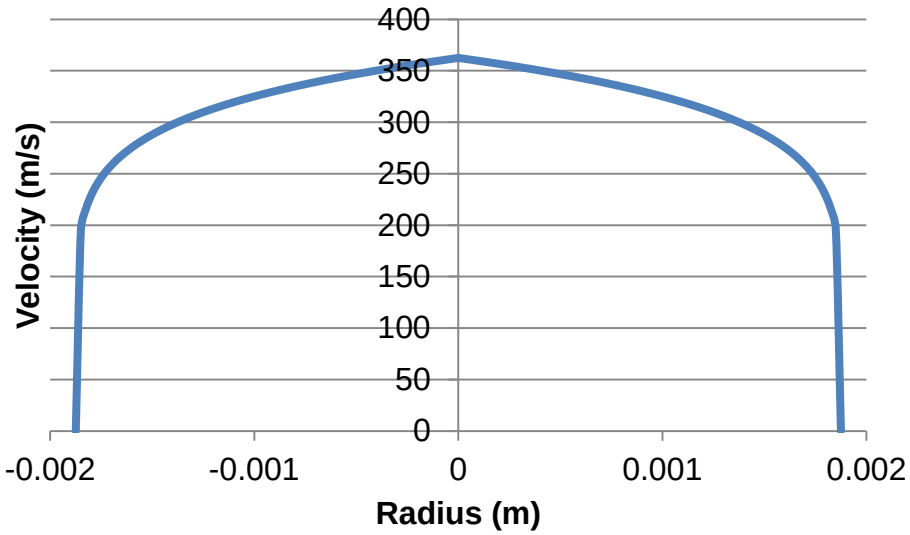

Figure 66 Graph showing radial velocity profile for flame H2.

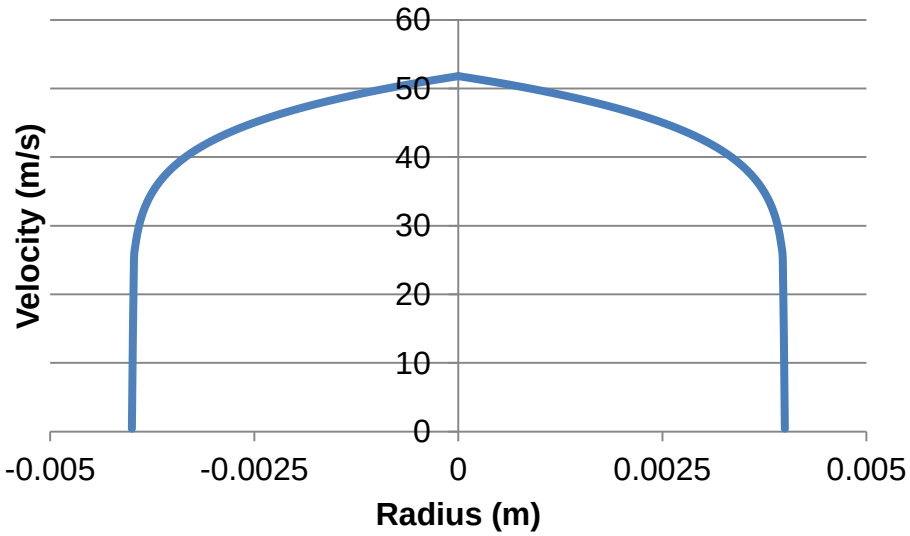

Figure 67 Graph showing radial velocity profile for flame H2N2.

7.2.2 Numerical Model

The numerical model used is a steady state model. This is because the end result is a constant non-changing flame. The turbulence model employed is the standard k-epsilon model, section 3.3.3.1. This is used because of a need to alter the turbulence decay model coefficients (Hassel, 1997). These adjustments are well known for the standard k-epsilon model (Hassel, 1997; Versteeg and Malalasekera, 2007). This is especially the case for flames that involve hydrogen, due to the buoyancy and higher diffusivity of the chemical.

The recommendations from the 1997 meeting of the TNF network (Hassel, 1997), for hydrogen flames, are that the $C_{\varepsilon 2}$ constant should be changed. This coefficient should be changed from 1.92, the default value, to 1.83 for hydrogen-helium mixture, of 80:20. The coefficient is suggested to be at the default value of 1.92 for 50:50 mixtures of hydrogen-nitrogen.

The pure hydrogen flame (flame H2) uses the model coefficient set to 1.83 whilst a mesh study is performed. A polyhedral mesh and two hexahedral meshes are examined. The first hexahedral mesh utilises a constant cell size of 2 mm. The other two meshes both use varying cell sizes, from 0.6 mm up to 5 mm. Table 43 contains the details for the meshes investigated alongside the designation as well.

Table 43 Mesh types used for Flame H2.

Mesh	Cell Shape	Smallest Cell Size (mm)	Largest Cell Size (mm)	Total Cells
A	Hexahedral	2.0	2.0	4031409
B	Polyhedral	0.6	5.0	3828566
C	Hexahedral	0.6	5.0	1917828

The most suitable mesh is then applied to the hydrogen-nitrogen mixture (flame H2N2) where the turbulence model coefficient is tested to determine the suitability for the problem. This is investigated as there are no recommendations for the model coefficient of such a mixture. Flame H2 also tests the differences between the flamelet and equilibrium variants of the PPDF combustion model, section 3.4.3.2. This is because the software has an inbuilt PPDF library for pure hydrogen flames, however it does not contain one suitable for the flame H2N2. The initial conditions and boundary conditions for both flames are the same, with the exception of the inlet conditions given in Table 42.

Although the simulations are in steady state, the initial conditions still need to be defined. These conditions will no longer exist as soon as the iterative procedure begins. The initial conditions used for turbulence are intensity of 5%, length scale of 1 mm and velocity scale of 2 m/s. Air is in the entire domain and is modelled as being

at atmospheric pressure with a temperature of 300 K. The air inlet is modelled as a velocity inlet, with velocity 1 m/s. The turbulence intensity is 1% and the length scale is 1 cm. The fuel inlet is also modelled as a velocity inlet. The turbulence conditions are intensity of 10% and length scale of 1 mm. The velocity is prescribed as an input table assuming the profiles given above, in Figure 66 and Figure 67. The shear stress at the walls is modelled with the slip condition, whilst the thermal treatment of the walls is adiabatic. The outlet at the top is modelled as a flow split outlet, such that no physics is defined for it.

7.2.3 Results

The results are split between Flame H2 and Flame H2N2. Each flame has graphs, for each height as well as planar images for the mixture fraction, temperature and water mass fraction. Planar images are used because the nature of RANS modelling means that the turbulent fluctuations, that you would expect to see in the flame, are not captured accurately.

7.2.3.1 Flame H2

The results for flame H2 are given in this section. They are divided into mixture fraction, followed by temperature and lastly H_2O mass fraction. Different mesh types and sizes are compared as well as a variation with the combustion model for some meshes. Table 44 gives the simulation designations alongside the meshes and PPDF model variations used.

Table 44 Information for the Flame H2 simulations performed.

Simulation	Mesh Designation	PPDF Model Variation
1	A	Flamelet
2	B	Flamelet
3	B	Equilibrium
4	C	Flamelet
5	C	Equilibrium

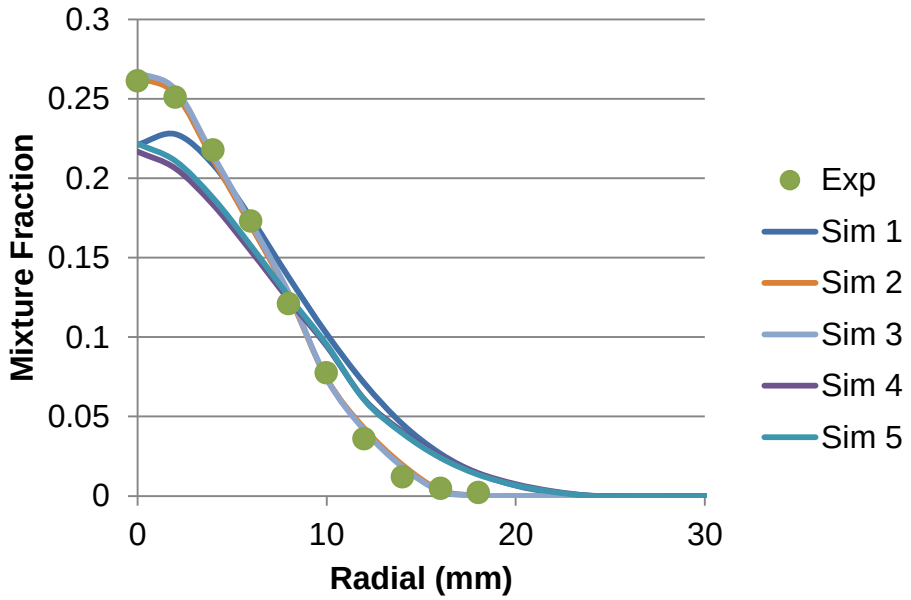

Figure 68 Graph of the mixture fraction at 84 mm for Flame H2.

Figure 68 shows the mixture fraction for the pure hydrogen flame at a height of 84 mm. It can be seen that the polyhedral mesh, simulations 2 and 3, performs better than the others. Interestingly, there are no distinguishable differences between the two types of PPDF model that were tested. Table 45 shows a comparison of the percentage error at different radial distances for the mixture fraction at 84 mm. The percentage error is calculated as follows:

$$Error\% = 100 * \left| \frac{Simulation - Experiment}{Experiment} \right|$$

Table 45 shows that the using a uniform hexahedral mesh, simulation 1, gives the highest average error. The other hexahedral mesh, simulations 4 and 5, are marginally more accurate. The polyhedral mesh, simulations 2 and 3, shows far greater accuracy with the average error being around 10 %.

Table 45 Error comparison for the mixture fraction at 84 mm for Flame H2.

Radial Distance (mm)	Simulation % Error				
	1	2	3	4	5
0	15.43	0.80	1.94	17.09	15.18
4	4.32	2.82	1.67	15.89	13.98
8	13.58	4.44	5.39	1.93	3.71
12	96.46	17.62	14.60	68.56	67.31
16	449.51	22.44	34.62	418.98	395.06
AVERAGE	115.86	9.62	11.64	104.49	99.05

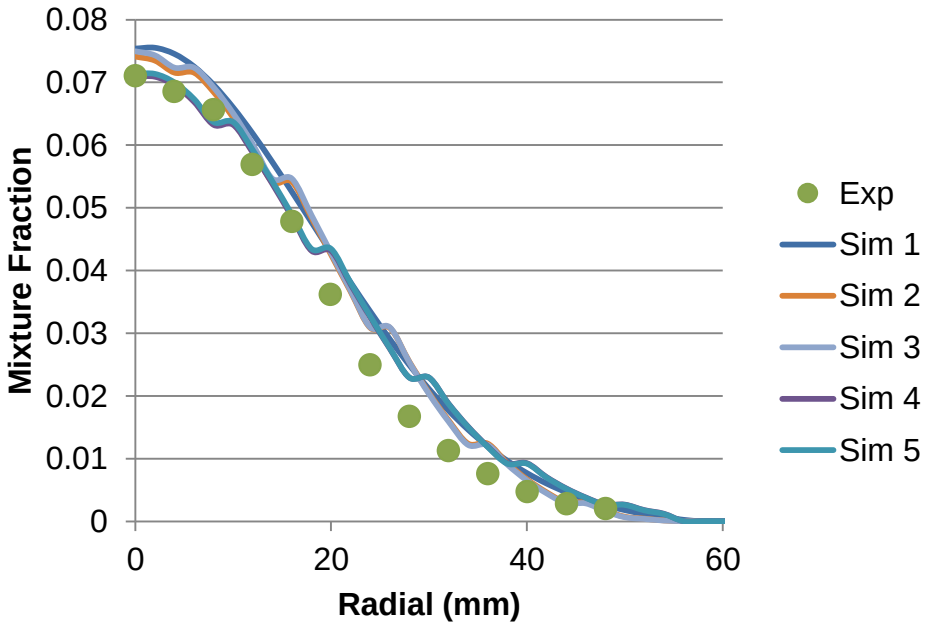

Figure 69 Graph of the mixture fraction at 253 mm for Flame H2.

Figure 69 shows the radial mixture fraction at a height of 253 mm. The graph shows that there are minimal differences between any of the mesh types. The second hexahedral mesh, simulations 4 and 5, seem to predict the mixture fraction better at the centre but over predicts further from the centre. Whilst the first hexahedral mesh and polyhedral mesh, simulations 1 – 3, seem to over predict slightly more at the

centre but are more accurate further afield. There seems to be very slight differences between the combustion models again. Some of the results plateau at various levels due to the mesh used and the method in which the software records data at defined points. Namely, that the software takes the maximum of the cell/s at the defined point. Table 46 compares the percentage error of the simulations for the mixture fraction at a height of 253 mm.

Table 46 shows that the polyhedral mesh, simulations 2 and 3, is again the most accurate. However all of the simulations have errors circa 24 %, ± 2 %. There is approximately a 1 % difference between the two combustion models investigated.

Table 46 Error comparison for the mixture fraction at 253 mm for Flame H2.

Radial Distance (mm)	**Simulation % Error**				
	1	**2**	**3**	**4**	**5**
0	6.06	4.27	5.45	0.25	0.38
12	8.54	4.54	5.58	3.23	3.95
24	33.87	23.49	23.80	30.17	30.85
36	57.36	63.03	60.34	57.06	56.13
48	24.90	15.13	20.98	29.89	27.69
AVERAGE	26.15	22.09	23.23	24.12	23.80

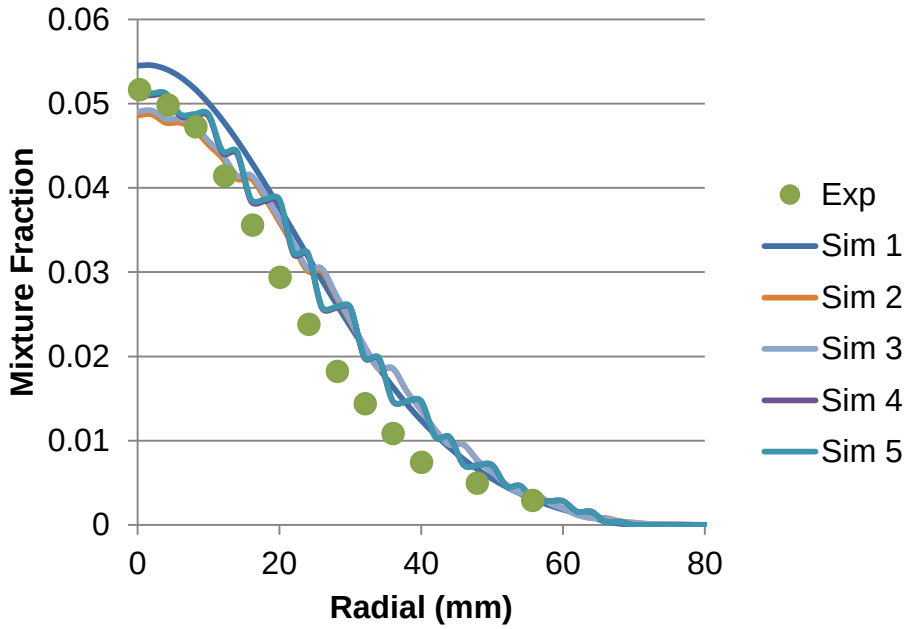

Figure 70 Graph of the mixture fraction at 338 mm for Flame H2.

Figure 70 shows the mixture fraction comparison at 338 mm. It is clear that the first hexahedral mesh, simulation 1, over predicts at the centre although matches the others after 20 mm. There seems to be negligible differences between the polyhedral and second hexahedral meshes, simulations 2 – 5. There are also no discernible differences between the combustion models. Table 47 compares the percentage error of the simulations for the mixture fraction at a height of 338 mm.

Table 47 Error comparison for the mixture fraction at 338 mm for Flame H2.

Radial Distance (mm)	Simulation % Error				
	1	**2**	**3**	**4**	**5**
0	5.56	5.89	4.99	1.35	0.90
12	15.81	4.90	5.95	6.41	6.99
24	34.00	26.51	27.81	34.87	35.71
32	45.96	46.77	47.47	37.55	37.98
48	32.02	53.44	52.54	43.20	42.93
AVERAGE	26.67	27.50	27.75	24.68	24.90

Table 47 shows that the error across all of the simulations is similar, approximately 26 %, ± 2%. The most suitable mesh at this height is the non-uniform hexahedral mesh, simulations 4 and 5, with an error of 24.68 %. The polyhedral mesh, simulations 2 and 3, is the worst mesh with an error of 27.5 %. There is less than a 1% difference between the combustion models that are investigated.

Figure 71 shows contour plots across the central plane for the mixture fraction. It is clear that the jet disperses symmetrically, which is not realistic and is due to the modelling technique utilised. It is evident that the hydrogen decreases rapidly, visualised by the quick decrease in mixture fraction. The majority of the mixture within the jet has a mixture fraction around 0.3.

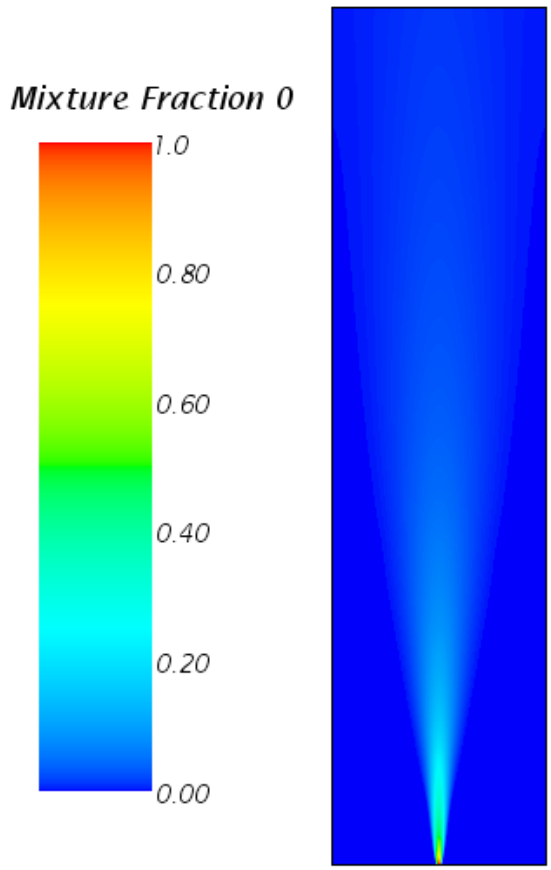

Figure 71 Planar image of the mixture fraction for Flame H2 from the polyhedral mesh.

Overall, the mixture fraction is captured accurately with no discernible difference between the two variations of the combustion model used. The polyhedral mesh is better at heights of 84 and 253 mm, whilst the non-uniform hexahedral mesh is slightly better at the upper height. The difference between the two types is negligible at the upper heights although is quite profound at the lowest height.

Table 48 compares the average error at all of the heights. There is also an average error for the mixture fraction at the bottom of the table. It is evident that at heights of 253 and 338 mm there are negligible differences between the simulations, the maximum error difference is circa 4%. The major difference between the simulations is at the lower height where the error difference is vast, at least 90%. This creates higher average errors for the mixture fraction. The polyhedral mesh, simulations 2 and 3, has an average error of 20 %, whilst the other simulations are around 50 %. The error difference between the combustion models is up to 2%.

Table 48 Error comparison for the mixture fraction at all heights.

Height (mm)	Simulation % Error				
	1	**2**	**3**	**4**	**5**
84	115.86	9.62	11.64	104.49	99.05
253	26.15	22.09	23.23	24.12	23.80
338	26.67	27.50	27.75	24.68	24.90
AVERAGE	56.22	19.74	20.88	51.10	49.25

The next criterion for comparison is the temperature profiles, again at the same heights as the mixture fraction comparisons.

Figure 72 shows the temperature profiles at 84 mm for the various mesh types and the different combustion models employed. It is clear that the equilibrium variation of the PPDF model, simulations 3 and 5, over predicts the peak temperature more than the flamelet variation. The flamelet variation, simulations 1, 2 and 4, over predicts the temperature by up to 100 K, whilst the equilibrium variety is up to 200 K higher than the experimental peak temperature.

The polyhedral mesh, simulation 2, matches the experimental data more closely compared to the hexahedral meshes, simulations 1 and 4. The peak temperatures for the hexahedral meshes seem to be 5 mm further from the centre than the experimental peak. The hexahedral meshes do have slightly lower peak

temperatures compared to the polyhedral mesh, although they do over predict the temperature at the centre, radius 0 mm.

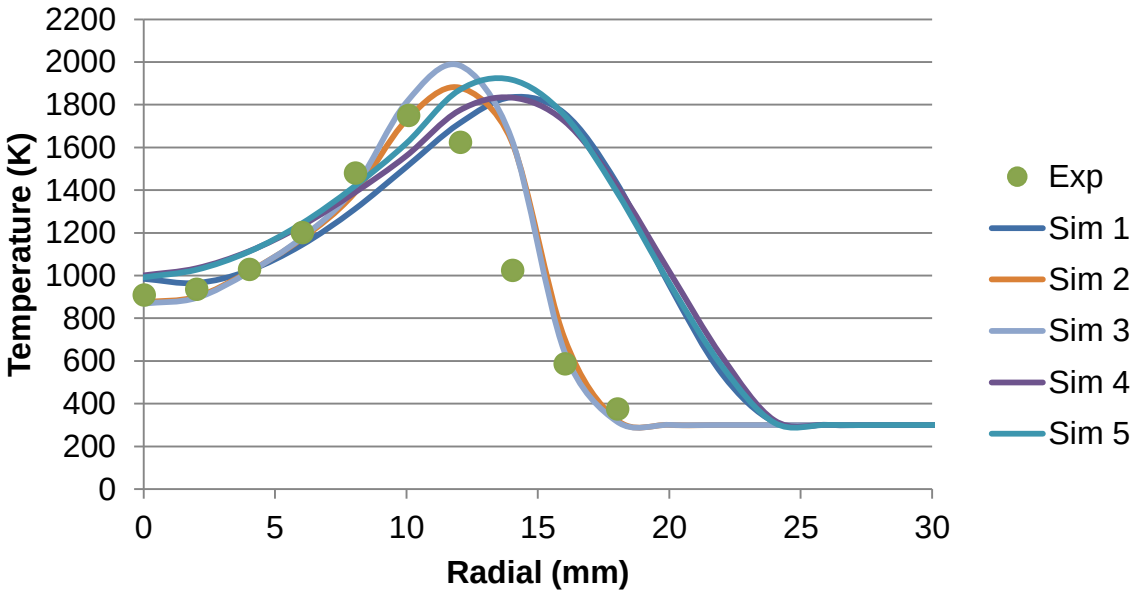

Figure 72 Graphical representation of the temperature distribution at 84 mm for Flame H2.

Table 49 shows the error comparison of the temperature at a height of 84 mm.

Table 49 Error comparison of the temperature at a height of 84 mm.

Radial Distance (mm)	Simulation % Error				
	1	**2**	**3**	**4**	**5**
0	8.21	3.88	4.53	9.97	8.98
4	0.64	1.10	1.35	8.14	7.98
8	11.62	6.56	5.01	6.34	4.35
12	5.31	15.74	22.16	9.04	14.93
16	200.31	21.13	10.38	193.98	198.83
AVERAGE	45.22	9.68	8.69	45.49	47.01

Table 49 shows that the polyhedral mesh, simulations 2 and 3, predicts the temperature better than the hexahedral meshes quite significantly. The average error

for the polyhedral mesh is circa 9% whilst the hexahedral meshes have errors around 45%. There seems to be negligible difference between the two combustion model variations, up to 2% difference.

Figure 73 shows the temperature distribution at 253 mm for the pure hydrogen flame. It is clear that there are negligible differences between the mesh types near the centre, with the polyhedral mesh, simulations 2 and 3, performing more accurately further afield. All mesh types have a shift in the peak temperature compared to the experimental peak. The equilibrium variant of the PPDF model, simulations 3 and 5, causes a greater peak in temperature, up to 2200 K, 200 K greater than the experimental peak. The difference between the two varieties is circa 50 K.

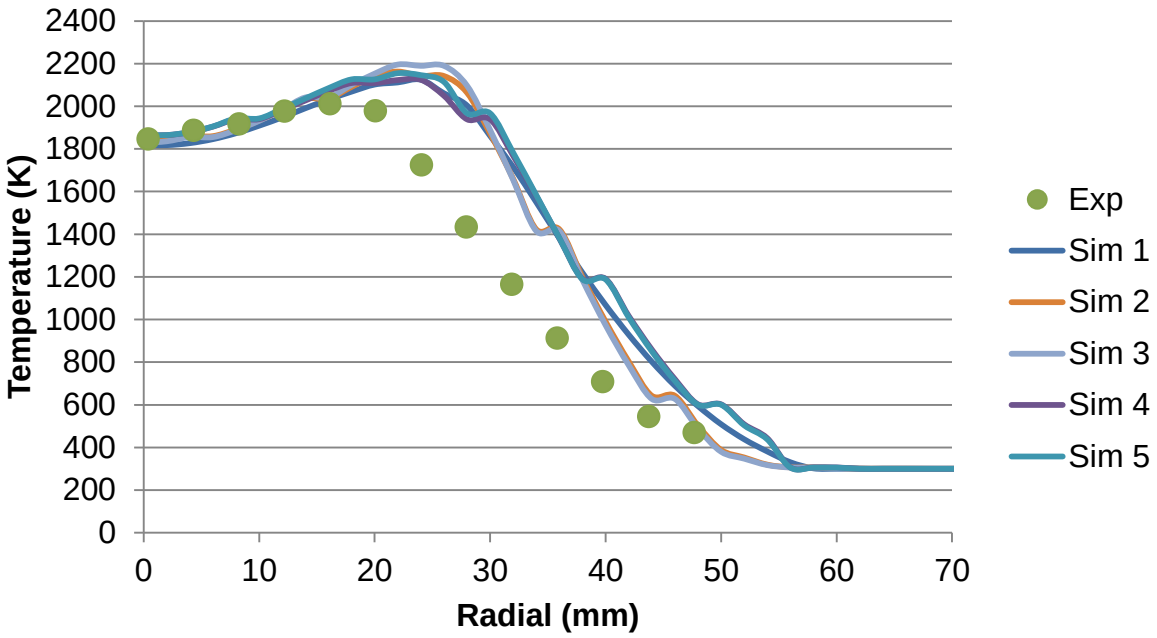

Figure 73 Graphical representation of the temperature distribution at 253 mm for Flame H2.

Table 50 shows the error comparison of the temperature at a height of 253 mm.

Table 50 Error comparison of the temperature at a height of 253 mm.

Radial Distance (mm)	Simulation % Error				
	1	**2**	**3**	**4**	**5**
0	1.45	0.60	0.90	1.04	1.03
12	1.44	0.35	0.39	0.36	0.59
24	23.20	24.18	26.96	23.18	24.42
36	51.21	55.82	54.96	51.17	51.29
48	26.56	7.09	4.23	28.35	27.95
AVERAGE	20.77	17.61	17.49	20.82	21.06

Table 50 shows that all of the simulations have an error around 19%, ± 2%. The major cause for the high errors is at heights of 24 and 36 mm. This is where the over-prediction is quite profound. The polyhedral mesh, simulations 2 and 3, predicts the temperature more accurately, around 17.5 % error, whilst the hexahedral simulations are around 21 % error. There is no discernible difference between the two combustion models yet again.

Figure 74 shows the temperature distribution at 338 mm. Once again the equilibrium variant, simulations 3 and 5, has a higher peak temperature than the flamelet variant of the PPDF model. The polyhedral meshes, simulations 2 and 3, have higher peak temperatures compared to the hexahedral meshes, simulations 1, 4 and 5. The peak temperature is approximately 100 K higher than the experimental peak temperature. The main issue is that all meshes have a radial shift, from the centre, of the peak temperature compared to the experiments. The further afield the less noticeable the differences become.

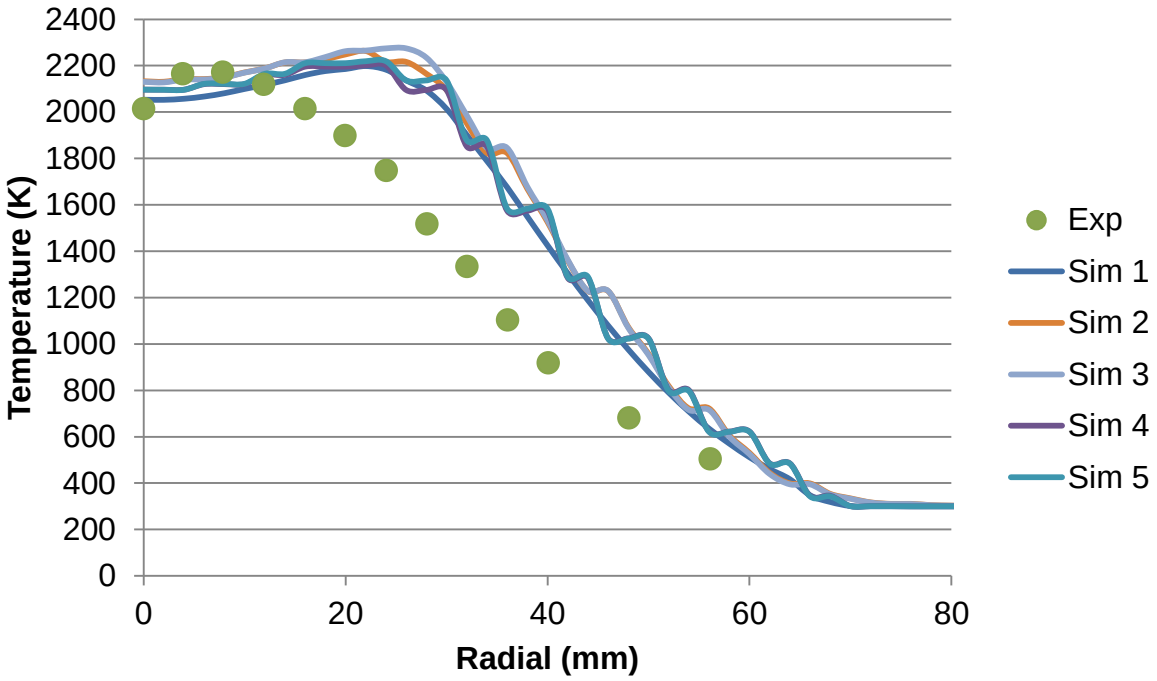

Figure 74 Graphical representation of the temperature distribution at 338 mm for Flame H2.

Table 51 compares the percentage error of the simulations for the temperature at a height of 338 mm.

Table 51 Error comparison of the temperature at a height of 338 mm.

Radial Distance (mm)	Simulation % Error				
	1	**2**	**3**	**4**	**5**
0	1.93	5.88	5.74	4.09	4.08
12	0.12	3.23	3.22	1.93	2.14
24	24.84	26.77	30.10	25.90	26.93
32	42.53	46.32	48.85	38.84	40.81
48	43.11	57.28	56.80	50.17	49.95
AVERAGE	22.51	27.90	28.94	24.19	24.78

Table 51 shows that the percentage error is around 25 %, ± 4%. The polyhedral mesh, simulations 2 and 3, is the least accurate at this height, with an error around

28 %. The uniform hexahedral mesh, simulation 1, is the most accurate with an error of 22.5 %. The other hexahedral mesh, simulations 4 and 5, has an error around 24.5 %. The combustion models show a maximum difference of 1%.

Figure 75 shows contour plots across the central plane of the temperature distribution for flame H2. It is clear that the higher temperatures are further down field compared to the higher mixture fractions, in Figure 71. There also seems to be symmetric distribution of the temperature which is due to the modelling techniques applied. The further down field of the release, the greater the increase in temperature.

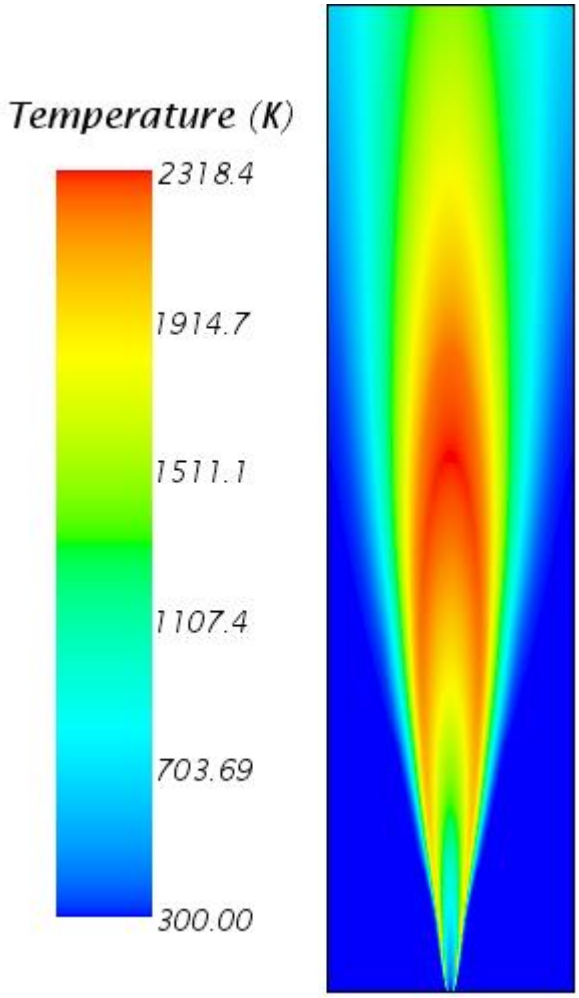

Figure 75 Planar image of the temperature distribution for Flame H2 from the polyhedral mesh.

The flamelet PPDF model performs far better than the equilibrium variation, which over predicts the temperature, by up to 200 K, at all heights. The most suitable mesh

seems to be the polyhedral shaped cells, predicting more accurately for the lower two heights.

Table 52 compares the error for the temperature at all of the heights investigated. There is an average error at the bottom of the table, which concludes the accuracy for the temperature data investigated.

Table 52 Error comparison for the temperature at all heights.

Height (mm)	Simulation % Error				
	1	**2**	**3**	**4**	**5**
84	45.22	9.68	8.69	45.49	47.01
253	20.77	17.61	17.49	20.82	21.06
338	22.51	27.90	28.94	24.19	24.78
AVERAGE	29.50	18.39	18.37	30.17	30.95

Table 52 shows that the polyhedral mesh, simulations 2 and 3, yields more accurate results than the hexahedral meshes used. This is caused by the vast difference between the predicted results at the height of 84 mm. The table shows that there is a minimal difference between the two combustion models. Although the graphs show that the equilibrium variation, simulations 3 and 5, over predicts the temperature by up to 200 K compared to the flamelet model.

The final criterion used, for validation of Flame H2, is the H_2O mass fraction. This is again portrayed in exactly the same way as the previous two criteria.

Figure 76 is the comparison of the H_2O mass fractions at 84 mm. There is a clear difference between the hexahedral, simulations 1, 4 and 5, and polyhedral meshes, simulations 2 and 3. The hexahedral meshes decay at a slower rate compared to the polyhedral mesh, which matches the experimental data accurately. All mesh types under predict the peak H_2O mass fraction, by approximately 0.02. Similar to the mixture fraction there are negligible differences between the two variations of the PPDF model.

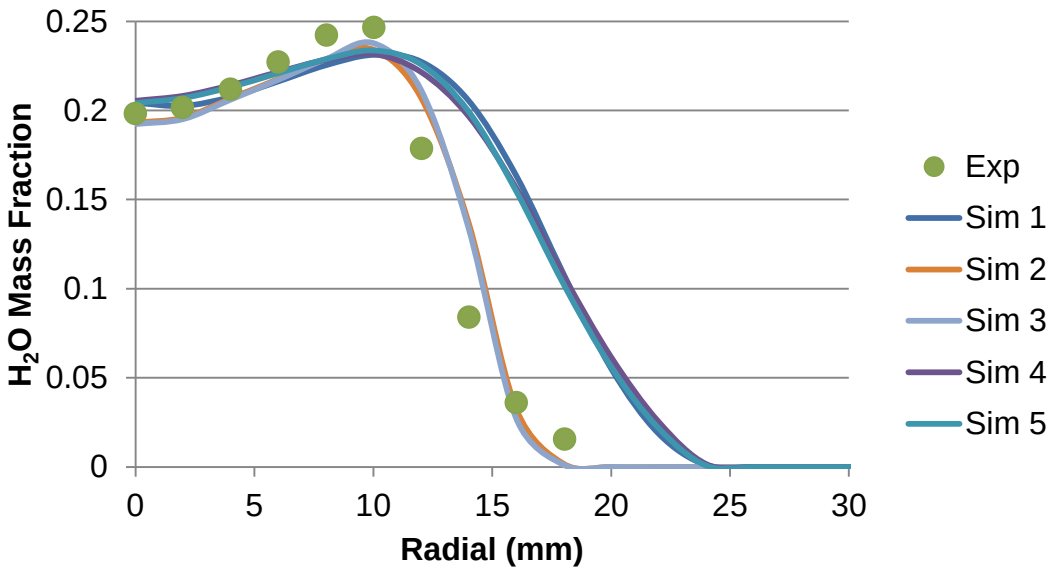

Figure 76 Graphical representation of the H_2O mass fraction distribution at 84 mm for Flame H2.

Table 53 shows the error between the simulations at various distances for the H_2O mass fractions at a height of 84 mm.

Table 53 Error comparison for the H_2O mass fraction at a height of 84 mm.

Radial Distance (mm)	Simulation % Error				
	1	2	3	4	5
0	3.01	2.60	2.99	3.58	2.92
4	2.04	2.44	2.75	1.07	0.57
8	6.99	5.59	5.59	5.73	5.60
12	27.18	15.92	18.37	23.94	26.31
16	353.15	8.93	23.75	333.56	329.08
AVERAGE	78.47	7.09	10.69	73.58	72.90

Table 53 shows that the polyhedral mesh, simulations 2 and 3, has the smallest error of circa 9%, ± 2%. Whilst the hexahedral meshes have errors around 75 %, ± 3%. This vast difference is caused by the high errors at 16 mm, which is also shown in

Figure 76. The combustion model variations show a difference of up to 3%, with the flamelet model the more accurate for the polyhedral mesh, simulation 2.

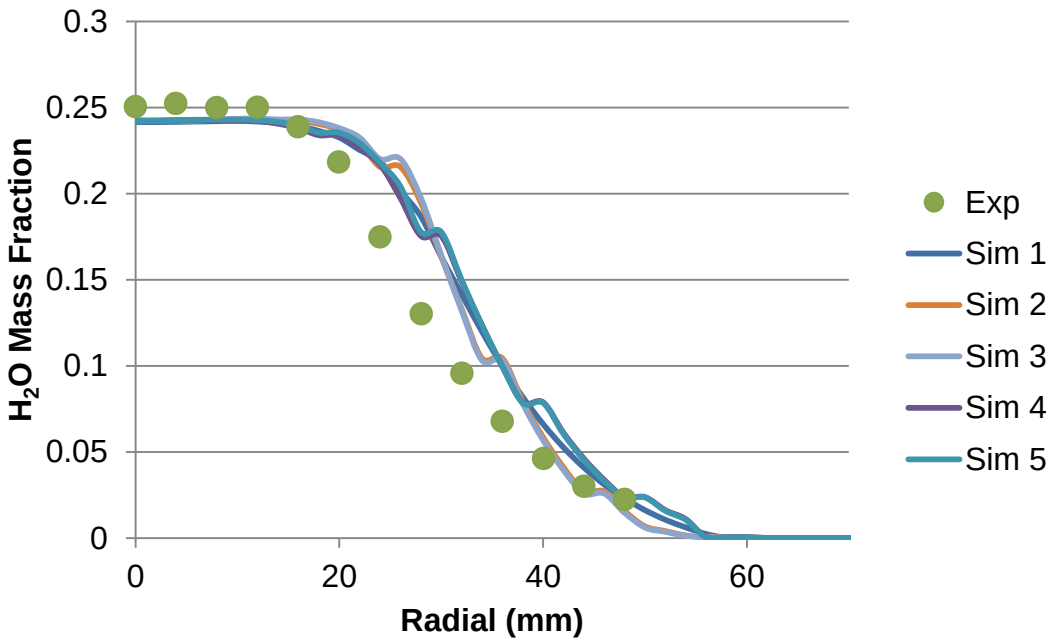

Figure 77 Graphical representation of the H_2O mass fraction distribution at 253 mm for Flame H2.

Figure 77 is the H_2O mass fraction distribution at 253 mm for the pure hydrogen flame. Near the centre of release there are no differences between the meshes or model variations. Further afield the polyhedral mesh, simulations 2 and 3, is more accurate whilst the mesh types have negligible differences in the between regions. The combustion model variation had no effect on the H_2O mass fraction.

Table 54 shows the error comparison for the H_2O mass fractions at a height of 253 mm.

Table 54 Error comparison for the H_2O mass fraction at a height of 253 mm.

Radial Distance (mm)	Simulation % Error				
	1	**2**	**3**	**4**	**5**
0	3.65	3.44	3.46	3.34	3.28
12	3.39	2.85	2.69	3.25	3.05
24	25.09	23.21	25.83	23.92	24.57
36	46.87	53.64	51.88	46.78	46.56
48	2.70	30.22	34.99	5.85	5.06
AVERAGE	16.34	22.67	23.77	16.63	16.50

Table 54 shows that the polyhedral mesh, simulations 2 and 3, is the least accurate, with an error around 23 %. The hexahedral meshes all show an error around 16 %. This difference is caused by the high errors at a distance of 48 mm for simulations 2 and 3. There is a negligible difference, maximum 1.1%, between the combustion models.

Figure 78 compares the H_2O mass fractions at 338 mm. Similar to the other heights, there are minimal differences near the centre line. The polyhedral mesh, simulations 2 and 3, has an over prediction greater than the hexahedral mesh over predictions, simulations 1, 4 and 5, circa 30 mm. Although this over prediction is no longer present further afield. There is a small difference between the two PPDF options, again circa 30 mm, however this again settles back to identical readings after 40 mm. It would seem that the flame is again wider than the experimental flame, indicative of the higher concentrations further afield.

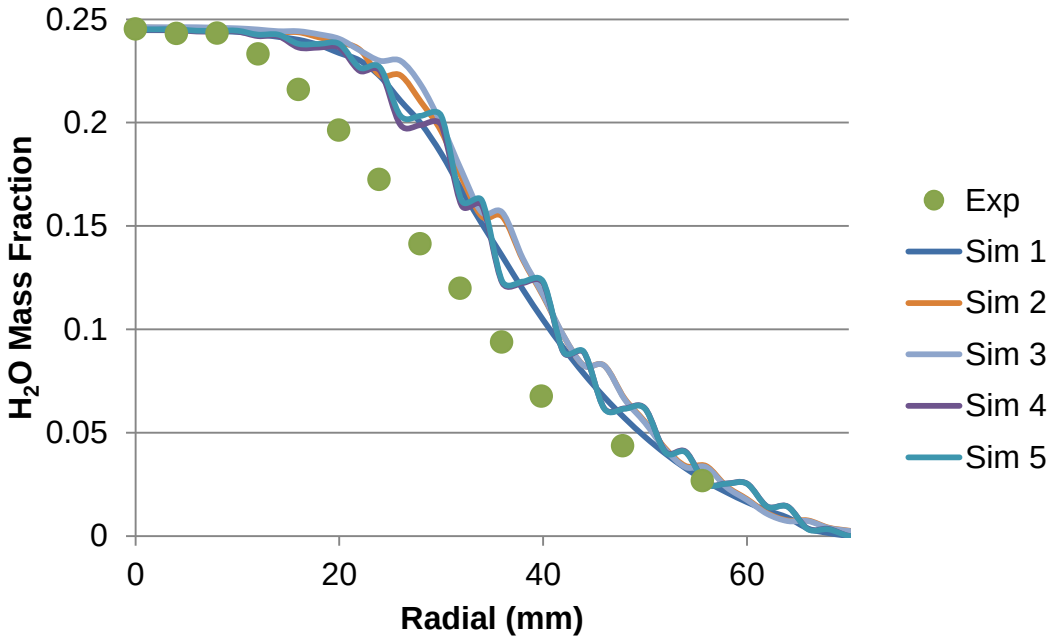

Figure 78 Graphical representation of the H_2O mass fraction distribution at 338 mm for Flame H2.

Table 55 shows the error comparison between the predicted and recorded results for the H_2O mass fractions at a height of 338 mm.

Table 55 Error comparison of the H_2O mass fractions at a height of 338 mm.

Radial Distance (mm)	Simulation % Error				
	1	2	3	4	5
0	0.24	0.29	0.38	0.16	0.08
12	4.11	4.88	5.08	3.71	4.02
24	28.81	29.13	33.20	30.37	31.28
32	39.80	44.74	47.40	33.45	35.40
48	30.55	52.09	51.24	41.25	40.85
AVERAGE	20.70	26.23	27.46	21.79	22.32

Table 55 shows that the uniform hexahedral mesh, simulation 1, gives the more accurate results with an error of 20.7 %. The polyhedral mesh, simulations 2 and 3,

produces the least accurate results with an error around 27 %. Whilst the non-uniform hexahedral mesh, simulations 4 and 5, yields an error around 22 %. This is again caused by the larger errors further from the centreline. The combustion models show a maximum error difference of less than 1.5 %.

Table 56 compares the average errors across all of the heights investigated for the H_2O mass fraction. The final row gives an average error for the H_2O mass fraction.

Table 56 Error comparison for the H_2O mass fraction for all of the heights.

Height (mm)	Simulation % Error				
	1	**2**	**3**	**4**	**5**
84	78.47	7.09	10.69	73.58	72.90
253	16.34	22.67	23.77	16.63	16.50
338	20.70	26.23	27.46	21.79	22.32
AVERAGE	38.50	18.66	20.64	37.33	37.24

Table 56 shows again that the polyhedral mesh, simulations 2 and 3, produces the most accurate results. This is caused by the severe errors that the hexahedral mesh predictions incur for the lowest height of 84 mm. There is a 1% difference between the uniform and non-uniform hexahedral meshes. Whilst the combustion models yield a maximum difference of 2%.

Figure 79 is a contour plot through the central plane of the H_2O mass fraction. The trend is similar to that of the temperature, and opposite to the mixture fraction, as expected. There are also lower levels of water around the inlet, where the jet of the release is located. This is because combustion is not present here.

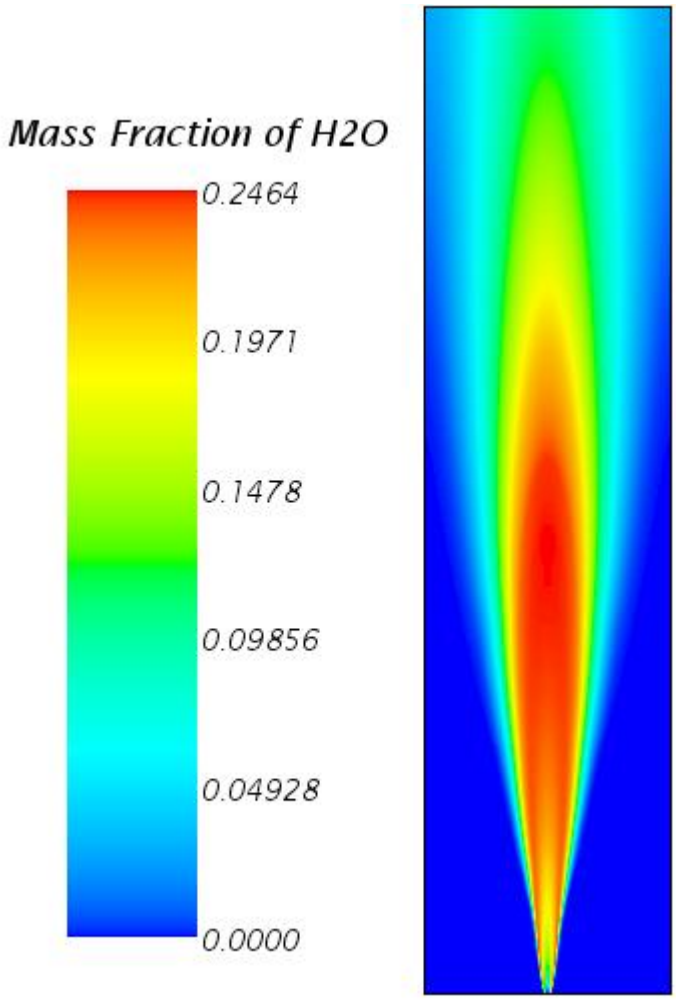

Figure 79 Planar image of the H_2O mass fraction for flame H2 polyhedral mesh.

Table 57 combines the average errors for all of the data investigated and gives a final average error for all of the simulations for this investigation.

Table 57 Error comparison for all of the data for flame H2.

Data Set	**Simulation % Error**				
	1	**2**	**3**	**4**	**5**
Mixture Fraction	56.22	19.74	20.88	51.10	49.25
Temperature	29.50	18.39	18.37	30.17	30.95
H_2O Mass Fraction	38.50	18.66	20.64	37.33	37.24
AVERAGE	41.41	18.93	19.96	39.53	39.15

Table 57 shows that the polyhedral mesh, simulations 2 and 3, is more accurate than the hexahedral meshes. This is because it predicts the behaviour at the lower heights, especially 84 mm, more accurately. Whilst the table suggests that the equilibrium PPDF model, simulation 3, is more accurate act predicting the temperature it has been shown that this model gives a greater over prediction of the recorded results. Overall there is a 1% difference between the two combustion models, simulations 2 and 3. This would suggest that when modelling pure hydrogen flames, to use the flamelet option. However, there is no inbuilt library for the hydrogen-nitrogen mixtures and therefore only the equilibrium option is employed for that flame.

7.2.3.2 Flame H2N2

The H2N2 flame is compared against experimental data for a hydrogen-nitrogen mixture flame, using the mixture fraction, temperature and H_2O mass fraction. The modelling utilises the polyhedral mesh and equilibrium variation of the PPDF model used previously. The area under investigation is the $C_{\varepsilon 2}$ coefficient of the standard k-epsilon turbulence model, as there is no recommendation for this mixture. Therefore values of 1.83 and 1.92 are used for comparison, these are the recommended value for pure H_2 flames and the default value (Hassel, 1997).

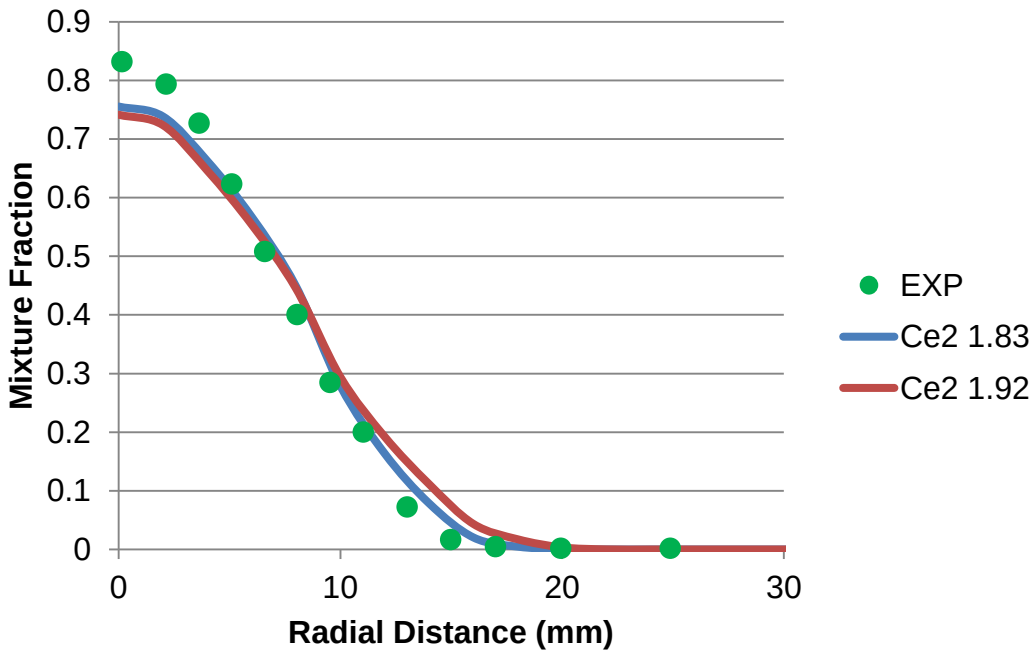

Figure 80 Mixture fraction graph for the H2N2 flame at 80 mm.

Figure 80 shows the mixture fraction distribution at 80 mm for the H2N2 flame. The graph shows that there are negligible differences between the two values of $C_{\varepsilon 2}$. The lower value is slightly more accurate than the higher value. The lower value, of 1.83, matches the experimental data very well, except for the near centre region, 0 – 5 mm.

Table 58 shows the error comparison between the coefficients at a height of 80 mm. It can be seen that the simulation with the lower coefficient predicts the results more accurately. The vast difference in the average error is due to the error at 18 mm for the larger coefficient. Otherwise the results would have been more comparable. Never the less, this creates a difference of almost 50 %.

Table 58 Error comparison of the mixture fraction at a height of 80 mm for the H2N2 flame.

Radial Distance (mm)	Coefficient % Error	
	1.83	**1.92**
0	9.20	10.88
2	6.94	8.81
10	2.21	3.19
18	0.58	257.42
20	76.75	63.56
AVERAGE	19.14	68.77

Figure 81 shows the mixture fraction distribution at 160 mm, for the hydrogen-nitrogen mixture. There is a bigger difference between the two coefficients tested compared to the lower height previously discussed. The lower coefficient, 1.83, matches the experimental data almost identically. The higher coefficient, 1.92, has an under prediction near the centre, approximately 0.05 mixture fraction lower. Then in the far field it shows a slight over prediction, although the difference is lower than the initial under prediction.

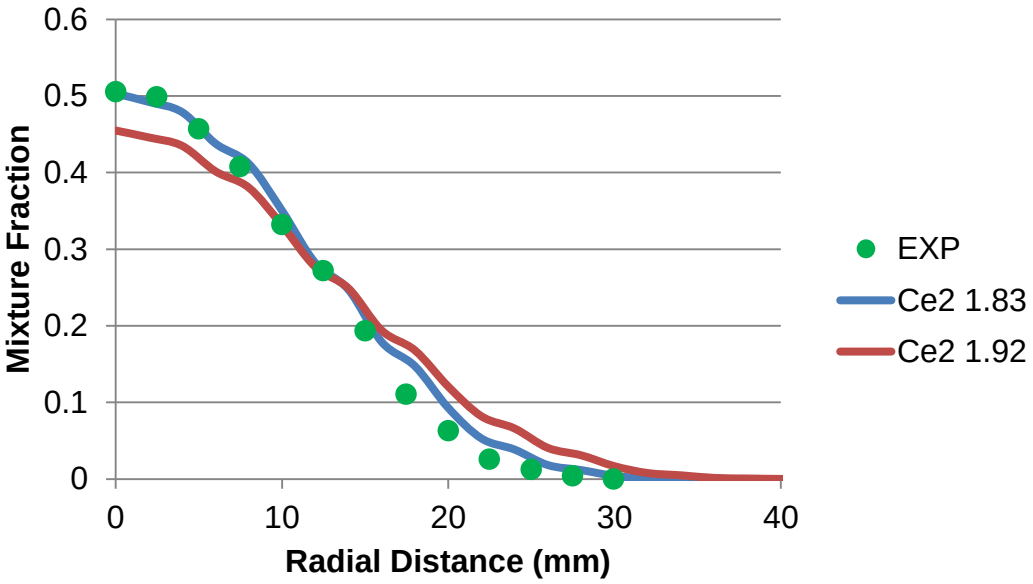

Figure 81 Mixture fraction graph for the H2N2 flame at 160 mm.

Table 59 compares the errors at a height of 160 mm.

Table 59 Error Comparison of the mixture fraction at 160 mm.

Radial Distance (mm)	Coefficient % Error	
	1.83	**1.92**
0	0.45	10.01
8	0.89	6.75
12	3.67	1.73
20	47.19	91.37
28	188.67	665.01
AVERAGE	48.17	154.97

Table 59 compares the errors for the simulations with the two different coefficients. The larger coefficient creates an average error of 155 %, although this is mainly due to a significant error at a distance of 28 mm. The simulations using the lower coefficient produced an average error of 48 %. This big error is also due to the last measurement used, of 28 mm.

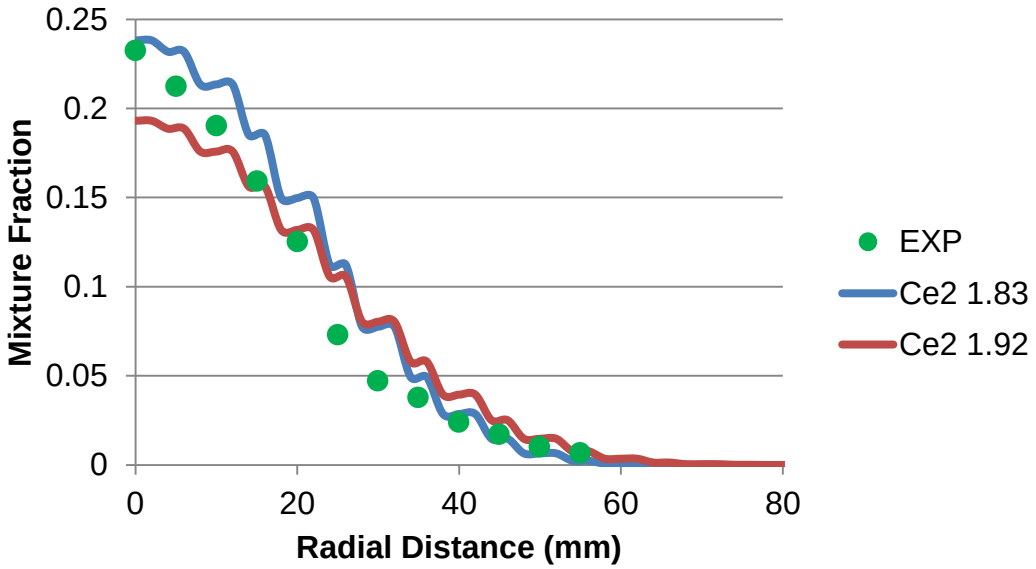

Figure 82 Mixture fraction graph for the H2N2 flame at 320 mm.

Figure 82 shows the mixture fraction comparison at 320 mm for the H2N2 flame. Similar to the previous (middle) height, there is a distinct separation between the two model coefficients. The lower value, 1.83, matches the experimental data initially, with a slight over prediction circa 20 mm before matching the data again. Whilst the higher value, 1.92, has an under prediction of 0.05 at the centre line, before transferring to a slight over prediction circa 30 mm before matching the experiment at the far field. Table 60 shows the comparison of the errors for the coefficient changes at a height of 320 mm.

Table 60 shows that the simulations are far closer in the errors compared to the previous heights. Once again the smaller coefficient yields predictions that are more accurate, 25.5 % error. The larger coefficient causes an error of 34.36 %. The large errors are due to the over prediction around the middle distance, circa 30 mm from the centre line.

Table 60 Error comparison of the mixture fraction at a height of 320 mm.

Radial Distance (mm)	Coefficient % Error	
	1.83	**1.92**
0	2.42	16.97
10	12.08	7.68
20	19.43	5.15
30	64.28	70.27
40	18.27	63.15
50	36.55	42.94
AVERAGE	25.50	34.36

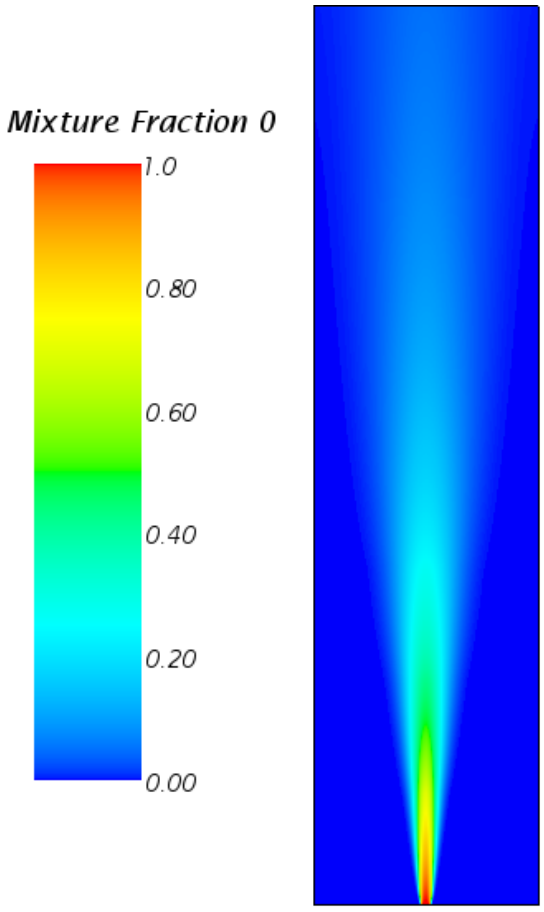

Figure 83 Planar image of the mixture fraction for the H2N2 flame for the coefficient 1.83.

Figure 83 shows a contour plot across the central plane of the mixture fraction for the hydrogen-nitrogen flame. Compared to the pure hydrogen flame (Figure 71), there is greater penetration of the mixture into the domain. This is shown by the fact that the mixture almost reaches the top of the enclosure. There is also less diffusion, which would be indicative of the nitrogen within the mixture.

Table 61 compares the errors for the mixture fraction at all heights investigated.

Table 61 Average error comparison of the mixture fractions for flame H2N2.

Height (mm)	Coefficient % Error	
	1.83	**1.92**
80	19.14	68.77
160	48.17	154.97
320	25.50	34.36
AVERAGE	30.94	86.04

Table 61 shows that using the smaller coefficient alters the turbulence levels such that the simulation is more accurate, when investigating the mixture fractions. The difference between the average errors is around 56 %. This would suggest that the turbulence levels need to be altered when investigating flames with hydrogen.

The next criteria for comparison is the temperature, this is performed at the same heights as the mixture fraction.

Figure 84 is the temperature comparison at 80 mm. Initially there are no differences between the two coefficient values, with both being marginally higher than the experiments. The peak of the lower value is more profound than the higher value, although both under predict the peak temperature. The lower value has an under prediction of 50 – 100 K whilst the higher value is circa 200 K lower. Both of the values follow the trend towards the peak temperature. The slope after the peak temperature is predicted well by the lower coefficient.

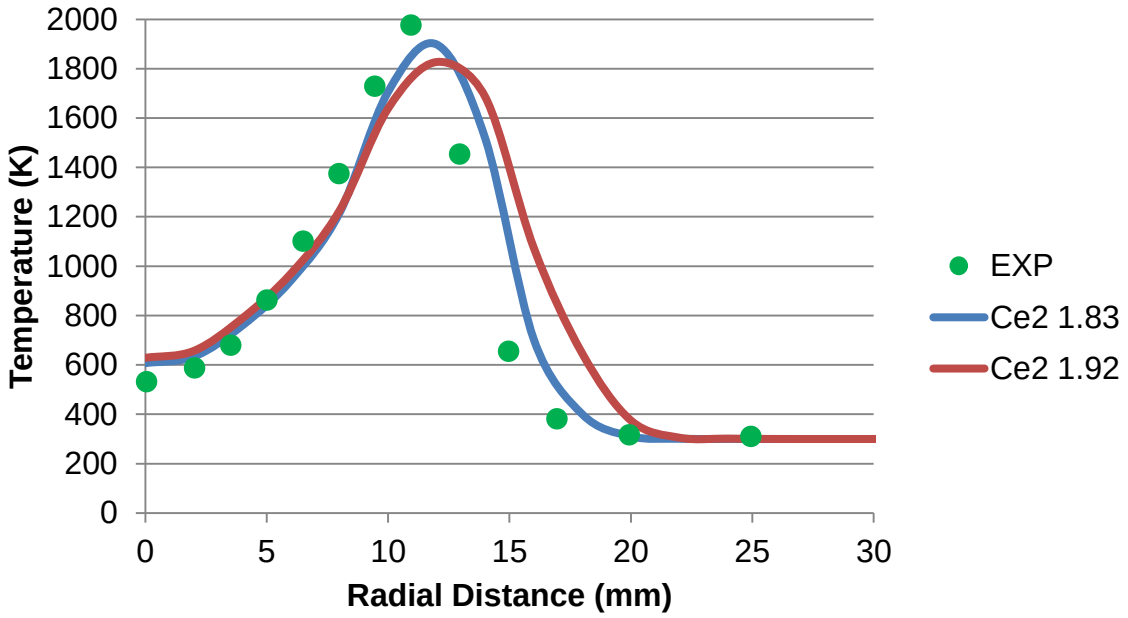

Figure 84 Temperature distribution for flame H2N2 at 80 mm.

Table 62 shows the percentage error between the results, for the two coefficients, of the temperature at a height of 80 mm.

Table 62 Error comparison for the temperature predictions at a height of 80 mm.

Radial Distance (mm)	Coefficient % Error	
	1.83	**1.92**
0	14.07	18.10
2	7.74	11.74
10	1.32	5.23
18	4.76	69.09
20	2.01	18.31
AVERAGE	5.98	24.49

Table 62 shows that the lower coefficient alters the turbulence levels such that the predicted results are far more accurate. The error for the results using the smaller coefficient is 6 %, compared to 24.5 % for the larger coefficient. This greater error is due to the inaccuracy further afield from the centre line, especially at 18 mm.

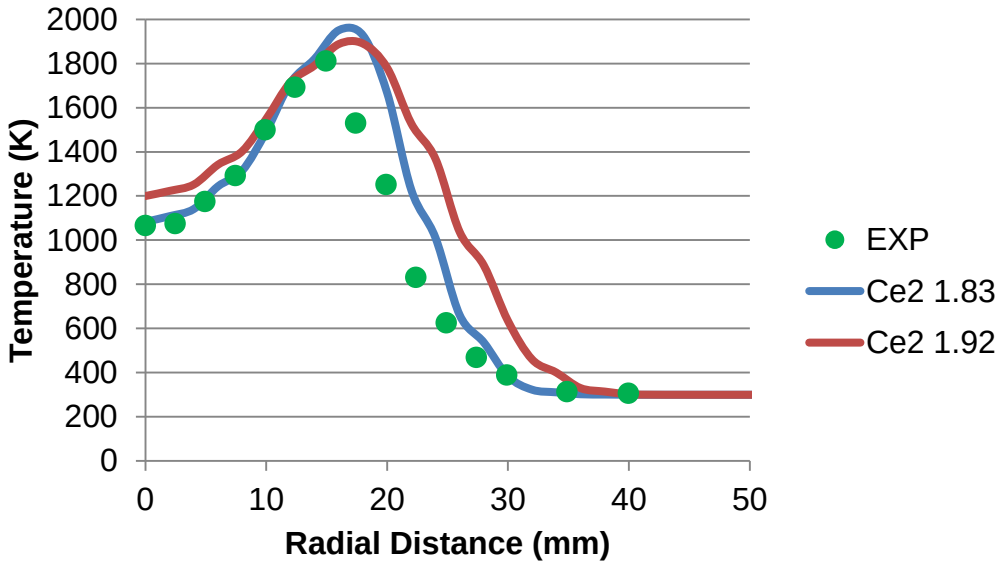

Figure 85 Temperature distribution for flame H2N2 at 160 mm.

Figure 85 shows the temperature distribution at 160 mm. Unlike the lower height, there is a distinct difference between the two coefficient values at the centre line. The higher value over predicts compared to the lower value which matches the experimental values. The peak temperatures are over predicted at this height, compared to the lower height of 80 mm. The lower coefficient over predicts by almost 200 K whilst the higher value is circa 100 K above the experimental peak. The simulation peak temperatures are shifted away from the experimental slightly. The lower coefficient follows a similar trend to the experiment, regarding the decline after the peak. Similar to the lower height, all curves are aligned before the final experimental point, at 40 mm from the centre.

Table 63 shows the error comparison for the predicted temperatures at a height of 160 mm.

Table 63 Error comparison for the predicted temperature results at 160 mm.

Radial Distance (mm)	Coefficient % Error	
	1.83	**1.92**
0	1.55	12.52
8	1.71	8.52
12	1.15	1.34
20	33.10	42.16
28	14.48	88.80
AVERAGE	10.40	30.67

Table 63 shows that the turbulence levels using the smaller coefficient are altered such that the results are more accurate, by 20%. The average error for the smaller coefficient is 10.4 %, whilst the larger coefficient creates a larger error, 30.67 %. Both simulations have a high error around 20 mm from the centre line, whilst the greater coefficient has an even larger error at a distance of 28 mm.

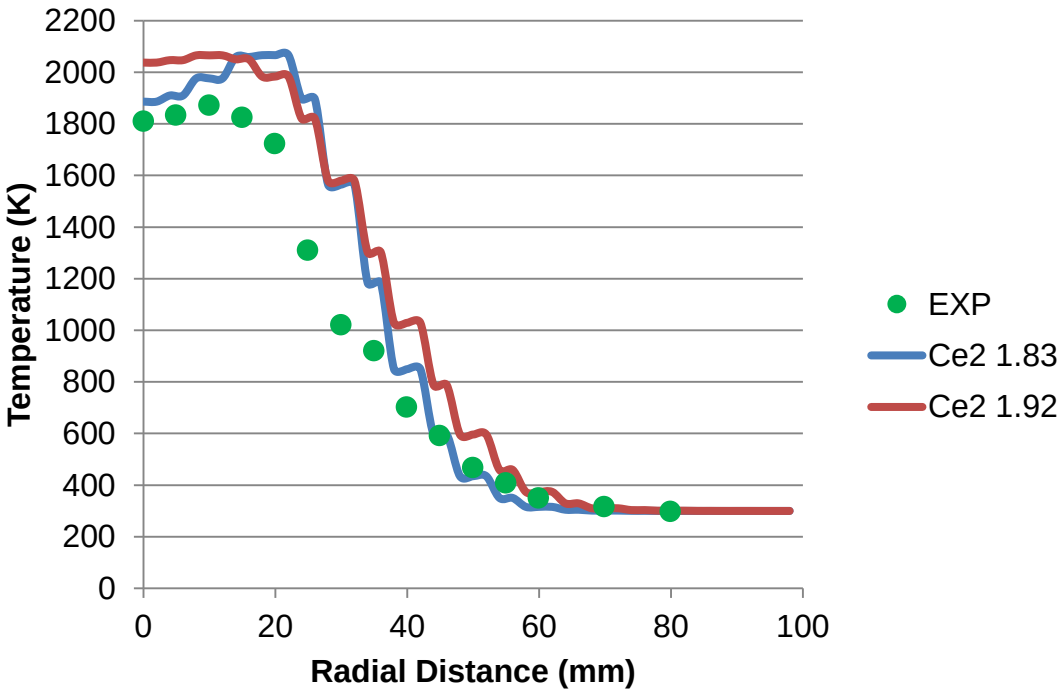

Figure 86 Temperature distribution for flame H2N2 at 320 mm.

All curves converge to the same temperature measurements by 60 mm from the centreline. The lower coefficient shows the temperature reduces at a faster rate compared to the higher value, reaching the experimental curve by 35 mm from the centreline. Table 64 shows the error comparison for the predicted temperatures at a height of 320 mm.

Table 64 Error comparison for the predicted temperatures at a height of 320 mm.

Radial Distance (mm)	Coefficient % Error	
	1.83	**1.92**
0	4.15	12.51
10	5.52	10.28
20	19.81	15.01
30	53.05	54.54
40	20.77	46.29
50	7.21	27.24
AVERAGE	18.42	27.65

Table 64 shows that once again the smaller coefficient alters the turbulence levels such that the simulation predicts the temperatures better. The lower coefficient has an average error of 18.42 %, whilst the larger coefficient has an error of 27.65 %. Both simulations have large errors around 30 mm from the centre line. The lower coefficient is more accurate closer to the centre line.

Figure 87 shows contour plots across the central plane of the temperature distribution for the H2N2 flame. The temperature distribution is more concentrated to the centre of the enclosure compared to the pure hydrogen flame, whilst the maximum temperature is lower as well. This is to be expected with the addition of nitrogen. The pure hydrogen flame reaches a peak temperature of 2318.4 K compared to the 2196.2 K observed for the diluted flame. The temperature

distribution at the exit of the enclosure is less for the diluted flame compared to the pure flame. Similar to the mixture fraction, the diluted flame seems to penetrate further into the enclosure compared to the pure hydrogen flame.

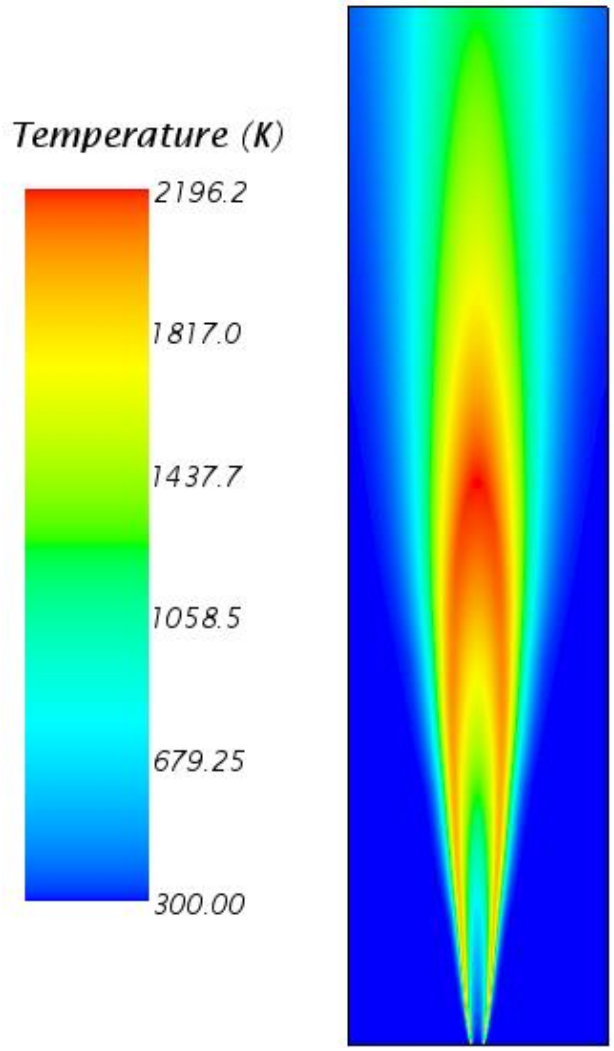

Figure 87 Planar image of the temperature distribution for flame H2N2 for the coefficient 1.83.

Table 65 contains the average errors of the predictions for the temperatures at all heights.

Table 65 shows that the smaller coefficient alters the turbulence levels such that the predicted temperatures are more accurate. The average error is 11.6 % compared to the larger coefficient which results in an error of 27.6 %. The lower height, of 80 mm, is predicted more accurately than the other levels.

Table 65 Average error comparison for the temperatures across all of the heights.

Height (mm)	Coefficient % Error	
	1.83	**1.92**
80	5.98	24.49
160	10.40	30.67
320	18.42	27.65
AVERAGE	11.60	27.60

The final criterion for analysis is the H_2O mass fraction, again at the same heights as before.

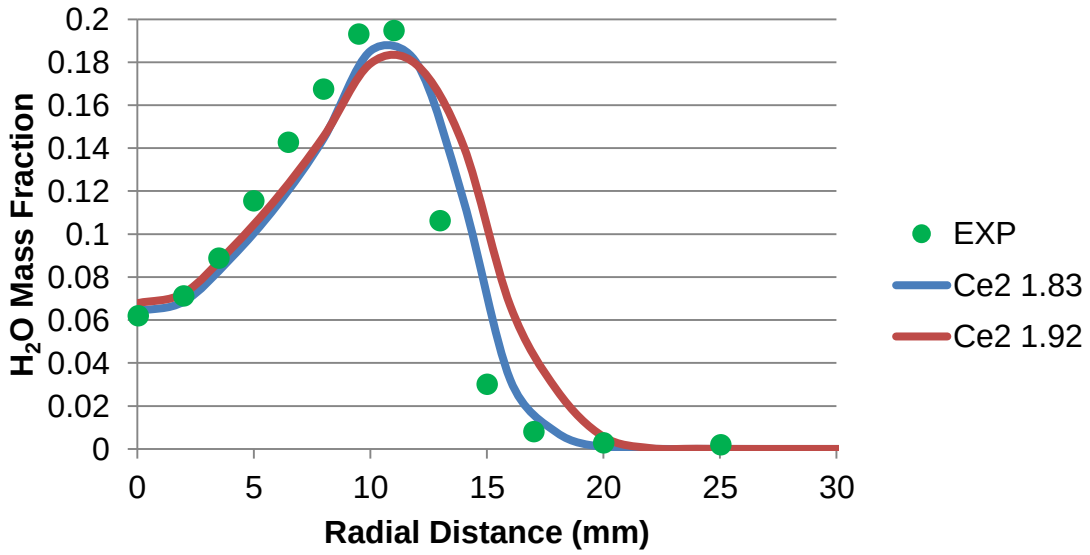

Figure 88 H_2O mass fraction distribution at 80 mm for flame H2N2.

Figure 88 shows the H_2O mass fraction distribution at 80 mm. The centreline shows minimal differences between the two values of the coefficients. After 5 mm there is separation between the numerical and experimental results. The peak mass fractions are all similar with the lower coefficient closer to the experimental although still under predicting slightly, approximately 0.005 below the experimental peak. The higher coefficient is approximately 0.015 below the experimental peak. The smaller coefficient is far closer to the experimental curve than the larger value used.

Table 66 shows the comparison of the predicted H_2O mass fractions at a height of 80 mm.

Table 66 Error comparison for the predicted H_2O mass fractions at 80 mm.

Radial Distance (mm)	Coefficient % Error	
	1.83	**1.92**
0	3.37	9.28
2	3.70	1.78
10	4.08	7.12
18	5.12	240.15
20	71.77	98.82
AVERAGE	17.61	71.43

Table 66 shows that the smaller coefficient alters the turbulence such that the simulation results are more accurate, creating an average error of 17.61 %. The results using the larger coefficient have an average error of 71.43 %. This vast difference is caused by the inability to replicate the recorded results further afield from the centre line, especially at 18 mm.

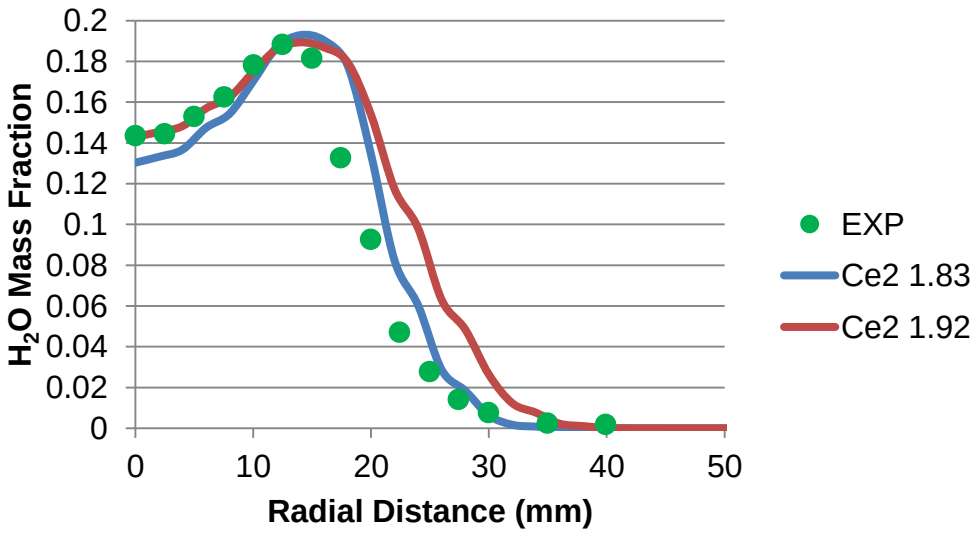

Figure 89 H_2O mass fraction distribution for flame H2N2 at 160 mm.

Figure 89 shows the radial H_2O mass fraction distribution at 160 mm above the release. Here, the centreline shows that the higher value of the coefficient matches the experimental curve better than the under predicting smaller coefficient. The peak mass fractions seem to all coincide at 0.19 for the experiment and both simulations. The predicted mass fractions do decrease slower than the recorded mass fractions. The lower coefficient matches the experimental trend far better than the higher coefficient. Similar to all of the previous graphs, all the data agree well at 35 mm for this criterion. Table 67 shows the errors for the predicted H_2O mass fractions at a height of 160 mm.

Table 67 Error comparison for the predicted H_2O mass fractions at 160 mm.

Radial Distance (mm)	**Coefficient % Error**	
	1.83	**1.92**
0	9.23	0.40
8	5.11	0.10
12	0.83	1.28
20	44.70	65.69
28	29.97	241.81
AVERAGE	17.97	61.86

Table 67 shows that again the smaller coefficient alters the turbulence levels such that predicted H_2O mass fractions are more accurate, with an average error of 18 %. The predictions with the larger coefficient have an average error of almost 62 %. Yet again this vast difference is caused by poor predictions further from the centre line, especially at 28 mm. The errors near the centre line suggest that the larger coefficient is more accurate.

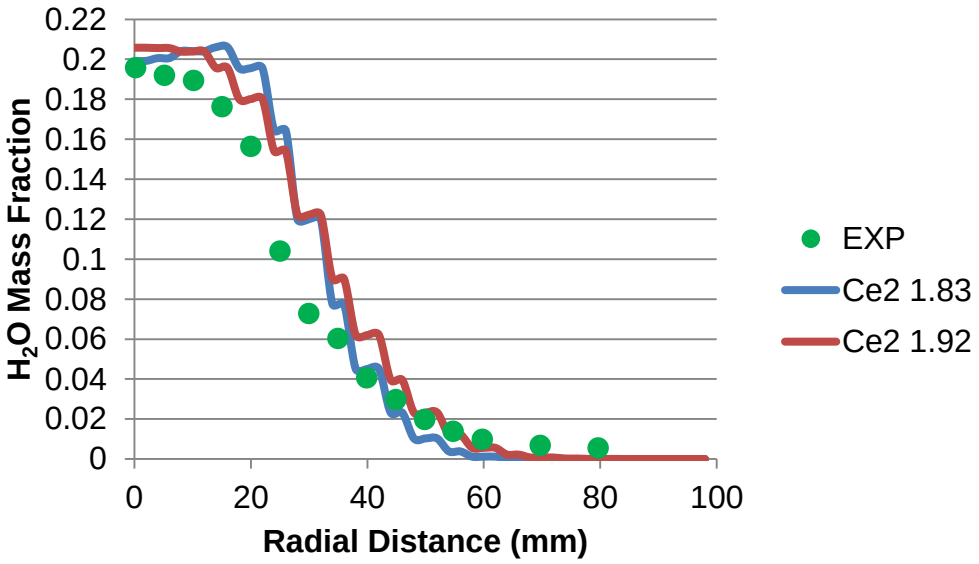

Figure 90 H_2O mass fraction distribution at 320 mm for flame H2N2.

Figure 90 depicts the radial H_2O mass fraction distribution at 320 mm. The experimental peak is at the centreline, with a value of 0.2. The predicted results using the smaller coefficient share the same reading at the centreline, whilst the predicted results for the greater coefficient have a slight over prediction. The predicted results for the larger coefficient show a peak at the centreline. The other coefficient shows a peak mass fraction approximately 20 mm from the centreline. The results for the greater coefficient decrease quicker around 20 mm although it does not rise from the centreline. The smaller coefficient predictions reduce quicker from the peak that it reaches. The lower coefficient prediction aligns with the experimental data by 35 mm, whilst the other prediction aligns around 45 mm from the centreline.

Table 68 gives the error comparison of the predicted H_2O mass fractions at 320 mm.

Table 68 shows that there is a negligible difference between the predicted H_2O mass fractions, just 1.32 % separates the average errors. Both of the predicted results have large errors, above 60%, midway from the centre line, 30 mm.

Table 68 Error comparison for the predicted H_2O mass fractions at 320 mm.

Radial Distance (mm)	Coefficient % Error	
	1.83	**1.92**
0	1.70	5.07
10	7.76	7.66
20	25.06	15.18
30	64.85	67.90
40	11.06	52.74
50	47.78	17.60
AVERAGE	26.37	27.69

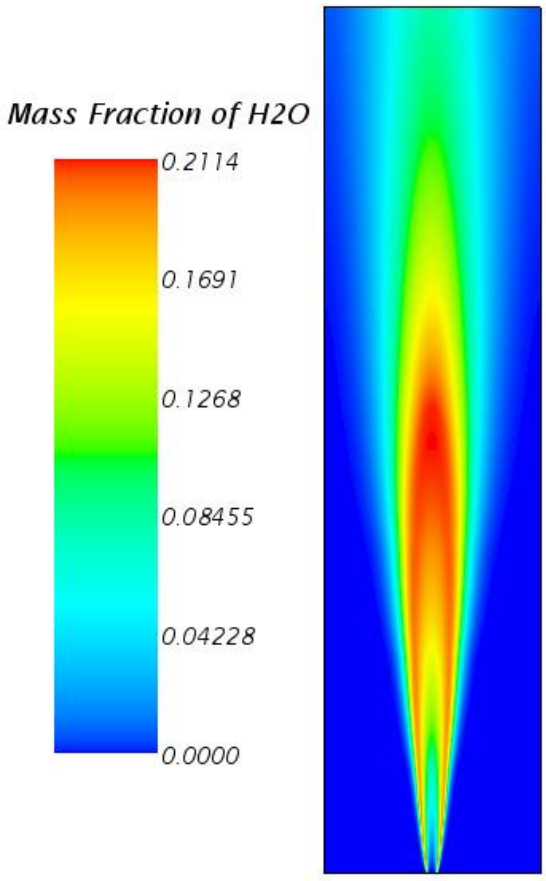

Figure 91 H_2O mass fraction planar image for flame H2N2 for the coefficient 1.83.

Figure 91 shows the contour plots across the centre for H_2O mass fraction distribution for the diluted flame. The first observation is that the maximum water mass fraction is lower for the diluted flame (0.2114) compared to the pure hydrogen flame (0.2464). This is expected due to the lower amount of hydrogen available. Similar to all the other images for the hydrogen-nitrogen mixture, there is greater penetration into the enclosure compared to the pure hydrogen flame. It also seems that the pure hydrogen flame is longer than the diluted flame.

Table 69 compares the average errors of the predicted H_2O mass fractions at all of the heights investigated.

Table 69 Error comparison of the average predicted H_2O mass fractions at all heights.

Height (mm)	Coefficient % Error	
	1.83	**1.92**
80	17.61	71.43
160	17.97	61.86
320	26.37	27.69
AVERAGE	20.65	53.66

Table 69 shows that the smaller coefficient produces a better representation of the turbulence levels and as such more accurate H_2O mass fractions, an average error of 20.65 %. This is 33 % smaller than the corresponding value for the greater coefficient. This is caused by the poor predictions at the lower heights, 80 and 160 mm, compared to the smaller coefficients.

Table 70 shows the errors for all of the predicted results for the H2N2 flame.

Table 70 Overall error comparison for the H2N2 flame.

Data Set	Coefficient % Error	
	1.83	**1.92**
Mixture Fraction	30.94	86.04
Temperature	11.60	27.60
H2O Mass Fraction	20.65	53.66
AVERAGE	21.06	55.77

Table 70 shows that using the smaller coefficient creates a more realistic representation of the turbulence levels, the average error for the H2N2 flame is 21 %. This is almost 35 % lower than the corresponding value for the larger coefficient. This is due to the change in the turbulence decay that is associated with the coefficient. This seems to be necessary for flames that involve hydrogen greater than 50%, as explained by work within the TNF network (Hassel, 1997).

The addition of diluent, nitrogen, decreases the temperature. The diluted jet penetrates into the enclosure more than the pure jet. This is even with a decreased velocity and increased pipe radius. This is due to the decrease in diffusion due to the presence of nitrogen, in the diluted flame.

7.3 Conclusion

This chapter has utilised the PPDF model for non-premixed combustion against published data. Firstly, various meshes have been investigated alongside the two variations of the combustion model available. This was followed by a further investigation into the $C_{\varepsilon 2}$ coefficient, which uses the mesh suggested from the first work, as it is suggested that this coefficient needs to be adjusted to capture the turbulence decay appropriately.

The mesh study shows that using a non-uniform polyhedral mesh produces more accurate results, as shown in Table 57. The polyhedral mesh gives an overall error

20 % lower than the other meshes under investigation. This arises from better predictions at lower heights. The average error between the two combustion models is negligible, although the equilibrium variation over predicts the peak temperature more than the flamelet variation.

The second study investigating the alteration of a turbulence model coefficient utilises the polyhedral mesh suggested before. The coefficient investigation is performed to give confidence in the alteration of the coefficient. The investigation utilised data for a diluted hydrogen flame, which did not have a suggested value. Changing the coefficient from the default value alters the turbulence levels such that the predictions are almost 35 % more accurate.

This gives confidence in the simulation methodology for further investigation, which is in the following chapter.

Chapter 8 – Modelling of Reacting Scenarios

8.1 Introduction

This chapter utilises the results of the previous two chapters, in two separate studies. The first is an investigation into non-premixed combustion within a geometry that resembles a residential garage. This utilises data from experiments performed at HSL. The other investigation is for premixed combustion within a geometry that resembles a residential garage.

The non-premixed combustion is investigated due to the geometrical resemblance with a residential garage. The experiments used, were performed as part of the Hyindoor project (Jallais et al., 2014). These experiments investigate hydrogen jet flames within a partially enclosed geometry, which is similar to that used previously in section 4.3. The modelling strategies employed use the suggestions from Chapter 7.

The premixed combustion is investigated to determine the potential outcomes from the ignition of a homogeneous hydrogen-air mixture within a residential garage. This is a likely scenario to occur, as shown in Chapter 5, when there is a strong wind. This may also occur if the vents were to become blocked. The geometry used is similar to that of Chapter 5, with and without the presence of an obstacle. The obstacle in question is a vehicle. The modelling for this scenario utilises the outcomes from Chapter 6.

The chapter is split between non-premixed modelling of the HSL experiments and premixed modelling of the garage scenario. Each section contains the geometrical configurations, and experimental details for the HSL case, followed by the numerical implementation. After this are the analysis criteria, then the results for the problems.

8.2 Non-Premixed – HSL Data

This work is performed to determine the potential harm to people if a release was to ignite and become a jet flame. The work follows on from that in Chapter 7.

8.2.1 Geometrical Configuration

The HSL experiments were performed externally, using a similar set up to that discussed previously. The burner is located at the centre of the enclosure near the floor, with a pilot light used for ignition. The geometry has various vents that may be utilised, alongside different release rates for investigations. The aim for the experiments is to investigate the flame dynamics under various conditions.

The configuration used is identical to that in section 4.3, as seen in Figure 92.

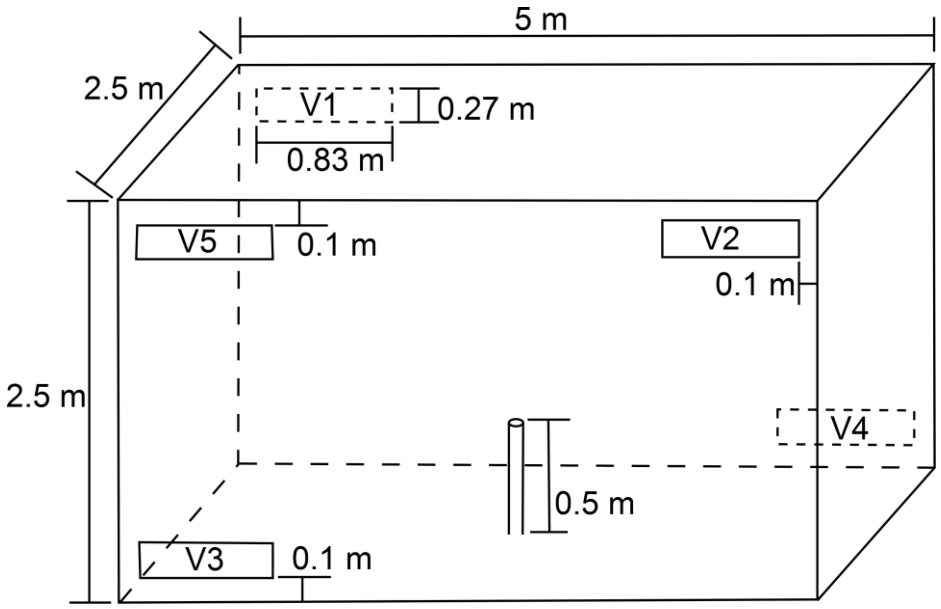

Figure 92 Diagram of the HSL experimental chamber.

Two different release rates were used for different ventilation configurations. A slower release of 0.2 g/s, with vent 1 (V1) open (Hooker et al., 2015), as well as a quicker release of 0.878 g/s with vents 1 and 3 (V1 and V3) open (Hooker, 2014). The temperature was recorded using 24 type K thermocouples.

Figure 93 shows the locations of all 24 type K thermocouples that are used for temperature measurements during the experiments. The experimental data is given as layer averages for the different heights. The slower release has experimental data for the time frame 0 – 1000 seconds, whilst the quicker release has the time frame of 200 – 1000 seconds. The presence of atmospheric conditions is not mentioned and must therefore be ignored. However, the initial temperature, 283 K, can be deduced from the start temperature of the thermocouples for the slower release experiment. It

is then inferred that the temperature is similar and thus is not changed for the quicker release experiments.

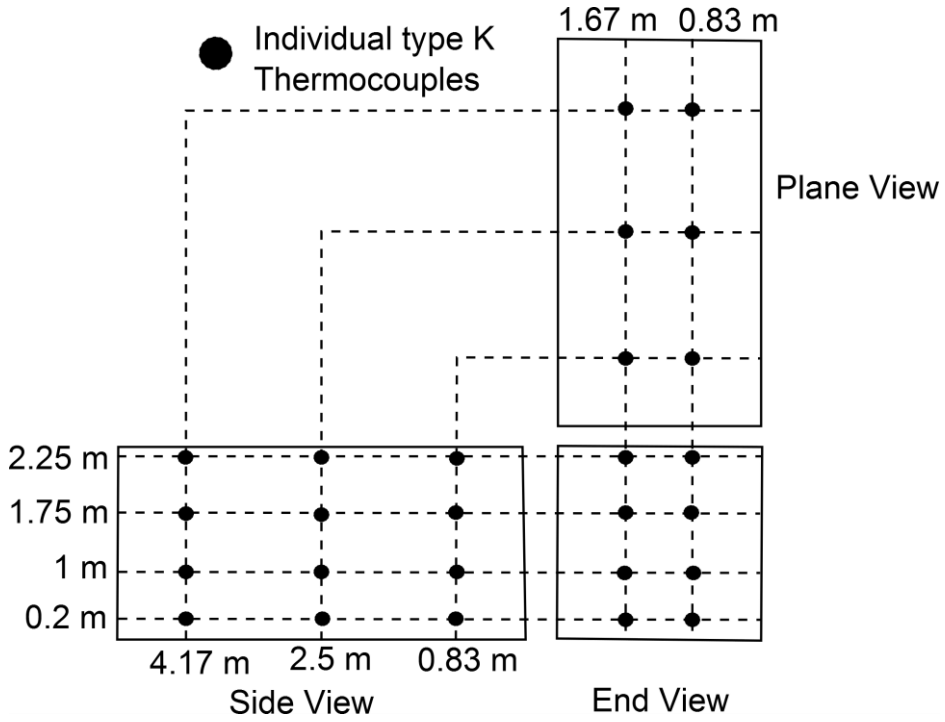

Figure 93 Thermocouple positions for the HSL reacting experiments (Hooker et al., 2015).

8.2.2 Numerical Implementation

The numerical implementation is similar to that of Chapter 7. The combustion model used is the recommended flamelet variant of the PPDF model, in section 3.4.3.2. The standard k-epsilon turbulence model is used due to the reasoning explained previously in Chapter 7. The major difference between the modelling employed here and that of Chapter 7 is that previously it was assumed to be steady state. This time the models are all transient, due to the nature of the scenarios that are being investigated. The mesh is identical to that used for the non-reacting validation in section 4.3. The time step used is 0.005 seconds for both flames. The walls are treated as a fixed temperature of 283 K, this is due to the thermal inertia within the steel structure, with the no-slip condition. The inlet is a mass flow inlet with the corresponding flow rates for the experiments. Vents are treated as interfaces, such that no boundary conditions are applied to them. The outer domain has pressure outlet on all of the boundaries.

8.2.3 Analysis Criterion

The criterion for the non-premixed combustion is the temperature. The predicted temperature at the various sensors is averaged for each height of the sensors. This is then compared against the recorded average temperatures for the corresponding heights.

8.2.4 Results

The results are given for the slower release, 0.2 g/s, and then the quicker release, 0.878 g/s. The slower release consists of predicted and recorded average temperatures at three different heights, for the time frame of 0 – 1000 seconds. The quicker release rate consists of the predicted and recorded average temperatures at the same heights, although the timeframe is 200 – 1000 seconds.

The results, using graphical representations, for the slower release are given along with the analysis.

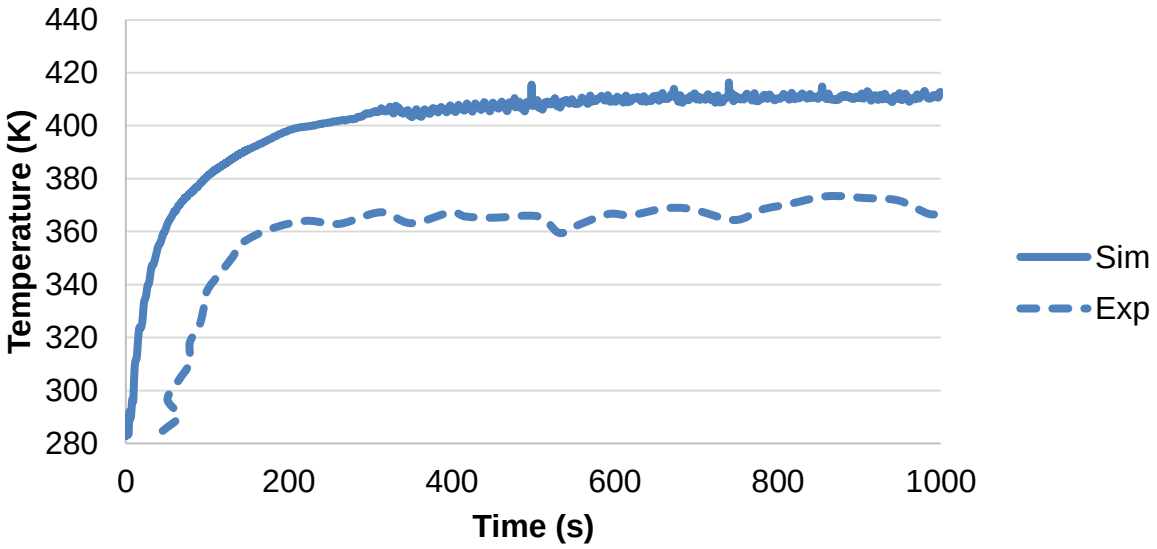

Figure 94 Average temperatures at a height of 2.25 m for the 0.2 g/s HSL validation.

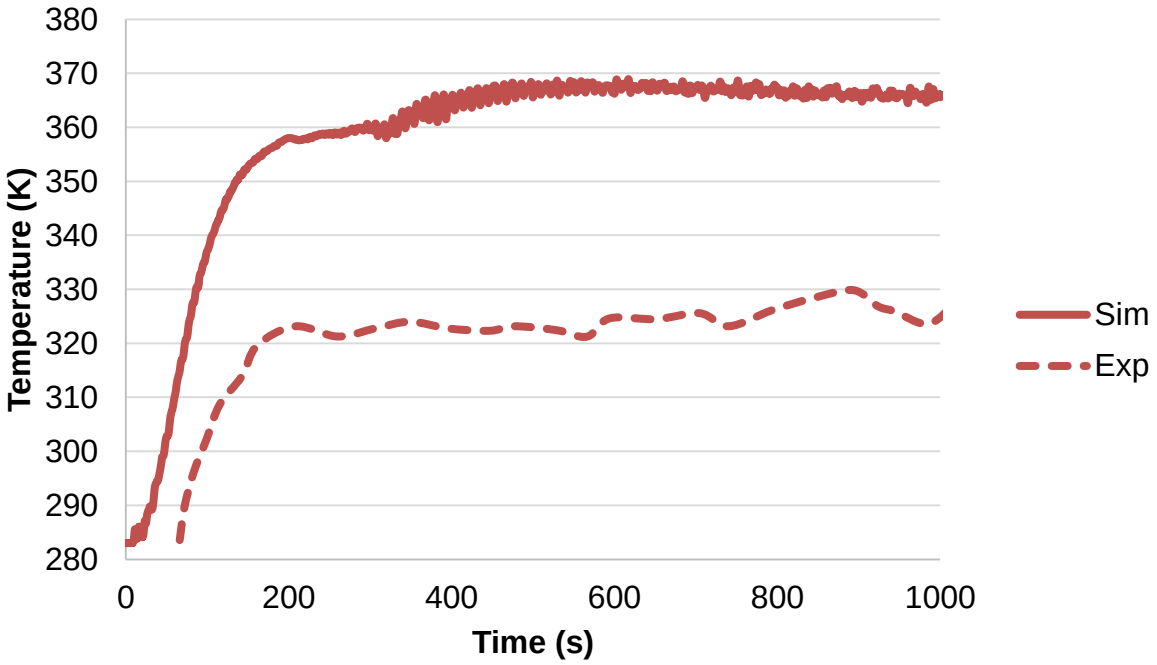

Figure 95 Average temperatures at a height of 1.75 m for the 0.2 g/s HSL validation.

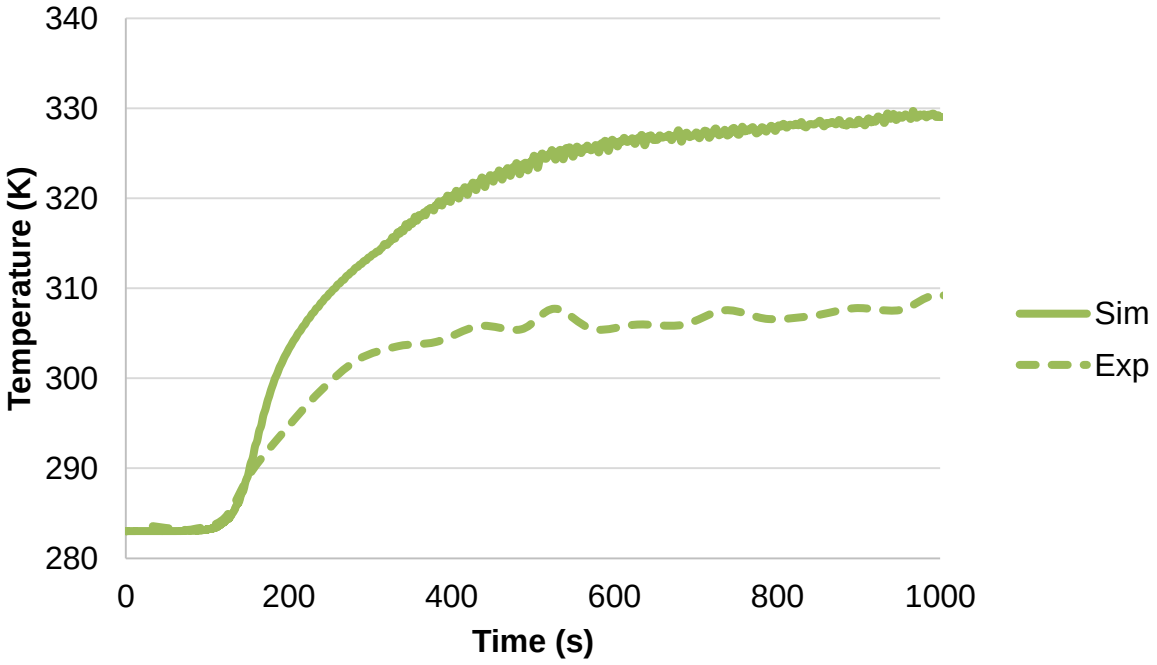

Figure 96 Average temperatures at a height of 1.00 m for the 0.2 g/s HSL validation.

Figure 94 – Figure 96 shows the average temperature comparisons, between the predicted and recorded results, at the different heights for the 0.2 g/s release rate. The predicted results are all over-predictions compared to the recorded results (Hooker et al., 2015). The maximum over-prediction is around 40 K, at the upper layer of 2.25 m, Figure 94. The next layer, Figure 95, shows a predicted over-

prediction circa 40 K. The lowest layer shown, Figure 96, again shows an over-prediction, although this is circa 20 K.

The predicted temperatures during the initial phases of the combustion differ, especially at the upper height of 2.25 m and to a lesser extent at 1.75 m. The predicted temperatures at these heights show almost instantaneous temperature rises compared to delayed increases in the recorded results. This is because the combustion model used does not have an ignition model and as such means that the combustion process cannot be delayed. This would happen in the experiments as the pilot light would need to ignite the diffusion flame caused by the hydrogen release.

The next results are for the quicker release rate. Again the results, in graph form, are given first followed by the analysis.

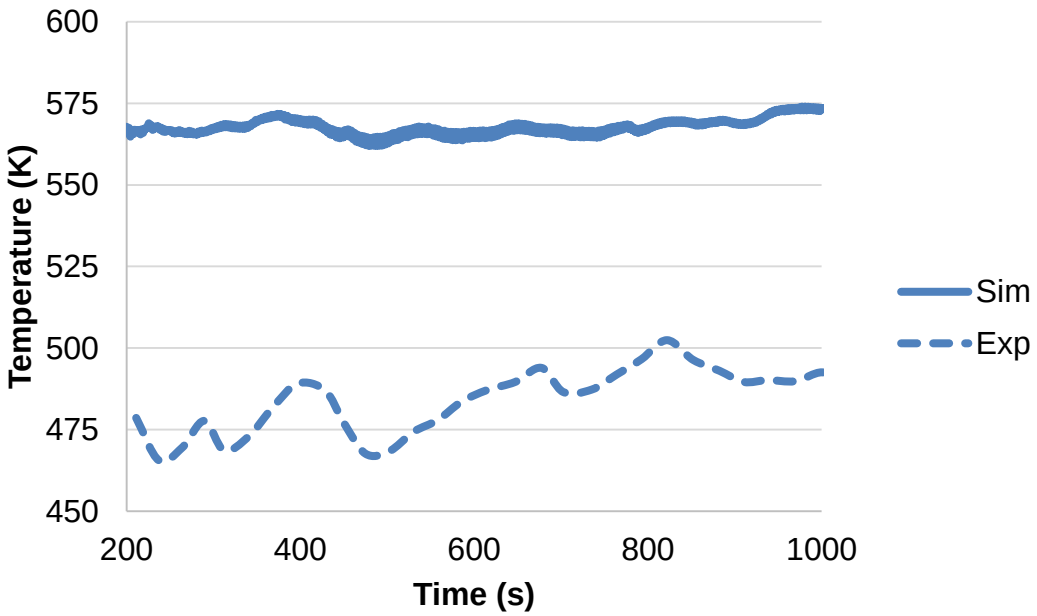

Figure 97 Average temperatures at a height of 2.25 m for the 0.878 g/s HSL validation.

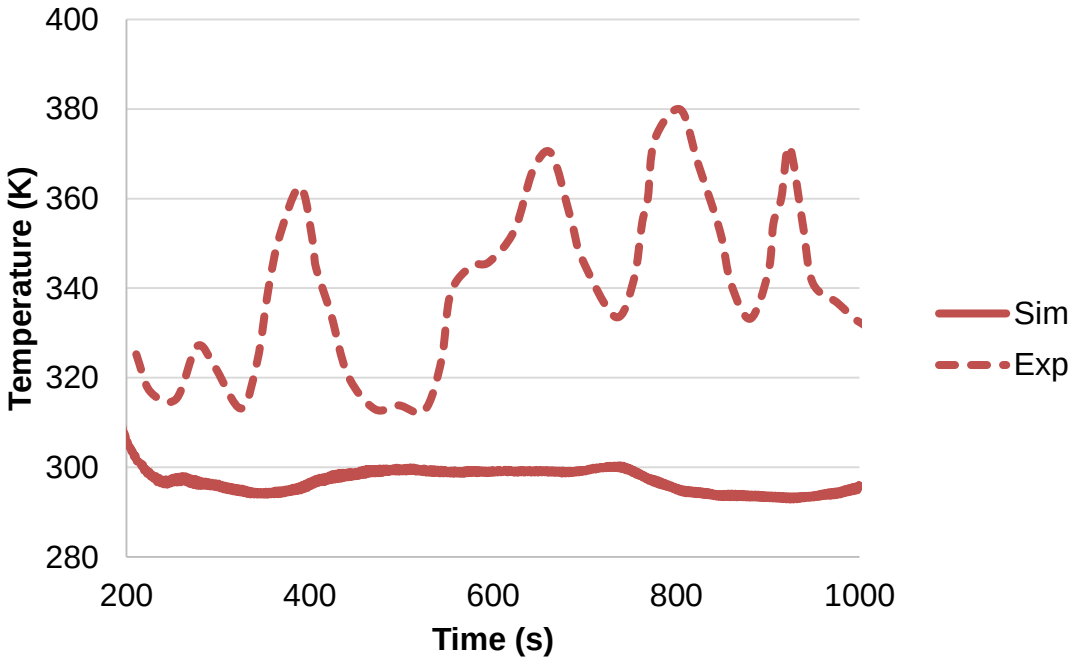

Figure 98 Average temperatures at a height of 1.75 m for the 0.878 g/s HSL validation.

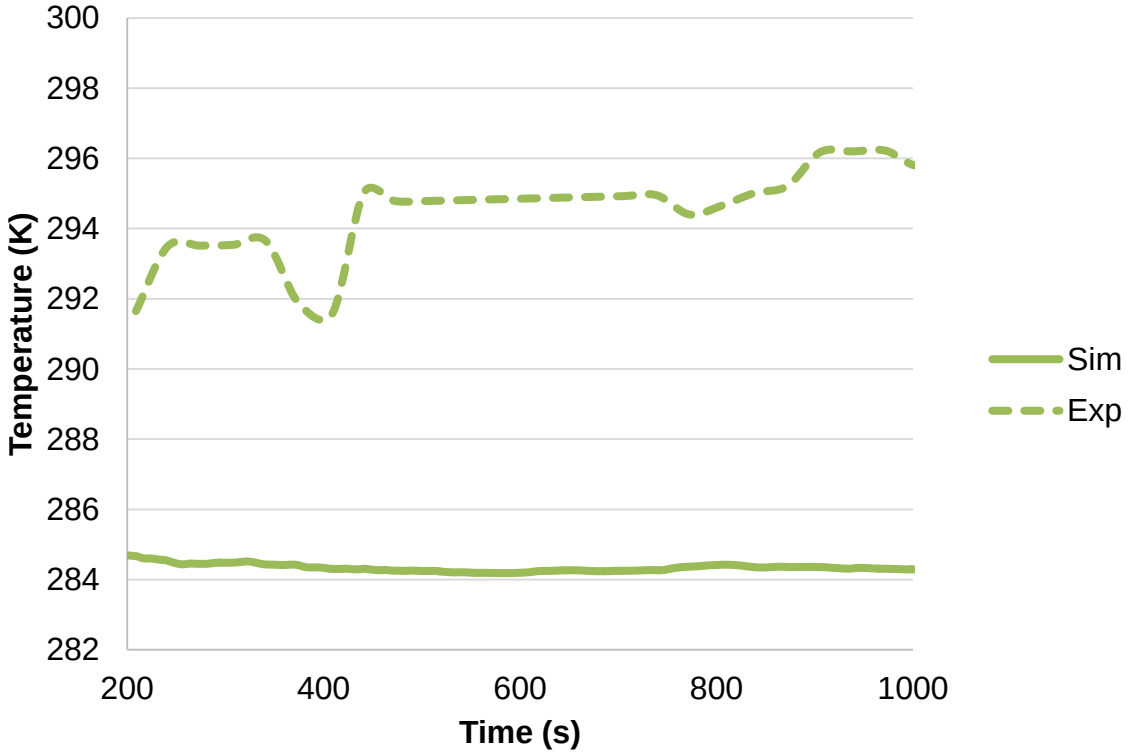

Figure 99 Average temperatures at a height of 1.00 m for the 0.878 g/s HSL validation.

Figure 97 – Figure 99 show the comparison between the average temperatures, within the layers, for the 0.878 g/s release. The results given are for the timeframe 200 – 1000 seconds, thus ignoring the initial phases of the combustion process.

Interestingly, the problem of over-prediction with the slower release is not as profound for the quicker release. Only the greatest height, Figure 97, shows an over-prediction. The other two heights, Figure 98 and Figure 99 show under-predictions.

Figure 97 shows an over-prediction of approximately 90 K. The oscillations within the simulated results are not as profound as the experiment but are still present. Figure 98 shows an under-prediction of circa 50 K, whilst the oscillations are almost non-existent compared to the experiment. The lowest height of 1.00 m, Figure 99, shows a negligible under-prediction, of at most 10 K, whilst the trends seem to be similar.

The distinct separation between 2.25 m and 1.75 m for the quicker release suggests that the velocity of the jet leaving the inlet, is sufficient to extend the flame position further up the enclosure. This could also be caused by the use of multiple vents, as there are two vents open. This could drive the temperature to the upper regions whilst cooling the lower regions with the inflow of colder air from outside, similar to the hydrogen dispersion theories in section 2.4.

8.3 Premixed Garage Scenario

This study investigates the potential damage and harm if a release was to become homogeneous. The work follows on from that in Chapter 6, applying the modelling to a larger geometry which is the same as that in Chapter 5.

8.3.1 Premixed Garage Configurations

The section uses the best ventilation configuration from Chapter 5, namely the two vent configuration. There is a lower vent opposite where the release would be and an upper vent near the location a release would be expected. These studies do not contain the outer geometry that was used for the non-reacting modelling. This is because the premixed combustion model requires the external domain to have the same homogeneous mixture as the enclosure, rather than pure air. Therefore it is deemed suitable that the outer domain starts at the open vents. The configuration used is shown in Figure 100.

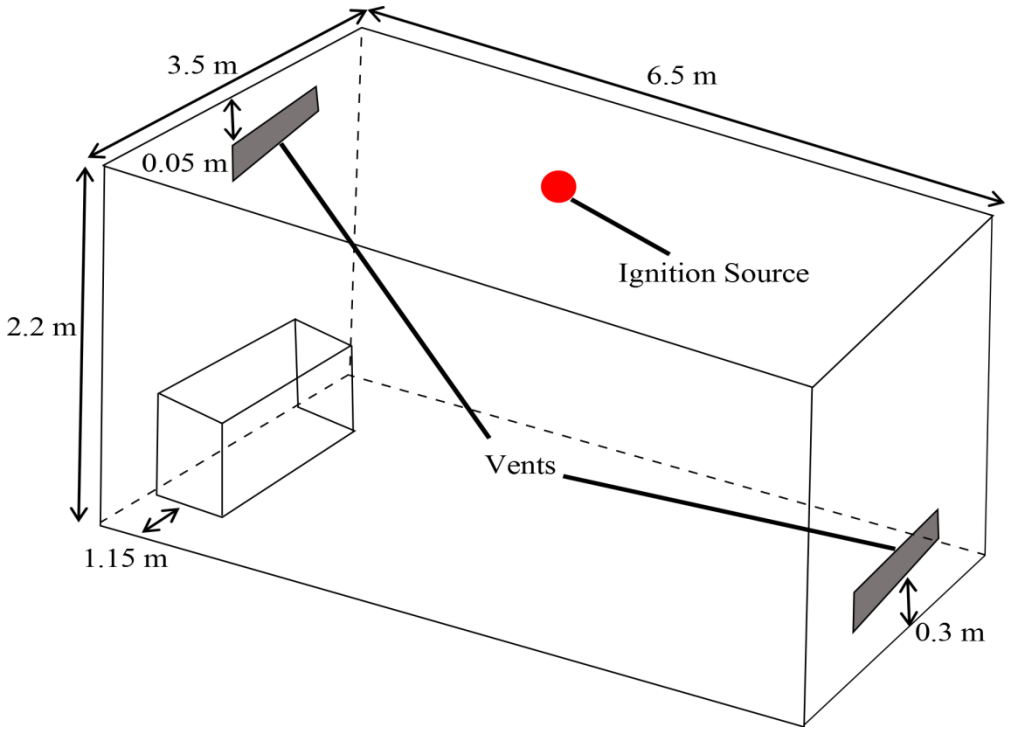

Figure 100 Geometry used for the premixed blind studies.

The validation of this regime utilised obstacles and as such the presence of a vehicle is also investigated. The positioning of the vehicle within the enclosure is shown in Figure 101.

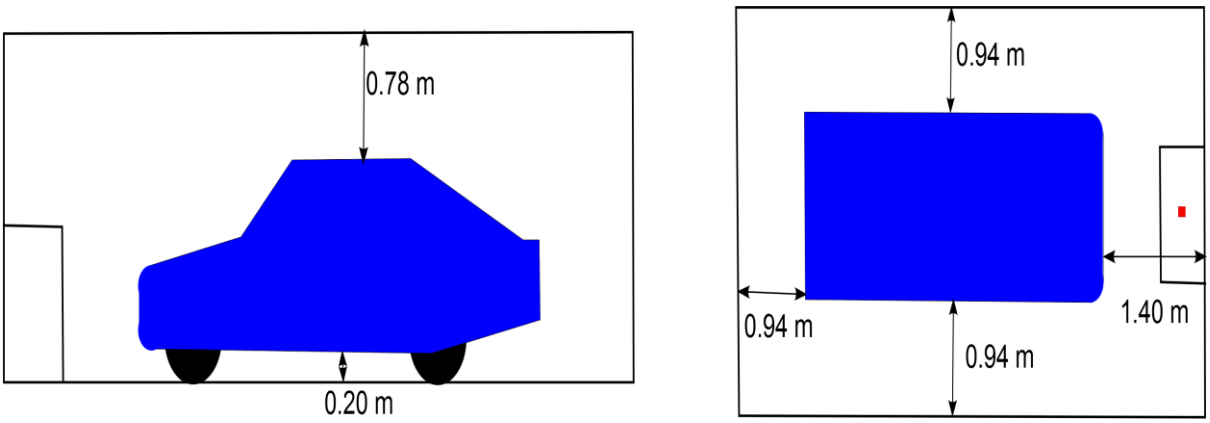

Figure 101 Position of vehicle for the premixed blind studies.

There are minimal differences between the configurations used here and those used within Chapter 5. The major difference is the lack of the external domain, as explained previously. The release source which was used previously is no longer used, as the addition of hydrogen is not required. This is because these scenarios assume hydrogen has already leaked into the garage, either from the car or the hydrogen refuelling system. The homogeneous mixture could form due to blockages

at the vents or from strong wind blowing into the garage. The mixture has an equivalence ratio of 0.8, the same as that in Chapter 6.

The assumption laid out to set the scenario is such that the ventilation that would normally work is not able to operate. Any flow into the garage needs to be of the same mixture, at least whilst combustion occurs, to preserve the full premixed regime that is under investigation.

8.3.2 Numerical Implementation

The numerical model used for the premixed garage studies is similar to that of Chapter 6. The combustion model is the premixed version of the EBU model with the coefficient used, 8, identical to that validated. The equivalence ratio used for these simulations is also the same as that used before, 0.8. This equivalence ratio on the current geometry would mean that approximately 0.9 kg of hydrogen released. This is because the model was validated for quite precise conditions and as such these need to be maintained. The turbulence model used is the k-omega SST model.

The differences between the implementation here and that used before revolve around the mesh and time step. This is because the geometry used here is greater than that for the validation. This means that the time for complete combustion is greater than before. The timescale used here is seconds, compared to previously being within microseconds. The mesh used here is the same as that in Chapter 5, whilst the time step used is 0.001 seconds. This is two orders of magnitude greater than that used in Chapter 6.

8.3.3 Analysis Criteria

The criteria used for analysing the premixed scenarios are the overpressures and temperatures that are predicted. These can be compared to the data given in section 2.3.2.

The overpressures that are of importance are the maximum overpressure within the garage and the overpressures incurred at the vents. The maximum overpressure is used to determine the potential damage to the garage, as well as the potential direct and indirect consequences on people. The overpressures at the vents are used to

determine the potential damage to the surroundings and people that could be near the garage.

The temperature that is investigated is the maximum temperature and the temperature increase against time. The maximum temperature determines the potential dangers to people, both inside and to first responders, which may occur. The temperature rise against time is used such that it gives indications of the time for evacuations to occur. The maximum temperature is recorded over the whole garage, such that the location may change.

8.3.4 Results

The analysis of the premixed garage studies compares the behaviour of the empty garage with that of a vehicle inside. The main criteria for analysis have been discussed above. However to show the time scale of the combustion process, the burnt volume has been plotted. This also gives evidence that the combustion process did occur for both scenarios.

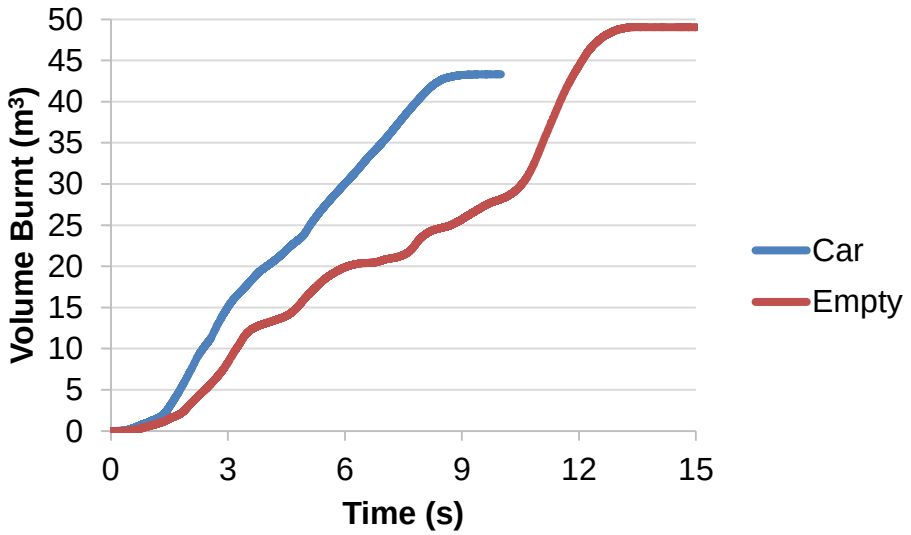

Figure 102 Burnt volume comparison graph for the premixed garage scenarios.

Figure 102 shows the time taken for the entire enclosure to be engulfed and fully burnt. It is worth remembering that the volume of the empty garage is 49.33 m^3 whilst with the vehicle present the volume becomes 43.54 m^3. The burnt volume of the case with the vehicle plateaus at 43.3 m^3, whilst the case without the vehicle plateaus at 49.05 m^3. The maximum never quite reaches the total capacity of the garage due to

the behaviour at the vents. This is because the lower vent allows flow into the domain and thus does not allow the entire enclosure to be consumed. Interestingly the presence of a vehicle is quicker than without. This is due to the vehicle acting as an obstacle and as such increasing the flame speed.

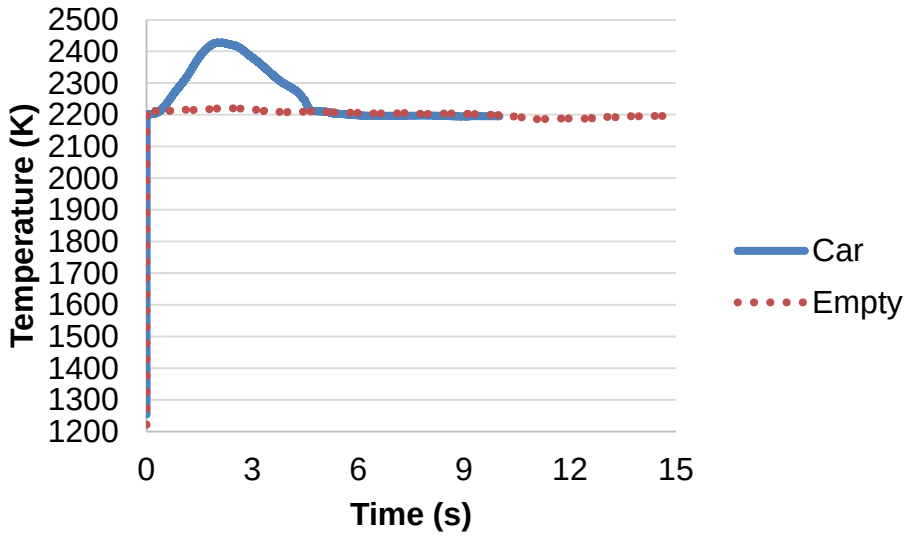

Figure 103 Comparison of the maximum temperatures for the premixed garage scenarios.

Figure 103 shows the maximum temperatures obtained for the two scenarios. The presence of a vehicle causes the peak temperature to rise to circa 2400 K, before plateauing at 2200 K. The simulation without a vehicle seems to plateau at 2200 K almost instantaneously. This would suggest that the combustion process is not captured accurately, although Figure 102 does show that it is not the case. If the process was not captured accurately then the burnt volume would be portrayed differently. This could be caused by either the time discretisation or the ignition process. The maximum temperature, after the peak temperature, is still well above the temperature that is not survivable of 582 K, as shown in Table 2.

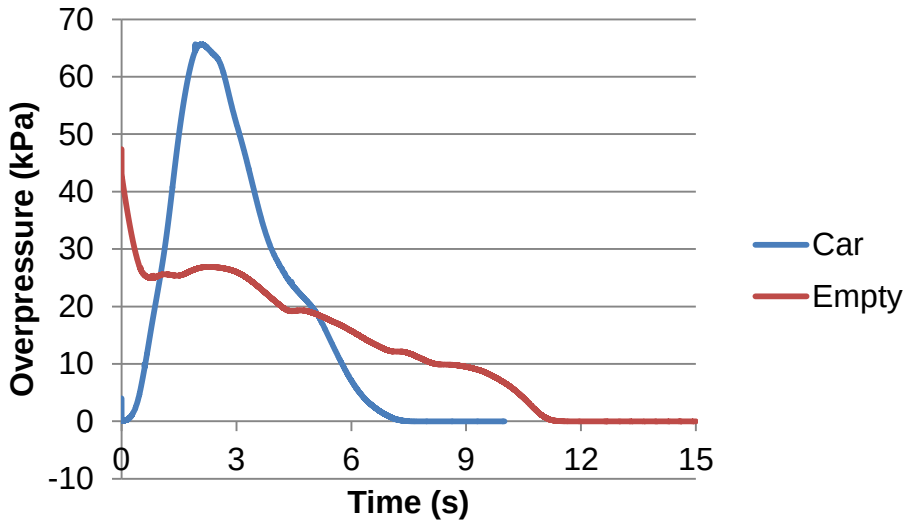

Figure 104 Comparison of the maximum overpressures induced for the premixed garage scenarios.

Figure 104 compares the maximum overpressures that are induced by the combustion process. The simulation without the vehicular presence again shows that the overpressure increases instantaneously. This is because there is no rise to the peak overpressure, instead the pressures decrease from the start. It is unknown why this occurs and requires further investigation.

The overpressure for the simulation with vehicular presence has captured the physical processes accurately. The overpressure does not become negative, like the overpressures seen in Chapter 6, due to the presence of both vents. The other reason for not seeing this phenomenon is that the maximum overpressure is taken over the entire garage and not at any specific locations. The maximum overpressure reached is circa 65 kPa. The strength of such an overpressure is easily great enough for destruction of a garage and almost 100% fatalities, caused by wounding from missiles, as shown in Table 5 – Table 7.

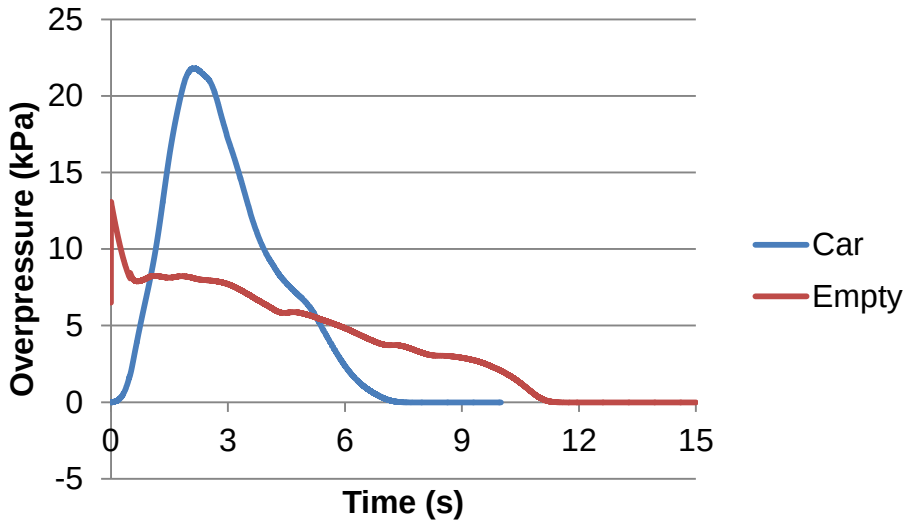

Figure 105 Comparison of the upper vent overpressures for the premixed garage scenarios.

Figure 105 shows the overpressures that are induced at the upper vent. Once again the empty garage shows an almost instantaneous peak overpressure. The vehicular presence again shows a slower time to peak overpressure. The peak overpressure at this location is not as large as the maximum overpressure predicted earlier, almost two thirds lower, at 22 kPa. The peak overpressure at this location is still enough to cause destruction of the garage. This would create projectiles which could cause injury, whilst also knocking people down as well, as shown in Table 5 – Table 7.

Figure 106 shows the overpressures induced at the lower vent. The empty garage shows an almost instantaneous peak overpressure again. The presence of a vehicle shows a slower rate to reach the peak overpressure.

The peak overpressure at the lower vent reaches 32.5 kPa with a vehicle present, which is greater than that reached at the upper vent. This is still almost half as large as the maximum peak overpressure that occurs. Due to the overpressure being greater than the upper vent overpressure, it is already known that this would again cause destruction of the enclosure which could increase fatalities compared to the overpressure at the upper vent, as shown in Table 5 – Table 7.

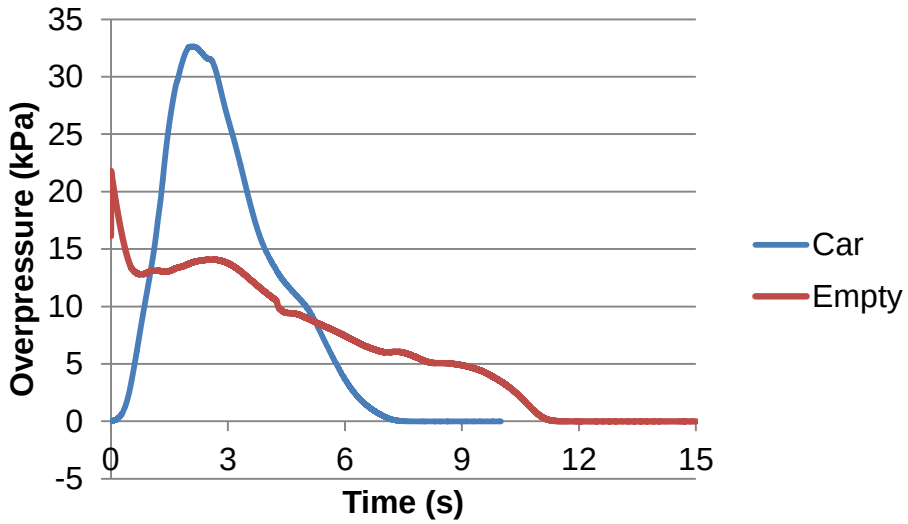

Figure 106 Comparison of the overpressures induced at the lower vent for the premixed garage scenarios.

Comparing the results against the damage and harm criteria laid out in section 2.3.2, it is quite clear that the predicted maximum temperature is well over the temperature for survival. Whilst the temperature distribution may differ, due to the strength of the maximum temperature this is not going to be possible at the end of the combustion process. There may however be some possibility of escape during the early phases of the combustion process as explained by the criteria in section 2.3.2.2.

The criteria for overpressure are different to that of temperature. Mainly because the overpressures have many different consequences; direct, indirect and structural. It is worth noting that the maximum overpressure was 65 kPa, whilst the upper vent recorded 22 kPa and the lower vent 32.5 kPa. These are all predicted in the presence of a vehicle.

For direct contact with humans the maximum overpressure is strong enough for fatal head injuries (54 kPa). The wall vent overpressure is such that there is no direct risk to people outside, only minor injuries (8 kPa). The overpressure reached at the door vent is almost strong enough to rupture ear drums, 34 kPa.

The indirect consequence on humans caused by the maximum overpressure fits into the range of a 100% mortality rate caused by missile wounds, 48.3 – 68.9 kPa. Obviously this is dependent on potential missiles being inside the enclosure, although this is likely as it is a garage. Depending on the structural consequences, this could be exacerbated to people that are not inside the garage. The

overpressures reached at the vents would also cause fatalities due to missile wounds. A 50% mortality rate by missile wounds is reached at an overpressure range of 27.6 – 34.5 kPa. The overpressures are also strong enough to knock people down that are walking past, 10.3 – 20.0 kPa will cause this.

The structural consequences of the overpressure are also a major concern, as this could create the missiles to cause damage further afield. The overpressures reached at all locations fall into the range that shatters non-reinforced concrete/cinderblock walls, 14 – 28 kPa. This is a common material for making a garage and they are rarely reinforced and as such would cause a vast amount of missiles to be produced. In fact the overpressures reached would destroy any buildings not specifically designed to deal with overpressures, 30 kPa is the threshold for this criterion. The maximum overpressure would likely destroy the majority of external brickwork, threshold for which is 35 – 80 kPa, to destroy 50 – 75%. The maximum overpressure could also cause damage to pipework, the threshold of which is 50 – 100 kPa. This last one could have an even greater catastrophic consequence were gas pipes to become ruptured.

The information that has been discovered for the equivalence ratio investigated, suggests that it is incredibly dangerous with almost certain death sustained inside the enclosure and significant damage caused externally. This would create the suggestion that it be brought into law that covering of vents is illegal and also voids insurance.

8.4 Conclusion

This chapter consists of two different investigations. The first is for non-premixed combustion in an enclosure that resembles a garage. This is compared against recorded data. The other is for premixed combustion, with an equivalence ratio of 0.8, for a garage. This is compared against damage and harm criteria that is introduced in section 2.3.2.

The predicted results for the non-premixed combustion show good agreement with the recorded results. This is especially the case for the slower release rate, which shows the largest over prediction is around 50 K. The quicker release rate shows an over prediction of around 100 K, for the average temperature at the highest level of

sensors. The quicker release has a greater temperature at the highest layer of sensors whilst the lower levels show similar temperatures between the release rates.

The premixed garage scenarios are an extension to the work performed in Chapter 6. These are then compared to the harm criteria in section 2.3.2. It can be seen that if such an event were to occur then the outcomes could be catastrophic. Hence the need to mitigate this occurring and the work performed within Chapter 5. It also shows that the presence of a vehicle increases the peak overpressures.

Chapter 9 – Conclusion

The modelling of hydrogen releases for safety investigations is a growing field, currently the focus has been on the storage tank of the vehicles. However with minimal means to refuel a hydrogen vehicle, a new system for refuelling is under development within the ESCHER project.

This work is performed as the safety constituent of the ESCHER project, which is designing a residential hydrogen refuelling system. Currently, such systems are not covered within the remit of the HSE as they would be residential, hence the use of the commercial software and RANS modelling. RANS modelling is generally quicker to use than LES which is needed when limited computational resources are available. This work was performed using the commercial software STAR-CCM+®. This is such that regulatory bodies would be able to recruit and/or train staff to use the modelling strategies used in the investigations. The modelling strategies which have been validated could be applied to other geometries to investigate problems for more specific garage configurations.

This work focuses on three main areas for hydrogen safety, which are necessary for the advancement of the hydrogen economy and infrastructure. These are; non-reacting dispersion/ventilation scenarios, premixed combustion of homogeneous mixtures and non-premixed combustion of hydrogen releases. The latter two investigations were performed to gain insight into the potential damage and harm that could arise were a leak to ignite under various conditions.

The non-reacting studies were performed to investigate the most suitable and realistic venting configuration to mitigate the accumulation of a flammable cloud after a release occurs. Atmospheric conditions, wind, and the presence of a vehicle were also investigated to determine what effect these have on the accumulation and dissipation of the flammable cloud for the best performing ventilation configurations. This is because mitigating the accumulation and dissipating the flammable volume is preferable to the ignition of the flammable cloud.

9.1 Summary and Conclusions

The non-reacting work was deemed important as it is necessary to mitigate the accumulation of a flammable mixture. This work began with a validation of a meshing strategy and an investigation into various turbulence models. The meshing strategy was developed as it is evident that there would be regions of less interest and this also has the added benefit of saving computational time. The meshing strategy that showed grid independence utilised a smallest cell size of 0.025 m with the largest being 0.25 m. The different turbulence models were investigated as the literature showed various models are in use, the k-omega SST model was the most accurate. The findings from the meshing strategy and turbulence model comparison were then applied for further validation. This involved a larger geometry with experimental data for comparison, for two different experiments. The first experiment did not take into account atmospheric conditions, whilst the second did. The results for the validation against the first experiment show good agreement between the predicted and recorded results. This instils confidence in the methodology proposed. The second experiment took into account atmospheric conditions, although the predicted results did not compare to the experimental results. This was because the experimental data started at 400 seconds and as such any information prior to this was not available. This included the wind profile which meant that an average wind speed was used. However because the first validation matched well the methodology is used further. These recommendations were used to investigate the most suitable venting configuration for a geometry that resembles a residential garage, under various conditions.

The ventilation studies investigated various configurations, whilst keeping the total venting area constant. The ventilation studies also investigated the presence of a vehicle as well as atmospheric conditions. This was performed such that the comparison was against developed criteria. The most important criteria are the flammable volume and the time for this to dissipate. The maximum concentration at the centre of the roof is also important as this is the most likely position for an ignition source. The final criterion is the flammable depth this is chosen such that the level to avoid for ignition sources is known.

The ventilation studies showed that a two vent configuration, with an upper vent near the release and a lower vent opposite performed best. A three vent configuration, utilising an extra upper vent opposite the release with a reduction in the vent sizes opposite the release, performed slightly worse. The two configurations were used to investigate the effect of a vehicle as well as atmospheric conditions. The two vent configuration performed marginally better for all of the conditions examined. When the wind investigated used was strong, 5 m/s, the result was unexpected. The mixture within garage was homogeneous, except above the hydrogen release. There are many possible reasons for this outcome, namely the release location or the method for modelling the wind phenomenon. The majority of literature and experiments use a centrally located release source, whilst wind profiles are rarely constant.

The reacting flow investigations were for both premixed and non-premixed combustion. This is to investigate the outcomes if a release was to ignite. The premixed combustion studies are for a worst case scenario. The first part of the premixed combustion investigations was the validation of the modelling process. The experimental data used is for the University of Sydney combustion chamber, using an equivalence ratio of 0.8 and three different configurations of the available obstacles. The combustion model that is investigated is the EBU model, with the turbulence modelled via the k-omega SST model.

The first investigation was into the EBU model coefficient, for the full configuration with all of the obstacles. This was performed to investigate the most suitable value to use that predicts the combustion process accurately, especially the peak overpressure. This showed that a value of 7 matches the experimental peak overpressure however the recorded peak overpressure plateaus at 1000 mbar. This is caused by the pressure transducers used. The predicted peak overpressure using a value of 8, seems to match an extrapolated experimental overpressure. This was then applied to two other configurations which showed good agreement between the predicted and recorded peak overpressures, after a time shift has been applied. The time shift, of 2.4 ms, for all configurations aligns the predicted overpressures with the recorded. The time shift is needed due to the inability to capture the initial phases of the combustion accurately. This is because the combustion model relies upon turbulence to propagate the flame, whilst there is minimal turbulence initially. This

can also cause over predictions in highly strained regions, such as walls, which is evident after the final obstacle.

The flame position shows that the predicted flame proceeds slower than the recorded. This could be caused by the flame front definition and the comparison of the experimental results. The problem with the flame position creates errors with the flame speed, as the position is used to calculate the flame speed. The flame structure proceeds correctly after the first obstacle. The structure is deformed initially which is not correct as the flame is laminar until the first baffle. This is caused by the combustion model, as explained before. The peak overpressure is the most important criteria for the analysis as it would suggest the potential damage that can occur. The investigations show good agreement of the peak overpressures and as such this work is utilised for investigating premixed combustion within a garage.

The final premixed investigation is for a residential garage and utilises the methodology used within the validation. The mixture has an equivalence ratio of 0.8, which is that used before. The garage geometry used was the best performing vent configuration from the non-reacting ventilation studies, with the ignition source at the centre of the roof. The presence of a vehicle was also examined. The analysis criteria were the peak overpressure and temperature, compared against the harm and damage criteria in the literature review. When the garage was empty, the results seemed to show almost instantaneous peaks for overpressure and temperature. However when the vehicle was considered the results showed that the peak overpressures and temperature were not reached instantaneously. This is because the car acts as an obstacle for the modelling process, whilst the empty garage seems to be modelled incorrectly and requires further investigation. The temperatures that were reached would be fatal for anyone within the garage. The maximum overpressures within the garage would be capable of causing complete destruction of the garage. The overpressures may also cause serious harm and/or fatalities for anyone within the garage due to indirect injuries.

The last investigations involve non-premixed combustion. Firstly the combustion model, both the equilibrium and flamelet variations of the PPDF model, as well as the mesh was investigated. There is then an investigation into a turbulence model coefficient, followed by the application of the results on a more realistic configuration.

The combustion model used is the PPDF model and is first examined on established data. This data is not transient and as such is modelled in the steady state. The turbulence model used for these investigations was the standard k-epsilon model, this is used due to the need to adjust a model coefficient to capture the turbulence decay more accurately. There are recommendations for the value of the coefficient that needs changing.

The first study found that there were negligible differences between the two variations of the combustion model, although the equilibrium model did over predict the peak flame temperature more than the flamelet model. All of the criteria for comparison showed the most suitable mesh to use was a non-uniform polyhedral mesh. The alteration of the turbulence model coefficient was examined for a diluted hydrogen flame, a hydrogen-nitrogen mixture. The modelling of this flame used the equilibrium combustion model, as there was no library for this mixture available. The predicted results showed that decreasing the turbulence coefficient increased the accuracy. This gave confidence in the methodology.

The suggestions were then applied to a different geometry that resembles a residential garage with a release located centrally. Two different release rates have been examined with differing ventilation for each release rate. This scenario is more realistic than that which was investigated previously, with the data being transient. The recorded data consists of average temperatures at different heights. The slower release rate used, which had a single vent open, showed the predicted results were greater by up to 50 K. The quicker release rate, which had two vents open, showed an over prediction at the upper layer of almost 100 K. The lower layers showed under predictions of the average temperatures. This showed that increasing the release rate only increases the temperatures at the upper height. This is useful as it would allow evacuation of people present.

9.2 Present Contributions

The main contributions of this work are:

1. A comprehensive validation of non-reacting hydrogen dispersion on two different configurations. This is to gain confidence in the suggested

methodology, meshing strategy and turbulence model, for modelling the phenomenon within partially enclosed geometries.

2. Determining the most suitable venting configuration for a hydrogen release into a residential garage. This included investigating both atmospheric conditions, wind, and the presence of obstacles, a car. The ventilation strategy that performed best was a two vent configuration with an upper vent near the release and a lower vent opposite the release. This configuration has the smallest accumulation of flammable volume and dissipates this cloud into the surroundings quickest. This is also the case in the presence of a vehicle and when there are atmospheric conditions.

3. RANS validation using simple combustion modelling, EBU model, for the University of Sydney combustion chamber. This was performed on three different obstacle configurations. The main area of concern was the prediction of the peak overpressure, as to ascertain the validity of the numerical model for further investigations. The numerical model predicted the peak overpressure accurately although there was a delay in the arrival of the incident peak overpressure. This is believed to be due to inaccuracy of capturing the initial phases of the combustion process.

4. Non-premixed combustion was investigated using the PPDF model. Initial investigation was on two different Sandia flames, pure hydrogen and a hydrogen-nitrogen mixture. The flamelet variation of the model and a non-uniform mesh showed the best accuracy amongst the various parameters studied for the pure hydrogen flame. The second part of the study investigated a turbulence model coefficient and the effect that has on the combustion results, for the hydrogen-nitrogen mixture. This showed that altering the model coefficient increases the accuracy of the combustion process, as expressed in the literature.

5. The results from the non-premixed investigation into the Sandia flame were applied to a more realistic geometry, an ISO container that bares resemblance to a residential garage. The results showed that the temperature was over-predicted at higher levels although this was to be expected due to slight over-prediction in the initial studies. However the largest over-prediction was 100 K. The investigation also showed that a quicker release rate yields safer areas lower into the geometry, as the higher temperature is higher up the domain.

6. The application of the premixed modelling to more realistic configurations showed that for an equivalence ratio of 0.8, there is significant potential for harm and destruction. The geometry used was the two vent configuration that

performed best for the non-reacting ventilation/dispersion studies. The presence of a vehicle was investigated alongside the empty garage. The empty garage scenario did not seem to capture the physics correctly and requires further investigation. When a vehicle was present the physics was captured correctly. The criteria for analysis were the temperature and maximum peak overpressure. The temperature shows that it would not sustain life and would be fatal. The maximum overpressure would not directly kill people inside, although it would cause significant damage to the structure. This is turn becomes lethal to humans due to the indirect consequences, namely the debris from the collapsing structure becoming missiles.

9.3 Further Work

- Whilst simulations have been performed for non-reacting releases, this is only for a single geometry and some vent positions. This work could be investigated extensively with many geometries, vent configurations and release locations. There is also scope to include the vehicle as a release source. This would increase the amount of potential work vastly.

- Currently only constant release rates are used for this work and by many others. The use of variable release rates would be more realistic and beneficial. There is however a problem in deciding how to define the variable release rate. This depends on the source of the leak but would give greater insight into the problems.

- The premixed validation performed within this work could be extended for different equivalence ratios of the mixture. This could then be extended to modelling the garage scenarios using differing equivalence ratios. This could give vast amounts of information and help to design buildings such that dangers are mitigated.

- The non-premixed combustion could be extended to model releases with differing locations. This would need to be accompanied with experiments, to ensure the physics is captured accurately. This would provide understanding for more realistic scenarios of hydrogen jet flames within enclosures.

- Finally, the current work utilised RANS modelling with simple combustion models. It would be interesting to compare the current work to LES modelling and more complex combustion models.

References

Abdel-Raheem, M.A., 2015. Numerical study of the Characteristics of CNG, LPG and Hydrogen Turbulent Premixed Flames. Loughborough University.

airships.net, 2009. Hindenburg disaster [WWW Document]. URL http://www.airships.net/hindenburg/disaster (accessed 8.1.14).

Al-Harbi, A.A., 2013. Turbulent Premixed Flames Propagating Past Repeated Obstacles. University of Sydney.

Atkins, P., de Paula, J., 2009. Elements of Physical Chemistry, Fifth. ed. Oxford University Press.

Atkins, P., Overton, T., Rourke, J., Weller, M., Armstrong, F., 2010. Inorganic Chemistry, Fifth. ed. Oxford University Press.

Barlow, R.S., Carter, C.D., 1994. Raman/Rayleigh/LIF measurements of nitric oxide formation in turbulent hydrogen jet flames. Combust. Flame 97, 261–280.

Barlow, R.S., Carter, C.D., 1996. Relationships among nitric oxide, temperature, and mixture fraction in hydrogen jet flames. Combust. Flame 104, 288–299.

BBC, 2015. First “zero-emissions” hydrogen filling station opens [WWW Document]. URL http://www.bbc.co.uk/news/uk-england-south-yorkshire-34278051 (accessed 2.9.16).

Bédard-Tremblay, L., Fang, L., Bauwens, L., Cheng, Z., Tchouvelev, a. V., 2008. Numerical simulation of hydrogen–air detonation for damage assessment in realistic accident scenarios. J. Loss Prev. Process Ind. 21, 154–161.

Bhuiya, M.M.H., Lee, C.Y., Hwang, T., Munira, S., Hopkins, R., Yoon, H., Park, S.H., Kim, K.J., 2014. Experimentally tuned dual stage hydrogen compressor for improved compression ratio. Int. J. Hydrogen Energy 39, 12924–12933.

Bilger, R.W., Kent, J.H., 1974. Concentration Fluctuations in Turbulent Jet Diffusion Flames. Combust. Sci. Technol. 9, 25–29.

Blais, M., Joyce, A., 2010. Hydrogen Release and Combustion Measurements in a Full Scale Garage.

Brady, K., Sung, C.-J., T’ien, J., 2012. Dispersion and catalytic ignition of hydrogen leaks within enclosed spaces. Int. J. Hydrogen Energy 37, 10405–10415.

Brennan, S., Molkov, V., 2013. Safety assessment of unignited hydrogen discharge from onboard storage in garages with low levels of natural ventilation. Int. J. Hydrogen Energy 38, 8159–8166.

Bryan, J.L., 1986. Damageability of buildings, contents and personnel from exposure to fire. Fire Saf. J. 11, 15–31.

Carbuyer, 2015. Hydrogen cars: all you need to know [WWW Document]. URL http://www.carbuyer.co.uk/tips-and-advice/144957/hydrogen-cars-all-you-need-to-know (accessed 2.9.16).

Carbuyer, 2016. Best electric cars [WWW Document]. URL

http://www.carbuyer.co.uk/reviews/recommended/best-electric-cars (accessed 2.9.16).

CD-adapco, 2015. STAR-CCM + User Guide.

CD-adapco, 2016. DARS [WWW Document]. URL http://www.cd-adapco.com/products/star-ccm®/dars (accessed 8.23.16).

Choi, J., Hur, N., Kang, S., Lee, E.D., Lee, K.-B., 2013. A CFD simulation of hydrogen dispersion for the hydrogen leakage from a fuel cell vehicle in an underground parking garage. Int. J. Hydrogen Energy 38, 8084–8091.

Cisse, P., Karim, G., 2007. The rapid formation and dispersion of flammable zones within cylindrical vertical enclosures following the release of a fixed mass of hydrogen and other gaseous fuels into air. Int. J. Hydrogen Energy 32, 630–636.

Demuren, A.O., Rodi, W., 1984. Calculation of Turbulence-driven Secondary Motion in Non-circular Ducts. Fluid Mech. 140, 189–222.

El-Amin, M., Inoue, M., Kanayama, H., 2008. Boundary layer theory approach to the concentration layer adjacent to a ceiling wall of a hydrogen leakage: Far region. Int. J. Hydrogen Energy 33, 7642–7647.

El-Amin, M., Kanayama, H., 2008. Boundary layer theory approach to the concentration layer adjacent to a ceiling wall at impinging region of a hydrogen leakage. Int. J. Hydrogen Energy 33, 6393–6400.

El-Amin, M., Kanayama, H., 2009. Boundary layer theory approach to the concentration layer adjacent to the ceiling wall of a hydrogen leakage: Axisymmetric impinging and far regions. Int. J. Hydrogen Energy 34, 1620–1626.

Ertesvåg, I.S., Magnussen, B.F., 2000. The Eddy Dissipation Turbulence Energy Cascade Model. Combust. Sci. Technol. 159, 213–235.

European Parliament, 1994. ATEX 95.

European Parliament, 2000. ATEX 137 57–64.

Favre, A., 1969. Statistical Equations of Turbulent Gases. In: Problems of Hydrodynamics and Continuum Mechanics. SIAM, pp. 231–266.

Ferziger, J.H., 1977. Large Eddy Numerical Simulations of Turbulent Flows. AIAA 15, 1261–1267.

Ferziger, J.H., Perić, M., 2002. Computational Methods for Fluid Dynamics, Third. ed. Springer-Verlag, Berlin, Heidelberg.

Financial Post, 2015. Toyota open patents to competitors [WWW Document]. Toyota opens fuel-cell patents to Compet. bid to spur Dev. Hydrog. Veh. URL http://business.financialpost.com/news/transportation/toyota-opens-fuel-cell-patents-to-competitors-in-bid-to-spur-development-of-hydrogen-powered-vehicles (accessed 5.14.15).

Gallego, J.I.., Valero, J.., n.d. AN INTRODUCTION TO THE EFFECTS OF EXPLOSIONS AND BLAST INJURIES [WWW Document]. URL http://www.ciedcoe.org/Galerias/documents/Jose_Yenes_and_Joaquin_Martinez_article.pdf (accessed 6.20.17).

Gambini, M., Manno, M., Vellini, M., 2008. Numerical analysis and performance assessment of metal hydride-based hydrogen storage systems. Int. J. Hydrogen Energy 33, 6178–6187.

Gamezo, V.N., Ogawa, T., Oran, E.S., 2007. Numerical simulations of flame propagation and DDT in obstructed channels filled with hydrogen–air mixture. Proc. Combust. Inst. 31, 2463–2471.

GEXCON, 2012. GEXCON Handbook [WWW Document]. URL http://www.gexcon.com/article/handbook-chapter-1

Gkanas, E.I., Grant, D.M., Stuart, A.D., Eastwick, C.N., Book, D., Nayebossadri, S., Pickering, L., Walker, G.S., 2015. Numerical study on a two-stage Metal Hydride Hydrogen Compression system. J. Alloys Compd. 645, S18–S22.

Gubba, S.R., 2009. Development of a Dynamic LES Model for Premixed Turbulent Flames. Loughborough University.

H2tools.org, n.d. Hydrogen Tools [WWW Document]. URL https://h2tools.org/bestpractices/h2properties (accessed 6.21.17).

Hajji, Y., Bouteraa, M., Cafsi, A. El, Belghith, A., Bournot, P., Kallel, F., 2014. Dispersion and behavior of hydrogen during a leak in a prismatic cavity. Int. J. Hydrogen Energy 39, 6111–6119.

Hassel, E.P., 1997. Proceedings of the 2nd International Workshop on Measurement and Computation of Turbulent Nonpremixed Flames. In: International Workshop on Measurement and Computation of Turbulent Nonpremixed Flames. Heppenheim, Germany, p. 82.

Hawksworth, S., 2000. Hydrogen Safety Standards and the HyPER Project.

Health and Safety Executive, 2002. The Dangerous Substances and Explosive Atmospheres Regulations 2002 1–20.

Heidari, a., Ferraris, S., Wen, J.X., Tam, V.H.Y., 2011. Numerical simulation of large scale hydrogen detonation. Int. J. Hydrogen Energy 36, 2538–2544.

Heidari, a., Wen, J.X., 2014. Flame acceleration and transition from deflagration to detonation in hydrogen explosions. Int. J. Hydrogen Energy 39, 6184–6200.

Hong, Z., Davidson, D.F., Hanson, R.K., 2011. An improved H2/O2 mechanism based on recent shock tube/laser absorption measurements. Combust. Flame 158, 633–644.

Hooker, P., 2014. HSL Presentation.

Hooker, P., Hall, J., Hoyes, J.R., Newton, A., Willoughby, D., 2015. Hydrogen jet fires in a passively ventilated enclosure. In: International Conference on Hydrogen Safety. Yokohama.

Hooker, P., Willoughby, D., Hall, J., Hoyes, J.R., 2013. Accumulation of Hydrogen Released into a Vented Enclosure - Experimental Results. In: International Conference on Hydrogen Safety. Brussels, pp. 1–10.

Hundseid, H., Ingebrigtsen, K.O., 2001. Human resistance against thermal effects, explosion effects, toxic effects and obscuration of vision.

Hyindoor, 2012. Pre normative research on the indoor use of duel cells and hydrogen systems [WWW Document]. URL http://www.hyindoor.eu/

HySafe, 2007. Biennial Report on Hydrogen Safety.

Ivanov, M.F., Kiverin, a. D., Yakovenko, I.S., Liberman, M. a., 2013. Hydrogen–oxygen flame acceleration and deflagration-to-detonation transition in three-dimensional rectangular channels with no-slip walls. Int. J. Hydrogen Energy 38, 16427–16440.

Jallais, S., Houssin, D., Vyazmina, E., Bernard-Michel, G., Kuznetsov, M., Shentsov, V., Molkov, V., Makarov, D., Dey, R., Dang-Nhu, G., Melideo, D., Palmisano, V., Weidner, E., Baraldi, D., Hooker, P., der Kinderen, J., Venetsanos, A., 2014. Work Package 6 Hyindoor Final Report.

Jemni, A., Ben Nasrallah, S., 1995. Study of two-dimensional heat and mass transfer during desorption in a metal-hydrogen reactor. Int. J. Hydrogen Energy 20, 881–891.

Jones, W., 1980. Prediction Methods for Turbulent Flames. In: Kollman, W. (Ed.), Prediction Methods for Turbulent Flow. Hemisphere, Washington D.C., pp. 1–45.

Kent, J.H., Bilger, R.W., 1973. Turbulent diffusion flames. Symp. Combust. 14, 615–625.

Konnov, A. a., 2008. Remaining uncertainties in the kinetic mechanism of hydrogen combustion. Combust. Flame 152, 507–528.

Kuo, K.K., 1986. Principles of Combustion. John Wiley & Sons, Inc.

Kyoung, S., Ferekh, S., Gwak, G., Jo, A., Ju, H., 2015. Three-dimensional modeling and simulation of hydrogen desorption in metal hydride hydrogen storage vessels. Int. J. Hydrogen Energy 40, 14322–14330.

Launder, B.E., Reece, G.J., Rodi, W., 1975. Progress in the Development of a Reynolds-stress Turbulence Closure. Fluid Mech. 68, 537–566.

Launder, B.E., Spalding, D.B., 1974. The numerical computation of turbulent flows. Comput. Methods Appl. Mech. Eng. 3, 269–289.

Laurencelle, F., Goyette, J., 2007. Simulation of heat transfer in a metal hydride reactor with aluminium foam. Int. J. Hydrogen Energy 32, 2957–2964.

Lee, J.H.S., Knystautas, R., Yoshikawa, N., 1978. Photochemical initiation of gaseous detonations. Acta Astronaut. 5, 971–982.

Lee, J.H.S., Moen, I.O., 1980. The mechans of transition from deflagration to detonation in vapor cloud explosions. Prog. Energy Combust. Sci. 6, 359–389.

Lees, F., 1996. Loss prevention in the process industries, Second. ed. Butterworth-Heinemann, Oxford, UK.

Lewis, B., von Elbe, G., 1987. Combustion, Flames and Explosions of Gases, Third. ed. Academic Press Inc.

Li, H., Wang, X., Dong, Z., Xu, L., Chen, C., 2010. A study on 70MPa metal hydride hydrogen compressor. J. Alloys Compd. 502, 503–507.

Lockwood, F.C., Naguib, A.S., 1975. The prediction of the fluctuations in the

properties of free, round-jet, turbulent, diffusion flames. Combust. Flame 24, 109–124.

Lototskyy, M.V., Yartys, V. a., Pollet, B.G., Bowman, R.C., 2014. Metal hydride hydrogen compressors: A review. Int. J. Hydrogen Energy 39, 5818–5851.

Markillie, R., 2015. Launch of M1 Wind Hydrogen Refuelling station [WWW Document]. URL http://www.itm-power.com/news-item/launch-of-m1-wind-hydrogen-refuelling-station (accessed 2.9.16).

Matsuura, K., Kanayama, H., Tsukikawa, H., Inoue, M., 2008. Numerical simulation of leaking hydrogen dispersion behavior in a partially open space. Int. J. Hydrogen Energy 33, 240–247.

Meier, W., Vyrodov, A.O., Bergmann, V., Stricker, W., 1996. Simultaneous Raman/LIF measurements of major species and NO in turbulent H2/air diffusion flames. Appl. Phys. B Lasers Opt. 63, 79–90.

Menter, F., 1992a. Improved Two-equation k-ω Turbulence Models for Aerodynamic Flows.

Menter, F., 1992b. Performance of Popular Turbulence Models for Attached and Separated Adverse Pressure Gradient Flow. AIAA 30, 2066–2072.

Menter, F., 1994. Two-equation Eddy-viscosity Turbulence Model for Engineering Applications. AIAA 32, 1598–1605.

Menter, F.R., Kuntz, M., Langtry, R., 2003. Ten Years of Industrial Experience with the SST Turbulence Model. Turbul. Heat Mass Transf. 4 4, 625–632.

Mercx, W.P.., Verhagen, T.L.., Weerheijm, J., 1991. SOME CONSIDERATIONS ON THE DAMAGE CRITERIA AND SAFETY DISTANCES FOR INDUSTRIAL EXPLOSIONS. In: ICHEME Symposium Series No. 124.

Middha, P., Hansen, O.R., Storvik, I.E., 2009. Validation of CFD-model for hydrogen dispersion. J. Loss Prev. Process Ind. 22, 1034–1038.

Moin, P., Mahesh, K., 1998. Direct Numerical Simulations: A Tool in Turbulence Research. Annu. Rev. Fluid Mech. 30, 539–578.

Molkov, V., 2012. Fundamentals of Hydrogen Safety Engineering I.

Molkov, V., Shentsov, V., Brennan, S., Makarov, D., 2014. Hydrogen non-premixed combustion in enclosure with one vent and sustained release: Numerical experiments. Int. J. Hydrogen Energy 39, 10788–10801.

Mueller, M.A., Kim, T.J., Yetter, R.A., Dryer, F.L., 1999. Flow reactor studies and kinetic modeling of the H2/O2 reaction. Int. J. Chem. Kinet. 31, 113–125.

Muthukumar, P., Singh Patel, K., Sachan, P., Singhal, N., 2012. Computational study on metal hydride based three-stage hydrogen compressor. Int. J. Hydrogen Energy 37, 3797–3806.

National Transportation Safety Board, 2000. Aircraft Accident Report. Washington D.C.

Nayebossadri, S., Book, D., Harris, R., 2015. University of Birmingham ESCHER Update.

NIST, 2013. Fire Dynamics Simulator [WWW Document]. URL http://www.nist.gov/el/fire_research/fds_smokeview.cfm

Papanikolaou, E., Venetsanos, A.G., Cerchiara, G.M., Carcassi, M., Markatos, N., 2011. CFD simulations on small hydrogen releases inside a ventilated facility and assessment of ventilation efficiency. Int. J. Hydrogen Energy 36, 2597–2605.

Patankar, S.., Spalding, D.., 1972. A calculation procedure for heat, mass and momentum transfer in three-dimensional parabolic flows. Int. J. Heat Mass Transf. 15, 1787–1806.

Peters, N., 1984. Laminar diffusion flamelet models in non-premixed turbulent combustion. Prog. Energy Combust. Sci. 10, 319–339.

Peters, N., 1986. Laminar flamelet concepts in turbulent combustion. Symp. Combust. 21, 1231–1250.

Pitts, W.M., Yang, J.C., Blais, M., Joyce, A., 2012. Dispersion and burning behavior of hydrogen released in a full-scale residential garage in the presence and absence of conventional automobiles. Int. J. Hydrogen Energy 37, 17457–17469.

Poinsot, T., Veynante, D., 2005. Theoretical and Numerical Combustion, Second. ed. Edwards, Philadelphia.

Poling, B., Prausnitz, J., O'Connell, J., 2001. The Properties of Gases and Liquids, Fifth. ed. McGraw-Hill.

Pope, S.B., 1976. The probability approach to the modelling of turbulent reacting flows. Combust. Flame 27, 299–312.

Prasad, K., 2014. High-pressure release and dispersion of hydrogen in a partially enclosed compartment: Effect of natural and forced ventilation. Int. J. Hydrogen Energy 39, 6518–6532.

Prasad, K., Pitts, W.M., Yang, J.C., 2010. Effect of wind and buoyancy on hydrogen release and dispersion in a compartment with vents at multiple levels. Int. J. Hydrogen Energy 35, 9218–9231.

Prasad, K., Pitts, W.M., Yang, J.C., 2011. A numerical study of the release and dispersion of a buoyant gas in partially confined spaces. Int. J. Hydrogen Energy 36, 5200–5210.

Pritchard, D.K., Royle, M., Willoughby, D., 2009. Installation permitting guidance for hydrogen and fuel cell stationary applications : UK version RR715 Installation permitting guidance for hydrogen and fuel cell stationary applications : UK version.

Raj, P.K., 2008. A review of the criteria for people exposure to radiant heat flux from fires. J. Hazard. Mater. 159, 61–71.

Ramamurthi, K., Bhadraiah, K., Murthy, S.S., 2009. Formation of flammable hydrogen–air clouds from hydrogen leakage. Int. J. Hydrogen Energy 34, 8428–8437.

Ranga Dinesh, K.K.J., Jiang, X., Kirkpatrick, M.P., Malalasekera, W., 2012.

Combustion characteristics of H2/N2 and H2/CO syngas nonpremixed flames. Int. J. Hydrogen Energy 37, 16186–16200.

Ranga Dinesh, K.K.J., Jiang, X., Malalasekera, W., Odedra, A., 2013. Large eddy simulation of fuel variability and flame dynamics of hydrogen-enriched nonpremixed flames. Fuel Process. Technol. 107, 2–13.

Reaction Design, 2014. Chemkin [WWW Document]. URL http://www.reactiondesign.com/products/chemkin/

Rocourt, X., Awamat, S., Sochet, I., Jallais, S., 2014. Vented hydrogen–air deflagration in a small enclosed volume. Int. J. Hydrogen Energy 3–7.

Rodi, W., 1980. Turbulence Models and their Applications in Hydraulics - A State of the Art Review, Third. ed. IAHR.

SAE, 2012. SAE J2600.

SAE, 2014a. SAE J2601.

SAE, 2014b. SAE J2799.

Saffers, J.-B., 2010. Principles of hydrogen safety engineering. University of Ulster.

Saffers, J.-B., Molkov, V.V., 2014. Hydrogen safety engineering framework and elementary design safety tools. Int. J. Hydrogen Energy 39, 6268–6285.

Sandrock, G., Thomas, G., 2010. Hydride Databases Introduction - Hydrogen Storage Materials.

Sathiah, P., Komen, E., Roekaerts, D., 2014. The role of CFD combustion modeling in hydrogen safety management – III: Validation based on homogeneous hydrogen–air–diluent experiments. Nucl. Eng. Des.

Sathiah, P., van Haren, S., Komen, E., Roekaerts, D., 2012. The role of CFD combustion modeling in hydrogen safety management—II: Validation based on homogeneous hydrogen–air experiments. Nucl. Eng. Des. 252, 289–302.

Schaal, E., 2015. 10 Electric Vehicles With the Best Range in 2015 [WWW Document]. URL http://www.cheatsheet.com/automobiles/top-10-electric-vehicles-with-the-longest-driving-range.html/?a=viewall (accessed 2.9.16).

Schmidt, D., 1999. Numerical simulation of hydrogen gas releases between buildings. Int. J. Hydrogen Energy 24, 479–488.

Shih, T.H., Liou, W.W., Shabbir, A., Yang, Z., Zhu, J., 1994. A New K-epsilon Eddy Viscosity Model for High Reynolds Number Turbulent Flows: Model Development and Validation, NASA Technical Memorandum 106721. Cleveland, Ohio, USA.

Shishehgaran, N., Paraschivoiu, M., 2014. CFD based simulation of hydrogen release through elliptical orifices. Int. J. Hydrogen Energy 1–7.

Smagorinsky, J., 1963. General Circulation Experiments with the Primitive Equations. I. The Basic Experiment. Mon. Weather Rev. 91, 99–164.

Spalart, P., Allmaras, S.A., 1992. A One-Equation Turbulence Model for Aerodynamic Flows. AIAA.

Spalding, D.B., 1971. Mixing and chemical reaction in steady confined turbulent flames. Symp. Combust. 13, 649–657.

Stewart, C., 2010. Blast Injuries ”True Weapons of Mass Destruction”. University of Oklahoma.

Strohle, J., Myhrvold, T., 2006. Reduction of a detailed reaction mechanism for hydrogen combustion under gas turbine conditions. Combust. Flame 144, 545–557.

Strohle, J., Myhrvold, T., 2007. An evaluation of detailed reaction mechanisms for hydrogen combustion under gas turbine conditions. Int. J. Hydrogen Energy 32, 125–135.

Swain, M., 1996. Passive ventilation systems for the safe use of hydrogen. Int. J. Hydrogen Energy 21, 823–835.

Swain, M., 1998. Proceedings of the 1998 U.S. DOE Hydrogen Program Review NREL/CP-570-25315.

Swain, M., 2001. Fuel Leak Simulation. In: Department of Energy Hydrogen Program Review.

The Committee on Climate Change, 2015. The Fifth Carbon Budget.

Tobin, D., 2015. The future of hydrogen filling stations in Britain [WWW Document]. URL http://www.driving.co.uk/news/the-future-of-hydrogen-filing-stations-in-britain/ (accessed 2.9.16).

Tolias, I.C., Venetsanos, A.G., Markatos, N., Kiranoudis, C.T., 2014. CFD modeling of hydrogen deflagration in a tunnel. Int. J. Hydrogen Energy 39, 20538–20546.

Turns, S.R., 2000. An Introduction to Combustion, Second. ed. McGraw-Hill.

U.S. DOE, 2009. A Comparison of Hydrogen and Propane Fuels [WWW Document]. URL http://cafr1.com/Hydrogen_vs_Propane.pdf (accessed 6.21.17).

U.S. DOE, 2015. Comparative Properties of Hydrogen and Other Fuels [WWW Document]. URL http://hydrogen.pnl.gov/hydrogen-data/comparative-properties-hydrogen-and-other-fuels (accessed 6.21.17).

Vaughan, A., 2015. The future is here: mass-market hydrogen cars take to Britain’s roads [WWW Document]. URL http://www.theguardian.com/environment/2015/nov/04/the-future-is-here-mass-market-hydrogen-cars-take-to-britains-roads (accessed 2.9.16).

Venetsanos, a. ., Huld, T., Adams, P., Bartzis, J.., 2003. Source, dispersion and combustion modelling of an accidental release of hydrogen in an urban environment. J. Hazard. Mater. 105, 1–25.

Versteeg, H.K., Malalasekera, W., 2007. An Introduction to Computational Fluid Dynamics: The Finite Volume Method, Second. ed. Pearson Education Limited.

Veynante, D., Vervisch, L., 2002. Turbulent combustion modeling. Prog. Energy Combust. Sci. 28, 193–266.

Warnatz, J., Maas, U., Dibble, R.., 1999. Combustion; Physical and Chemical Fundamentals, Modeling and Simulation, Second. ed. Springer-Verlag.

Wilcox, D.C., 1988. Reassessment of the Scale-determining Equation for Advanced Turbulence Models. AIAA 26, 1299–1310.

Wilcox, D.C., 1993. Turbulence Modelling for CFD. DCW Industries Inc.

World Nuclear Organisiation, 2015. Fukushima Disaster [WWW Document]. URL http://www.world-nuclear.org/info/safety-and-security/safety-of-plants/fukushima-accident/ (accessed 1.26.16).

Young, D., Munson, B., Okiishi, T., Huebsch, W., 2012. Introduction to Fluid Mechanics, Fifth. ed. John Wiley & Sons, Inc.

Zap Map, 2016. Map of charging points for electric car drivers in UK: Zap-Map [WWW Document]. URL https://www.zap-map.com/live/ (accessed 7.27.16).

Zhang, J., Delichatsios, M. a., Venetsanos, a. G., 2010. Numerical studies of dispersion and flammable volume of hydrogen in enclosures. Int. J. Hydrogen Energy 35, 6431–6437.

Zipf, R.., Cashdollar, K.L., n.d. Explosions and Refuge Chambers [WWW Document]. URL https://www.cdc.gov/niosh/docket/archive/pdfs/niosh-125/125-explosionsandrefugechambers.pdf (accessed 6.20.17).

Züttel, A., 2003. Materials for hydrogen storage. Mater. Today 6, 24–33.